**Shower Development of High Energy Gluons in the Quark Gluon Plasma**

Omar Ashraf Aly Mohamed Elgedawy

Alexandria, Egypt

Bachelor of Science Physics of Universe, University of Science and Technology at

Zewail City, 2017

A Dissertation submitted to the Graduate Faculty

of the University of Virginia in Candidacy for the Degree of

Doctor of Philosophy

Department of Physics

University of Virginia

August 2023

Peter Arnold, Chair

Diana Vaman

Julian Heeck

Zhi-Yun Li

ii

# Shower Development of High Energy Gluons in the Quark Gluon Plasma

Omar Ashraf Aly Mohamed Elgedawy

(ABSTRACT)

Jets produced from colliding two heavy nuclei play an important role in understanding properties of the Quark Gluon Plasma. During their travel through the medium, high energy partons lose energy through splitting processes like bremsstrahlung and pair production, induced by elastic scatterings with the medium. In the high energy limit, these splitting processes are coherent over large distances and the underlying elastic scatterings can no longer be treated as quantum mechanically independent, leading to a suppression of the splitting rate known as the Landau-Pomeranchuk-Migdal effect. An important question is whether consecutive splittings are themselves quantum mechanically independent or instead overlap significantly. Previously, the overlap of splitting rates has been calculated in the soft bremsstrahlung limit and it was found that such corrections are large but can be absorbed into an effective value of the jet-quenching parameter $\hat{q}$ that characterises properties of the medium. In ref [50, 56], we investigated a measure of overlap effects that cannot be absorbed into an effective value of $\hat{q}$ in the simplest theoretical situation, which includes imagining a very large, static, homogeneous medium and taking the large $N_c$ limit. The latter assumption is challenged in ref [49], where we calculated the $1/N_c^2$ correction to the previous $N_c=\infty$ results for overlap $g{\to}gg{\to}ggg$ of two consecutive gluon splittings $g{\to}gg$. We found that, at order $1/N_c^2$, there is interesting and non-trivial color dynamics that must be accounted for during the overlap of formation time.

# Dedication

*To my grandparents and my friend Mohamed Ayman Moshtohry, in loving memory.*

# Acknowledgments

I am thankful to God for giving me the strength to complete my PhD and write this dissertation. I would also like to thank my advisor and mentor Peter Arnold who is not only one of the smartest persons I have ever met, but also one of the most understanding and kind persons you could ever meet. He has been always a source of inspiration and guidance in physics and life too. I will always be grateful to him. I would like also to thank all my professors here at UVA especially Diana Vaman. I am also grateful to all my teachers throughout my education especially Ali Nassar and Sayed Abdelmoneim. I would also like to thank my parents, my siblings and my friends for their continued love and support throughout my life. Most importantly, I could not have undertaken this journey without my wife, Arwa. Her love and belief in me has kept my spirits and motivation high during this process while being a graduate student herself. Thank you for being my muse, editor, proofreader and best friend. I love you.

# Contents

# List of Figures

# List of Tables

# Chapter 1

# Introduction

A few millionths of a second after the Big Bang, the universe was filled with a dense soup made of all kinds of particles moving at speed close to the speed of light. This state was dominated by quarks and gluons which are normally bound together in protons and neutrons and other hadrons. In this extreme temperature and density, quarks and gluons were free to move on their own in what is called a quark-gluon plasma (QGP). Collisions of large nuclei at the Relativistic Heavy Ion Collider (RHIC) and the Large Hadron Collider (LHC) create a plasma of quarks and gluons with properties similar to the one that existed shortly after the Big Bang. This hot state of matter lies at the intersection of nuclear physics with many-body quantum field theory, relativistic fluid dynamics, and condensed matter, probing the dynamical properties of quarks and gluons at extreme densities and temperature. In such collisions, the hundreds of protons and neutrons in the nuclei smash into one another at energies of order trillion electron volts. This forms a fireball in which everything melts into a quark-gluon plasma. This fireball will instantly cool down, and the individual quarks and gluons (partons) recombine into ordinary matter. For example, mesons as kaons and pions are (roughly speaking) made of a quark and an anti quark; hadrons like protons and neutrons are made of three quarks. In an initial heavy-ion collision, pairs of quarks and gluons may happen to collide into each other and scatter in opposite directions. This clump of energy condenses to a jet of pions, kaons and
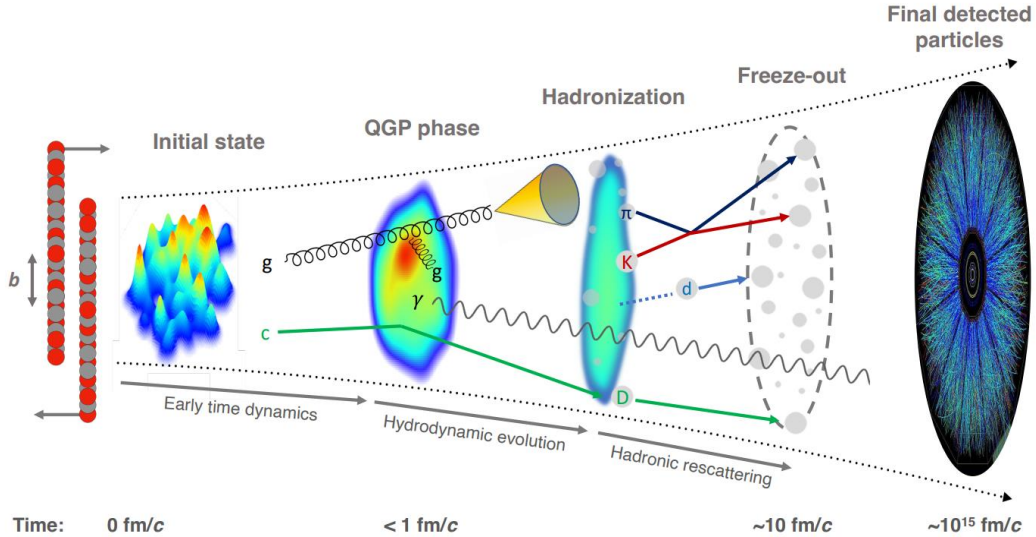
Figure 1.1: The time evolution of a high energy heavy ion collision. As the colliding nuclei recede from each other, a large amount of energy is deposited in a small region of space and in a short duration of time. The matter thus created may have very high energy density and temperature, sufficient to form a baryon free region of QGP. The hot and dense plasma may not be initially in thermal equilibrium. Subsequently, thermal equilibrium might set in, after which the evolution may be governed by the laws of thermodynamics. As the plasma expands and cools, hadronization takes place and after some time the interactions seize (freeze-out)[57].

other particles. This was first observed in 2003 in the STAR and PHENIX experiments at Brookhaven National Laboratory's Relativistic Heavy Ion Collider (RHIC) in the US [15, 14, 16, 12, 13]. They also found that an outgoing jet may interact with the surrounding hot, dense medium, as if moving through a dense liquid that slows down the jet. This can reduce the energy of a jet, causing large imbalances of energy between opposite jets. The more a jet travels through the QGP, the more energy it loses. So, the degree of jet quenching and the jets' orientation, directionality, composition, and how they transfer energy and momentum to the medium will help us
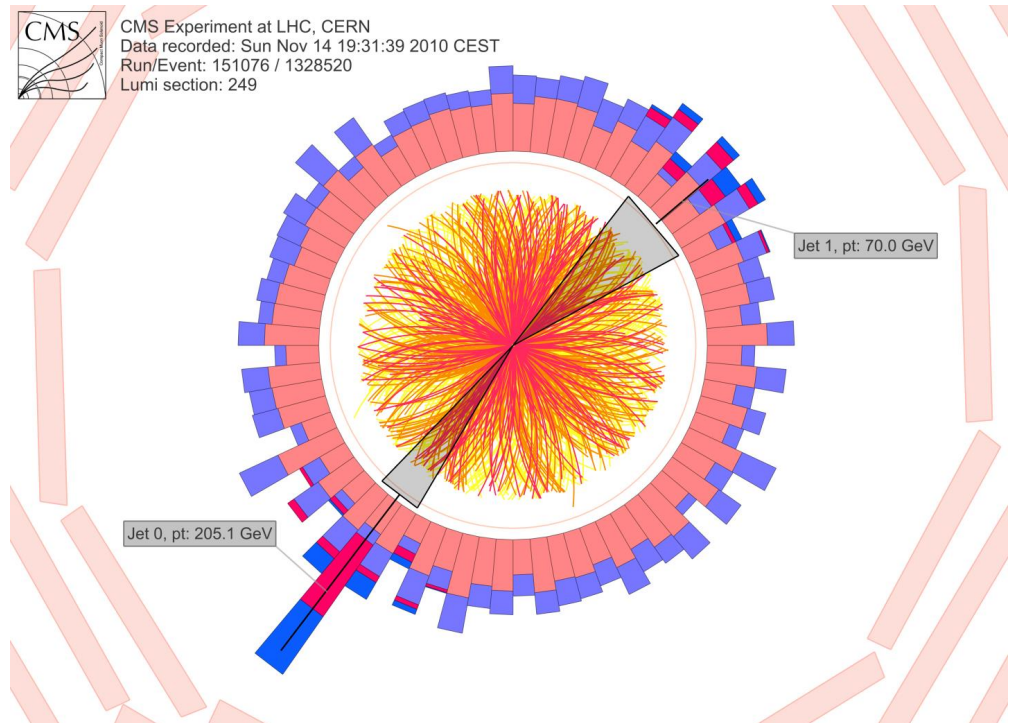
Figure 1.2: LHC lead-lead collision in the CMS detector showing particles (yellow and red tracks) radiating from the collision point. The particles deposit their energy in the calorimeters (salmon, mauve, red and blue towers with a height proportional to energy). Two back-to-back jets are seen with a large energy asymmetry, as expected from the jet-quenching mechanism [23].

understand the properties of the quark-gluon plasma. Recently the ALICE, ATLAS and CMS experiments at CERN's Large Hadron Collider (LHC) [29, 27, 26, 58, 25, 24, 23] have confirmed the phenomenon of jet quenching in heavy-ion collisions. See fig 1.2.

## 1.1 The Landau-Pomeranchuk-Migdal effect

We now discuss the importance of splitting processes for jet energy which could happen by two processes: pair production or hard bremsstrahlung. When repeated,
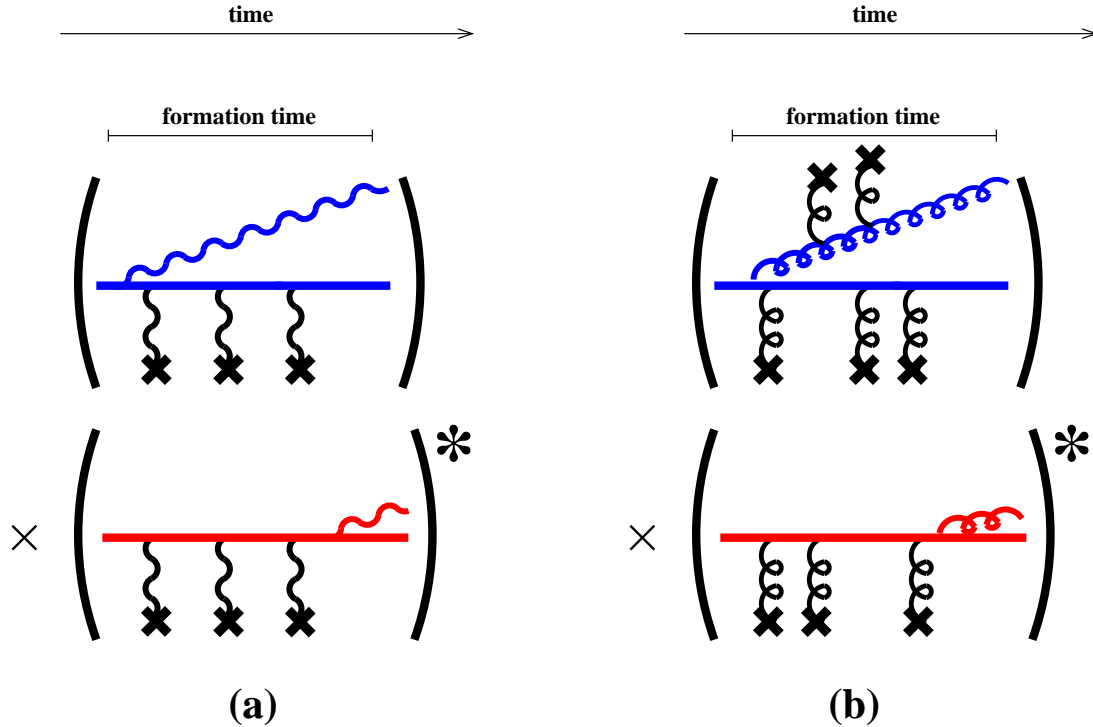
Figure 1.3: Examples of interference terms contributing to the LPM effect in (a) QED and (b) QCD. Blue represents high-energy particles in the amplitude and red represents for high-energy particles in the conjugate amplitude. The curly line ending in a cross represents the electromagnetic or gluonic fields in the medium created by sources, such as by a nucleus or a passing thermal parton.

these processes produce a shower of lower energy particles. We start by a simple example to show qualitatively the main idea. Consider a non-relativistic electron going through the atmosphere. As it is going through, it receives transverse kicks that offer a chance for a bremsstrahlung. Naively, the probability for splitting is of order $\alpha_{EM}$ per collision. For a photon with a large wavelength compared to the mean free path for collisions, it cannot resolve details smaller than its wavelength, and so this will create a region of *fuzziness* around the time of splitting. In particular, one cannot tell from which particular scattering the photon originated or whether it originated from a single scattering or multiple scatterings.

Now imagine looking at this process from the frame of a rocket going at speed near the speed of light. In this frame, the particles including the photon have very high energy and the process is more collinear. Nonetheless, because of time dilation, the circular region of fuzziness will become *elongated* like an ellipse. The duration of this region is called the *formation time* of the bremsstrahlung photon. The bigger the formation time than the mean free time, the more collisions the electron would have during the photon formation time. So we cannot determine at which moment or from which collision the electron emitted the photon, and the probability for splitting becomes of order $\alpha_{EM}$ per *formation time*. This suppression of the rate is called the Landau-Pomeranchuk-Migdal (LPM) effect [2, 1, 3] and was discovered in the 1950s. In the language of Feynman diagrams, the LPM effect represents important interferences between splitting before and after a sequence of elastic collisions from the medium as in fig 1.3a for QED and fig 1.3b for QCD. The analysis for the LPM effect in QCD was worked out in the 1990s by Baier et al. [7, 9] and Zakharov [8], known collectively as BDMPS-Z.

## 1.2   A correction to the LPM effect

One could extend this idea and ask whether consecutive *splittings* of the high energy particle, and not only consecutive collisions with particles in the medium, happen within one formation time. That is, once we use the BDMPS-Z formalism to calculate the rate for a single splitting, can we treat consecutive splittings as independent and simply use a Monte Carlo (where particles are treated classically between splittings) to compute the development of the shower which enable us to answer the question about energy loss? If so, we call this a *weakly-coupled* shower. See figure 1.4 for a
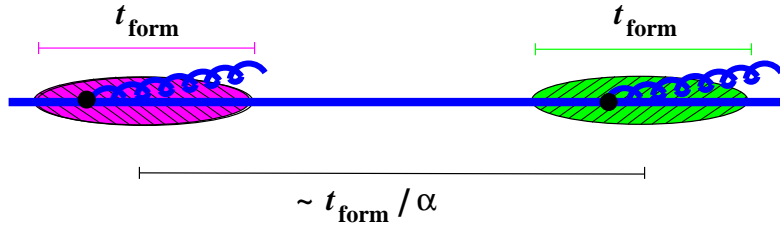
Figure 1.4: The hierarchy of scales for typical consecutive splitting, if the relevant $\alpha$ is small and if one ignores logarithmic enhancements in QCD associated with one of the daughters becoming soft. (The cartoon in this picture assumes that the momenta of the two bremsstrahlung gauge bosons are parametrically similar. In QCD, formation times shrink as bremsstrahlung gluons become soft.)[34]
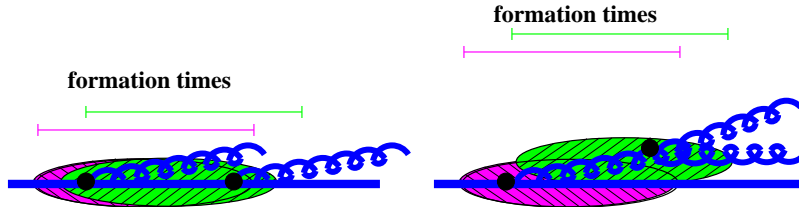


Figure 1.5: Two consecutive splittings that are close enough that their formation times overlap. Each formation time region is depicted by a green or blue, hatched oval. [34]

typical picture of splitting if one considers $\alpha_s$ to be small.

Or is there a significant contribution from processes where the formation time associated with consecutive splittings overlap, as depicted in fig 1.5? In that picture, one cannot treat different splittings as quantum mechanically independent, and any classical picture of the shower breaks down. We call this a *strongly-coupled* shower. It is worth noting here that we are not asking whether the QGP is strongly or weakly coupled, our analysis applies for both cases, we are asking whether the *in-medium shower development* of very high energy partons is strongly or weakly coupled. This has been a long-standing problem in field theory and several authors [35, 32, 33] previously analyzed this issue for QCD at leading-log order, which arises from the limit where one bremsstrahlung gluon is soft compared to the other very-high energy partons.

In our case of splitting of a high-energy particle of energy $E$ in a thick quark-gluon plasma of temperature $T$, "soft" gluon energy $\omega$ means $T \ll \omega \ll E$, which is the range that contributes to the double logarithm. The authors of [35, 32, 33] found that the probability of such overlapping at high energy is large because it is enhanced by a double logarithm $\alpha_{\rm s}(\mu) \ln^2(E/T)$ where the typical scale $\mu$ of transverse momentum transferred from the medium during the formation time is of order

$$\mu \sim \sqrt{\hat{q} t_{\rm form}} \sim (\hat{q}\omega)^{1/4}. \tag{1.1}$$

This is also the typical scale of the relative transverse momenta of the two daughters of the splitting. However, they found that these soft-bremsstrahlung effects can be absorbed into an effective value $\hat{q}_{\rm eff}$ of the medium parameter $\hat{q}$ that encodes the rate of transverse momentum kicks to a high-energy particle by the medium subsequently. In our situation here, that means that the potentially large effects of a soft gluon bremsstrahlung overlapping a hard splitting process can be absorbed into the original LPM/BDMPS-Z calculation of the hard $g{\to}gg$ splitting rate by taking $\hat{q} \to \hat{q}_{\rm eff}(E) = \hat{q} + \delta\hat{q}$ in that calculation, where $\delta\hat{q}(E) \sim \alpha_{\rm s}\hat{q} \ln^2(E/T)$. They also showed (following [30]) how to resum leading logs to all orders in $\alpha_{\rm s}(\mu)$. The authors of refs.[34, 37, 39, 38, 41, 47, 52] avoided taking the limit where one bremsstrahlung gluon is soft and provided the answer for the general case where neither splitting is necessarily soft. However, the analysis of this more general case has used the large-$N_{\rm c}$ approximation. We will be using these rates throughout our work. In ref [50, 56], we showed a method for investigating the size of overlapping formation times that *cannot* be absorbed into $\hat{q}$.

## 1.3 Review of the calculation

### 1.3.1 Assumptions

The formalism for doing this calculation is challenging, and so we take the simplest possible theoretical situation outlined in ref.[50, 56], which mostly follow the rate calculation developed in refs.[34, 37, 39, 38, 41, 47, 52]. (i) Imagine a quark-gluon plasma that is static, homogeneous, and large enough to completely stop the shower. (ii) Imagine that we start with a single high-energy parton that is very close to on-shell. This means we are ignoring the initial shower of decreasing virtuality that takes place when a high-energy parton scatters from a nucleon in a relativistic collision. (iii) Treat the elastic scattering of high-energy partons from the medium in multiple scattering ($\hat{q}$) approximation, which is that the typical total transverse momentum change $p_\perp$ after traveling through a length $L$ of the medium behaves like a random walk, $\langle p_\perp^2 \rangle = \hat{q}L$, where the proportionality constant $\hat{q}$ is determined by the medium. (iv) Take the large-$N_c$ limit, where $N_c$ is the number of quark colors. However, this assumption will be avoided in chapter 3. (v) Focus on gluon-initiated showers, and so the only relevant splittings are $g \to gg$ in the large-$N_c$ limit.

### 1.3.2 Diagrams

The LPM effect calculation, which was generalized from QED to QCD collectively by BDMPS-Z, when specialized to an infinite medium in the $\hat{q}$ approximation gives

the in-medium $g \rightarrow gg$ splitting rate[1]

$$\left[\frac{d\Gamma}{dx}\right]^{\mathrm{LO}} = \frac{\alpha_{\mathrm{s}} P_{g \rightarrow gg}(x)}{2\pi} \sqrt{\frac{(1-x+x^2)\hat{q}_{\mathrm{A}}}{x(1-x)E}} \qquad (1.2)$$

for energies $E \rightarrow xE + (1-x)E$. the subscript on $\hat{q}_{\mathrm{A}}$ indicates the $\hat{q}$ appropriate for the adjoint color representation, i.e. for gluons, and $C_{\mathrm{A}} = N_{\mathrm{c}}$ is the adjoint-representation quadratic Casimir. The $P_{g \rightarrow gg}(x)$ is the Dokshitzer-Gribov-Lipatov-Altarelli-Parisi (DGLAP) splitting function.[2] We will refer to (1.2) as the "leading-order" (LO) result for $g \rightarrow gg$. What we mean by a leading order rate is that it is a single splitting which includes the effects of an arbitrary number of interactions with the medium. We will adopt Zakharov's picture [**Zakharov2**, 8] of LPM rate calculations, which is to think of the rate for $g \rightarrow gg$ as time-ordered diagrams, such as fig. 1.6, combining the amplitude for $g \rightarrow gg$ (blue) with the conjugate amplitude (red). Then, Zakharov thought of fig. 1.6b as three particles propagating forward in time which, in the high-energy limit, could be described (between the splitting vertices) as a 3-particle, two-dimensional quantum mechanics problem in the transverse plane. The medium-averaged effect of interactions with the medium can be described by a non-Hermitian, effective "potential energy" between the three particles in the quantum mechanics problem. So the $\hat{q}$ approximation corresponds to a harmonic oscillator problem (with imaginary-valued spring constants). This is discussed more in refs. [34] and [48].

---

[1]It's difficult to figure out whom to reference for the first appearance of (1.2). BDMS [10] give the $q \rightarrow qg$ formula in their eq. (42b) [with the relevant limit here being the infinite volume limit $\tau_0 \rightarrow \infty$ for their time $\tau_0$]. They then discuss elements of the $g \rightarrow gg$ case after that but don't quite give an explicit formula for the entire rate. (They are not explicit about the formula for $\omega_0$.) Zakharov makes a few general statements about the $g \rightarrow gg$ case after eq. (75) of ref. [11]. As an example from ten years later, the explicit formula is given by eqs. (2.26) and (4.6) of ref. [21] in the case where $s$ represents a gluon.

[2]Our $P_{g \rightarrow gg}(x) = 2C_{\mathrm{A}}(1 - x + x^2)^2/x(1 - x)$ does *not* contain the pieces of the usual DGLAP splitting function used to include the effect of virtual diagrams. In particular, the $1/(1-x)$ in our formula for $P_{g \rightarrow gg}$ is just the ordinary function $1/(1-x)$ and not the distribution $1/(1-x)_+$, and our $P_{g \rightarrow gg}$ does not contain a $\delta$-function term $\delta(1-x)$. .
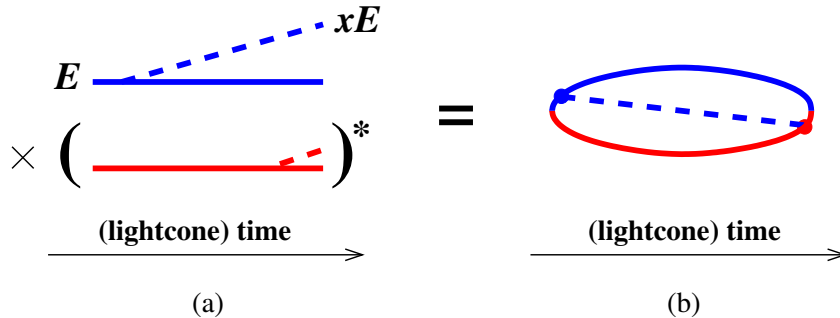
Figure 1.6: (a) A time-ordered contribution to the LO rate for single splitting $g \to gg$, with amplitude in blue and conjugate amplitude in red. (b) A single diagram representing this contribution to the rate. In both cases, all lines implicitly interact with the medium. We need not follow particles after the emission has occurred in both the amplitude and conjugate amplitude because we will consider only the $p_\perp$-integrated rate. (See, for example, section 4.1 of ref. [34] for a more explicit argument, although applied there to a more complicated diagram.) Nor need we follow them before the first emission because we approximate the initial particle as on-shell. Only one of the two time orderings that contribute to the LO rate is shown above.

The effects of two overlapping formation times (two $g{\to}gg$ splittings), such as fig. 1.7, are referred to as one type of next-to-leading-order (NLO) effect. Since there are four high-energy splitting vertices in this rate diagram, it is suppressed by one power of high-energy $\alpha_{\rm s}(\mu)$ compared to the leading-order splitting of fig. 1.6. In fig. 1.8, we show examples of diagrams that contribute to the NLO rate, using the same convention as in fig. 1.6b. The subtraction used in fig. 1.8 means that our rates represents the difference between (i) a full calculation of (potentially overlapping) $g \to gg \to ggg$ and (ii) approximating a double splitting as two independent, consecutive single splittings $g{\to}gg$ that each occur with the LO single splitting rate (1.2).[3] There are also virtual corrections to single splitting $g{\to}gg$ that contribute to the NLO rate (at the same order in $\alpha_{\rm s}(\mu)$), for which we show a few examples in fig. 1.9. There are also direct $g{\to}ggg$ processes that also contribute at the same order in $\alpha_{\rm s}(\mu)$ which we show examples of in fig. 1.10. The complete list of the diagrams contained in our

---

[3]The key importance of this subtraction is explained in section 1.1 of ref. [37].
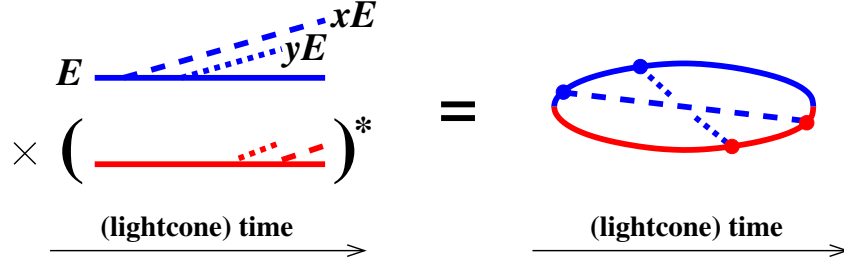
Figure 1.7: A particular example of two overlapping splittings.
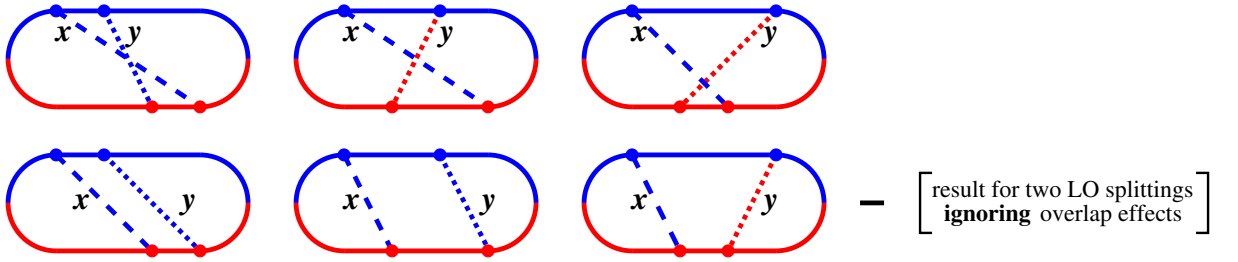


Figure 1.8: Examples of diagrams contributing to the effects of overlapping formation times for two splittings $g \rightarrow gg \rightarrow ggg$. The first and second rows (when combined with their conjugates and appropriate permutations of the daughters) were analyzed in refs. [34] and [37], respectively.

analysis could be found in refs. [47, 52].

Note that we will always refer to high-energy $\alpha_{\rm s}(\mu)$ by just using $\alpha_{\rm s}$ unless stated otherwise. We will discuss later the energy dependence of $\mu$.

### 1.3.3   Notation for rates

We will refer to the leading-order $g \rightarrow gg$ rate, its NLO correction, and the $g \rightarrow ggg$ rate as

$$\left[\frac{d\Gamma}{dx}\right]^{\rm LO}, \qquad \left[\Delta\frac{d\Gamma}{dx}\right]^{\rm NLO}_{g \rightarrow gg}, \qquad \left[\Delta\frac{d\Gamma}{dx\,dy}\right]_{g \rightarrow ggg} \tag{1.3}$$

following the notation of ref. [47]. The $[\Delta\,d\Gamma/dx\,dy]_{g \rightarrow ggg}$ represents both (i) overlap corrections to two consecutive splittings, such as in fig. 1.8, and (ii) processes
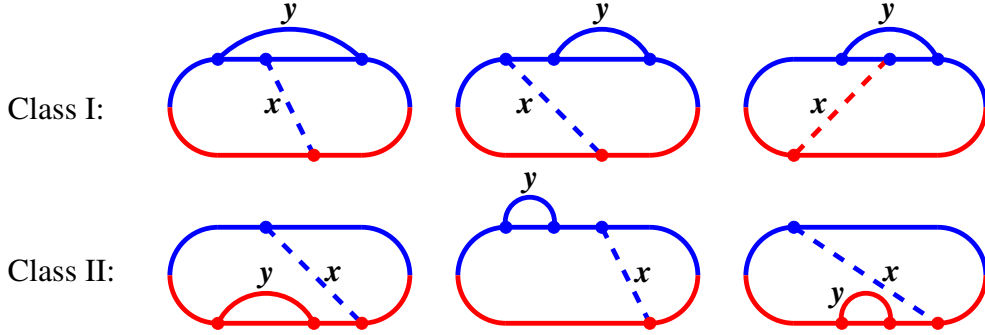
Figure 1.9: Some examples from ref. [47] of NLO virtual corrections to single splitting $g{\to}gg$.
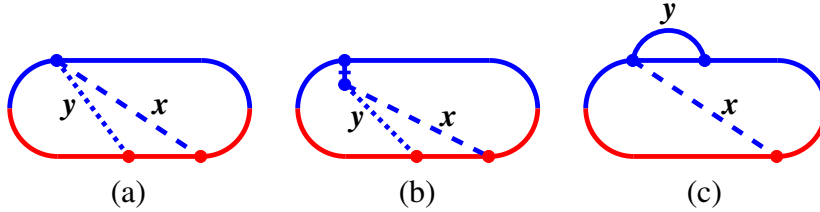


Figure 1.10: Some examples from ref. [52] that involve (a,c) a 4-gluon vertex or (b) exchange of a longitudinally polarized gluon (denoted by the vertical line crossed by a bar) in Light Cone Perturbation Theory (LCPT).

involving direct $g{\to}ggg$, such as figs. 1.10a,b. In both case, energy is being split as $E \to xE+yE+(1-x-y)E$. The symbol "$\Delta$" in front of that rate means it is a correction to an LO-based calculation of double splitting as two, consecutive, independent $g{\to}gg$ splitting events. Similarly, $[\Delta\, d\Gamma/dx]^{\mathrm{NLO}}_{g\to gg}$ represents the corresponding virtual corrections to single splitting, such as in figs. 1.9 and 1.10c, and so energy is being split as $E \to xE+(1-x)E$. The rates (1.3) are given in refs. [47, 52],[4] which are calculated using Light Cone Perturbation Theory (LCPT). We will refer to $x$ and $y$ simply as "energy fractions" in our applications.[5] However, one should define $x$ and $y$ by

---

[4]More specifically, see Appendix A of ref. [47], but supplement the formulas there as explained in Appendix A of ref. [52] in order to include diagrams like fig. 1.10. Various pieces of these formulas are taken from earlier papers [34, 37, 39, 38, 41].

[5]More specifically, the difference between $p^+/P^+$ and $p^0/E$ is suppressed by $p_\perp^2/E^2 \sim \hat{q}t_{\mathrm{form}}/E^2 \sim \hat{q}^{1/2}/E^{3/2}$, and in all of our analysis we ignore effects that are suppressed by pow-

the splitting of lightcone longitudinal momentum: $P^+ \to xP^+ + yP^+ + (1-x-y)P^+$ for $g \to ggg$ and $P^+ \to xP^+ + (1-x)P^+$ for $g \to gg$. Since the splittings relevant to shower development are high energy and nearly collinear, we will be sloppy and call them "energy fractions".

For virtual diagrams, the rate calculation involves integration over the lightcone longitudinal momentum fraction $y$ of one of the loop lines, as labeled in figs. 1.9 and 1.10c. Because of using LCPT, $p^+$ of every (transverse-polarized) gluon must be non-negative which puts constraints on the allowed range of $y$ in the virtual diagrams. As shown in ref. [47, 52], the virtual diagrams can be divided into two classes. Class I is shown at the top line of fig. 1.9 and it means that (i) $y$ should be integrated over $0 < y < 1-x$ and (ii) the substitution $x \to 1-x$ generates a distinct set of diagrams that must also be included. Class II is shown at the bottom line of fig. 1.9, and it means that (i) $y$ should be integrated over $0 < y < 1$ and (ii) the substitution $x \to 1-x$ does not generate any new diagrams. Given these notations, one can write the virtual diagrams contribution as,

$$
\begin{aligned}
\left[\Delta\frac{d\Gamma}{dx}\right]_{g\to gg}^{\mathrm{NLO}} &= \left(\left[\Delta\frac{d\Gamma}{dx}\right]_{\mathrm{class\,I}}^{\mathrm{NLO}}\right) + (x \to 1-x) + \left[\Delta\frac{d\Gamma}{dx}\right]_{\mathrm{class\,II}}^{\mathrm{NLO}} \\
&= \left(\int_0^{1-x} dy \left[\Delta\frac{d\Gamma}{dx\,dy}\right]_{\mathrm{class\,I}}^{\mathrm{NLO}}\right) + (x \to 1-x) + \int_0^1 dy \left[\Delta\frac{d\Gamma}{dx\,dy}\right]_{\mathrm{class\,II}}^{\mathrm{NLO}},
\end{aligned}
$$

$$(1.4)$$

where the subscripts refer to Class I and Class II virtual diagrams.[6] The Virtual diagrams were calculated in the $\overline{\mathrm{MS}}$ ultraviolet (UV) renormalization, and so $\alpha_{\mathrm{s}}(\mu)$ will refer to the $\overline{\mathrm{MS}}$ coupling. The $y$-integral will be done numerically. In ref. [47], it was

---

ers of $E$.

[6]Following ref. [47], our convention is that, when there is a loop in the amplitude (or a loop in the conjugate amplitude), the loop symmetry factor (if any) is already accounted for in the formulas for $[\Delta d\Gamma/dx\,dy]_{\mathrm{class\,I}}^{\mathrm{NLO}}$ and $[\Delta d\Gamma/dx\,dy]_{\mathrm{class\,II}}^{\mathrm{NLO}}$.

convenient to separate out the piece containing the renormalization scale $\mu$ dependence from the integrals in (1.4) and to integrate that piece analytically. However, we don't need to do that here, and so we will show in appendix A.1 the connection with the rate formulas as they are presented in refs. [47, 52].[7] We will consider the shower made of 1→2 splittings and effective 1→3 splittings. So we find it convenient to use the notation

$$\left[\frac{d\Gamma}{dx}\right]_{1\to2} \equiv \left[\frac{d\Gamma}{dx}\right]^{\mathrm{LO}} + \left[\Delta\frac{d\Gamma}{dx}\right]^{\mathrm{NLO}}_{g\to gg}, \tag{1.5a}$$

$$\left[\frac{d\Gamma}{dx\,dy}\right]_{1\to3} \equiv \left[\Delta\frac{d\Gamma}{dx\,dy}\right]_{g\to ggg}. \tag{1.5b}$$

Since we consider only purely gluonic showers, the daughters of every splitting are identical particles. We will not add the final-state identical particle factors to the differential rates, and so the total rate for any sort of 1→2 or 1→3 splittings would be

$$\Gamma = \frac{1}{2!}\int_0^1 dx \left[\frac{d\Gamma}{dx}\right]_{1\to2} + \frac{1}{3!}\int_0^1 dx \int_0^{1-x} dy \left[\frac{d\Gamma}{dx\,dy}\right]_{1\to3}, \tag{1.6}$$

or, equivalently,

$$\Gamma = \int_{x<1-x} dx \left[\frac{d\Gamma}{dx}\right]_{1\to2} + \int_{y<x<1-x-y} dx\,dy \left[\frac{d\Gamma}{dx\,dy}\right]_{1\to3}. \tag{1.7}$$

However, it turns out that the total rate is infrared divergent, so it won't be of much use except in intermediate steps of our derivation. Note that the "1→3" rate (1.5b) can have either sign [37] because, as mentioned earlier, part of it represents an overlap *correction* to a shower of LO 1→2 splittings, and so it can be positive or negative.

---

[7] We've intentionally used subscript names "class I" and "class II" in (1.4) that are different from those used in ref. [47] to avoid confusing the formulas given there, where some pieces have been separated out, with the integrands in (1.4), where they have not. See appendix A.1.

# Chapter 2

# Gluon shower development

In ref. [50, 56], we showed a method for investigating the size of overlapping formation time effects that *cannot* be absorbed into $\hat{q}$, and we presented our results. We start with the idea presented in [44]. Imagine for a moment a shower composed of democratic splittings. The distance between consecutive splittings is of order $t_{\text{form}}/\alpha \sim \alpha^{-1}\sqrt{E/\hat{q}}$, where the typical energy $E$ of the individual shower particles decreases rapidly as the shower develops. So, a shower initiated by a particle of energy $E_0$, moving in the $z$ direction, will therefore stop and deposit all its energy into the medium in a distance of order $\ell_{\text{stop}} \sim \alpha^{-1}\sqrt{E_0/\hat{q}}$, which depends on $\hat{q}$. As a thought experiment, imagine measuring the distribution $\epsilon(z)$ in $z$ of where that energy is deposited into the medium, statistically averaged over many such showers. We do not track the parametrically small spread of the shower in the transverse directions. A qualitative picture is shown in fig. 2.8. We define $\ell_{\text{stop}}$ as the first moment of this distribution:

$$\langle z \rangle \equiv \frac{1}{E_0} \int_0^\infty dz\, z\, \epsilon(z). \tag{2.1}$$

We could also define other features of the distribution such as its width $\sigma = \sqrt{\langle z^2 \rangle - \langle z \rangle^2}$ which are parametrically the same order as $\ell_{\text{stop}} \sim \alpha^{-1}\sqrt{E_0/\hat{q}}$. Naively, the dependence on $\hat{q}$ would then *cancel* in a ratio such as $\sigma/\ell_{\text{stop}}$. In general, one may study any aspect of what we will call the "shape" $S(Z)$ of the energy deposition distribution $\epsilon(z)$. By shape, we mean fig. 2.8 rescaled to units where $\ell_{\text{stop}} = 1$ and normalized to
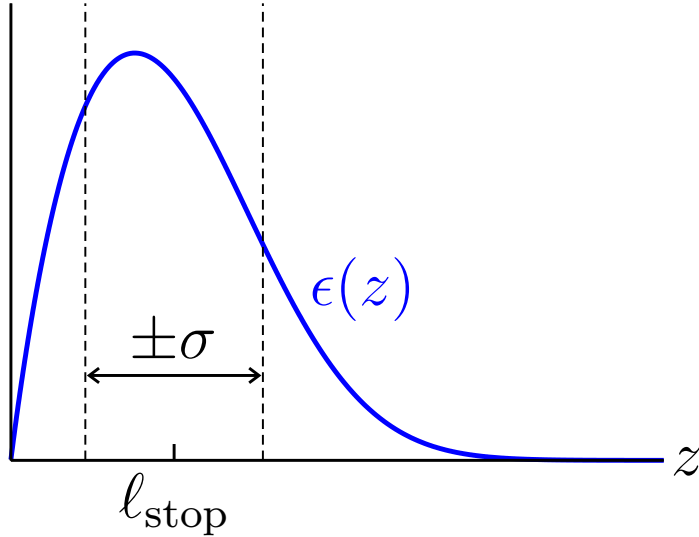
Figure 2.1: Energy deposition distribution $\epsilon(z)$.

have unit area under the curve:

$$S(Z) \equiv \frac{\langle z \rangle}{E_0} \, \epsilon\big(\langle z \rangle Z\big), \tag{2.2}$$

where $Z \equiv z/\langle z \rangle$. Naively, this shape function is insensitive to any physics (such as soft bremsstrahlung) that can be absorbed into the value of $\hat{q}$.

The shape $S(Z)$ and its moments are insensitive to *constant* shifts $\delta\hat{q}$ to $\hat{q}$. However, the potentially double log correction (discussed in 1.2) arising from a soft bremsstrahlung overlapping a hard splitting, is not constant: it depends logarithmically on the energy scale $E$ of the underlying hard splitting. So $\delta\hat{q}$ is different for different splittings in the shower, and those differences do not exactly cancel in $S(Z)$. As discussed in ref. [44] in the specific context of $\sigma/\ell_{\text{stop}}$ (which is the width of $S$), the energy dependence of the double-log corrections from overlapping soft bremsstrahlung will lead to potentially large single-log corrections to the shape — that is, corrections that are $O\big(\alpha_{\text{s}} \ln(E_0/T)\big)$ instead of $O(\alpha_{\text{s}})$. The naive calculation of overlap correc-

tions to $S(Z)$ will not be completely independent of soft bremsstrahlung physics. In subsection 2.1.3 and section 2.2, we discuss how we will overcome this difficulty.

Our results will all be derived in terms of what we call the net rate $[d\Gamma/dx]_{\text{net}}$ for splitting [47], defined as the rate for splittings (including the case of two overlapping splittings) to produce one daughter of energy $xE$ plus any other daughters from a parent of energy $E$. We will be using the formulas for overlapping formation time effects developed in refs. [34, 37, 39, 38, 41, 47, 52], which are extremely long, complicated and time-consuming to evaluate numerically. So, we will present a simple function that fits our numerical results (at first order in overlap effects) for $[d\Gamma/dx]_{\text{net}}$. This function will make our life easier in terms of evaluating the energy deposition distribution $\epsilon(z)$ and its shape $S(Z)$.

## 2.1 The net rate and its factorization

### 2.1.1 Definition and Properties

We define the net rate $[d\Gamma/dx]_{net}$ as the probability per unit time for a splitting of a parent with energy $E$ to create a daughter with energy $xE$ along with any other daughters. For a shower made up of $1 \to 2$ and $1 \to 3$ splittings,

$$\left[\frac{d\Gamma}{dx}\right]_{\text{net}} = \left[\frac{d\Gamma}{dx}\right]_{1\to 2} + \frac{1}{2!} \int_0^{1-x} dy \left[\frac{d\Gamma}{dx\,dy}\right]_{1\to 3} \tag{2.3}$$

if all the particles are identical. The reason for the $\frac{1}{2!}$ factor on the $1 \to 3$ splitting term is that one of the three daughters has been distinguished with having energy $xE$, but we don't want to double count the integration region over the energies of the

other two identical gluons.

Note the total rate is not equal to $\int dx \left[ d\Gamma/dx \right]_{net}$. Instead, it is equal to

$$\Gamma = \int_0^1 dx \, x \left[ \frac{d\Gamma}{dx} \right]_{net}. \qquad (2.4)$$

That's because you can write the right-hand side using (2.3) as

$$\int_0^1 dx \, x \left[ \frac{d\Gamma}{dx} \right]_{net} = \int_0^1 dx \, x \left[ \frac{d\Gamma}{dx} \right]_{1\to 2} + \frac{1}{2!} \int_0^1 dx \, x \int_0^{1-x} dy \left[ \frac{d\Gamma}{dx \, dy} \right]_{1\to 3}. \qquad (2.5)$$

For the $1 \to 2$ integral in (2.5), average (i) the integral with (ii) itself after the change of integration variable $x \to 1 - x$. Since the daughters with energies $(xE \, , \, (1-x)E \, )$ are identical particles, $[d\Gamma/dx]_{1\to 2}$ is symmetric under the change $x \to 1 - x$, and so

$$\int_0^1 dx \, x \left[ \frac{d\Gamma}{dx} \right]_{1\to 2} = \int_0^1 dx \, \frac{x + (1-x)}{2} \left[ \frac{d\Gamma}{dx} \right]_{1\to 2} = \frac{1}{2} \int_0^1 dx \left[ \frac{d\Gamma}{dx} \right]_{1\to 2}. \qquad (2.6)$$

We can do the same for the $1 \to 3$ integral in (2.5) except average over (i) the original integral, (ii) the integral after the change $x \leftrightarrow y$ , and (iii) $x \leftrightarrow 1 - x - y$. These are just certain permutations of the three identical daughters $(xE, yE, (1 - x - y))E$, and so $[d\Gamma/dx]_{1\to 3}$ does not change, and we get

$$\frac{1}{2!} \int_0^1 dx \, x \left[ \frac{d\Gamma}{dx} \right]_{1\to 3} = \frac{1}{2!} \int_0^1 dx \frac{x + y + (1 - x - y)}{3} \left[ \frac{d\Gamma}{dx} \right]_{1\to 3} = \frac{1}{3!} \int_0^1 dx \left[ \frac{d\Gamma}{dx} \right]_{1\to 3}. \qquad (2.7)$$

Comparing the resulting rewriting of (2.5) to (1.6) gives (2.4).

### 2.1.2 IR divergences and factorization

The definition (2.3) is plagued with infrared divergences. First, there are power-law infrared divergences associated with different boundaries $(0, 1-x, 1)$ of the $y$-integration in (2.3) and (1.4), but these divergences cancel each other when all added together. It is possible to rearrange the $y$-integrals so that (i) the IR divergences (for fixed $x$) all become associated with $y \to 0$ and (ii) the terms which generate power-law IR divergences all cancel in the integrand. In particular, ref. [47] showed that (2.3) could be written as

$$\left[\frac{d\Gamma}{dx}\right]_{\text{net}} = \left[\frac{d\Gamma}{dx}\right]^{\text{LO}} + \left[\frac{d\Gamma}{dx}\right]^{\text{NLO}}_{\text{net}} \tag{2.8}$$

with

$$\left[\frac{d\Gamma}{dx}\right]^{\text{NLO}}_{\text{net}} = \int_0^{1/2} dy \left\{ V(x,y)\,\theta(y < \tfrac{1-x}{2}) + V(1-x,y)\,\theta(y < \tfrac{x}{2}) + R(x,y)\,\theta(y < \tfrac{1-x}{2}) \right\}, \tag{2.9}$$

where

$$V(x,y) \equiv \left( \left[\Delta\frac{d\Gamma}{dx\,dy}\right]^{\text{NLO}}_{\text{class I}} + \left[\Delta\frac{d\Gamma}{dx\,dy}\right]^{\text{NLO}}_{\text{class II}} \right) + (y \leftrightarrow 1-x-y), \tag{2.10a}$$

$$R(x,y) \equiv \left[\Delta\frac{d\Gamma}{dx\,dy}\right]_{g\to ggg}. \tag{2.10b}$$

Note that here we use a capital letter for the function $V$ to distinguish it from the lower-case $v$ of ref. [47]. This is a technical point arising from the fact that we use the full NLO virtual rates $\left[\Delta\frac{d\Gamma}{dx\,dy}\right]^{\text{NLO}}_{\text{class I}}$ and $\left[\Delta\frac{d\Gamma}{dx\,dy}\right]^{\text{NLO}}_{\text{class II}}$ here instead of the $\overline{\text{NLO}}$ in ref.[47] (where a piece including the renormalization scale dependence has been separated out). The function $R$ is capitalized for consistency, but it is identical

to the function $r$ in ref.[47]. The $\theta$ functions in (2.9) represent unit step functions $\big[\theta(True) = 1$ and $\theta(False) = 0\big]$, and they just implement the upper limits on the $y$-integration. Using the $\theta$ function is advantageous in combining the integrals so that the power-law IR divergences cancel out. The explicit upper limit $1/2$ on the $y$-integral in (2.9) could just be replaced by $\infty$ because the actual limit of integration for the various terms are implemented by the $\theta$ function. We have put $1/2$ as the upper limit because it is simply the largest any of those limits could ever be.

The power-law IR divergences aren't the only divergence we have; after their cancellation, you are left with an uncanceled IR double-log divergence associated with $y \to 0$ in (2.9). This is the same double log that was originally calculated by considering radiative corrections to $\hat{q}$ in the context of momentum broadening [30]. In our application here, this corresponds to soft radiative corrections to an underlying, hard single-splitting process $\big[d\Gamma/dx\big]^{\mathrm{LO}}$ which gives rise to this double logarithm [35, 32, 33]. Physically, this double log is cut off in the infrared, where the $\hat{q}$ approximation breaks down. If one always uses the $\hat{q}$ approximation (as we do), then the double log must be regularized and/or subtracted. Eq (2.9) also generate a sub-leading single log IR divergence that was extracted analytically in ref.[51] and alternatively derived from the known radiative corrections to $\hat{q}$ in ref. [48]. The small-$y$ behavior of the integral in (2.9) was found to be

$$-\frac{C_{\mathrm{A}}\alpha_{\mathrm{s}}}{4\pi}\left[\frac{d\Gamma}{dx}\right]^{\mathrm{LO}}\int_{y\ll\min(x,1-x)}\frac{dy}{y}\left[\ln y + \bar{s}(x)\right] \tag{2.11}$$

for fixed $x$, where

$$\bar{s}(x) = -\ln\big(16\,x(1{-}x)(1{-}x{+}x^2)\big) + 2\,\frac{\big[x^2\big(\ln x - \frac{\pi}{8}\big) + (1{-}x)^2\big(\ln(1{-}x) - \frac{\pi}{8}\big)\big]}{(1 - x + x^2)}.$$

$$\tag{2.12}$$

For us, "soft" radiation means soft compared to both high energy daughters of the underlying LO splitting $E \to xE + (1-x)E$, and so the small-$y$ approximation used in (2.11) is only valid for $y \ll \min(x, 1-x)$, which is parametrically equivalent to $y \ll x(1-x)$.

Since $\bar{s}(x)$ diverges like $\ln(x(1-x))$ for $x \to 0$ or $x \to 1$, it's natural to rewrite the $\ln y + \bar{s}(x)$ in a way that combines the $\ln y$ and $\ln(x(1-x))$ behavior:

$$\ln y + \bar{s}(x) = \ln\left(\frac{y}{x(1-x)}\right) + \hat{s}(x) \tag{2.13}$$

with

$$\hat{s}(x) = -\ln\left(16(1-x+x^2)\right) + 2\frac{\left[x^2\left(\ln x - \frac{\pi}{8}\right) + (1-x)^2\left(\ln(1-x) - \frac{\pi}{8}\right)\right]}{(1-x+x^2)}. \tag{2.14}$$

$\hat{s}(x)$ remains finite for $x \to 0$ and $x \to 1$. It will also sometimes be useful to think of the integral (2.11) in terms of energy and so rewrite it as

$$-\frac{C_A \alpha_s}{4\pi}\left[\frac{d\Gamma}{dx}\right]^{\mathrm{LO}} \int_{\omega_y \ll \min(x,1-x)E} \frac{d\omega_y}{\omega_y}\left[\ln\left(\frac{\omega_y}{x(1-x)E}\right) + \hat{s}(x)\right], \tag{2.15}$$

where $\omega_y \equiv yE$ is the energy of the soft $y$ daughter.

The integral in (2.15) is IR-divergent and so ultimately depends on the IR regulator that cuts off those divergences. Our answer will not be sensitive to the IR details because we intend to study the infrared-safe characteristics of the shower, namely the *shape* (2.2) of the energy deposition distribution $\epsilon(z)$. To do this, we will introduce an energy factorization scale $\Lambda_{\mathrm{fac}}$ and separate the NLO contribution to the net rate

into,

$$\left[\frac{d\Gamma}{dx}\right]^{\text{NLO}}_{\text{net}} = \left[\frac{d\Gamma}{dx}\right]^{\text{NLO,fac}}_{\text{net}} - \frac{C_{\text{A}}\alpha_{\text{s}}}{4\pi}\left[\frac{d\Gamma}{dx}\right]^{\text{LO}}\int_0^{\Lambda_{\text{fac}}}\frac{d\omega_y}{\omega_y}\left[\ln\left(\frac{\omega_y}{x(1-x)E}\right)+\hat{s}(x)\right], \quad (2.16)$$

where the superscript "fac" above stands for "factorized." The IR-subtracted net rate

$$\left[\frac{d\Gamma}{dx}\right]^{\text{NLO,fac}}_{\text{net}} \equiv \int_0^\infty dy \left\{ V(x,y)\,\theta(y<\tfrac{1-x}{2}) + V(1-x,y)\,\theta(y<\tfrac{x}{2}) + R(x,y)\,\theta(y<\tfrac{1-x}{2}) \right.$$
$$\left. + \frac{C_{\text{A}}\alpha_{\text{s}}}{4\pi}\left[\frac{d\Gamma}{dx}\right]^{\text{LO}}\frac{\ln y + \bar{s}(x)}{y}\,\theta(yE<\Lambda_{\text{fac}}) \right\} \quad (2.17)$$

is then finite, and it can be computed numerically.

Our program is to absorb the last (IR-sensitive) terms of (2.16) into an effective value $\hat{q}_{\text{eff}}$ of $\hat{q}$ and so into an effective value $[d\Gamma/dx]^{\text{LO}}_{\text{eff}}$ of the leading-order $g\to gg$ splitting rate. In principle, this will move the problem of IR-sensitive physics to $[d\Gamma/dx]^{\text{LO}}_{\text{eff}}$. Then, the large double and single IR logarithms in $[d\Gamma/dx]^{\text{LO}}_{\text{eff}}$ would have to be tamed by a next-to-leading-log order (NLLO) resummation of IR logarithms to all orders in $\alpha_{\text{s}}(\mu)$. However, we will find that we can ignore the replacement of $[d\Gamma/dx]^{\text{LO}}$ by $[d\Gamma/dx]^{\text{LO}}_{\text{eff}}$ in evaluating whether those overlap effects that cannot be absorbed into $\hat{q}$ are large or small. This is because (i) constant shifts $\delta\hat{q}$ to the value of $\hat{q}$ will have no effect on the shape function (2.2) — that's precisely why we choose to study the shape function — and (ii) we found that changes that could affect the leading-order shape function do not affect the relative sizes NLO/LO of overlap effects at the order of our calculation. For now, the upshot is that we will focus on the IR-subtracted version (2.17) of the net splitting rate. Note that we've written the integral as $\int_0^\infty dy$ in (2.17). However, the largest $y$ for which the integrand is non-zero is $\max\big(x/2, (1-x)/2, \Lambda_{\text{fac}}/E\big)$.

### 2.1.3 Choice of factorization and renormalization scales

The idea of introducing a factorization scale to absorb the soft radiation up to that scale is not new, it is actually similar to parton distribution functions (PDFs) in the context of deep inelastic scattering (DIS) and other inclusive processes. In that application, the cross-section factorizes into (i) constituent cross-sections of the partons and (ii) PDFs. Beyond leading order (LO), the constituent cross-sections suffer from initial-state collinear divergences in perturbation theory that must be absorbed into the PDFs. This requires introducing a factorization scale $M_{\mathrm{fac}}$ to specify exactly how much to absorb, which is also similar to the idea of introducing the renormalization scale $\mu$ when absorbing the ultraviolet divergences. In next-to-leading order perturbative calculations, the answer depends on the choice of the factorization scale ($M_{\mathrm{fac}}$), just like it depends on the renormalization scale $\mu$. One usually chooses $M_{\mathrm{fac}}$ and $\mu$ to be the same and of order the relevant scale of the problem (e.g. $\sqrt{|Q^2|}$) in order to avoid large logarithms in the perturbative expansion. Typically, the exact choice of scale is varied over a reasonable range to give a theory guess of uncertainty. The higher the order in perturbation theory, the less sensitive the result to that variation. We adopt a similar strategy here. We define $\hat{q}(\Lambda_{\mathrm{fac}})$ to absorb all the double and sub-leading single log behaviour from overlapping soft bremsstrahlung that has $\omega_y \leq \Lambda_{\mathrm{fac}}$. Then we will choose $\Lambda_{\mathrm{fac}}$ to be of order the relevant scale in our problem (in the rest frame of the plasma).

**Our canonical choice**

As mentioned earlier, the IR logs come from soft radiation with energies $\min(x, 1{-}x)E$. The natural choice of $\Lambda_{fac}$ that subtracts the IR is then,

$$\Lambda_{\text{fac}} = \kappa x(1{-}x)E, \tag{2.18}$$

where $\kappa$ is an $O(1)$ constant that we will canonically choose to be 1, but which we will vary later.

Our UV renormalization scale $\mu$ should be chosen so that the explicit $\alpha_{\text{s}}$ in the LO splitting rate $[d\Gamma/dx]^{\text{LO}}$ (the $\alpha_{\text{s}}$ associated with the high-energy splitting vertex) is evaluated at an appropriate physics scale to account for anti-screening from virtual particle pairs present in the vacuum. During a formation time, the transverse separation $b$ of the daughters of a $g{\to}gg$ splitting is of order $(\hat{q}\omega)^{-1/4}$, where $\omega = \min(x, 1{-}x)E$. Note that this is parametrically small compared to medium scales in the high-energy limit. Therefore, we want $\alpha_{\text{s}}(1/b)$ which is $\alpha_{\text{s}}(\mu)$ with $\mu \sim (\hat{q}\omega)^{1/4}$. We will choose $\mu$ to be written in terms of $\Lambda_{\text{fac}}$ as

$$\Lambda_{\text{fac}} = \kappa x(1{-}x)E, \qquad \mu = (\hat{q}_{\text{A}}\Lambda_{\text{fac}})^{1/4}. \tag{2.19}$$

**An alternate choice**

We will consider another choice of the factorization scale for comparison. In our limit of high energy showers and infinite-size medium, an underlying LO single splitting process $g \to gg$ should not affect where the energy is deposited (along the $z$-direction) in the limit that the radiated energy is soft. Meaning that for daughters of energy

$xE$ or $(1-x)E$ that are extremely small, the energy deposited is not affected by the soft daughter because it carries negligible energy. The big effect of energy deposition comes from the hard splittings where $x$ is of $O(1)$. So it won't matter if we make a poor estimate of the size of the IR logarithms for the even-softer radiative corrections to such an already very soft process. In fact, we only need to do a reasonable job with choosing the factorization scale for the case where $\min(x, 1-x) \sim 1$. This means that our choice in (2.19) is a more physically sensible choice, for the purpose of calculating $\epsilon(z)$ and then its shape $S(Z)$, one can in principle get away with

$$\Lambda_{\text{fac}} = rE, \qquad \mu = (\hat{q}_{\text{A}} \Lambda_{\text{fac}})^{1/4} \tag{2.20}$$

instead, where $r$ is an $O(1)$ constant. We will later compare results using (2.19) and (2.20) to check the robustness of our conclusions about the importance of overlap corrections that cannot be absorbed into $\hat{q}$. Note that, for a perfectly democratic splitting with $x = \frac{1}{2}$, our two different choices (2.19) and (2.20) match up when $r = \kappa/4$.

### 2.1.4 Numerical results

We have numerically computed [1] the $[d\Gamma/dx]_{\text{net}}^{\text{NLO,fac}}$ represented by the data points in fig. 2.2 and the last column of table 2.1 using (2.17), using the rate formulas of refs. [47, 52] as described in appendix A.1 of this thesis, and choosing $\Lambda_{\text{fac}} = x(1-x)E$

---

[1] See appendix A.2.1 for some information on our numerical methods.
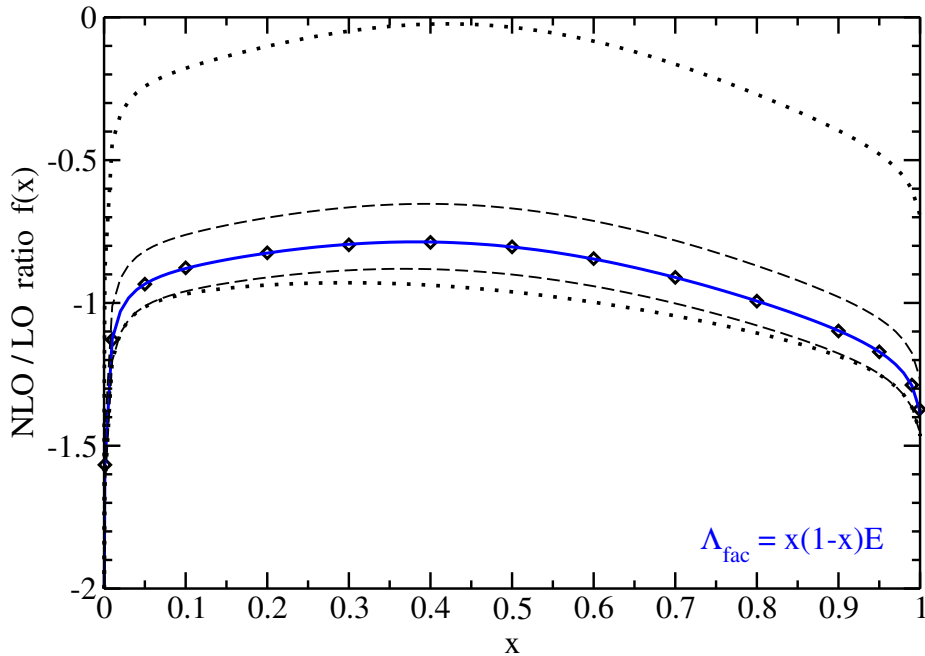
Figure 2.2: Plot of the ratio (2.21) vs. $x$ for $\Lambda_{\text{fac}} = \kappa x(1-x)E$ and $\mu = (\hat{q}_A \Lambda_{\text{fac}})^{1/4}$. The diamonds are numerically-computed data points for $\kappa = 1$, and the solid curve is a fit (2.22) to those points. For the sake of later discussion, the dashed lines show the results for $\kappa = \frac{1}{2}$ (upper) and $\kappa = 2$ (lower), and the dotted lines for $\kappa = \frac{1}{16}$ (upper) and $\kappa = 16$ (lower).

with $\kappa = 1$. [2] Specifically, we show the values of

$$f(x) \equiv \frac{\left[\frac{d\Gamma}{dx}\right]_{\text{net}}^{\text{NLO,fac}}}{C_A \alpha_s \left[\frac{d\Gamma}{dx}\right]^{\text{LO}}}. \tag{2.21}$$

The reason for using such a ratio is that it's more convenient for comparing the size of the NLO rate to the LO rate and, more importantly, the numerator and the denominator blow up proportional to $[x(1-x)]^{-3/2}$ (up to logarithms) as $x \to 0$ or $x \to 1$, and so $f(x)$ is a smoother function than $[d\Gamma/dx]_{\text{net}}^{\text{NLO,fac}}$.

---

[2]The data points in Table 2.1 and fig. 2.4 that have extremely tiny $x$ or $1-x$ are not intended to be relevant to any actual phenomenological situation, since our high-energy approximations fail when $xE$ or $(1-x)E$ are $\lesssim T$. They are included just for the purpose of understanding the asymptotic behavior of our formulas.

| $x$ | $f(x)$ | | |
|---|---|---|---|
| | non-F | F diags | total |
| 0.0001 | -2.0716 | | |
| 0.001 | -1.5231 | -0.0438 | -1.5670 |
| 0.01 | -1.0819 | -0.0473 | -1.1292 |
| 0.05 | -0.8792 | -0.0552 | -0.9343 |
| 0.1 | -0.8185 | -0.0586 | -0.8771 |
| 0.2 | -0.7674 | -0.0571 | -0.8245 |
| 0.3 | -0.7456 | -0.0509 | -0.7965 |
| 0.4 | -0.7422 | -0.0459 | -0.7881 |
| 0.5 | -0.7573 | -0.0463 | -0.8037 |
| 0.6 | -0.7924 | -0.0525 | -0.8448 |
| 0.7 | -0.8479 | -0.0628 | -0.9106 |
| 0.8 | -0.9239 | -0.0697 | -0.9936 |
| 0.9 | -1.0287 | -0.0697 | -1.0984 |
| 0.95 | -1.1057 | -0.0654 | -1.1711 |
| 0.99 | -1.2293 | -0.0580 | -1.2873 |
| 0.999 | -1.3171 | -0.0555 | -1.3727 |
| 0.9999 | -1.3339 | | |

Table 2.1: Our numerical results for $f(x)$ for $\Lambda_{\text{fac}} = x(1-x)E$ and $\mu = (\hat{q}_{\text{A}}\Lambda_{\text{fac}})^{1/4}$. The last column shows values for the ratio (2.21), as plotted by the diamonds in fig. 2.2. The second and third columns are respectively the pieces of that result without or with F=4+I vertices [52], with the latter plotted by the diamonds in fig. 2.3.

It's important to note that the relative size of the (factorized) NLO contribution to $[d\Gamma/dx]_{\text{net}}$ is a roughly $C_A\alpha_s \times 100\%$ correction to $[d\Gamma/dx]^{\text{LO}}$. You also need $C_A\alpha_s = N_c\alpha_s$ to be small for this to be a small correction. However, we want to measure overlap effects that cannot be absorbed into $\hat{q}$, and so we should compute the shape function $S(Z)$ of the energy deposition distribution. If $f(x)$ were independent of $x$, then the NLO corrections would simply rescale the size of $[d\Gamma/dx]^{\text{LO}}$. But we know that we could absorb that into $\hat{q}$, which would have no effect on the shape $S(Z)$ of the energy deposition distribution because it is insensitive to constant shifts to $\hat{q}$. So what is important is how $f(x)$ varies with $x$, not its value, and it is clear from fig. 2.2 that $f(x)$ is not constant. So we should wait until we compute the NLO effect on the shape before we can draw conclusions.

The leading-order rate $[d\Gamma/dx]^{\text{LO}}$ for $g{\to}gg$ is symmetric under swapping the two daughters via $x \leftrightarrow 1{-}x$, but this not the case for $f(x)$ and so not for $[d\Gamma/dx]^{\text{NLO}}_{\text{fac}}$. The $1{\to}3$ processes are not symmetric under $x \leftrightarrow 1{-}x$ because, by integrating over $y$, one breaks the permutation symmetry between $(x, y, 1{-}x{-}y)$. So $[d\Gamma/dx]_{\text{net}}$ won't be symmetric under $x \leftrightarrow 1{-}x$.

The data points in table 2.1 are slow to compute numerically, and we need to use $[d\Gamma/dx]_{\text{net}}$ in calculating the energy deposition distribution, so we decided to do a reasonable fit that is quick to evaluate. We tried our best in fitting the data of table 2.1, and found a fairly accurate functional form. Before showing the fit function, let's introduce our notation in defining the two fit functions that we have. Following ref. [52], we call diagrams such as the ones in fig. 1.10 the fundamental or effective 4-gluon interactions. These include "F=4+I" interactions, where "F" is meant to be evocative of the word "four"; "4" stands for fundamental 4-gluon vertices; and "I" stands for interactions via longitudinally polarized gluon exchange, which are "instantaneous"
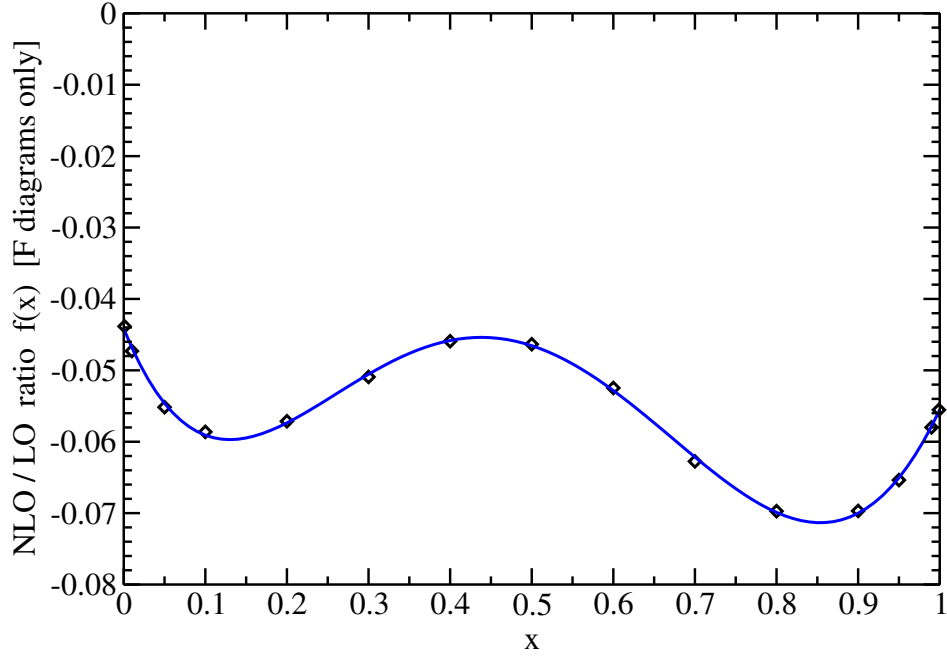
Figure 2.3: Like fig. 2.2 but here showing *only* the contribution from diagrams that contain at least one F=4+I interaction [52], like the examples in fig. 1.10. These diagrams do not have IR divergences and so do not require factorization, and so they do not participate in the infrared subtraction of (2.17) and are not sensitive to the choice of $\Lambda_{\text{fac}}$. These diagrams are also UV convergent and are not sensitive to the choice of renormalization scale $\mu$. The solid curve corresponds to the fit (2.22c).

in LCPT. Fig. 2.3 shows our result for the piece of fig. 2.2 that comes from processes involving F interactions [52]. We will continue to distinguish the contribution of the "F" diagrams, and write

$$f(x) = f_{\text{non-F}}(x) + f_{\text{F}}(x). \tag{2.22a}$$

We have found a good fit of the non-F contributions (the second column of table 2.1)
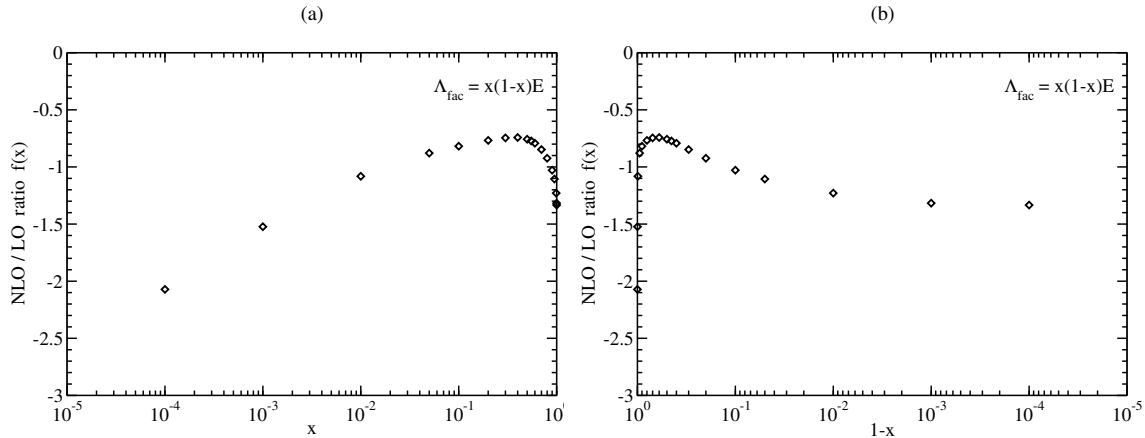
Figure 2.4: (a) A log-linear plot of the non-F contributions to the ratio $f(x)$ of (2.21). (b) The same data plotted vs. $1-x$ instead of $x$. Note that we've arranged both plots so that $x \to 0$ is on the left and $x \to 1$ is on the right.

to the function

$$f_{\text{non-F}}(x) = 0.259531 \ln x - 0.00762944 \ln(1-x) - 7.11257 + 11.7493\,x - 3.83207\,x^2$$

$$- 2.53558\,x^{1/2} + 0.307523\,x^{3/2} + 1.8688\,(1-x)^{1/2} + 5.58862\,(1-x)^{3/2}. \quad (2.22\text{b})$$

The non-F data points of the table have been fit to better than 0.003 absolute error and 0.3% relative error. The $\ln x$ behavior as $x \to 0$ is clear from the log-linear plot of the non-F data in fig. 2.4a, but there is no evidence of $\ln(1-x)$ behavior as $x \to 1$, and so one shouldn't pay much attention to the small coefficient of the $\ln(1-x)$ term in our fit (2.22b). In principle, one can push the calculations further to smaller values of $(1-x)$, but we didn't see the need for that. For the rest of the terms in (2.22b), we found that the use of the half powers of $x$ and $1-x$ was necessary to fit the data well.

For the F-diagrams in fig. 2.3, we found that a good fit for the data given in the third column of table 2.1 is just a simple polynomial:

$$f_{\mathrm{F}}(x) = -0.0441533 - 0.283453\,x + 1.63849\,x^2 - 3.20205\,x^3 + 2.32331\,x^4 - 0.48766\,x^5,$$

$$(2.22c)$$

which is the solid curve plotted in fig. 2.3. This fits the data points to better than 0.001 absolute error, which is small when combined with the non-F diagrams. The solid curve plotted in fig. 2.2 is the total ratio (2.22a).

### 2.1.5 The dependence on the factorization scale and the renormalization scale

**From $\Lambda_{fac} = x(1-x)E$ to $\Lambda_{fac} = \kappa x(1-x)E$**

The dependence of $[d\Gamma/dx]^{\mathrm{NLO,fac}}_{\mathrm{net}}$ on the factorization scale is captured in the last term of (2.17):

$$\left[\frac{d\Gamma}{dx}\right]^{\mathrm{NLO,fac}}_{\mathrm{net}} = (\Lambda_{\mathrm{fac}}\text{ independent}) + \frac{C_A \alpha_{\mathrm{s}}}{4\pi}\left[\frac{d\Gamma}{dx}\right]^{\mathrm{LO}}\int_0^\infty dy\,\frac{\ln y + \bar{s}(x)}{y}\,\theta(yE < \Lambda_{\mathrm{fac}})$$
$$= (\Lambda_{\mathrm{fac}}\text{ independent}) + \frac{C_A \alpha_{\mathrm{s}}}{4\pi}\left[\frac{d\Gamma}{dx}\right]^{\mathrm{LO}}\left\{\frac{1}{2}\ln^2\left(\frac{\Lambda_{\mathrm{fac}}}{E}\right) + \bar{s}(x)\,\ln\left(\frac{\Lambda_{\mathrm{fac}}}{E}\right)\right\}.$$

$$(2.23)$$

Note that the infrared divergence of (2.23) does not matter because it does not depend on $\Lambda_{\mathrm{fac}}$ and it cancels against the other $\Lambda_{\mathrm{fac}}$-independent terms in (2.17). The renormalization scale $\mu$ dependence can be obtained easily from the fact that the implicit dependence of the coupling constant $\alpha_{\mathrm{s}}(\mu)$ in the leading-order rate (1.2)

should cancel the explicit $\ln \mu$ dependence of the NLO rate, so

$$\left[\frac{d\Gamma}{dx}\right]_{\text{net}}^{\text{NLO,fac}} = (\mu \text{ independent}) - \beta_0 \alpha_{\text{s}} \left[\frac{d\Gamma}{dx}\right]^{\text{LO}} \ln \mu, \qquad (2.24)$$

where $\beta_0$ is the leading-order coefficient of the renormalization group $\beta$ function for $\alpha_{\text{s}}$. Since we are considering purely gluonic showers in the large-$N_{\text{c}}$ limit, only the gluonic contribution matters:

$$\beta_0 = -\frac{11C_{\text{A}}}{6\pi} . \qquad (2.25)$$

Putting together (2.23) and (2.24), the change $\delta[d\Gamma/dx]$ in the net rate due to changing $\Lambda_{\text{fac}}$ and/or $\mu$ is

$$\delta\left[\frac{d\Gamma}{dx}\right]_{\text{net}}^{\text{NLO,fac}} = \frac{C_{\text{A}}\alpha_{\text{s}}}{4\pi} \left[\frac{d\Gamma}{dx}\right]^{\text{LO}} \times \delta\left\{\frac{1}{2}\ln^2\left(\frac{\Lambda_{\text{fac}}}{E}\right) + \bar{s}(x)\ln\left(\frac{\Lambda_{\text{fac}}}{E}\right) - \frac{4\pi\beta_0}{C_{\text{A}}}\ln\mu\right\}. \qquad (2.26)$$

For a change from $\Lambda_{\text{fac}} = x(1-x)E$ to $\Lambda_{\text{fac}} = \kappa x(1-x)E$, with $\mu = (\hat{q}_{\text{A}}\Lambda_{\text{fac}})^{1/4}$ in both cases, this gives

$$\left[\frac{d\Gamma}{dx}\right]_{\text{net}}^{\text{NLO,fac}}\Bigg|_{\substack{\Lambda_{\text{fac}}=\kappa x(1-x)E \\ \mu=(\hat{q}_{\text{A}}\Lambda_{\text{fac}})^{1/4}}} =$$
$$\left[\frac{d\Gamma}{dx}\right]_{\text{net}}^{\text{NLO,fac}}\Bigg|_{\kappa=1} + \frac{C_{\text{A}}\alpha_{\text{s}}}{4\pi}\left[\frac{d\Gamma}{dx}\right]^{\text{LO}}\left\{\tfrac{1}{2}\ln^2\kappa + \left(\hat{s}(x) - \frac{\pi\beta_0}{C_{\text{A}}}\right)\ln\kappa\right\}. \qquad (2.27)$$

One may wonder whether it's more physically relevant to vary the factorization scale $\Lambda_{fac}$ by a factor of 2 or so or instead vary the renormalization scale $\mu$ (the associated transverse momentum scale $(\hat{q}\Lambda_{fac})^{1/4}$) by a factor of 2 or so. We decided to do both. Fig. 2.2 shows the variation of the ratio $f(x)$ of (2.21) from changing the choice of $\kappa$ up or down by a factor of 2. We also show the variation if one changed the renormalization scale up or down by a factor of 2 which corresponds to changing $\Lambda_{\text{fac}}$

up or down by a factor of 16, shown by the dotted curves in fig. 2.2. The conclusion is that $f(x)$ (and so $[d\Gamma/dx]_{\text{net}}^{\text{NLO,fac}}$ ) is potentially very sensitive to the choice of the factorization scale. Fortunately, the overlap corrections to the shape function $S(Z)$ will be dramatically less sensitive. Note that the $x$-independent term in the rescaling (2.27) could be absorbed into a constant shift in $\hat{q}$ and so will not affect the shape function $S(Z)$. It's only the $x$-dependent term that will change the shape function. However, the renormalization scale $\mu$ has no explicit effect on the size of the NLO correction to $S(Z)$, since it doesn't have explicit $x$-dependence.

**An alternate choice**

As mentioned earlier, our alternate choice of the factorization scale is an $x$-independent scale $\Lambda_{fac} = rE$ as in (2.20). In that case, the relation to our numerical results for $\Lambda_{\text{fac}} = x(1-x)E$ is just (2.27) with $\kappa$ replaced by $r/x(1-x)$:

$$\left[\frac{d\Gamma}{dx}\right]_{\text{net}}^{\text{NLO,fac}}\Bigg|_{\substack{\Lambda_{\text{fac}}=rE \\ \mu=(\hat{q}_A\Lambda_{\text{fac}})^{1/4}}} = \left[\frac{d\Gamma}{dx}\right]_{\text{net}}^{\text{NLO,fac}}\Bigg|_{\substack{\Lambda_{\text{fac}}=x(1-x)E \\ \mu=(\hat{q}_A\Lambda_{\text{fac}})^{1/4}}} + \frac{C_A\alpha_s}{4\pi}\left[\frac{d\Gamma}{dx}\right]^{\text{LO}}\left\{\frac{1}{2}\ln^2\left(\frac{r}{x(1-x)}\right)\right.$$
$$\left. + \left(\hat{s}(x) - \frac{\pi\beta_0}{C_A}\right)\ln\left(\frac{r}{x(1-x)}\right)\right\}. \quad (2.28)$$

Note that the NLO/LO ratio $f(x)$ will diverge like $\ln^2\big(x(1-x)\big)$ for $\Lambda_{\text{fac}} = rE$ as $x \to 0$ or $x{\to}1$ instead of the milder $\ln x$ divergence as $x \to 0$ (and perhaps no divergence for $x \to 1$) that we found numerically for $\Lambda_{\text{fac}} = x(1-x)$, and that's because of the double log in (2.28). This worse divergence is actually an indication that our earlier choice $\Lambda_{\text{fac}} = x(1-x)$ is better in capturing the physics at $x{\to}0$ and $x{\to}1$.

**Yet another choice**

We will not use this choice for numerics, but it will be useful in some of the discussions later. We could choose

$$\Lambda_{\text{fac}} = rE_0, \qquad \mu = (\hat{q}_A \Lambda_{\text{fac}})^{1/4}, \tag{2.29}$$

where $E_0$ is the energy of the original particle that initiates the shower, and $r$ is again a fixed, $O(1)$ constant. This choice fails in capturing the correct scale in the shower development when particle energies dropped to $E \ll E_0$. However, those particles are effectively stopped, because their remaining stopping distance $\ell_{\text{stop}}(E) \sim \alpha_s^{-1}\sqrt{E/\hat{q}}$ is then parametrically small compared to the overall stopping distance $\ell_{\text{stop}}(E_0) \sim \alpha_s^{-1}\sqrt{E_0/\hat{q}}$. The poor choice of $\Lambda_{\text{fac}}$ for those $E \ll E_0$ splittings will not have a significant effect on the energy deposition distribution $\epsilon(z)$. The conversion from $\Lambda_{\text{fac}} = x(1-x)E$ is

$$\left[\frac{d\Gamma}{dx}\right]^{\text{NLO,fac}}_{\text{net}}\Bigg|_{\substack{\Lambda_{\text{fac}}=rE_0 \\ \mu=(\hat{q}_A\Lambda_{\text{fac}})^{1/4}}} = \left[\frac{d\Gamma}{dx}\right]^{\text{NLO,fac}}_{\text{net}}\Bigg|_{\substack{\Lambda_{\text{fac}}=x(1-x)E \\ \mu=(\hat{q}_A\Lambda_{\text{fac}})^{1/4}}} + \frac{C_A\alpha_s}{4\pi}\left[\frac{d\Gamma}{dx}\right]^{\text{LO}}\left\{\tfrac{1}{2}\ln^2\left(\frac{rE_0}{x(1-x)E}\right)\right.$$

$$\left. + \left(\hat{s}(x) - \frac{\pi\beta_0}{C_A}\right)\ln\left(\frac{rE_0}{x(1-x)E}\right)\right\}. \tag{2.30}$$

## 2.1.6 Scaling of $[d\Gamma/dx]^{\text{fac}}_{\text{net}}$ with energy $E$

The original NLO differential rates $\Delta\,d\Gamma/dx\,dy$ depend only on two dimensionful scales: $\hat{q}$ and the parent energy $E$. Those differential rates are proportional to $\sqrt{\hat{q}/E}$ and so scale like $E^{-1/2}$ for fixed $x$ and $y$, just like the LO rate (1.2). However, the integration over $y$ as in (2.9) to get $[d\Gamma/dx]^{\text{NLO}}_{\text{net}}$ produced IR log divergences.

To factorize out those divergences, we introduced a new energy scale $\Lambda_{\text{fac}}$ to define $[d\Gamma/dx]_{\text{net}}^{\text{NLO,fac}}$ in (2.17). If one chooses $\Lambda_{\text{fac}} = \kappa x(1-x)E$ or the alternate choice $\Lambda_{\text{fac}} = rE$, then we are not introducing any new dimensionful parameter, and $[d\Gamma/dx]_{\text{net}}^{\text{NLO,fac}}$ will scale as $E^{-1/2}$. However, this is not the case for the choice in (2.29) where $\Lambda_{\text{fac}} = rE_0$. Eq (2.30) shows that this choice would introduce a term into $[d\Gamma/dx]_{\text{net}}^{\text{NLO,fac}}$ that scales as $E^{-1/2}\ln^2(E_0/E)$. We will later want $[d\Gamma/dx]_{\text{net}}^{\text{fac}}$ to scale exactly as $E^{-1/2}$ in order to simplify the shower development equation. So, We will only consider for now the choices where $\Lambda_{\text{fac}} \propto E$, like $\Lambda_{\text{fac}} = x(1-x)E$ or $\Lambda_{\text{fac}} = rE$, rather than $\Lambda_{\text{fac}} \propto E_0$.

## 2.2 LO vs. effective LO rates

So far, we subtracted the IR log divergences and absorbed them into an effective value of $\hat{q}$, which in turn means an effective value of the leading order rate given by:[3]

$$\left[\frac{d\Gamma}{dx}\right]_{\text{eff}}^{\text{LO}} = \left[\frac{d\Gamma}{dx}\right]^{\text{LO}} \left\{1 - \frac{C_A\alpha_s}{4\pi} \int_0^{\Lambda_{\text{fac}}} \frac{d\omega_y}{\omega_y} \left[\ln\left(\frac{\omega_y}{x(1-x)E}\right) + \hat{s}(x)\right]\right\}. \qquad (2.31)$$

However, this integral has infrared divergence and one needs to account for the physics that cuts off the IR divergence above. The result at leading-log order is

$$\left[\frac{d\Gamma}{dx}\right]_{\text{eff}}^{\text{LO}} \approx \left[\frac{d\Gamma}{dx}\right]^{\text{LO}} \left\{1 - \frac{C_A\alpha_s}{8\pi} \ln^2\left(\frac{\Lambda_{\text{fac}}}{T}\right)\right\}. \qquad (2.32)$$

In the high energy limit, $T \ll \Lambda_{\text{fac}}$, where $T$ is the temprature of the quark-gluon plasma, because we always choose $\Lambda_{\text{fac}} \propto E$, and so the double log becomes large. This means that $\alpha_s \ln^2(\Lambda_{\text{fac}}/T)$ is not small at high energy, even for small $\alpha_s$, and one

---

[3]In (2.31), we are using the version of the integral from (2.16).

must resum logarithms to all orders in $\alpha_s$ to get a usable result for $[d\Gamma/dx]_{\text{eff}}^{\text{LO}}$.

Ignoring the resummation of the double log for now, imagine instead that these double logs are small and that $\alpha_s \ln^2(\Lambda_{\text{fac}}/T)$ had size $O(\alpha_s)$. To determine the size of overlap effect, we look into the relative size of NLO corrections that cannot be absorbed into $\hat{q}$, as measured by the shape function $S(Z)$. This means that the ratio of the factorized NLO correction to the effective LO result for $S(Z)$ is what we are looking for. But this ratio would be

$$\frac{\text{NLO}_{\text{fac}}}{\text{LO}_{\text{eff}}} = \frac{\text{NLO}_{\text{fac}}}{\text{LO} \times [1 + O(\alpha_s)]} = \frac{\text{NLO}_{\text{fac}}}{\text{LO}} \times [1 + O(\alpha_s)]. \qquad (2.33)$$

This means that one can ignore the replacement of the LO by $\text{LO}_{\text{eff}}$, and do fine by just using the LO rate in calculating the ratio $\text{NLO}_{\text{fac}}/\text{LO}_{\text{eff}}$ which is itself $O(\alpha_s)$.

So the effect of using the $\text{LO}_{\text{eff}}$ in the denominator is a *yet-higher* order correction to the ratio and so can be ignored. Unfortunately, the logic of (2.33) fails because the accompanying logarithms are large.[4]

So let's discuss how the fact that the leading log is large and our need to resum to all orders in $\alpha_s$ will change the above argument. At first order in $\alpha_s$, (2.31) absorbs not only a leading double log but also a sub-leading single log. So one needs to consider NLLO resummation of large logs. We don't know how to do the full NLLO resummation, but we do not need it because the shape function $S(Z)$ and its moments are insensitive to any constant shifts to $\hat{q}$. So all we need to do is to resum the $x$ and $E$ dependence of the NLLO resummation, and we can ignore any constant (i.e. $x$ and $E$ independent) contributions to the braces $\{\cdots\}$ in (2.31). It turns out that resumming the $x$ and $E$ dependence is much easier than understanding the full

---

[4]In fact, such logarithms have to be large if we wish to treat our high-energy $\alpha_s(\mu)$ as smaller than the $\alpha_s(T)$ of the medium.

NLLO resummation, and we will see later for large logarithms, the resummed version of (2.33) is

$$\frac{\text{NLO}_{\text{fac}}}{\text{LO}_{\text{eff}}} = \frac{\text{NLO}_{\text{fac}}}{\text{LO} \times [1 + O(\sqrt{\alpha_{\text{s}}})]} = \frac{\text{NLO}_{\text{fac}}}{\text{LO}} \times [1 + O(\sqrt{\alpha_{\text{s}}})] \qquad (2.34)$$

provided that the LO quantity is insensitive to constant shifts of $\hat{q}$ which is exactly why we chose the shape function $S(Z)$ and its moments.

In the following discussion, we will remove any $x$ and $E$ dependence from the factorization scale $\Lambda_{fac}$ to keep the focus on the resummation argument. We will choose $\Lambda_{\text{fac}} = rE_0$ as in (2.29) for the purpose of this argument. The conversion (2.30) between this scale and our usual choice $\Lambda_{\text{fac}} = x(1-x)E$ is finite and is free of large logarithms unless $x(1-x) \ll 1$ or $E \ll E_0$. As discussed in the subsections 2.1.5, these cases will not affect the calculation of the shower energy deposition distribution $\epsilon(z)$ and its shape, so the conversion (2.30) does not need to be resummed.

## 2.2.1 Review of the IR double and single logs in (2.15)

We need to review the origin of the explicit $x$ and $E$ dependence (2.31) so that we can discuss how to resum it. We will start first with an overview of the calculation presented in ref. [48]. There, the leading-order BDMPS-Z calculation was modified by replacing the $\hat{q}$ by the effective value of $\hat{q}(\Delta b)$ which was originally calculated by Liou, Mueller and Wu (LMW) [30], which incorporates the effect of soft radiation carrying away transverse momentum in the context of momentum broadening. The $\Delta b$ in $\hat{q}_{\text{eff}}(\Delta b)$ represents transverse separation. In principle, $\hat{q}_{\text{eff}}(\Delta b)$ is obtained from the thermal expectation of a Wilson loop with long, time-like sides separated by transverse distance $\Delta b$, as depicted in fig. 2.5a. The bare $\hat{q}_{(0)}$ corresponds to the
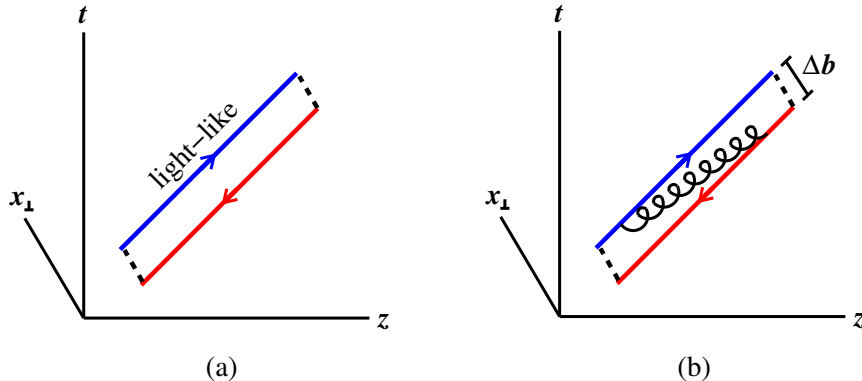
Figure 2.5: (a) A Wilson loop with long, light-like sides and transverse spatial width $\Delta b$, whose expectation gives $\exp\left(-\frac{1}{4}\hat{q}(\Delta b)\,\mathbb{T}\,(\Delta b)^2\right)$ for small $\Delta b$ and large extent $\mathbb{T}$ in time $t$. (b) An example of a high-energy nearly-collinear radiative contribution to the Wilson loop.

contribution from thermal-scale correlations in the medium; the double and single logarithms come from the exchange of a nearly collinear, high-energy gluon ($\omega \gg T$) as in fig. 2.5b. In our application, those logarithms are cut-off at high energy by the factorization scale $\Lambda_{\text{fac}}$, so that $T \ll \omega \leq \Lambda_{\text{fac}}$, and so we should write $\hat{q}_{\text{eff}}(\Delta b\,;\Lambda_{\text{fac}})$ instead of just $\hat{q}_{\text{eff}}(\Delta b)$. However, we will stick with the shorter notation $\hat{q}_{\text{eff}}(\Delta b)$ for now, with the $\Lambda_{\text{fac}}$ dependence implicit.[5]

Let's now review the calculation done in ref. [48]. The Zakharov picture of the LO BDMPS-Z calculation for $g \to gg$ involves solving for the propagator of 3-particle quantum mechanics in the two-dimensional transverse plane with Hamiltonian

$$H = \frac{p_{\perp 1}^2}{2|p_{z_1}|} + \frac{p_{\perp 2}^2}{2|p_{z_2}|} - \frac{p_{\perp 3}^2}{2|p_{z_3}|} - \frac{i\hat{q}_{\text{A}}}{8}\,(b_{12}^2 + b_{23}^2 + b_{31}^2), \qquad (2.35)$$

where $\boldsymbol{b}_{ij} \equiv \boldsymbol{b}_i - \boldsymbol{b}_j$ are the transverse separations between the three "particles" in fig.

---

[5]In the original work of LMW [30] on momentum broadening, the role of our "$\Lambda_{\text{fac}}$" is played by the largest "soft" bremsstrahlung energy $\omega$ that has a formation time that fits inside the length $L$ of the medium, which corresponds to $\Lambda_{\text{fac}} \sim \hat{q}L^2$. Our canonical choice (2.19) of $\Lambda_{\text{fac}}$ in this calculation corresponds to replacing that $L$ by the formation time of the underlying hard single-splitting process $E \to xE + (1-x)E$ that one is computing soft radiative corrections to.

**(lightcone) time**
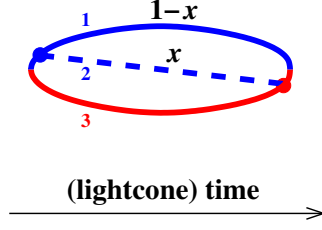
Figure 2.6: This is fig. 1.6b for LO splitting $g \to gg$, but here with the three lines labeled (1,2,3).

2.6, $(p_{z1}, p_{z2}, p_{z3}) = (1-x, x, -1)E$ are the corresponding energies of those particles and $E$ is the energy of the initial particle in the single splitting process. Symmetries are used to reduce the problem to a 1-particle quantum mechanics problem in a single transverse position variable $\boldsymbol{B}$ related by,

$$\boldsymbol{b}_{12} = \boldsymbol{B}, \qquad \boldsymbol{b}_{23} = -(1-x)\boldsymbol{B}, \qquad \boldsymbol{b}_{31} = -x\boldsymbol{B}, \tag{2.36}$$

which reduces (2.35) to,

$$H = \frac{P^2}{2x(1-x)E} - \frac{i\hat{q}_{\mathrm{A}}}{8}\left(1 + (1-x)^2 + x^2\right)B^2, \tag{2.37}$$

where $\boldsymbol{P}$ is conjugate to $\boldsymbol{B}$. In the LO splitting process of fig. 2.6, transverse separations vary with time, but the typical value $\bar{\mathcal{B}}$ of $\boldsymbol{B}$ during the splitting is parametrically

$$\bar{\mathcal{B}} \sim [x(1-x)E\hat{q}]^{-1/4}. \tag{2.38}$$

In the Large-$N_c$ limit, ref. [48] showed that the modification of (2.35) that would reproduce the IR double and single logs from soft radiation corrections to the hard,

underlying $g \rightarrow gg$ process was

$$H = \frac{p_{\perp 1}^2}{2|p_{z_1}|} + \frac{p_{\perp 2}^2}{2|p_{z_2}|} - \frac{p_{\perp 3}^2}{2|p_{z_3}|} - \frac{i}{8}\left[\hat{q}_{\mathrm{A}}^{\mathrm{eff}}(b_{12})\, b_{12}^2 + \hat{q}_{\mathrm{A}}^{\mathrm{eff}}(b_{23})\, b_{23}^2 + \hat{q}_{\mathrm{A}}^{\mathrm{eff}}(b_{31})\, b_{31}^2\right]. \quad (2.39)$$

However, there is one caveat. That momentum broadening calculation done by LMW [30] gives the $\hat{q}_{\mathrm{eff}}$ between an amplitude (blue) line and a conjugate amplitude (red) line in fig. 2.6. In the LO splitting process of fig. 2.6, there is a transverse separation between two amplitude (blue) lines, which turns out to have a slightly different $\hat{q}_{\mathrm{eff}}$. In the analysis of ref. [48], this difference was equivalent to replacing

$$\hat{q}_{\mathrm{A}}^{\mathrm{eff}}(b_{12}) \longrightarrow \hat{q}_{\mathrm{A}}^{\mathrm{eff}}(e^{-i\pi/8} b_{12}). \quad (2.40)$$

in (2.39). The modified (2.39) then reduces to

$$H = \frac{P^2}{2x(1-x)E} - \frac{i}{8}\left[\hat{q}_{\mathrm{A}}^{\mathrm{eff}}\!\left(e^{-i\pi/8}B\right) + (1-x)^2\, \hat{q}_{\mathrm{A}}^{\mathrm{eff}}\!\left((1-x)B\right) + x^2\, \hat{q}_{\mathrm{A}}^{\mathrm{eff}}\!\left(xB\right)\right]B^2. \quad (2.41)$$

Using this Hamiltonian instead of (2.35) for the BDMPS-Z calculation, ref. [48] reproduced the soft radiative corrections (2.11) to the usual leading-order BDMPS-Z rate (1.2). The result may be summarized in the form[6]

$$\left[\frac{d\Gamma}{dx}\right]_{\mathrm{eff}}^{\mathrm{LO}} = \left[\frac{d\Gamma}{dx}\right]^{\mathrm{LO}} \quad (2.42)$$

$$\mathrm{Re}\left\{w_{12}\sqrt{\frac{\hat{q}_{\mathrm{A}}^{\mathrm{eff}}(\bar{\mathcal{B}})}{\hat{q}_{(0)}}} + w_{23}\sqrt{\frac{\hat{q}_{\mathrm{A}}^{\mathrm{eff}}\!\left(e^{-i\pi/8}(1-x)\bar{\mathcal{B}}\right)}{\hat{q}_{(0)}}} + w_{31}\sqrt{\frac{\hat{q}_{\mathrm{A}}^{\mathrm{eff}}\!\left(e^{-i\pi/8}x\bar{\mathcal{B}}\right)}{\hat{q}_{(0)}}}\right\},$$

$$(2.43)$$

---

[6]Though some broader claims were made at the end, ref. [48] only did explicit calculations for the part of the double log region to the right of the corner marked $\beta$ in our fig. 2.7. However, that region contains all of the $\Delta b$ dependence of the logarithms, which is our ultimate interest here.

where here[7]

$$\bar{\mathcal{B}} \equiv e^{-\gamma_{\mathrm{E}}/2} \big[ x(1-x)(1-x+x^2) \hat{q}_{\mathrm{A}} E \big]^{-1/4}, \tag{2.44}$$

and the weights $(w_{12}, w_{23}, w_{31})$ are defined by

$$w_{12} = \frac{1}{1 + (1-x)^2 + x^2}, \quad w_{23} = \frac{(1-x)^2}{1 + (1-x)^2 + x^2}, \quad w_{31} = \frac{x^2}{1 + (1-x)^2 + x^2} \tag{2.45}$$

with

$$w_{12} + w_{23} + w_{31} = 1. \tag{2.46}$$

The details of these formulas won't matter for our argument, but we just thought it would be useful to show the complete picture in here. There are two aspects of (2.43) that will matter.

The first is that, for our application, the $\Delta b$ of the three $\hat{q}_{\mathrm{A}}^{\mathrm{eff}}(\Delta b)$'s in (2.43) are all of order

$$\Delta b \sim \mathcal{B}_0 \equiv (\hat{q}_{\mathrm{A}} E_0)^{-1/4}. \tag{2.47}$$

This is because processes with (i) $E \ll E_0$ or (ii) $x \ll 1$ or $1-x \ll 1$ are not important to determining the shape function $S(Z)$.

The second is that, if we replace all three different $\hat{q}_{\mathrm{A}}^{\mathrm{eff}}(\Delta b)$'s in (2.43) by the fixed ($x$ and $E$ independent) value $\hat{q}_{\mathrm{A}}^{\mathrm{eff}}(\mathcal{B}_0)$, then the effective LO rate $[d\Gamma/dx]_{\mathrm{eff}}^{\mathrm{LO}}$ would be a fixed multiple of the original $[d\Gamma/dx]_{\mathrm{eff}}^{\mathrm{LO}}$ (i.e. something that could be absorbed by a constant shift of $\hat{q}$), and so the shape of the energy deposition distribution would be unchanged: $S_{\mathrm{eff}}^{\mathrm{LO}}(Z) = S^{\mathrm{LO}}(Z)$. One can see this by just replacing $\hat{q}_{\mathrm{A}}^{\mathrm{eff}}(\Delta b)$ with $\hat{q}_{(0)} + \delta\hat{q}$, where $\delta\hat{q}$ represents the constant shifts to $\hat{q}$ coming from using $\hat{q}_{\mathrm{A}}^{\mathrm{eff}}(\mathcal{B}_0)$, and remembering that $w_{12} + w_{23} + w_{31} = 1$. That means that the actual difference

---

[7]Our $\bar{\mathcal{B}}$ defined in (2.44) differs from the $\bar{B}$ defined in ref. [48]) by a factor of $(2i)^{1/4} = 2^{1/4} e^{i\pi/8}$.

between $S_{\text{eff}}^{\text{LO}}(Z)$ and $S^{\text{LO}}(Z)$ depends specifically on how $\hat{q}_{\text{A}}^{\text{eff}}(\Delta b)$ varies when one varies $\Delta b$.

## 2.2.2 The dependence of resummed $\hat{q}_{\text{A}}^{\text{eff}}(\Delta b)$ on $\Delta b$

We can extract the dependence of the original LMW $\hat{q}_{\text{eff}}(\Delta b)$ on $\Delta b$ from the parametric arguments for the the double log in ref. [30] if we write their answer in terms of variables that are relevant to our problem. Fig. 2.7 shows the double log region, where $\tau_0$ is the scale of the mean free path for elastic scattering of high-energy particles from the medium. The difference with the similar discussion in the LMW calculation, is that they were interested in the problem of transverse momentum broadening after passing through a large length of the $L$ of the medium, and so they set the transverse separation to be $\Delta b \sim (\hat{q}L)^{-1/2}$. To keep their result general, we need to restore back the $\Delta b$ dependence by substituting back $L \sim 1/\hat{q}(\Delta b)^2$ in their answer. After doing that, we get

$$\hat{q}_{\text{eff}}(\Delta b) = \hat{q}_{(0)} + \delta\hat{q}(\Delta b) \approx \hat{q}_{(0)} \left[ 1 + \frac{C_{\text{A}}\alpha_{\text{s}}}{2\pi} \ln^2 \left( \frac{1}{\hat{q}\tau_0(\Delta b)^2} \right) \right] \qquad (2.48)$$

at leading log order, to first order in $\alpha_{\text{s}}(\mu)$. The $\Delta b$ dependence of the double log above in fact contains all of the $\Delta b$ dependence including the single log as well [30]. We can therefore use LMW's results for leading-log order resummation to all orders in $\alpha_{\text{s}}(\mu)$ to also obtain the results for the $\Delta b$ *dependence* of a NLLO resummation. (We briefly give a more detailed argument of this claim in appendix A.3.)

Eq. (2.48) was derived for the case of a fixed coupling constant $\alpha_{\text{s}}$. They were able to resum the leading-log result to all orders in $\alpha_{\text{s}}$, and so we will use their answer for the fixed-coupling case. We will argue later that letting the coupling constant to depend
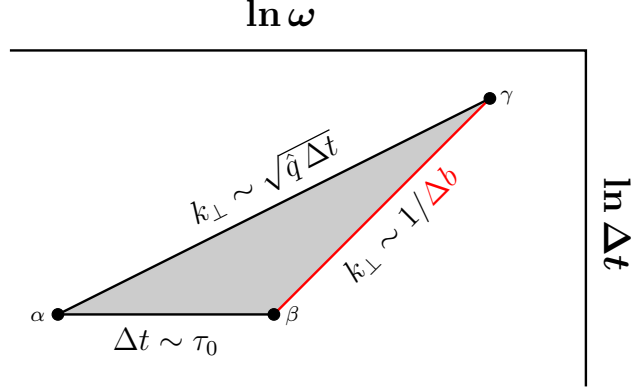
Figure 2.7: The integration region giving rise to the double logs of LMW [30]. Here $\omega$ is the energy of the soft radiated gluon (which we called $yE$ earlier), and $\Delta t$ is the time over which it is radiated (the difference of the emission time in the amplitude and the emission time in the conjugate amplitude). The transverse momentum of the soft radiated gluon is $k_\perp \sim \sqrt{\omega/\Delta t}$. The only boundary that is sensitive to $\Delta b$ is the red one. For a quark-gluon plasma, the three vertices $(\alpha, \beta, \gamma)$ above respectively correspond to $(\omega, \Delta t)$ of order $(T, \tau_0)$, $\big(\tau_0/(\Delta b)^2, \tau_0\big)$, and $\big((\hat{q}\,\Delta b)^{1/4}, 1/\hat{q}(\Delta b)^2\big)$. The last one is also parametrically $\sim \big(\Lambda_{\rm fac}, t_{\rm form}(\Lambda_{\rm fac})\big)$ for our application. We have not shown any vertical snip off the $\gamma$ corner corresponding to constraining $\omega \leq \Lambda_{\rm fac}$ because it is unimportant as far as large logarithms are concerned and so, for this purpose, is a detail hidden inside the circle marking that corner.

on the energy scale wouldn't matter for our conclusion. Their resummed result is

$$\hat{q}_{\rm eff}(\Delta b) \approx \hat{q}_{(0)}\, \frac{I_1\left(2\big(\frac{C_{\rm A}\alpha_{\rm s}}{\pi}\big)^{1/2}\ln\big(\frac{1}{\hat{q}\tau_0(\Delta b)^2}\big)\right)}{\big(\frac{C_{\rm A}\alpha_{\rm s}}{\pi}\big)^{1/2}\ln\big(\frac{1}{\hat{q}\tau_0(\Delta b)^2}\big)}, \tag{2.49}$$

where $I_1$ is the modified Bessel function. Note that we had already restored back the $\Delta b$ dependence in their answer. Remember that in our problem $\Delta b \sim \mathcal{B}_0 = (\hat{q}_{\rm A} E_0)^{-1/4}$, and so[8]

$$\frac{1}{\hat{q}\tau_0(\Delta b)^2} \sim \sqrt{\frac{E_0}{T}}\,. \tag{2.50}$$

---

[8]In the case of a weakly-coupled QGP with gauge coupling $g$, we've used $\hat{q}_{(0)} \sim g^4 T$ and $\tau_0 \sim 1/g^2 T$ and so $\hat{q}_{(0)}\tau_0^2 \sim T$ in (2.50). For a strongly-coupled QGP, the only relevant scale here is $T$.

In the high-energy limit of large logarithms, (2.49) becomes

$$\hat{q}_{\text{eff}}(\Delta b) \approx \hat{q}_{(0)} \left( \frac{1}{\hat{q}\tau_0(\Delta b)^2} \right)^{\sqrt{C_A \alpha_s/\pi}}. \qquad (2.51)$$

Since $\Delta b \sim \mathcal{B}_0$, this can be expanded as

$$\hat{q}_{\text{eff}}(\Delta b) \approx \hat{q}_{(0)} \left( \frac{1}{\hat{q}\tau_0 \mathcal{B}_0^2} \right)^{\sqrt{C_A \alpha_s/\pi}} \left[ 1 - \left( \frac{C_A \alpha_s}{\pi} \right)^{1/2} \ln \left( \frac{(\Delta b)^2}{\mathcal{B}_0^2} \right) \right] \qquad (2.52)$$

and so

$$\hat{q}_{\text{eff}}(\Delta b) = \hat{q}_{\text{eff}}(\mathcal{B}_0) \left[ 1 + O(\sqrt{\alpha_s}) \right] = (\text{fixed constant}) \times \left[ 1 + O(\sqrt{\alpha_s}) \right]. \qquad (2.53)$$

The expansion in $\sqrt{\alpha_s}$ made here is valid because $\ln(\Delta b/\mathcal{B}_0)$ is not a large logarithm in our application. As we see the resummed version of $\hat{q}_A^{\text{eff}}$ in eq. (2.53) introduces corrections of $O(\sqrt{\alpha_s})$ which is why we could ignore the difference between $S^{\text{LO}}(Z)$ and $S_{\text{eff}}^{\text{LO}}(Z)$ when computing the relative size of NLO corrections to $S_{\text{eff}}^{\text{LO}}(Z)$.

One can worry that one should self-consistently use $\hat{q}_{\text{eff}}$ instead of $\hat{q}_{(0)}$ for $\hat{q}$ in (2.50). Let's look at the ratio

$$\left( \frac{\hat{q}_{\text{eff}}}{\hat{q}_{(0)}} \right)^{\sqrt{\alpha_s}} = e^{\sqrt{\alpha_s} \ln \frac{\hat{q}_{\text{eff}}}{\hat{q}_{(0)}}} \simeq \left( \frac{1}{\hat{q}_{(0)}\tau_0(\Delta b)^2} \right)^{\alpha_s} \qquad (2.54)$$

where we used eq (2.51) for $\hat{q}_{\text{eff}}(\Delta b)$. Now if we multiply both the numerator and denominator of the left hand side by $\tau_0(\Delta b)^2$, we get

$$\left( \frac{\hat{q}_{\text{eff}}\tau_0(\Delta b)^2}{\hat{q}_{(0)}\tau_0(\Delta b)^2} \right)^{\sqrt{\alpha_s}} \simeq \left( \frac{1}{\hat{q}_{(0)}\tau_0(\Delta b)^2} \right)^{\alpha_s}. \qquad (2.55)$$

Rearranging the equation,

$$\left(\frac{1}{\hat{q}_{\text{eff}}\tau_0(\Delta b)^2}\right)^{\sqrt{\alpha_s}} = \left(\frac{1}{\hat{q}_{(0)}\tau_0(\Delta b)^2}\right)^{\sqrt{\alpha_s}-\alpha_s}. \tag{2.56}$$

So we see that the difference would only generate a sub-leading $O(\alpha_s)$ correction to the $O(\sqrt{\alpha_s})$ exponents in (2.51) and (2.52) and will not affect the conclusion (2.53).

### 2.2.3 Running of $\alpha_s(k_\perp)$

So far, we used an explicit resummation formula (2.49) that ignored running of $\alpha_s(k_\perp)$. At leading-log order, one may find more sophisticated discussions in refs. [31, 53, 54]. However, that analysis is not needed for our argument. In fig. 2.7 the largest value of $k_\perp$ happens at the red boundary $k_\perp = 1/\Delta b$, which means this is the smallest value for $\alpha_s(k_\perp)$. In our previous argument, we showed that

$$\frac{\hat{q}_{\text{eff}}(\Delta b) - \hat{q}_{\text{eff}}(\mathcal{B}_0)}{\hat{q}_{\text{eff}}(\mathcal{B}_0)} \ll 1, \tag{2.57}$$

so that $\hat{q}_{\text{eff}}(\Delta b)$ could be replaced by $\hat{q}_{\text{eff}}(\mathcal{B}_0)$ and that this ratio was $O(\sqrt{\alpha_s})$. Imagine that we choose that the fixed coupling was the coupling associated with the red boundary, $\alpha_s(1/\Delta b)$. Remember that $1/\Delta b \sim 1/\mathcal{B}_0 \sim (\hat{q}E_0)^{1/4} \sim \mu$ in our application, and so up to higher-order corrections, $\alpha_s(1/\Delta b)$ is just the $\alpha_s = \alpha_s(\mu)$ that we have been using. Now imagine we replace the fixed $\alpha_s = \alpha_s(1/\Delta b)$ by a running $\alpha_s(k_\perp)$. In that case, the numerator (2.57) does not change because it only involves the physics of $k_\perp \sim 1/\Delta b$. But the denominator gets bigger because, in the *rest* of the double-log region, $\alpha_s(k_\perp)$ is bigger than before. So, the parametric inequality (2.57) remains

valid for small $\alpha_{\mathrm{s}}(\mu)$.

### 2.2.4 Notation: LO vs. bare

Going forward, it will be helpful to somewhat streamline our notation. From now on, we will use the "LO" to refer to calculations based on the leading-order splitting rates (1.2) with $\hat{q}$ taken to be $\hat{q}_{\mathrm{eff}}(\mathcal{B}_0)$, as opposed to the bare coupling $\hat{q}_{(0)}$. With this nomenclature, we now formally have

$$\mathrm{LO}_{\mathrm{eff}} = \mathrm{LO} \times [1 + O(\sqrt{\alpha_{\mathrm{s}}})] \tag{2.58}$$

for all the quantities that we have in this discussion even the ones that are sensitive to constant shifts in $\hat{q}$.

## 2.3 Energy deposition equation

Now, we will derive the energy deposition equation satisfied by the energy deposition distribution $\epsilon(z)$. We will use the methods of refs. [22, 44].[9] We will start by reviewing the earlier results written in terms of $[d\Gamma/dx]_{1\to 2}$ and $[d\Gamma/dx]_{1\to 3}$, then we write the final formula in terms of the net rate $[d\Gamma/dx]_{\mathrm{net}}$.

Consider a shower composed of $1\to 2$ splittings, let $\epsilon(E, z)$ represent the distribution of deposited energy as a function of position $z$ for a shower initiated by a particle of

---

[9]See in particular appendix A.1 of ref. [44], but specialize throughout to the case of a single type of particle (namely gluons). Warning: Our $\epsilon(E, z)$ in this calculation is normalized as in (2.59), whereas the $\varepsilon(E, z)$ of ref. [44] is normalized so that $\int_0^\infty dz\, \varepsilon(E, z) = 1$. The conversion is simply that our $\epsilon(E, z) = E\, \varepsilon(E, z)$.

energy $E$, with

$$\int_0^\infty dz\, \epsilon(E, z) = E. \tag{2.59}$$

The starting equation is

$$\epsilon(E, z + \Delta z) \simeq [1 - \Gamma(E)\,\Delta z]\,\epsilon(E, z)$$
$$+ \frac{1}{2} \int_0^1 dx\, \left[\frac{d\Gamma}{dx}(E, x)\right]_{1\to 2} \Delta z \left\{\epsilon(xE, z) + \epsilon\big((1{-}x)E, z\big)\right\} \tag{2.60}$$

for small $\Delta z$. To see this, imagine traveling the distance $z + \Delta z$ on the left-hand side as first travelling $\Delta z$ followed by traveling distance $z$. In the first $\Delta z$ of distance, the particle has a chance $1 - \Gamma(E)\,\Delta z$ of not splitting at all, and then the energy density deposited after traveling the remaining distance $z$ will just be $\epsilon(E, z)$. This is represented by the first term on the right hand side of (2.60). Another possibility would be that the particle splits in the first $\Delta z$. In this case, we get two particles with energies $xE$ and $(1{-}x)E$, and with energy deposition distributions $\epsilon(xE, z)$ and $\epsilon\big((1{-}x)E, z\big)$ respectively after traveling the remaining distance $z$. The contribution from the two daughters to the energy deposited in the medium are added together in the second term of (2.60). The $\frac{1}{2}$ in the second term is the identical final-state particle factor for the two daughter gluons:

$$\Gamma(E) = \frac{1}{2} \int_0^1 dx\, \left[\frac{d\Gamma}{dx}(E, x)\right]_{1\to 2}. \tag{2.61}$$

Rearranging the terms in (2.60) and taking the limit $\Delta z \to 0$ yields the integro-differential equation

$$\frac{\partial \epsilon(E, z)}{\partial z} = -\Gamma(E)\,\epsilon(E, z) + \frac{1}{2} \int_0^1 dx\, \left[\frac{d\Gamma}{dx}(E, x)\right]_{1\to 2} \left\{\epsilon(xE, z) + \epsilon\big((1{-}x)E, z\big)\right\}. \tag{2.62}$$

Now use the symmetry of the LO rate $[d\Gamma/dx]_{1\to2}$ under exchange of the final-state daughters $x$ and $1-x$ to rewrite this as

$$\frac{\partial\epsilon(E,z)}{\partial z} = -\Gamma(E)\,\epsilon(E,z) + \int_0^1 dx \left[\frac{d\Gamma}{dx}(E,x)\right]_{1\to2} \epsilon(xE,z). \qquad (2.63)$$

We can do the same with $1\to3$ splittings by following the same steps. First, we add a term

$$+\frac{1}{3!}\int_0^1 dx \int_0^{1-x} dy \left[\frac{d\Gamma}{dx\,dy}(E,x,y)\right]_{1\to3} \left\{\epsilon(xE,z) + \epsilon(yE,z) + \epsilon\big((1-x-y)E,z\big)\right\}$$
$$(2.64)$$

to the right-hand side of (2.62). Using the symmetry of the three daughters, (2.63) generalizes to

$$\frac{\partial\epsilon(E,z)}{\partial z} = -\Gamma(E)\,\epsilon(E,z) + \int_0^1 dx \left[\frac{d\Gamma}{dx}(E,x)\right]_{1\to2} \epsilon(xE,z)$$
$$+ \frac{1}{2}\int_0^1 dx \int_0^{1-x} dy \left[\frac{d\Gamma}{dx\,dy}(E,x,y)\right]_{1\to3} \epsilon(xE,z)$$
$$= -\Gamma(E)\,\epsilon(E,z) + \int_0^1 dx \left[\frac{d\Gamma}{dx}(E,x)\right]_{\text{net}} \epsilon(xE,z), \qquad (2.65)$$

where the last equality uses (2.3). One can now express everything in terms of $[d\Gamma/dx]_{\text{net}}$ by (i) using (2.4) to rewrite $\Gamma$ as $\int dx\, x[d\Gamma/dx]_{\text{net}}$ and (ii) combining the $x$ integrals:

$$\frac{\partial\epsilon(E,z)}{\partial z} = \int_0^1 dx \left[\frac{d\Gamma}{dx}(E,x)\right]_{\text{net}} \left\{\epsilon(xE,z) - x\,\epsilon(E,z)\right\}. \qquad (2.66)$$

If $[d\Gamma/dx]_{\text{net}}$ scales with parent energy as $E^{-1/2}$, e.g. like the leading-order rate (1.2)

does, we can then define an energy-independent, rescaled rate $[d\tilde{\Gamma}/dx]_{\text{net}}$ by[10]

$$\left[\frac{d\Gamma}{dx}(E,x)\right]_{\text{net}} = E^{-1/2} \left[\frac{d\tilde{\Gamma}}{dx}(x)\right]_{\text{net}}. \tag{2.67}$$

Since the rates scale like $E^{-1/2}$, the distances $z$ characteristic of shower development will scale like $E^{1/2}$, and so the energy deposition distribution should scale as

$$\epsilon(E,z) \propto \tilde{\epsilon}(E^{-1/2}z). \tag{2.68}$$

We want the rescaled function $\tilde{\epsilon}(s)$ to be independent of $E$ and so have a normalization independent of $E$. We choose to normalize it as

$$\int_0^\infty ds\, \tilde{\epsilon}(s) = 1, \tag{2.69}$$

which, together with (2.59), fixes the proportionality constant in (2.68):

$$\epsilon(E,z) = E^{1/2}\, \tilde{\epsilon}(E^{-1/2}z). \tag{2.70}$$

For a shower initiated by a particle of energy $E_0$, (2.66) becomes

$$\frac{\partial \tilde{\epsilon}(\tilde{z})}{\partial \tilde{z}} = \int_0^1 dx\, x \left[\frac{d\tilde{\Gamma}}{dx}(x)\right]_{\text{net}} \left\{x^{-1/2}\, \tilde{\epsilon}(x^{-1/2}\tilde{z}) - \tilde{\epsilon}(\tilde{z})\right\}, \tag{2.71}$$

where

$$\tilde{z} \equiv E_0^{-1/2} z, \tag{2.72a}$$

---

[10]It might be more elegant to scale out a factor of $C_A \alpha_s \sqrt{\hat{q}_A/E}$ in (2.67) instead of just $E^{-1/2}$, so that the rescaled rate $[d\tilde{\Gamma}/dx]_{\text{net}}$ (and also eventually the coordinate $\tilde{z}$) would be dimensionless. We will find it convenient to do this later, in section 2.5. We don't do it now because it would slightly clutter our equations and de-emphasize the most essential point, the $E^{-1/2}$ dependence.

where the original energy deposition distribution $\epsilon(z)$ that we were looking for is

$$\epsilon(z) \equiv \epsilon(E_0, z) = E_0^{1/2}\tilde{\epsilon}(\tilde{z}). \tag{2.72b}$$

Now we can go back to the variable $z$ using (2.67) with $E = E_0$, along with (2.72), to rewrite (2.71) in terms of the original, unscaled variables as

$$\frac{\partial \epsilon(z)}{\partial z} = \int_0^1 dx\, x \left[\frac{d\Gamma}{dx}(E_0, x)\right]_{\text{net}} \left\{ x^{-1/2}\, \epsilon(x^{-1/2}z) - \epsilon(z) \right\}, \tag{2.73}$$

At this point, We need to emphasize that this formula is only valid if $[d\Gamma/dx]_{\text{net}}$ scales with energy as exactly $E^{-1/2}$. Note also that $[d\Gamma/dx]_{\text{net}}$ diverges $\propto [x(1-x)]^{-3/2}$ for $x \to 0$ and $x \to 1$. Having said that, the $x$ integration in (2.73) is convergent as $x \to 1$ because the two terms inside the braces then cancel, and it is also convergent as $x \to 0$ because of (i) the overall factor of $x$ in the integrand makes it goes as $x^{-1/2}$ and (ii) the fact that the energy deposition distribution $\epsilon(z')$ must fall rapidly (at least exponentially) to zero as $z' \to \infty$.

## 2.4 Moments of the shape $S(Z)$

The easiest thing to calculate from the energy deposition distribution $\epsilon(z)$ and its shape $S(Z)$, are their moments.

### 2.4.1 Recursion formula for moments of $\epsilon(z)$

The formula for the moments can be found by multiplying both sides of (2.73) by $z^n$ and integrate over $z$. Then, integrate by parts on the left-hand side of the equation.

We get the recursion relation:

$$-n\langle z^{n-1}\rangle = \int_0^1 dx\, x\left[\frac{d\Gamma}{dx}(E_0,x)\right]_{\text{net}}\left\{x^{n/2}\langle z^n\rangle - \langle z^n\rangle\right\}, \qquad (2.74)$$

giving

$$\langle z^n\rangle = \frac{n\langle z^{n-1}\rangle}{\text{Avg}[x(1-x^{n/2})]}, \qquad (2.75)$$

where we find it convenient to introduce the notation

$$\text{Avg}[g(x)] \equiv \int_0^1 dx\,\left[\frac{d\Gamma}{dx}(E_0,x)\right]_{\text{net}} g(x). \qquad (2.76)$$

The moments $\langle Z^n\rangle$ of the shape function $S(Z)$ [defined earlier by $(2.2)$] are given in terms of the moments $(2.75)$ as simply

$$\langle Z^n\rangle = \frac{\langle z^n\rangle}{\langle z\rangle^n}. \qquad (2.77)$$

As an example, the stopping distance is

$$\ell_{\text{stop}} \equiv \langle z\rangle = \frac{1}{\text{Avg}[x(1-\sqrt{x}\,)]}, \qquad (2.78)$$

and the width of the energy deposition distribution is $\sigma = \left(\langle z^2\rangle - \langle z\rangle^2\right)^{1/2}$ with

$$\langle z^2\rangle = \frac{2\ell_{\text{stop}}}{\text{Avg}[x(1-x)]}. \qquad (2.79)$$

The width of the shape function $S(Z)$ is then

$$\sigma_S = \frac{\sigma}{\ell_{\text{stop}}} = \left(\frac{2\,\text{Avg}[x(1-\sqrt{x}\,)]}{\text{Avg}[x(1-x)]} - 1\right)^{1/2}. \qquad (2.80)$$

## 2.4.2 Expansion in $\alpha_\mathrm{s}$ and results

We want to expand our results to NLO in $\alpha_\mathrm{s} = \alpha_\mathrm{s}(\mu)$ to calculate the relative size of the changes to the moments of the shape function due to overlapping formation times effects. We start by writting the splitting rate as

$$[d\Gamma/dx]_\mathrm{net} = [d\Gamma/dx]_\mathrm{eff}^\mathrm{LO} + [d\Gamma/dx]_\mathrm{net}^\mathrm{NLO,fac} \tag{2.81}$$

as discussed in subsection 2.1.2. Then, we expand the moments as

$$\langle z^n \rangle \simeq \langle z^n \rangle_\mathrm{LO}^\mathrm{eff} + \delta\langle z^n \rangle, \tag{2.82a}$$

where $\langle z^n \rangle_\mathrm{LO}^\mathrm{eff}$ represents the result obtained using $[d\Gamma/dx]_\mathrm{LO}^\mathrm{eff}$ instead of $[d\Gamma/dx]_\mathrm{net}$ in (2.75), and $\delta\langle z^n \rangle$ represents the result obtained using $[d\Gamma/dx]_\mathrm{net}^\mathrm{NLO,fac}$. The $\delta\langle z^n \rangle$ gives the correction to $\langle z^n \rangle_\mathrm{LO}^\mathrm{eff}$ at first order in $\alpha_\mathrm{s}(\mu)$. Note that, adopting the nomenclature of section 2.2.2,

$$\langle z^n \rangle_\mathrm{LO}^\mathrm{eff} = \langle z^n \rangle_\mathrm{LO} [1 + O(\sqrt{\alpha_\mathrm{s}})]. \tag{2.82b}$$

Expanding the recursion relation (2.75) gives

$$\delta\langle z^n \rangle = \langle z^n \rangle_\mathrm{LO} \left[ \frac{\delta\langle z^{n-1} \rangle}{\langle z^{n-1} \rangle_\mathrm{LO}} - \frac{\delta\mathrm{Avg}[x(1 - x^{n/2})]}{\mathrm{Avg}[x(1 - x^{n/2})]_\mathrm{LO}} \right], \tag{2.83}$$

where

$$\mathrm{Avg}[g(x)]_\mathrm{LO} \equiv \int_0^1 dx \left[ \frac{d\Gamma}{dx}(E_0, x) \right]^\mathrm{LO} g(x),$$

$$\delta\mathrm{Avg}[g(x)] \equiv \int_0^1 dx \left[ \frac{d\Gamma}{dx}(E_0, x) \right]_\mathrm{net}^\mathrm{NLO,fac} g(x), \tag{2.84a}$$

| $z^n$ | $\langle z^n \rangle_{\mathrm{LO}}$ | $\delta\langle z^n \rangle$ | $\langle z^n \rangle_{\mathrm{LO}}^{1/n}$ | $\delta[\langle z^n \rangle^{1/n}]$ |
|---|---|---|---|---|
| | in units of $\ell_0^n$ | | in units of $\ell_0$ | |
| $z$ | 2.1143 | $2.2326\, C_{\mathrm{A}}\alpha_{\mathrm{s}}$ | 2.1143 | $2.2326\, C_{\mathrm{A}}\alpha_{\mathrm{s}}$ |
| $z^2$ | 5.7937 | $12.185\, C_{\mathrm{A}}\alpha_{\mathrm{s}}$ | 2.4070 | $2.5312\, C_{\mathrm{A}}\alpha_{\mathrm{s}}$ |
| $z^3$ | 18.758 | $59.185\, C_{\mathrm{A}}\alpha_{\mathrm{s}}$ | 2.6570 | $2.7944\, C_{\mathrm{A}}\alpha_{\mathrm{s}}$ |
| $z^4$ | 68.533 | $288.85\, C_{\mathrm{A}}\alpha_{\mathrm{s}}$ | 2.8772 | $3.0317\, C_{\mathrm{A}}\alpha_{\mathrm{s}}$ |

Table 2.2: Expansions (2.82) of the moments $\langle z^n \rangle$ of the energy deposition distribution $\epsilon(z)$ for $\Lambda_{\mathrm{fac}} = x(1-x)E$ [(2.19) with $\kappa = 1$]. The last two columns show similar expansions of $\langle z^n \rangle^{1/n}$, for which $\delta[\langle z^n \rangle^{1/n}] = \frac{1}{n}\langle z^n \rangle_{\mathrm{LO}}^{(1/n)-1}\,\delta\langle z^n \rangle$. The unit $\ell_0$ is defined by (2.88).

and $\delta\langle z^0 \rangle \equiv 0$. The LO moments are determined recursively by the analog of (2.75),

$$\langle z^n \rangle_{\mathrm{LO}} = \frac{n\langle z^{n-1} \rangle_{\mathrm{LO}}}{\mathrm{Avg}[x(1-x^{n/2})]_{\mathrm{LO}}} \, . \tag{2.85}$$

In table 2.2, we give the results for the first few moments $\langle z^n \rangle$ which are calculated using (1.2) for the LO rate and

$$\left[\frac{d\Gamma}{dx}\right]_{\mathrm{net}}^{\mathrm{NLO,fac}} = C_{\mathrm{A}}\alpha_{\mathrm{s}} \left[\frac{d\Gamma}{dx}\right]^{\mathrm{LO}} f(x) \tag{2.86}$$

with fit function (2.22) and $\Lambda_{\mathrm{fac}} = x(1-x)E$ for the NLO rate. The parametric scale for the stopping distance ($\langle z \rangle$) is

$$\ell_{\mathrm{stop}} \sim \frac{1}{C_{\mathrm{A}}\alpha_{\mathrm{s}}}\sqrt{\frac{E}{\hat{q}_{\mathrm{A}}}}, \tag{2.87}$$

and so we expressed the moments in table 2.2 in appropriate units of

$$\ell_0 \equiv \frac{1}{C_{\mathrm{A}}\alpha_{\mathrm{s}}}\sqrt{\frac{E}{\hat{q}_{\mathrm{A}}}} \, . \tag{2.88}$$

To compare these moments, we need them to have the same dimensions, and so we converted all the moments into lengths $\langle z^n \rangle^{1/n}$ whose expansions are presented in the last two columns. We can see that the overlap corrections are $O(100\%) \times C_A \alpha_s$, similar to the size of NLO corrections that we saw for $[d\Gamma/dx]_{\text{net}}$ in section 2.1.4.

Let's now look at the analog of $\langle z^n \rangle^{1/n}$ for moments of the shape function $S(Z)$:

$$\langle Z^n \rangle^{1/n} = \frac{\langle z^n \rangle^{1/n}}{\langle z \rangle}. \tag{2.89}$$

The expansions to NLO for these moments are given in table 2.3, using the adjustable factorization scale $\Lambda_{\text{fac}} = \kappa x(1-x)$ and explicitly showing the $\kappa$ dependence of the results.[11] In all these entries, we use $\chi \alpha_s$ as our name for the relative size of NLO corrections:

$$\chi \alpha_s \equiv \frac{\delta Q}{Q_{\text{LO}}} \tag{2.90}$$

for any quantity $Q$. Table 2.3 similarly shows results for $(\mu_{n,S})^{1/n}$, where the reduced moment $\mu_{n,S}$ of the shape $S(Z)$ is

$$\mu_{n,S} \equiv \langle (Z - \langle Z \rangle)^n \rangle. \tag{2.91}$$

The first quantity we looked at is [50]

$$\sigma_S = \frac{\sigma}{\ell_{\text{stop}}} = \mu_{2,S}^{1/2}, \tag{2.92}$$

for which the relative size of the $\chi \alpha_s$ of NLO corrections is roughly $-2\% \times C_A \alpha_s$ for $\kappa = 1$ and which is small for any reasonable value of $\kappa$. All the other $\langle Z^n \rangle^{1/n}$ and

---

[11]If we had shown $\kappa$ dependence for the moments of table 2.2, they would have double log dependence on $\kappa$. For example, $\langle z \rangle = 2.1134 + (2.2364 + 0.3084 \ln \kappa - 0.0841 \ln^2 \kappa)$ in units of $\sqrt{E_0/\hat{q}_A}$. We didn't show this for everything since we are focused on the shape function, because it is not affected by constant changes in $\hat{q}$.

| quantity $Q$ | $Q_{\mathrm{LO}}$ | $\delta Q$ | $\chi\alpha_{\mathrm{s}}$ |
|---|---|---|---|
| $\langle Z \rangle$ | 1 | | |
| $\langle Z^2 \rangle^{1/2}$ | 1.1384 | $(-0.0050 + 0.0004\ln\kappa)\,C_{\mathrm{A}}\alpha_{\mathrm{s}}$ | $(-0.0044 + 0.0003\ln\kappa)\,C_{\mathrm{A}}\alpha_{\mathrm{s}}$ |
| $\langle Z^3 \rangle^{1/3}$ | 1.2567 | $(-0.0053 + 0.0006\ln\kappa)\,C_{\mathrm{A}}\alpha_{\mathrm{s}}$ | $(-0.0042 + 0.0005\ln\kappa)\,C_{\mathrm{A}}\alpha_{\mathrm{s}}$ |
| $\langle Z^4 \rangle^{1/4}$ | 1.3608 | $(-0.0031 + 0.0007\ln\kappa)\,C_{\mathrm{A}}\alpha_{\mathrm{s}}$ | $(-0.0023 + 0.0005\ln\kappa)\,C_{\mathrm{A}}\alpha_{\mathrm{s}}$ |
| $\mu_{2,S}^{1/2} = k_{2,S}^{1/2} = \sigma_S$ | 0.5441 | $(-0.0104 + 0.0008\ln\kappa)\,C_{\mathrm{A}}\alpha_{\mathrm{s}}$ | $(-0.0190 + 0.0014\ln\kappa)\,C_{\mathrm{A}}\alpha_{\mathrm{s}}$ |
| $\mu_{3,S}^{1/3} = k_{3,S}^{1/3}$ | 0.4587 | $(\phantom{-}0.0138 + 0.0004\ln\kappa)\,C_{\mathrm{A}}\alpha_{\mathrm{s}}$ | $(\phantom{-}0.0301 + 0.0010\ln\kappa)\,C_{\mathrm{A}}\alpha_{\mathrm{s}}$ |
| $\mu_{4,S}^{1/4}$ | 0.7189 | $(\phantom{-}0.0011 + 0.0006\ln\kappa)\,C_{\mathrm{A}}\alpha_{\mathrm{s}}$ | $(\phantom{-}0.0015 + 0.0009\ln\kappa)\,C_{\mathrm{A}}\alpha_{\mathrm{s}}$ |
| $k_{4,S}^{1/4}$ | 0.2561 | $(\phantom{-}0.3227 - 0.0086\ln\kappa)\,C_{\mathrm{A}}\alpha_{\mathrm{s}}$ | $(\phantom{-}1.2601 - 0.0338\ln\kappa)\,C_{\mathrm{A}}\alpha_{\mathrm{s}}$ |

Table 2.3: Expansions involving moments $\langle Z^n \rangle$, reduced moments $\mu_{n,S}$, and cumulants $k_{n,S}$ of the shape function $S(Z)$. Here we take $\Lambda_{\mathrm{fac}} = \kappa x(1-x)$ and show the $\kappa$ dependence of the results. There are no NLO entries for $\langle Z \rangle$ because $\langle Z \rangle = 1$ and $\langle Z \rangle_{\mathrm{LO}} = 1$ by definition of $Z \equiv z/\langle z \rangle$.

$(\mu_{n,\mathrm{S}})^{1/n}$ entries in table 2.3 have similarly small NLO corrections.

We also calculated the the cumulants $k_{n,S}$ of $S(Z)$ and their NLO expansions up through $n = 4$. For $n < 4$, cumulants are the same as reduced moments, but

$$k_{4,S} \equiv \mu_{4,S} - 3\mu_{2,S}^2. \tag{2.93}$$

The only quantity that had significantly large corrections was the $k_{4,S}^{1/4}$ which is more than 100% $C_{\mathrm{A}}\alpha_{\mathrm{s}}$ ! This is because there is cancellation between the LO values in the right-hand side of (2.93), and so the relatively small NLO corrections to $\mu_{4,S}$ and $3\mu_{2,S}^2$ become a large relative correction to what's left over. This large correction made us consider whether the NLO corrections is an important effect or whether we need to look at higher moments. To settle this, we decided to calculate the NLO corrections to the shape function $S(Z)$ not just its moments. We will see later that the NLO corrections to the shape function are very small and the effect of the fourth cumulant is not big.

### 2.4.3 A formula for later

For later reference, we will show one explicit example of how to write $\delta Q$ in table 2.2 in terms of the $\delta\langle z^n \rangle$ and $\langle z^n \rangle_{\mathrm{LO}}$. First, we start from $\sigma = (\langle z^2 \rangle - \langle z \rangle)^{1/2}$ and $\ell_{\mathrm{stop}} = \langle z \rangle$. We have

$$\delta\sigma_S = \delta\left(\frac{\sigma}{\ell_{\mathrm{stop}}}\right) = \sigma_{S,\mathrm{LO}}\left(\frac{\delta(\sigma^2)}{2\sigma_{\mathrm{LO}}^2} - \frac{\delta\langle z \rangle}{\langle z \rangle_{\mathrm{LO}}}\right) = \sigma_{S,\mathrm{LO}}\left(\frac{\delta\langle z^2 \rangle - 2\langle z \rangle_{\mathrm{LO}}\,\delta\langle z \rangle}{2(\langle z^2 \rangle_{\mathrm{LO}} - \langle z \rangle_{\mathrm{LO}}^2)} - \frac{\delta\langle z \rangle}{\langle z \rangle_{\mathrm{LO}}}\right), \tag{2.94}$$

and so

$$[\chi\alpha_{\mathrm{s}}]_{\sigma_S} = \frac{\delta\langle z^2 \rangle - 2\langle z \rangle_{\mathrm{LO}}\,\delta\langle z \rangle}{2(\langle z^2 \rangle_{\mathrm{LO}} - \langle z \rangle_{\mathrm{LO}}^2)} - \frac{\delta\langle z \rangle}{\langle z \rangle_{\mathrm{LO}}}. \tag{2.95}$$

Combined with (2.83) and (2.85), that's good enough for numerics. If desired, one may simplify this formula to[12]

$$[\chi\alpha_{\mathrm{s}}]_{\sigma_S} = \frac{\delta\mathrm{Avg}[x(1 - \sqrt{x})^2]}{2\,\mathrm{Avg}[x(1 - \sqrt{x})^2]_{\mathrm{LO}}} - \frac{\delta\mathrm{Avg}[x(1 - x)]}{2\,\mathrm{Avg}[x(1 - x)]_{\mathrm{LO}}}. \tag{2.96}$$

### 2.4.4 An alternate choice: $\Lambda_{\mathrm{fac}} = rE$

We can check the robustness of our conclusion, that the NLO corrections to moments (other than the fourth cumulant) are tiny relative to the LO results, by choosing a different factorization scale and see how different our results are. We argued back in section 2.1.3 that $\Lambda_{\mathrm{fac}} = rE$, where $r$ is an $O(1)$ constant, is a poor choice of $\Lambda_{\mathrm{fac}}$ for small $x(1-x)$ but should be adequate for defining the factorization of the shower's energy deposition distribution $\epsilon(z)$, and hence shape $S(Z)$ into $\mathrm{LO}_{\mathrm{eff}}$ and NLO pieces. We can convert $[d\Gamma/dx]_{\mathrm{net}}^{\mathrm{NLO,fac}}$ from our original choice $\Lambda_{\mathrm{fac}} = x(1-x)E$

---

[12]The averages in the first term of (2.96) are related to the averages of $x(1 - x^{n/2})$ that arise in an evaluation of (2.95) by the linearity of the definitions (2.84) of $\delta\mathrm{Avg}$ and $\mathrm{Avg}_{\mathrm{LO}}$ in their argument, which gives $\delta\mathrm{Avg}[x(1 - \sqrt{x})^2] = 2\,\delta\mathrm{Avg}[x(1 - \sqrt{x})] - \delta\mathrm{Avg}[x(1 - x)]$ and similarly for $\mathrm{Avg}_{\mathrm{LO}}$.

| quantity $Q$ | $\chi\alpha_\mathrm{s}$ ($\Lambda_\mathrm{fac}=rE$) |
|---|---|
| $\langle Z \rangle$ | |
| $\langle Z^2 \rangle^{1/2}$ | $(0.0024 + 0.0057\ln(4r))\,C_\mathrm{A}\alpha_\mathrm{s}$ |
| $\langle Z^3 \rangle^{1/3}$ | $(0.0052 + 0.0082\ln(4r))\,C_\mathrm{A}\alpha_\mathrm{s}$ |
| $\langle Z^4 \rangle^{1/4}$ | $(0.0081 + 0.0090\ln(4r))\,C_\mathrm{A}\alpha_\mathrm{s}$ |
| $\mu_{2,S}^{1/2} = k_{2,S}^{1/2} = \sigma_S$ | $(0.0104 + 0.0252\ln(4r))\,C_\mathrm{A}\alpha_\mathrm{s}$ |
| $\mu_{3,S}^{1/3} = k_{3,S}^{1/3}$ | $(0.0428 + 0.0140\ln(4r))\,C_\mathrm{A}\alpha_\mathrm{s}$ |
| $\mu_{4,S}^{1/4}$ | $(0.0237 + 0.0169\ln(4r))\,C_\mathrm{A}\alpha_\mathrm{s}$ |
| $k_{4,S}^{1/4}$ | $(0.8363 - 0.4878\ln(4r))\,C_\mathrm{A}\alpha_\mathrm{s}$ |

Table 2.4: Like the last column of table 2.3 (the relative size of NLO corrections) but computed here for factorization scale $\Lambda_\mathrm{fac} = rE$.

to $\Lambda_\mathrm{fac} = rE$ using (2.28) and then use it to compute moments. Table 2.4 shows the result of converting the last column $\chi\alpha_\mathrm{s}$ of table 2.3 to $\Lambda_\mathrm{fac} = rE$.[13]

Like table 2.3, the relative size of NLO corrections remain small, except for $k_{4,S}^{1/4}$. Note that results for $\Lambda_\mathrm{fac} = rE$ are more sensitive to the exact choice of $r$ than results for $\Lambda_\mathrm{fac} = \kappa x(1-x)E$ were to the choice of $\kappa$.

### 2.4.5 The relative importance of F diagrams

Table 2.1, or a comparison of figs. 2.2 and 2.3, shows that F=4+I diagrams (like those of fig. 1.10) make up a relatively small contribution to $[d\Gamma/dx]_\mathrm{net}^{\mathrm{NLO,fac}}$ for $\Lambda_\mathrm{fac} = x(1-x)E$. However, it is interesting to investigate their contribution to the shape $S(Z)$ of energy deposition, which is insensitive to changes that can be absorbed into $\hat{q}$.

---

[13]$\kappa = 1$ was our canonical choice for $\Lambda_\mathrm{fac} = \kappa x(1-x)E$. In table 2.4, we take made $r = \frac{1}{4}$ our "canonical" choice for $\Lambda_\mathrm{fac} = rE$, just because it matches $\Lambda_\mathrm{fac} = x(1-x)E$ for perfectly democratic splittings $x = 0.5$. This is the reason we write the logs in table 2.4 as $\ln(4r)$, so that the logs vanish for $r = \frac{1}{4}$.

| quantity $Q$ | $\dfrac{\chi\alpha_{\rm s}\ {\rm (F\ diags\ only)}}{\chi\alpha_{\rm s}\ {\rm (total)}}$ |
|---|---|
| $\langle Z \rangle$ | |
| $\langle Z^2 \rangle^{1/2}$ | $-14\%$ |
| $\langle Z^3 \rangle^{1/3}$ | $-25\%$ |
| $\langle Z^4 \rangle^{1/4}$ | $-63\%$ |
| $\mu_{2,S}^{1/2} = k_{2,S}^{1/2} = \sigma_S$ | $-14\%$ |
| $\mu_{3,S}^{1/3} = k_{3,S}^{1/3}$ | $18\%$ |
| $\mu_{4,S}^{1/4}$ | $216\%$ |
| $k_{4,S}^{1/4}$ | $4\%$ |

Table 2.5: The relative contribution of F=4+I diagrams to the $\chi\alpha_{\rm s}$ values listed in table 2.3 for $\kappa = 1$.

Table 2.5 shows the relative contribution of F diagrams to $\chi\alpha_{\rm s}$ compared to the total of all NLO diagrams. Their effect is very small for our favorite characteristic $\mu_{2,S}^{1/2} = \sigma/\ell_{\rm stop}$ of the shape. However, their relative effect is larger for higher moments like $\mu_{4,S}^{1/4}$. The upshot is that calculation of the F-diagrams [52] was important for getting good estimates of some of the shape moments in a particular factorization scheme, but their exclusion wouldn't have affected the answer to the qualitative question of whether NLO corrections are large.

## 2.5 The full shape $S(Z)$

Now we want to calculate the full shape function $S(Z)$ expanded to first order in $[d\Gamma/dx]_{\rm net}^{\rm NLO,fac}$.

## 2.5.1 Method

Starting from (2.73) for $\epsilon(z)$, we will switch to the dimensionless variables

$$\hat{z} \equiv \frac{z}{\ell_0}, \qquad \hat{\epsilon}(\hat{z}) \equiv \frac{\ell_0}{E_0}\, \epsilon(\ell_0 \hat{z}), \qquad \frac{d\hat{\Gamma}}{dx} = \ell_0\, \frac{d\Gamma}{dx}\,, \tag{2.97}$$

with $\ell_0$ defined by (2.88). Then

$$\frac{\partial \hat{\epsilon}(\hat{z})}{\partial \hat{z}} = \int_0^1 dx\, x \left[\frac{d\hat{\Gamma}}{dx}\right]_{\text{net}} \big\{ x^{-1/2}\, \hat{\epsilon}(x^{-1/2}\hat{z}) - \hat{\epsilon}(\hat{z}) \big\}. \tag{2.98}$$

The leading-order version is just

$$\frac{\partial \hat{\epsilon}_{\text{LO}}(\hat{z})}{\partial \hat{z}} = \int_0^1 dx\, x \left[\frac{d\hat{\Gamma}}{dx}\right]^{\text{LO}} \big\{ x^{-1/2}\, \hat{\epsilon}_{\text{LO}}(x^{-1/2}\hat{z}) - \hat{\epsilon}_{\text{LO}}(\hat{z}) \big\}. \tag{2.99}$$

To solve (2.99) numerically, we follow a procedure similar to ref. [44].[14] We will start with an approximate asymptotic solution for large $\hat{z}$,

$$\hat{\epsilon}_{\text{LO}}(\hat{z}) \sim e^{-\hat{z}^2/\pi}, \tag{2.100}$$

which is derived in appendix A.4. [ Note that the exponential dependence is the same as that for the Blaizot/Iancu/Mehtar-Tani (BIM) model for showers, discussed in appendix A.5.] We choose a large value for $\hat{z}_{\text{max}} \gg 1$ and use (2.100) for $\hat{z} > \hat{z}_{\text{max}}$. Eq (2.99) is a linear equation, and so it doesn't care about the overall normalization of $\hat{\epsilon}_{\text{LO}}$, and so we initially take $\hat{\epsilon}_{\text{LO}}(\hat{z}) = e^{-\hat{z}^2/\pi}$ for $\hat{z} > \hat{z}_{\text{max}}$ and we will normalize $\hat{\epsilon}_{\text{LO}}$ later.

---

[14]Specifically, see appendix B of ref. [44].

Next, we choose a small increment $\Delta\hat{z} \ll 1$ and approximate (2.99) by

$$\hat{\epsilon}_{\mathrm{LO}}(\hat{z} - \Delta z) \simeq \hat{\epsilon}_{\mathrm{LO}}(\hat{z}) - \Delta z \int_0^1 dx\, x \left[\frac{d\hat{\Gamma}}{dx}\right]^{\mathrm{LO}} \left\{ x^{-1/2}\, \hat{\epsilon}_{\mathrm{LO}}(x^{-1/2}\hat{z}) - \hat{\epsilon}_{\mathrm{LO}}(\hat{z}) \right\}. \quad (2.101)$$

Note that, for any value of $\hat{z}$, the arguments of the function $\hat{\epsilon}_{\mathrm{LO}}$ on the right-hand side of (2.101) are never smaller than $\hat{z}$ itself. So, starting with $\hat{z} = \hat{z}_{\max}$, we use (2.101) repeatedly, step by step, to calculate $\hat{\epsilon}_{\mathrm{LO}}(\hat{z})$ for smaller and smaller values of $\hat{z}$, until we get to $\hat{z} = 0$. Once we are done, we will normalize $\hat{\epsilon}_{\mathrm{LO}}(\hat{z})$ so that

$$\int_0^\infty d\hat{z}\, \hat{\epsilon}_{\mathrm{LO}}(\hat{z}) = 1. \quad (2.102)$$

More details are provided in appendix A.2.2.

Next, we substitute

$$\hat{\epsilon}(\hat{z}) \simeq \hat{\epsilon}_{\mathrm{LO}}(\hat{z}) + \delta\hat{\epsilon}(\hat{z}) \quad (2.103)$$

into (2.98) and expand to first order in NLO quantities, giving

$$\frac{\partial\, \delta\hat{\epsilon}(\hat{z})}{\partial\hat{z}} = \int_0^1 dx\, x \left[\frac{d\hat{\Gamma}}{dx}\right]^{\mathrm{LO}} \left\{ x^{-1/2}\, \delta\hat{\epsilon}(x^{-1/2}\hat{z}) - \delta\hat{\epsilon}(\hat{z}) \right\}$$
$$+ \int_0^1 dx\, x \left[\frac{d\hat{\Gamma}}{dx}\right]_{\mathrm{net}}^{\mathrm{NLO,fac}} \left\{ x^{-1/2}\, \hat{\epsilon}_{\mathrm{LO}}(x^{-1/2}\hat{z}) - \hat{\epsilon}_{\mathrm{LO}}(\hat{z}) \right\}. \quad (2.104)$$

This looks exactly like the LO equation (2.99) except for the last term which acts as a driving term generated by the previously computed $\hat{\epsilon}_{\mathrm{LO}}(\hat{z})$. To solve (2.104), we discretize it similar to (2.101) but start with $\delta\hat{\epsilon}(\hat{z}) = 0$ for $\hat{z} > \hat{z}_{\max}$. Let $\delta\hat{\epsilon}_1(\hat{z})$ be the solution obtained through this procedure.

If $\delta\hat{\epsilon}_1(\hat{z})$ is a solution to (2.104), then so is

$$\delta\hat{\epsilon}(\hat{z}) = \delta\hat{\epsilon}_1(\hat{z}) + c\,\hat{\epsilon}_{\mathrm{LO}}(\hat{z}) \tag{2.105}$$

for any constant $c$. The solution we need should be consistent with normalizing $\hat{\epsilon} = \hat{\epsilon}_{\mathrm{LO}} + \delta\hat{\epsilon}$ so that $\int d\hat{z}\,\hat{\epsilon}(\hat{z}) = 1$ through first order. That normalization requires

$$\int_0^\infty d\hat{z}\,\delta\hat{\epsilon}(\hat{z}) = 0. \tag{2.106}$$

The properly normalized solution (2.105) can be obtained from any particular solution $\delta\hat{\epsilon}_1$ by

$$\delta\hat{\epsilon}(\hat{z}) = \delta\hat{\epsilon}_1(\hat{z}) - \hat{\epsilon}_{\mathrm{LO}}(\hat{z}) \int_0^\infty d\hat{z}\,\delta\hat{\epsilon}_1(\hat{z}), \tag{2.107}$$

provided we have normalized $\hat{\epsilon}_{\mathrm{LO}}$ as in (2.102).

Finally, the expansion

$$S(Z) \simeq S_{\mathrm{LO}}(Z) + \delta S(Z) \tag{2.108}$$

of the shape function (2.2) to first order in $[d\Gamma/dx]_{\mathrm{net}}^{\mathrm{NLO,fac}}$ can be written in the form

$$S_{\mathrm{LO}}(Z) = \langle\hat{z}\rangle_{\mathrm{LO}}\,\hat{\epsilon}_{\mathrm{LO}}\big(Z\langle\hat{z}\rangle_{\mathrm{LO}}\big), \tag{2.109}$$

$$\delta S(Z) = \left[\langle\hat{z}\rangle_{\mathrm{LO}}\,\delta\hat{\epsilon}(\hat{\zeta}) + \delta\langle\hat{z}\rangle\,\frac{d}{d\hat{\zeta}}\big(\hat{\zeta}\,\hat{\epsilon}_{\mathrm{LO}}(\hat{\zeta})\big)\right]_{\hat{\zeta}=Z\langle\hat{z}\rangle_{\mathrm{LO}}}, \tag{2.110}$$

where $\langle\hat{z}\rangle_{\mathrm{LO}}$ is evaluated using $\hat{\epsilon}_{\mathrm{LO}}$, and $\delta\langle\hat{z}\rangle$ is

$$\delta\langle\hat{z}\rangle = \int_0^\infty d\hat{z}\,\hat{z}\,\delta\hat{\epsilon}(\hat{z}). \tag{2.111}$$

## 2.5.2   Results and Checks

We show our numerical results for $\hat{\epsilon}_{\text{LO}}(\hat{z})$ and $\delta\hat{\epsilon}(\hat{z})/C_A\alpha_s$ in fig. 2.8, and we see that NLO corrections to the leading-order energy deposition distribution are large unless $C_A\alpha_s$ is indeed small. However, this is not surprising because the NLO corrections for the net rate $[d\Gamma/dx]_{\text{net}}$ decreased the rate by $O(100\%) \times C_A\alpha_s$. This will change how soon the shower stops, and so will make a large change to where the energy is deposited. In fact, our expansion $\hat{\epsilon}(\hat{z}) \simeq \hat{\epsilon}_{\text{LO}}(\hat{z}) + \delta\hat{\epsilon}(\hat{z})$ would not make physical sense unless $C_A\alpha_s$ were smaller than roughly 0.25 because the energy distribution $\hat{\epsilon}(\hat{z})$ must be everywhere positive and $\hat{\epsilon}_{\text{LO}}(\hat{z}) + \delta\hat{\epsilon}(\hat{z})$ would not be. To understand the shape of $\delta\hat{\epsilon}(\hat{z})$ in fig. 2.8b, we will rescale the $\hat{z}$ axis such that

$$\hat{\epsilon}_{\text{LO}}(\hat{z}) \to \lambda\,\hat{\epsilon}_{\text{LO}}(\lambda\hat{z}). \tag{2.112}$$

Now we increase the stopping distance by choosing $\lambda = 1 - \xi$ and then expand to first order in $\xi$ just as we formally expand our overlap results to first order in $\alpha_s$. Then the change in $\hat{\epsilon}_{\text{LO}}$ is proportional to

$$-\left[\hat{\epsilon}_{\text{LO}}(\hat{z}) + \hat{z}\,\hat{\epsilon}'_{\text{LO}}(\hat{z})\right]. \tag{2.113}$$

The dashed line in fig. 2.8b is a plot of (2.113). Note that it is almost proportional to the solid curve for $\delta\hat{\epsilon}(\hat{z})/C_A\alpha_s$ which means that the corrections that we see in fig. 2.8b can mostly be absorbed into a change in the stopping distance and so into the value of $\hat{q}$.

Now we look at the shape function $S(Z) \simeq S_{\text{LO}}(Z) + \delta S(Z)$, which is insensitive to constant changes that can be absorbed into $\hat{q}$. Fig. 2.9 shows plots of $S_{\text{LO}}(Z)$

(a)



(b)
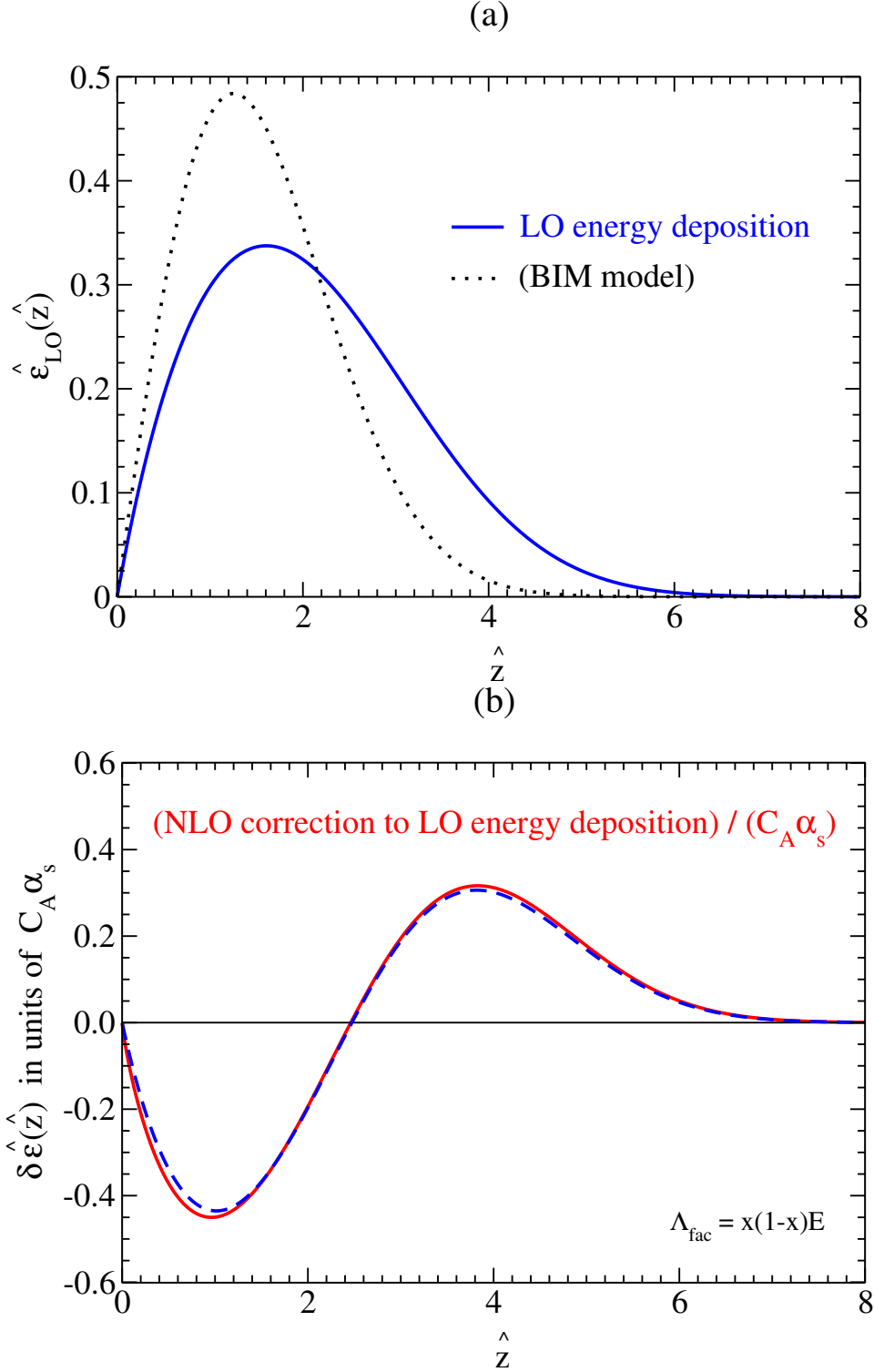


Figure 2.8: (a) The solid curve shows the energy deposition distribution $\hat{\epsilon}_{\rm LO}(\hat{z})$ vs. $\hat{z} \equiv z/\ell_0$, where the unit $\ell_0$ is defined in (2.88). [For comparison, the dotted curve shows an analytic result (A.68) derived from the BIM model.] (b) A similar plot of $\delta\hat{\epsilon}_{\rm LO}(\hat{z})/C_{\rm A}\alpha_{\rm s}$ for our canonical choice $\Lambda_{\rm fac} = x(1-x)E$ of factorization scale. For comparison, the dashed curve shows the first-order change (2.113) that would be induced in $\hat{\epsilon}_{\rm LO}(\hat{z})$ by rescaling the $\hat{z}$ axis in fig. (a).

64

and $\delta S(Z)$. The NLO corrections to $S_{\text{LO}}(Z)$ are small even for $C_A \alpha_s = 1$, which is consistent with our results for the moments of the shape function in table 2.3. This also shows that the relatively large correction to the 4th cumulant does not correspond to a significant change to the shape distribution $S(Z)$. Fig. 2.10 shows the comparison presented in our papers [50, 56] of $S_{\text{LO}}(Z)$ vs. $S(Z)$ for $C_A \alpha_s = 1$.

The shape functions shown in fig. 2.9 were linearly extrapolated to the continuum limit $\Delta\hat{z} = 0$ from simulations at $(\Delta\hat{z}, \hat{z}_{max}) = (0.0025, 20)$ and $(0.005, 20)$. We also checked whether the moments from our numerical results for $S_{\text{LO}}(Z)$ and $\delta S(Z)$ agree with the moments calculated in table 2.3. Fig. 2.11 shows the approach to the continuum limit of the relative size $\chi\alpha_s$ of NLO corrections to the reduced moments and cumulants. One can see from the figure that a linear extrapolation from our two smallest $\Delta\hat{z}$ values will do fairly well at reproducing our earlier (and more precise) moment results.[15]

---

[15]See appendix A.2.2 for a demonstration that errors associated with our choice of $\hat{z}_{max}$ were negligible.

(a)

(b)
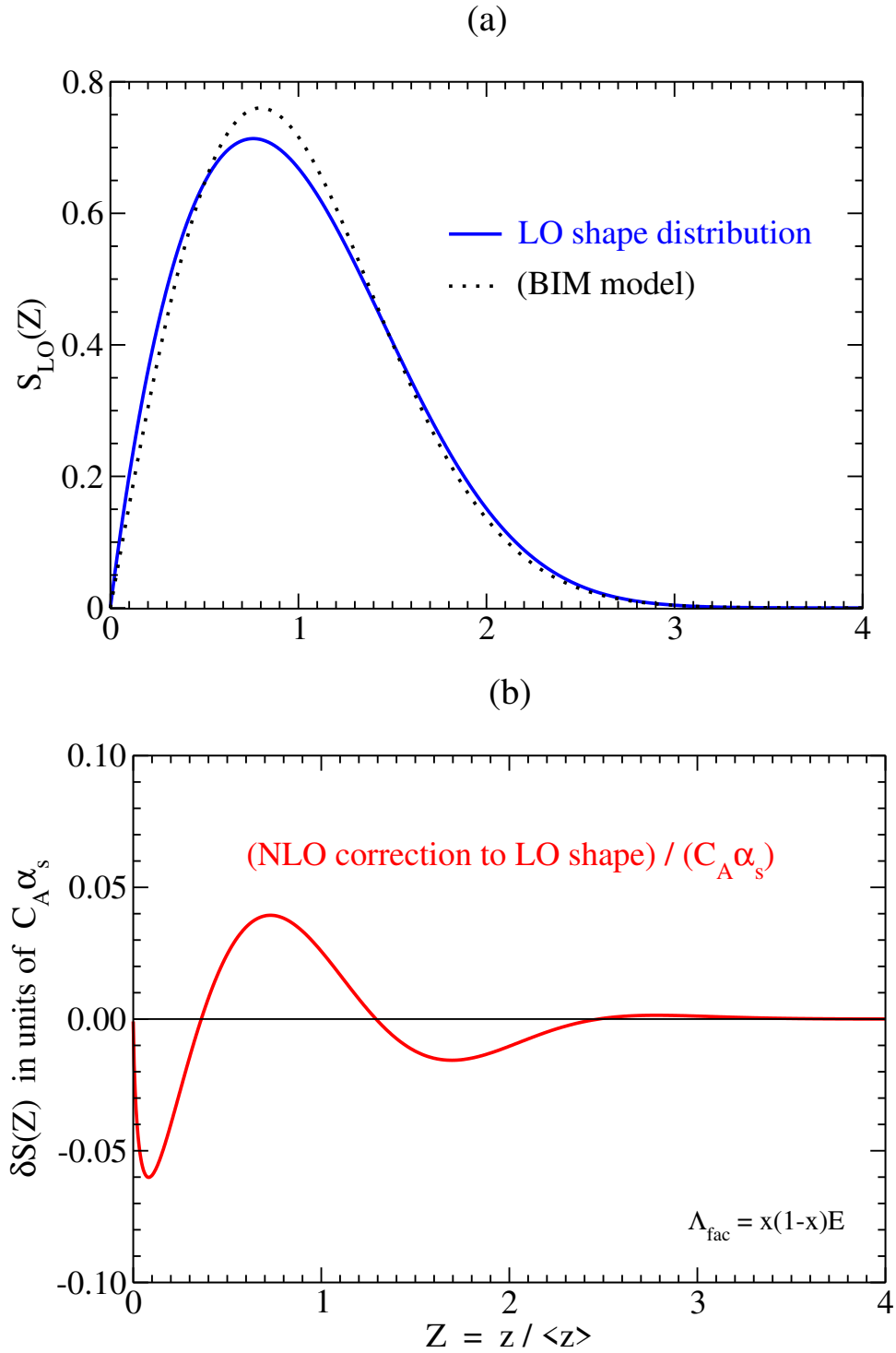
Figure 2.9: (a) The solid curve shows $S_{\mathrm{LO}}(Z)$ vs. $Z \equiv z/\langle z\rangle_{\mathrm{LO}}$. [For comparison, the dotted curve shows the analytic result (A.70) from the BIM model.] (b) A plot of $\delta S(Z)/C_{\mathrm{A}}\alpha_{\mathrm{s}}$ for our canonical choice $\Lambda_{\mathrm{fac}} = x(1-x)E$ of factorization scale. Note the different scale of the vertical axis compared to (a).
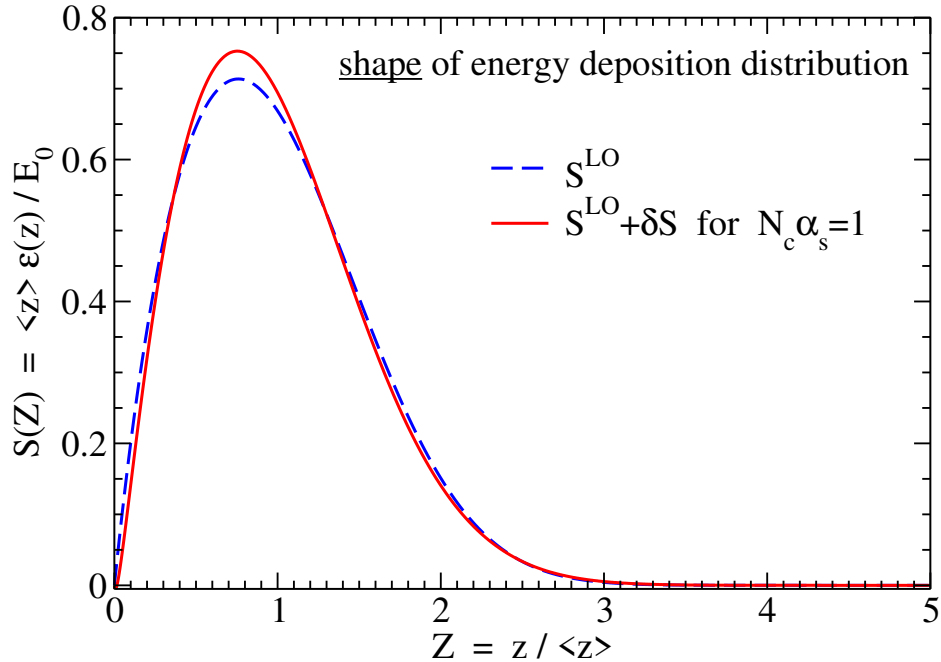
Figure 2.10: Energy deposition shape with and without first-order overlapping formation time effects $\delta S$, for $C_A \alpha_s = 1$.

The exact numbers do not matter: the upshot is that our numerical approach produced an accurate calculation for figs. 2.9 and 2.10 which supports our claim that the NLO corrections to the shape function are small for $C_A \alpha_s \leq 1$.

**The BIM model for LO results**

It's interesting to compare our numerical results for the LO energy deposition $\epsilon_{LO}(z)$ and shape function $S_{LO}(Z)$ in figs. 2.8a and 2.9a with a model of LO shower development investigated by Blaizot, Iancu, and Mehtar-Tani (BIM) [28, 40], which replaces the LO splitting rate (1.2) by something simpler that allows for analytic solutions. The BIM model of LO shower development gives the dotted curves in figs. 2.8a and 2.9a. Their result is different for the energy deposition $\epsilon_{LO}(z)$ but is close to the exact LO result for the shape function $S_{LO}(Z)$. However, the model seems to be a good

(a)



(b)
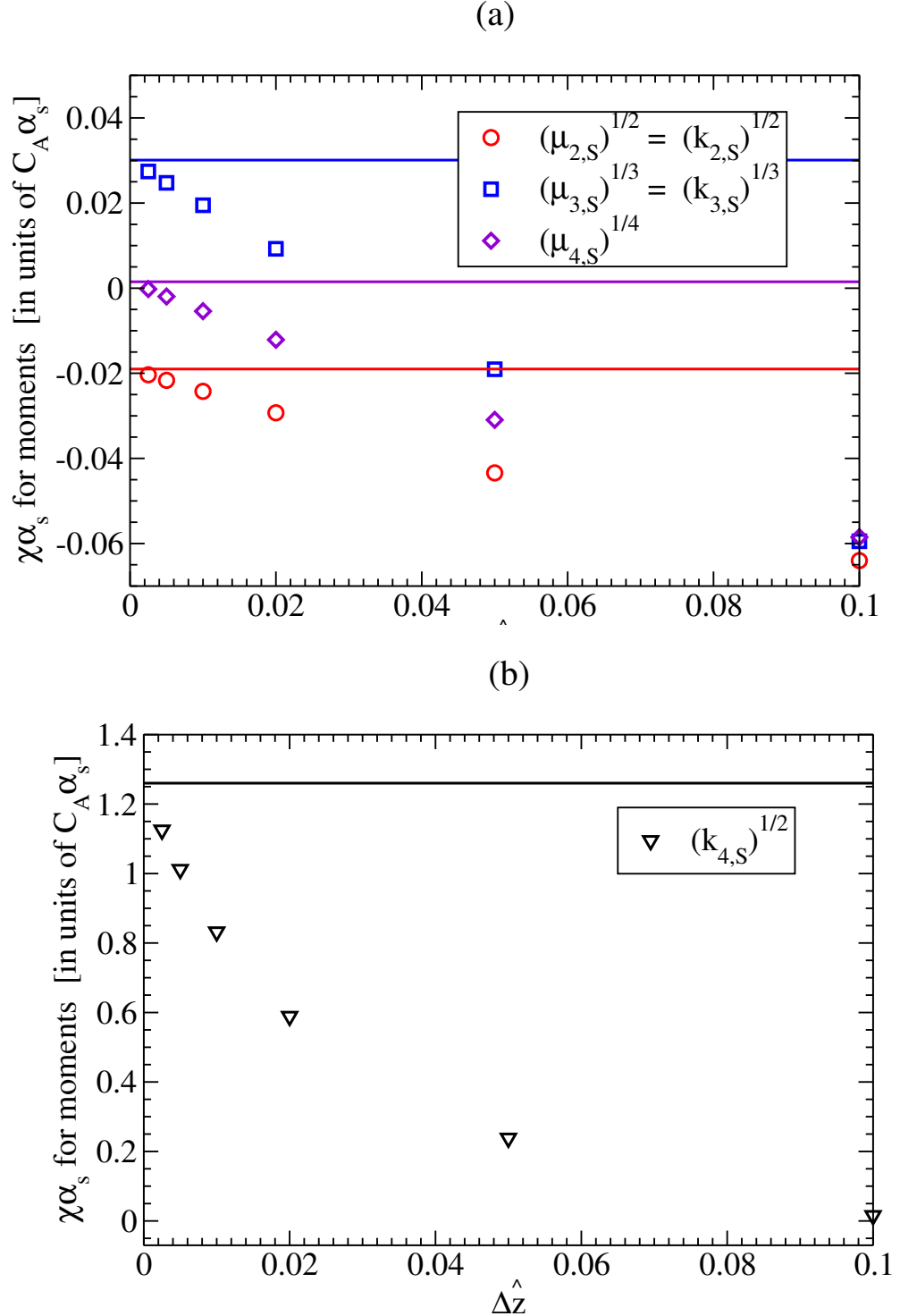


Figure 2.11: The horizontal lines show the $\chi\alpha_{\rm s}$ results of table 2.3 for the relative size of NLO corrections to reduced moments and cumulants, as computed using the direct integration method of section 2.4 for $\Lambda_{\rm fac} = x(1-x)E$, i.e. $\kappa = 1$. The data points show, as a function of step size $\Delta\hat{z}$ for $\hat{z}_{\rm max} = 20$, the same moments computed instead from the $S_{\rm LO}(Z)$ and $\delta S(Z)$ functions found by the numerical methods of the current section.

approximation to the shape $S(Z)$ of energy deposition (for the purely gluonic showers studied here).[16] That is, its more significant deviation in the case of $\epsilon(z)$ could be absorbed into the value of $\hat{q}$.

## 2.6 Time evolution of gluon distribution

So far, we focused on the energy deposition distribution $\epsilon(z)$ given by (2.66). One might also be interested in the time evolution of the distribution of all shower gluon energies as a function of time. Although we will not use it here, we present the basic evolution equation as another example that all the necessary information about splitting rates is encoded in the net rate $[d\Gamma/dx]_{\text{net}}$.

Ref. [47] packaged the basic evolution equation as[17]

$$\frac{\partial}{\partial t} n(\zeta, E_0, t) = -\Gamma(\zeta E_0) \, n(\zeta, E_0, t) + \int_\zeta^1 \frac{dx}{x} \left[ \frac{d\Gamma}{dx} \left( \tfrac{\zeta E_0}{x}, x \right) \right]_{\text{net}} n\left( \tfrac{\zeta}{x}, E_0, t \right), \quad (2.114)$$

where $n(\zeta, E_0, t) \, d\zeta$ represents the number of gluons with energy between $\zeta E_0$ and $(\zeta + d\zeta)E_0$ at time $t$. In terms of $[d\Gamma/dx]_{\text{net}}$, we can write (2.114) as :

$$\frac{\partial}{\partial t} n(\zeta, E_0, t) = \int_0^1 dx \left\{ \frac{\theta(x > \zeta)}{x} \left[ \frac{d\Gamma}{dx} \left( \tfrac{\zeta E_0}{x}, x \right) \right]_{\text{net}} n\left( \tfrac{\zeta}{x}, E_0, t \right) \right.$$
$$\left. - x \left[ \frac{d\Gamma}{dx} (\zeta E_0, x) \right]_{\text{net}} n(\zeta, E_0, t) \right\}. \quad (2.115)$$

---

[16]If one compares the BIM model curve in fig. 2.9a to the total LO+NLO curve in fig. 2.10, then the BIM curve looks like it matches the total curve even better than it matches the LO curve. But this is accidental and represents a somewhat faulty comparison: The BIM curve in fig. 2.9a is independent of the value of $C_A \alpha_s$, but the difference between the LO and LO+NLO curves in fig. 2.10 is proportional to $C_A \alpha_s$, which was somewhat arbitrarily chosen to be $C_A \alpha_s(\mu) = 1$ for the purpose of fig. 2.10.

[17]See section 3.1.1 of ref. [47], where our $n(\zeta, E_0, t)$ here is called $N(\zeta, E_0, t)$ there. For a sanity check of why $[d\Gamma/dz]_{\text{net}}$ is appropriate in (2.114), see footnote 27 of ref. [47].

It is easier to discuss the shower (following [28]) in terms of gluon energy density in $\zeta$,

$$D(\zeta, E_0, t) \equiv \zeta E_0 \, n(\zeta, E_0, t), \tag{2.116}$$

instead of $n(\zeta, E_0, t)$. The corresponding version of (2.115) is

$$\frac{\partial}{\partial t} D(\zeta, E_0, t) = \int_0^1 dx \left\{ \theta(x > \zeta) \left[ \frac{d\Gamma}{dx} \left( \frac{\zeta E_0}{x}, x \right) \right]_{\mathrm{net}} D\left( \frac{\zeta}{x}, E_0, t \right) \right.$$
$$\left. - x \left[ \frac{d\Gamma}{dx} (\zeta E_0, x) \right]_{\mathrm{net}} D(\zeta, E_0, t) \right\}. \tag{2.117}$$

As time goes on, $D(\zeta, E_0, t)$ develops a $\delta$-function piece representing the amount of energy that has been deposited in the medium:

$$D(\zeta, E_0, t) = E_{\mathrm{stopped}}(E_0, t) \, \delta(\zeta) + D_{\mathrm{moving}}(\zeta, E_0, t). \tag{2.118}$$

We will verify in appendix A.6 that the evolution equation (2.117) conserves total energy.

In applications where the relevant rates scale with energy exactly as $E^{-1/2}$, one may rescale variables as

$$t = E_0^{1/2} \tilde{t}, \qquad n(\zeta, E_0, t) = \tilde{n}(\zeta, \tilde{t}), \qquad D(\zeta, E_0, t) = E_0 \tilde{D}(\zeta, \tilde{t}) \tag{2.119a}$$

$$\left[ \frac{d\Gamma}{dx}(E, x) \right]_{\mathrm{net}} = E^{-1/2} \left[ \frac{d\tilde{\Gamma}}{dx}(x) \right]_{\mathrm{net}}, \tag{2.119b}$$

to simplify (2.115) to

$$\frac{\partial}{\partial \tilde{t}} \tilde{n}(\zeta, \tilde{t}) = \frac{1}{\zeta^{1/2}} \int_0^1 dx \left[ \frac{d\tilde{\Gamma}}{dx} \right]_{\mathrm{net}} \left\{ \frac{\theta(x > \zeta)}{x^{1/2}} \, \tilde{n}\left( \frac{\zeta}{x}, \tilde{t} \right) - x \, \tilde{n}(\zeta, \tilde{t}) \right\} \tag{2.120}$$

or equivalently

$$\frac{\partial}{\partial \tilde{t}}\, \tilde{D}(\zeta, \tilde{t}) = \frac{1}{\zeta^{1/2}} \int_0^1 dx \left[\frac{d\tilde{\Gamma}}{dx}\right]_{\text{net}} \left\{\theta(x > \zeta)\, x^{1/2}\, \tilde{D}\!\left(\tfrac{\zeta}{x}, \tilde{t}\right) - x\, \tilde{D}(\zeta, \tilde{t})\right\}. \quad (2.121)$$

At leading order, where there are only 1→2 splitting processes, (2.121) reduces to the evolution equation used by refs. [28, 40] to study leading-order shower development in the BIM model.[18] Our equation extends that equation to the case where we have more than just 1→2 splitting processes by using $[d\Gamma/dx]_{\text{net}}$.

One needs to keep in his mind that $E^{-1/2}$ energy scaling is subtle at NLO, even when one chooses a factorization scale $\Lambda_{\text{fac}} \propto E$ such that $[d\Gamma/dx]_{\text{net}}^{\text{NLO,fac}}$ scales as $E^{-1/2}$. This is because we shuffled the problem to the $[d\Gamma/dx]_{\text{eff}}^{\text{LO}}$ which now has $E^{-1/2} \ln^2 E$ instead of $E^{-1/2}$ dependence on energy. But we avoided then having to deal with $[d\Gamma/dx]_{\text{eff}}^{\text{LO}}$ by calculating the size of NLO/LO ratios, as discussed in section 2.2.

We expect eq. (2.121) to be more numerically difficult to reproduce the small NLO effects that we found in table 2.3.

## 2.7 Why are NLO effects so small?

We will try to answer the question: Why are our results for overlap effects on the shape of energy deposition very small? The simplest characteristic of the shape function, for example, is its width $\sigma_S = \sigma/\ell_{\text{stop}}$, for which the relative size of NLO corrections

---

[18] See eq. (4) of ref. [28], where their $(x, z)$ are our $(\zeta, x)$. Their $\mathcal{K}(x)$ (before they make the BIM model approximation of replacing $\mathcal{K}$ by $\mathcal{K}_0$) is our $[d\Gamma/dx]^{\text{LO}}$, up to a trivial overall normalization difference associated with their definition of rescaled time $\tau$ vs. our $\tilde{t}$.

listed in table 2.3 was

$$[\chi\alpha_{\mathrm{s}}]^{\mathrm{energy}}_{\sigma/\ell_{\mathrm{stop}}} = (-0.0190 + 0.0014\ln\kappa)C_{\mathrm{A}}\alpha_{\mathrm{s}} \tag{2.122}$$

It seems that the overlap effects which cannot be absorbed into $\hat{q}$ are almost negligible even for $C_{\mathrm{A}}\alpha_{\mathrm{s}}(\mu) = 1$ in large-$N_{\mathrm{c}}$ Yang-Mills theory. As we noted in [50, 56], this conclusion is different from an earlier analysis [44] of overlap effects in large-$N_{\mathrm{f}}$ QED for overlap effects on *charge* (rather than energy) deposition of a shower initiated by an electron. The authors found that

$$[\chi\alpha_{\mathrm{EM}}]^{\mathrm{charge}}_{\sigma/\ell_{\mathrm{stop}}} = -0.87\, N_{\mathrm{f}}\alpha_{\mathrm{EM}}, \tag{2.123}$$

which would be an $O(100\%)$ effect for $N_{\mathrm{f}}\alpha_{\mathrm{EM}}(\mu) = 1$.

One could wonder if there might be some reason why (2.122) should be exactly zero for a purely gluonic shower. Maybe there wasn't enough precision in the numerics or maybe a mistake in the rate formulas of refs. [34, 37, 39, 47]? However, $\kappa$ parameterizes our choice of the factorization scale $\Lambda = \kappa x(1-x)$, and the $\kappa$ dependence of (2.122) comes from the double and single IR logs subtracted by (2.16) and (2.17). These double logs have been known [35, 32, 33] and are well studied. The full single logarithms have been derived by two completely different methods [51, 48] which give the same result. The steps that lead from there to the $\kappa$ dependence (2.27) of the net rate, and then to the $\ln\kappa$ term in (2.122), are pretty straightforward.[19] Since one value of $\kappa$ is a good as another, it is hard to see how (2.122) could be a mistaken

---

[19]It's worth noting that the $x$-independent terms of the $\kappa$ dependence shown in (2.27) can be absorbed into a constant shift in $\hat{q}$ and so do not affect the shape distribution and so give no NLO corrections $\chi\alpha_{\mathrm{s}}$ to moments of the shape distribution. The only term in (2.27) that does affect $\chi\alpha_{\mathrm{s}}$ is the $\hat{s}(x)\ln\kappa$ term associated with IR single logs.

value for something that is actually exactly zero for all choices of $\kappa$.

Though we don't have an explanation of why (2.122) is as very small as it is, it is possible to investigate some aspects of the calculation in more detail. First, we will separate how the result (2.122) depends on $[d\Gamma/dx]_{\text{net}}^{\text{NLO,fac}}$ from how it depends on everything else. Eq. (2.96) for (2.122) can be rewritten as

$$[\chi\alpha_{\text{s}}]_{\sigma/\ell_{\text{stop}}}^{\text{energy}} = \int_0^1 dx\, W(x) \left[\frac{d\Gamma}{dx}\right]_{\text{net}}^{\text{NLO,fac}} \tag{2.124a}$$

with weight function $W$ defined by[20]

$$W(x') = \frac{x'(1 - \sqrt{x'})^2}{2\,\text{Avg}[x(1 - \sqrt{x})^2]_{\text{LO}}} - \frac{x'(1 - x')}{2\,\text{Avg}[x(1 - x)]_{\text{LO}}}. \tag{2.124b}$$

Now we write this in terms of the NLO/LO rate ratio $f(x)$ defined by (2.21):

$$[\chi\alpha_{\text{s}}]_{\sigma/\ell_{\text{stop}}}^{\text{energy}} = C_{\text{A}}\alpha_{\text{s}} \int_0^1 dx\, w(x)\, f(x), \tag{2.125a}$$

$$w(x') = \left[\frac{d\Gamma}{dx}(x')\right]^{\text{LO}} \left\{ \frac{x'(1 - \sqrt{x'})^2}{2\,\text{Avg}[x(1 - \sqrt{x})^2]_{\text{LO}}} - \frac{x'(1 - x')}{2\,\text{Avg}[x(1 - x)]_{\text{LO}}} \right\}. \tag{2.125b}$$

Note that the definition (2.84a) of $\text{Avg}[\cdots]_{\text{LO}}$ means that

$$\int_0^1 dx'\, w(x') = 0. \tag{2.126}$$

This is because if $f(x)$ had been an $x$-independent constant and $[d\Gamma/dx]_{\text{net}}^{\text{NLO,fac}} \propto [d\Gamma/dx]^{\text{LO}}$, then the NLO effects could be completely absorbed into a constant shift to $\hat{q}$. By definition, the shape function and its characteristics such as $\sigma_S$ are insensitive to

---

[20]Note that, in (2.124b), the variables $x$ appearing in the $\text{Avg}[\cdots]_{\text{LO}}$'s are dummy variables associated with the definition (2.84a), unrelated to the integration variable $x$ in (2.124a).

constant shifts in $\hat{q}$, and so the integral (2.125a) must vanish for constant $f$. Fig. 2.12a shows a plot of $w(x)$ and $f(x)$, where we can see that the function is positive on the right and negative on the left. It's not antisymmetric in $x \to 1{-}x$, but qualitatively it looks like a crude distortion of something "antisymmetric." In contrast, $f(x)$ has the same sign on both sides of the plot, and it is not symmetric but looks like a crude distortion of something symmetric. This is understandable, because the NLO contribution $g{\to}ggg$ doesn't respect the $x \to 1{-}x$ as the NLO $g{\to}gg$ contribution to $f(x)$ does.[21] These properties of $f(x)$ and $w(x)$ means that there will be some partial cancellation when we compute the integral (2.125a) of their product $w(x)\,f(x)$.

Since the integral (2.125a) for $\chi\alpha_{\mathrm{s}}$ will be unchanged if we replace $f(x)$ by $f(x){+}c$, for any constant $c$, we will replace fig. 2.12a by fig. 2.12b, where we've chosen $c$ to make $f(x){+}c$ small for the middle range of $x$ values, but still maintaining that $f(x){+}c$, like $f(x)$, has the same sign everywhere. Now we plot the product $w(x)\,[f(x) + c]$ as the solid curve in fig. 2.13 where the value of $\chi\alpha_{\mathrm{s}}$ is the area under that curve. We can see a positive contribution from the far right of the plot, partly canceled by a negative contribution from the far left, though it's hard to judge visually how precisely they cancel.

Now we look at the analysis for the charge stopping calculation for an electron-initiated shower in large-$N_f$ QED. In the large $N_{\mathrm{f}}$ limit, it is possible to distinguish the original electron throughout the evolution of the shower, and the overall charge deposition of the evolution of the shower is simply given by where the original electron stops and deposits its charge.[22] The relevant splitting rate for computing charge

---

[21]It wouldn't make sense to plot the NLO $g{\to}gg$ and $g{\to}ggg$ contributions separately because they have canceling *power*-law IR divergences [47], which are not handled by our factorization scheme (2.17). One might in principle imagine enhancing our factorization scheme to subtract power-law divergences for the separate contributions, but it doesn't seem worth the effort (and we do not currently have complete analytic results for all of the power-law divergences [47]).

[22]See the discussion in section 2.2 of ref. [44].

74
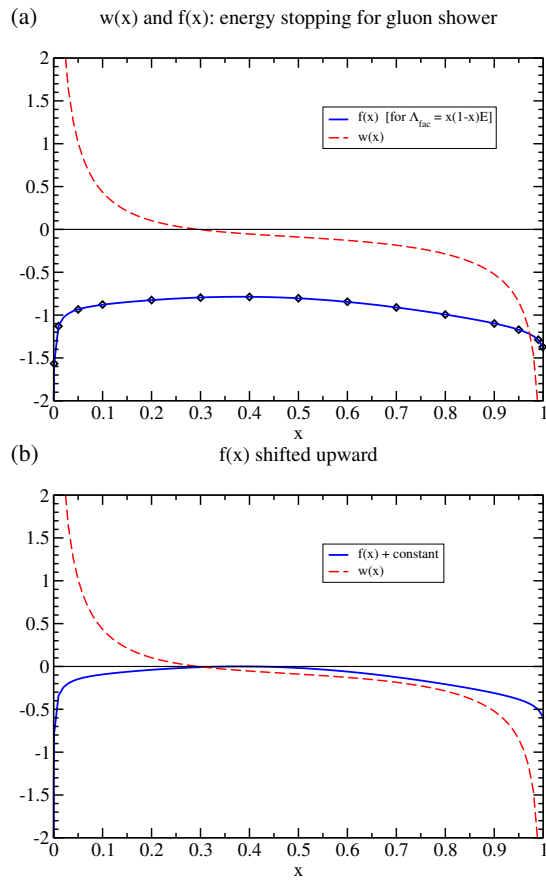


Figure 2.12: (a) Plot of the NLO/LO net rate ratio $f(x)$ (solid curve) and the weight function $w(x)$ in the integral (2.125a) that gives (2.122). (b) The same, but $f(x)$ is shifted upward by a constant, as described in the text.

deposition is then the electron splitting rate $[d\Gamma/dx]_e$, where $x$ represents the energy fraction of the original electron after the splitting compared to before the splitting. In ref. [44], the formula analogous to (2.124) was (with some minor changes[23])

$$[\chi\alpha_{\mathrm{EM}}]^{\mathrm{charge}}_{\sigma_S} = \frac{\delta\mathrm{Avg}[(1-\sqrt{x})^2]}{2\,\mathrm{Avg}[(1-\sqrt{x})^2]_{\mathrm{LO}}} - \frac{\delta\mathrm{Avg}[(1-x)]}{2\,\mathrm{Avg}[(1-x)]_{\mathrm{LO}}}, \qquad (2.127)$$

where the $\delta\mathrm{Avg}$ is computed using $[d\Gamma/dx]^{\mathrm{NLO}}_e$ instead of $[d\Gamma/dx]^{\mathrm{NLO,fac}}_{\mathrm{net}}$. There wasn't a factorization scale used here because the rate doesn't suffer from any IR divergences. Eq. (2.127) can now be rewritten as

$$[\chi\alpha]^{\mathrm{charge}}_{\sigma/\ell_{\mathrm{stop}}} = \int_0^1 dx\, W_e(x) \left[\frac{d\Gamma}{dx}\right]^{\mathrm{NLO}}_{e\to e} \qquad (2.128\mathrm{a})$$

with weight function

$$W_e(x') = \frac{(1-\sqrt{x'})^2}{2\,\mathrm{Avg}[(1-\sqrt{x})^2]_{\mathrm{LO}}} - \frac{(1-x')}{2\,\mathrm{Avg}[1-x]_{\mathrm{LO}}}. \qquad (2.128\mathrm{b})$$

To compare it to (2.125),

$$[\chi\alpha_{\mathrm{EM}}]^{\mathrm{charge}}_{\sigma/\ell_{\mathrm{stop}}} = N_{\mathrm{f}}\alpha_{\mathrm{EM}} \int_0^1 dx\, w_e(x)\, f_e(x), \qquad (2.129\mathrm{a})$$

$$w_e(x') = \left[\frac{d\Gamma}{dx}(x')\right]^{\mathrm{LO}}_{e\to e} \left\{ \frac{(1-\sqrt{x'})^2}{2\,\mathrm{Avg}[(1-\sqrt{x})^2]_{\mathrm{LO}}} - \frac{(1-x')}{2\,\mathrm{Avg}[(1-x)]_{\mathrm{LO}}} \right\}, \qquad (2.129\mathrm{b})$$

---

[23]Specifically, see eq. (2.17) of ref. [44]. The analysis of that paper later used a more complicated version, eq. (2.26) of ref. [44], which accounted for a piece of the rate that scaled with energy as $\beta_0 E^{-1/2}\ln E$, arising from a *fixed* choice of renormalization scale $\mu$. One will get the simpler equation we have used by instead choosing $\mu \propto (\hat{q}rE)^{1/4}$ with constant $r$, similar to our (2.20). The difference with the fixed-$\mu$ result turns out to be small and does not significantly affect (2.123). [The change is less than 3% and does not depend on the choice of $r$.] We have not shown other reasonable choices, such as $\mu = (\hat{q}\kappa xE)^{1/4}$ analogous to our (2.19).

$$f_e(x) \equiv \frac{\left[\frac{d\Gamma}{dx}\right]_{e \to e}^{\text{NLO}}}{N_{\text{f}} \alpha_{\text{EM}} \left[\frac{d\Gamma}{dx}\right]_{e \to e}^{\text{LO}}} \,. \tag{2.129c}$$

Fig. 2.14 shows plots of $w_e(x)$ and $f_e(x)$ analogous to the plots of $w(x)$ and $f(x)$ in fig. 2.12.

Unlike the previous energy deposition calculation, there is no distorted symmetry or anti-symmetry here. It is important also to note that even LO or NLO splitting rates for $e \to e\gamma$ will not be symmetric in $x \to 1-x$ because the two daughters are not identical particles. Looking at fig. 2.14, we see that it is almost as close as possible to zero while having the same sign of $f_e(x)$ for all $x$. The product of $w_e(x)$ and $f_e(x)$ is shown by the dotted curve in fig. 2.13. The qualitative difference with the gluonic case is that the area under the dotted curve doesn't have any significant cancellation between positive and negative contributions. In addition to that, the area associated with the right-hand side of the dotted curve is much bigger than that associated with the right-hand side of the solid curve. We find numerically that (up to logarithms) both curves blow up as $(1-x)^{-1/2}$ as $x \to 1$, which is an integrable divergence.

One might wonder how much of the big difference between the result of (2.122) and (2.123) are due to having fermions in large-$N_{\text{f}}$ QED (e.g. $e \to e\gamma$ and $\gamma \to e\bar{e}$ processes), and so how different our QCD results might be if we included quarks in addition to gluons (e.g. $q \to qg$ and $g \to q\bar{q}$). To include quark processes, one would need to treat $N_f$ as large as $N_c$, since $N_{\text{c}} = 3$ and $N_{\text{f}} = 3$ or more [depending on the size of $\mu \sim (\hat{q}E)^{1/4}$] in QCD. A more natural large-$N_{\text{c}}$ limit would be to include quarks and treat $N_{\text{f}}$ as also potentially large. Right now we are treating $N_f$ as fixed, and so the quark processes are suppressed in the large-$N_{\text{c}}$ limit.

Another possibility of the difference between the size of the two results is that electron-initiated showers in large-$N_{\text{f}}$ QED might have big a difference between the size of

overlap corrections for (i) the shape of the energy deposition distribution and (ii) the shape of the charge deposition distribution. The same may apply for quark-initiated showers in QCD, and so we will leave this for future work.

## 2.8 Concluding Remarks

The conclusion is that the effects of overlapping gluon splittings are numerically very small and don't noticeably affect the shape of the energy deposition of a purely-gluonic in-medium shower using the approximations we made. In other words, the effects of overlapping formation times on the energy deposition distribution $\epsilon(z)$ itself will be small if one allows $\hat{q}$ to be an energy-dependent phenomenological jet quenching parameter for this purpose. The energy dependence of $\hat{q}_{\mathrm{eff}}(\omega)$ was investigated at leading-log order by the early work of refs. [35, 32, 33], and expanded on in refs. [31, 53, 54]. It would be interesting if one extended their analysis to next-to-leading-log order, for which our limited NLLO analysis of section 2.2 would be inadequate.

As we discussed in section 2.7, in the future we will investigate whether overlap corrections become more important when quarks are incorporated into our gluonic showers.
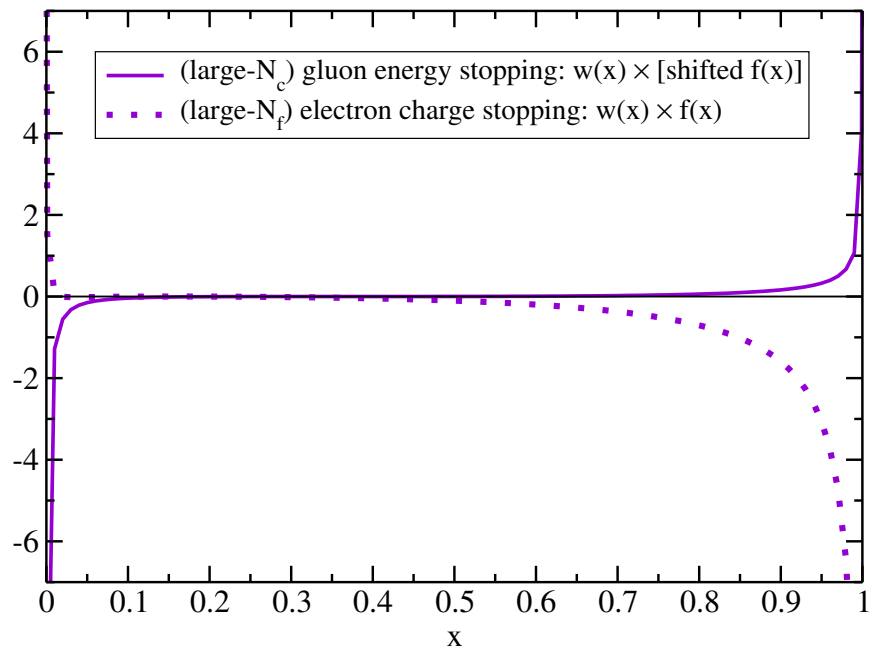
Figure 2.13: The solid curve is the product of the $w(x)$ and shifted $f(x)$ functions of fig. 2.12, and its integral gives (2.122).
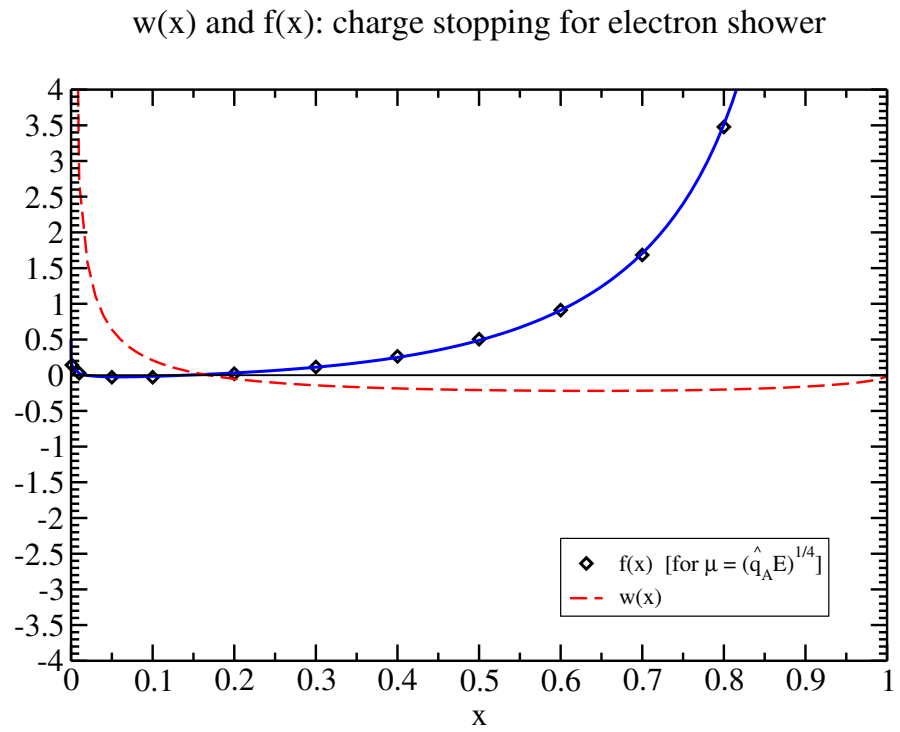
Figure 2.14: Like fig. 2.12a, but here for charge stopping of electron showers in large-$N_{\mathrm{f}}$ QED.

# Chapter 3

# The LPM Effect in sequential bremsstrahlung: $1/N_{\rm c}^2$ corrections

As mentioned earlier in section 1.2, the calculation for the correction to the LPM effect has resorted to the large-$N_{\rm c}$ limit or the case where at least one of the two overlapping splittings is relatively soft. The formalism for treating the $N_{\rm c}=3$ case is known [42] but may be challenging to evaluate numerically. So, we would like to know whether or not the $N_{\rm c}=\infty$ overlapping formation-time calculations in the literature are a reasonable or poor approximation to the physical case of $N_{\rm c}=3$. We investigate this question by calculating the $1/N_{\rm c}^2$ corrections to earlier $N_{\rm c}=\infty$ results [34, 37] for the effect of overlapping formation times on real double splitting $g \to gg \to ggg$. At the end we will extrapolate these corrections to $N_{\rm c}=3$ and see whether they are large, small, or comparable to the purely parametric estimate $O(1/N_{\rm c}^2) \sim 10\%$.

Other than going beyond the $N_{\rm c}=\infty$ approximation, we will make the same sort of simplifying assumptions and approximations as in the earlier work of refs. [34, 37, 39, 41, 44, 47] as mentioned in subsection 1.3.1.

Before proceeding, we should clarify why the first corrections to $N_{\rm c}=\infty$ are $O(1/N_{\rm c}^2)$ instead of $O(1/N_{\rm c})$. If we want to calculate the inclusive double splitting rate, then the $g{\to}gq\bar{q}$ (pair production overlapping bremsstrahlung) rate would be an $O(1/N_{\rm c})$ correction to the purely gluonic $g{\to}ggg$ rate because of the relative number of quark

colors vs. gluon colors. However, though a calculation of $g{\to}gq\bar{q}$ has not yet appeared in the literature without soft approximations, it may be computed using the same $N_c{=}\infty$ techniques that were used to compute $g{\to}ggg$ in refs. [34, 37]. So computing $g{\to}gq\bar{q}$ to leading order in the large-$N_c$ limit would give no information on the size of corrections to $N_c{=}\infty$ methods. Instead, we will focus in this chapter exclusively on purely gluonic (overlapping) $g{\to}ggg$. In the $\hat{q}$ approximation, the corrections to $N_c{=}\infty$ for the purely gluonic process will be $O(1/N_c^2)$.[1]

We should also mention that we will study $1/N_c^2$ corrections to only the subset of $g{\to}ggg$ processes that were studied for $N_c{=}\infty$ in refs. [34, 37]. This means that we are leaving out direct $g{\to}ggg$ through a 4-gluon vertex, as opposed to a sequence of two 3-gluon vertices with overlapping formation times. Such direct 4-gluon processes have been studied in ref. [38] and found to be numerically small for $N_c{=}\infty$. Our calculation also leaves out effective 4-gluon vertices that appear in Light Cone Perturbation Theory from integrating out longitudinally polarized gluons in light-cone gauge which turns out to be numerically small for $N_c{=}\infty$ as we showed in subsection 2.1.4.

## 3.1 Color Dynamics

### 3.1.1 The BDMPS-Z single splitting rate

As a warm-up example, we will discuss first the color dynamics of the BDMPS-Z single splitting rate. Adapting Zakharov's description of splitting rates [**Zakharov2**,

---

[1]In the $\hat{q}$ approximation, the details of the quark vs. gluonic content of the medium are swept up into the value of $\hat{q}$. When making $1/N_c$ expansions in this thesis, we treat $\hat{q}$ as fixed: we do not expand $\hat{q}$ in powers of $1/N_c$. Our calculation of overlap effects for $g{\to}ggg$ in the $\hat{q}$ approximation therefore effectively involves only gluons. In standard discussions of large $N_c$ for diagrams that involve only gluons, the expansion is an expansion in powers of $1/N_c^2$ [4].
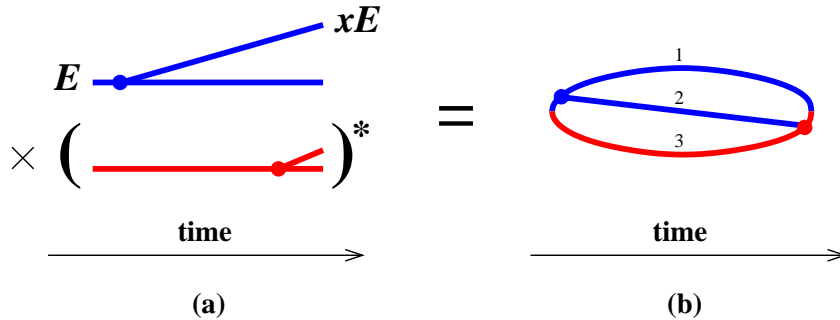
Figure 3.1: (a) A time-ordered contribution to the rate for single splitting, such as $g \to gg$, with amplitude in blue and conjugate amplitude in red. (b) A single diagram representing this contribution to the rate. In both cases, all lines implicitly interact with the medium. We need not follow particles after the emission has occurred in both the amplitude and conjugate amplitude because we will consider only $p_\perp$-integrated rates. (See, for example, section 4.1 of ref. [34] for a more explicit argument, although applied there to a more complicated diagram.) Nor need we follow them before the first emission because we approximate the initial particle as on-shell. Only one of the two time orderings that contribute to the rate is shown above.

8, 11], fig. 3.1b gives an example for single-splitting (e.g. $g \to gg$) in the medium.

The high-energy particle lines are implicitly interacting and scattering with the gluon fields of the medium as depicted in fig. 3.2a, and the rate is implicitly averaged over the randomness of the medium. These interactions with the medium change the color of each high-energy particle over time. Calculating the rate would seem to involve a complicated analysis of the time dependence of the color of each such particle. Fortunately, this is unnecessary for fig. 3.2a.[2] Consider for a moment the extreme case where the medium itself is weakly-coupled. Then (to leading order in the coupling of the medium) the medium-averaged correlations of interactions with the medium are 2-point correlations, as shown in fig. 3.2b. Let's focus on one of these correlations, such as the green line connecting particles 1 and 3 in fig. 3.2c. Consider

---

[2]Here and throughout, we will only be considering rates which are fully integrated over the transverse momenta of the daughter gluons. Otherwise, the color dynamics is more complicated even for $g \to gg$. See, for example, refs. [19, 45].

now the color generators and let $\mathbb{T}_n^a$ represent color generators $\mathbb{T}^a$ (in the appropriate representation) that act on the color state of particle $n$. The interaction of particle 1 with the gluonic field of the medium comes with a factor of $g\mathbb{T}_1^a$. The correlation of a pair of interactions between particles 1 and 3 with medium then comes with a factor of $(g\mathbb{T}_1^a)(g\mathbb{T}_3^a) = g^2\mathbb{T}_1 \cdot \mathbb{T}_3$. But this operator is trivial because by color conservation (after medium averaging),[3] the three high-energy particles in fig. 3.1b must form a color singlet, which means $\mathbb{T}_1+\mathbb{T}_2+\mathbb{T}_3 = 0$, and so $\mathbb{T}_1+\mathbb{T}_3 = -\mathbb{T}_2$. Thus, [4]

$$\mathbb{T}_1 \cdot \mathbb{T}_3 = \tfrac{1}{2}\left[(\mathbb{T}_1 + \mathbb{T}_3)^2 - \mathbb{T}_1^2 - \mathbb{T}_3^2\right] = \tfrac{1}{2}(\mathbb{T}_2^2 - \mathbb{T}_1^2 - \mathbb{T}_3^2) = \tfrac{1}{2}(C_2 - C_1 - C_3), \quad (3.1)$$

where $C_i$ is the quadratic Casimir associated with the color representation of particle

---

[3]Without medium averaging, the color neutrality of the 3-particle state would not be conserved over time. That's because the interactions in fig. 3.2a (via gluon exchange with the medium) may randomly change the color of just one of the three high-energy particles at a given moment, and exchanging one gluon with the medium turns a 3-particle color singlet into a 3-particle color octet. After medium averaging, however, the interactions with the medium must be *correlated*, such as in fig. 3.2b, and so color cannot flow out of the 3-particle system since these correlations are instantaneous on the time scales relevant to splitting processes. (In perturbative language, the medium-averaged correlator $\langle A_\mu^a A_\nu^b \rangle$ of background gluon gauge fields vanishes unless $a = b$.) The situation is analogous to translation invariance of a gas in thermal equilibrium: any particular configuration of the molecules is not translation invariant, but translation invariance is recovered after thermal averaging.

[4]This argument is a simple generalization of an argument from ordinary, non-relativistic quantum mechanics. Imagine three non-relativistic particles with spin angular momenta $S_1$, $S_2$, and $S_3$. If the three-particle system forms a spin singlet $|\chi\rangle$, then the operator $S_1+S_2+S_3$ applied to $|\chi\rangle$ gives zero. That means that $(S_1 + S_3)|\chi\rangle = -S_2|\chi\rangle$ and so (since the $S_n$ for different particles commute with each other) $(S_1 + S_3)^2|\chi\rangle = (S_2)^2|\chi\rangle$. From this, one finds $S_1 \cdot S_3|\chi\rangle = \tfrac{1}{2}[(S_2)^2 - (S_1)^2 - (S_3)^2]|\chi\rangle$. So, on the subspace of spin-singlet states, $S_1 \cdot S_3 = \tfrac{1}{2}[s_2(s_2+1) - s_1(s_1+1) - s_3(s_3+1)]$. Eq. (3.1) is just the generalization of this argument from the (covering) group SU(2) of rotations to other Lie groups such as SU(3). The $s_n(s_n + 1)$ in this footnote are just the quadratic Casimirs $C_n$ of SU(2). As in conventional in quantum mechanics, we are sloppy about explicitly writing identity operators. In terms of single-particle operators, our $S_1$ above is really $S_1 \otimes 1_2 \otimes 1_3$, our $S_2$ is really $1_1 \otimes S_2 \otimes 1_3$, etc.; our operator identity (3.1) is only true when the operator $\mathbb{T}_1 \cdot \mathbb{T}_3$ acts on the subspace of 3-particle color-singlet states; and the Casimirs on the right-hand side of (3.1) are multiplied by the identity operator for that subspace. To make all color indices explicit, consider a color-singlet state $|\chi\rangle = c_{ijk}|ijk\rangle$ (implicit sum over indices), where $(i, j, k)$ are the appropriate (e.g. fundamental or adjoint) color indices for particles (1,2,3) respectively, and $c_{ijk}$ are superposition coefficients that yield a color singlet. Then eq. (3.1) says that $(\mathbb{T}_{R_1}^a)_{ii'}(\mathbb{T}_{R_3}^a)_{kk'}c_{i'jk'} = \tfrac{1}{2}(C_2 - C_1 - C_3)c_{ijk}$, where the matrices $\mathbb{T}_{R_n}^a$ are the generators associated with the color representation $R_n$ (e.g. fundamental or adjoint) of particle $n$.
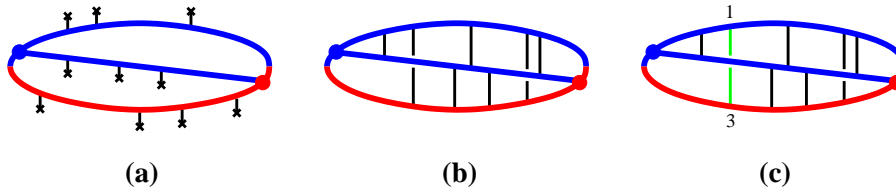
Figure 3.2: (a) $g \to gg$ but now depicting interactions with the medium. Here, each black line ending in a cross represents an interaction of a high-energy particle with the gluon field in the medium. (b) The medium average of those interactions in the case of a weakly-coupled medium. Here the black lines represent 2-point correlations of the medium interactions, which dominate for a weakly-coupled medium. (The 2-point correlations can be written in terms of correlations $\langle A_\mu^a A_\nu^b \rangle$ of the background gluon fields present in the medium.) The correlations are drawn as vertical in this time-ordered diagram because, in the high-energy limit, the correlation lengths in the medium are parametrically small compared to the length (time) scale of the high-energy splitting process. [Not shown but also present: short-time 2-point correlations between two medium interactions of the *same* high-energy particle.] (c) One correlation between particles 1 and 3 is highlighted.

*i*. This means that we can reduce $\mathbb{T}_1 \cdot \mathbb{T}_3$ to a simple fixed number in this context. Specifically, we can write $\mathbb{T}_1 \cdot \mathbb{T}_3 = -C_A/2 = -N_c/2$ in the case of $g \to gg$. Because of (3.1), we don't need to worry about the color dynamics of the three high-energy particles in order to calculate the rate for fig. 3.1.

This conclusion can be generalized to strongly-coupled media as well when one describes medium interactions using the $\hat{q}$ approximation. See ref. [43] for the argument.

## 3.1.2 SU(3) color states for overlapping, double splitting

An example of a contribution to the rate for overlapping double splitting such as $g \to ggg$ is shown in fig. 3.3. The shaded region has four high-energy particles: three in the amplitude and one in the conjugate amplitude. As we mentioned before, the particles
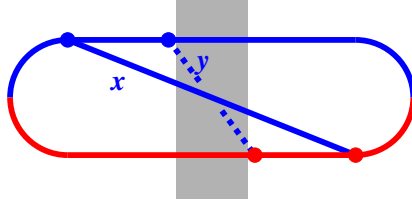
Figure 3.3: One diagrammatic contribution [34] to the rate for double splitting, such as $g \to ggg$.

have to form a color singlet. However, color conservation $\mathbb{T}_1 + \mathbb{T}_2 + \mathbb{T}_3 + \mathbb{T}_4 = 0$ is not enough to uniquely determine combinations like $\mathbb{T}_i \cdot \mathbb{T}_j$ which appear in correlations between high-energy particles' interactions with the medium. The same ambiguity appears in the context of the $\hat{q}$ approximation [43] using more general arguments.

The source of this ambiguity is that there are multiple ways to combine four gluons and form a color singlet. This is similar to how there are many ways to make a spin singlet from four spin-1 particles in quantum mechanics. In SU(3), the color representations of two gluons can be combined as

$$\mathbf{8} \otimes \mathbf{8} = \mathbf{1}_\mathrm{s} \oplus \mathbf{8}_\mathrm{a} \oplus \mathbf{8}_\mathrm{s} \oplus \mathbf{10}_\mathrm{a} \oplus \overline{\mathbf{10}}_\mathrm{a} \oplus \mathbf{27}_\mathrm{s}, \tag{3.2}$$

where the subscripts "s" and "a" indicate symmetric vs. antisymmetric color combinations of the two gluons. To make a color singlet out of four gluons, we would combine the first two gluons into any color representation $R$ from the right hand side of (3.2), then combine the other two gluons into its complex conjugate $\bar{R}$, and then combine the resulting $R$ and $\bar{R}$ into a color singlet. This process of forming color singlets is shown in fig. 3.4a, labeled "$s$-channel." The $s$-channel color states form a basis for all 4-gluon color singlet states, but one could have chosen a "$t$-channel" or
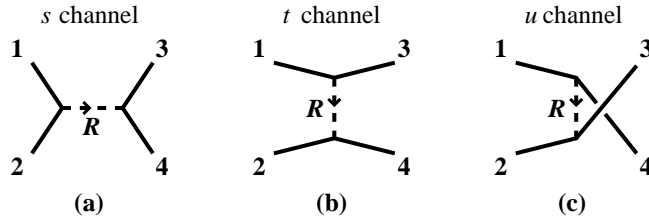
Figure 3.4: Three ways to form bases for 4-gluon color singlet states. (The terms *s*-channel, etc. are merely evocative here; we are *not* referring to 2↔2 scattering.)

"*u*-channel" basis, as indicated in the figure.[5]

We find it convenient to work in the *u*-channel basis because of particle numbering conventions used in earlier papers on overlapping formation times [34, 37]. We will call the *u*-basis singlet states $|R\rangle_u$. Our initial basis for discussing 4-gluon singlets is then

$$|\mathbf{1}\rangle_u, |\mathbf{8}_{\mathrm{aa}}\rangle_u, |\mathbf{8}_{\mathrm{as}}\rangle_u, |\mathbf{8}_{\mathrm{sa}}\rangle_u, |\mathbf{8}_{\mathrm{ss}}\rangle_u, |\mathbf{10}\rangle_u, |\overline{\mathbf{10}}\rangle_u, |\mathbf{27}\rangle_u. \tag{3.3}$$

Since $R = \mathbf{8}$ could be symmetric or antisymmetric, we have to label whether each pair of the four gluons formed the $\mathbf{8}$ by a symmetric (s) or antisymmetric (a) combination, as distinguished in (3.2). It is shown in ref. [42] [6] that only a 5-dimensional subspace of (3.3) appears in calculations of overlapping formation times (e.g. fig. 3.3):[7]

$$|\mathbf{1}\rangle_u, |\mathbf{8}_{\mathrm{aa}}\rangle_u, |\mathbf{8}_{\mathrm{ss}}\rangle_u, |\mathbf{10}{+}\overline{\mathbf{10}}\rangle_u, |\mathbf{27}\rangle_u, \tag{3.4}$$

where

$$|\mathbf{10}{+}\overline{\mathbf{10}}\rangle_u \equiv \tfrac{1}{\sqrt{2}}\big(|\mathbf{10}\rangle_u + |\overline{\mathbf{10}}\rangle_u\big). \tag{3.5}$$

---

[5]For a variety of papers related to these constructions (and discussion of the color generalization of $6j$-symbols to relate different channels), see, for example, refs. [42, 19, 45, 36, 18, 5, 17, 20].

[6]This 5-dimensional subspace was also discussed earlier in a closely related context by refs. [19, 45].

[7]The fact that the states in (3.4) are designated as *u*-channel is irrelevant. The analogous *s*-channel or *t*-channel states would span the same 5-dimensional subspace.

Before we discuss how the color singlet state of the four gluons evolves in the subspace (3.4) as gluons travel through the medium, we will discuss the generalization from SU(3) to SU($N$).

### 3.1.3   SU($N$) color dynamics for overlapping, double splitting

We will refer to the number of quark colors as $N$ rather than $N_c$ in the rest of the discussion. We will generalize the previous discussion to $N > 3$, where the tensor product (3.2) of two gluon colors becomes[8]

$$ \mathrm{A} \otimes \mathrm{A} = \mathbf{1}_\mathrm{s} \oplus \mathrm{A}_\mathrm{a} \oplus \mathrm{A}_\mathrm{s} \oplus \text{``}\mathbf{10}\text{''}_\mathrm{a} \oplus \text{``}\overline{\mathbf{10}}\text{''}_\mathrm{a} \oplus \text{``}\mathbf{27}\text{''}_\mathrm{s} \oplus \text{``}\mathbf{0}\text{''}_\mathrm{s} \,, \tag{3.6} $$

where $\mathbf{1}$ is the singlet representation, A is the adjoint representation of SU($N$), and, for example, "$\mathbf{27}$" means the SU($N$) representation that generalizes the 27-dimensional representation of SU(3). The scare quotes mean the corresponding representation for SU($N$) even though we write in terms of the size of the representation for $N$=3. Note that there is an extra representation that appears in (3.6) than in the original SU(3) product (3.2). This representation "$\mathbf{0}$" of SU($N$) smoothly decouples and disappears as one approaches $N \to 3$ from above.

For SU($N$) with $N > 3$, there is a 6-dimensional (rather than 5-dimensional) subspace of color singlet states relevant to calculations of overlapping formation times, which is spanned by the basis [42, 19]

$$ |\mathbf{1}\rangle_u, \ |\mathrm{A}_\mathrm{aa}\rangle_u, \ |\mathrm{A}_\mathrm{ss}\rangle_u, \ |\text{``}\mathbf{10}{+}\overline{\mathbf{10}}\text{''}\rangle_u, \ |\text{``}\mathbf{27}\text{''}\rangle_u, \ |\text{``}\mathbf{0}\text{''}\rangle_u. \tag{3.7} $$

---

[8]The SU($N$) Young tableaux corresponding to (3.6) and the actual dimensions of the representations may be found, for example, in eqs. (5.1) and (5.2) of ref. [42].

This is the generalization of (3.4). We are going to use some results from ref. [42] about the 4-particle color singlet states, but we are going to use slightly different overall sign conventions for the definitions of the $u$-channel states (3.7). We will show the relation between the two sign conventions in appendix B.1.1. The BDMPS-Z calculation of single splitting rates in Zakharov's version is set up as a two-dimensional quantum mechanics problem (in the transverse plane) with an imaginary-valued "potential energy" $V$. Ref. [34] extended this picture, in the large-$N$ limit, to calculations of overlap effects in double splitting, such as the contribution to the rate represented by fig. 3.3. We need the 4-gluon evolution in the shaded region of fig. 3.3 for finite $N$ which was worked out in ref. [42] for the $\hat{q}$ approximation. The resulting 2-dimensional Hamiltonian for the 4-gluon evolution in the shaded region of fig. 3.3 was found to be[9]

$$\underline{H} = \frac{P_{41}^2}{2x_4 x_1(x_4+x_1)E} + \frac{P_{23}^2}{2x_2 x_3(x_2+x_3)E} + \underline{V}(\boldsymbol{C}_{41}, \boldsymbol{C}_{23}) \qquad (3.8a)$$

with potential

$$\underline{V}(\boldsymbol{C}_{41}, \boldsymbol{C}_{23}) = -\tfrac{i}{4}\hat{q}_{\mathrm{A}}\Big\{(x_4^2 + 2x_4 x_1 \underline{S}_u + x_1^2)C_{41}^2 + (x_2^2 + 2x_2 x_3 \underline{S}_u + x_3^2)C_{23}^2$$
$$+ 2\big[\tfrac{1}{2}(x_4 - x_1)(x_2 - x_3)(\underline{S}_u - 1) - (x_4 + x_1)(x_2 + x_3)\underline{T}_u\big]\boldsymbol{C}_{41}\cdot\boldsymbol{C}_{23}\Big\}. \qquad (3.8b)$$

We used symmetries to reduce the 4-gluon quantum mechanics problem with transverse positions $(\boldsymbol{b}_1, \boldsymbol{b}_2, \boldsymbol{b}_3, \boldsymbol{b}_4)$ to an effective 2-particle quantum mechanics problem [34, 37] written in terms of $(\boldsymbol{C}_{41}, \boldsymbol{C}_{23})$ with $\boldsymbol{C}_{ij} \equiv (\boldsymbol{b}_i - \boldsymbol{b}_j)/(x_i + x_j)$. The $\boldsymbol{P}_{ij}$ are the canonical momenta conjugate to the $\boldsymbol{C}_{ij}$, $E$ is the energy of the initial particle in the double-splitting process, and $x_i$ represent the longitudinal momentum fractions of the four gluons. The underlined quantities in (3.8) represent $6 \times 6$ matrices (for

---

[9]See appendix B.1.1 for details of how the $s$-channel result of ref. [42] was translated to the $u$-channel version in (3.8).

$N > 3$) that act on the 6-dimensional space of relevant 4 gluon color singlet states. The matrices $\underline{S}_u$ and $\underline{T}_u$ have the effect of the action of $\mathbb{T}_i \cdot \mathbb{T}_j$ on this space in the $u$-channel basis (3.7) as [10]

$$\mathbb{T}_4 \cdot \mathbb{T}_1 = -C_A \underline{S}_u, \qquad \mathbb{T}_4 \cdot \mathbb{T}_2 = C_A \left[\tfrac{1}{2}(\underline{S}_u - \mathbb{1}) - \underline{T}_u\right], \qquad \mathbb{T}_4 \cdot \mathbb{T}_3 = C_A \left[\tfrac{1}{2}(\underline{S}_u - \mathbb{1}) + \underline{T}_u\right] \tag{3.9}$$

with

$$\underline{S}_u \equiv \begin{pmatrix} 1 & & & & & \\ & \frac{1}{2} & & & & \\ & & \frac{1}{2} & & & \\ & & & 0 & & \\ & & & & -\frac{1}{N} & \\ & & & & & \frac{1}{N} \end{pmatrix} \tag{3.10a}$$

and

$$\underline{T}_u \equiv \begin{pmatrix} 0 & \frac{1}{\sqrt{N^2-1}} & 0 & 0 & 0 & 0 \\ \frac{1}{\sqrt{N^2-1}} & 0 & \frac{1}{4} & 0 & \frac{1}{2N}\sqrt{\frac{N+3}{N+1}} & \frac{1}{2N}\sqrt{\frac{N-3}{N-1}} \\ 0 & \frac{1}{4} & 0 & \frac{1}{\sqrt{2(N^2-4)}} & 0 & 0 \\ 0 & 0 & \frac{1}{\sqrt{2(N^2-4)}} & 0 & \tau_+ & \tau_- \\ 0 & \frac{1}{2N}\sqrt{\frac{N+3}{N+1}} & 0 & \tau_+ & 0 & 0 \\ 0 & \frac{1}{2N}\sqrt{\frac{N-3}{N-1}} & 0 & \tau_- & 0 & 0 \end{pmatrix}, \tag{3.10b}$$

where

$$\tau_\pm \equiv \frac{1}{2N}\sqrt{\frac{(N\mp2)(N\pm1)(N\pm3)}{2(N\pm2)}}. \tag{3.11}$$

---

[10]Because $\mathbb{T}_1 + \mathbb{T}_2 + \mathbb{T}_4 + \mathbb{T}_4 = 0$ implies $(\mathbb{T}_4 + \mathbb{T}_1)^2 = (\mathbb{T}_2 + \mathbb{T}_3)^2$, and because all $\mathbb{T}_i^2 = C_A^2$ (since all four particles are gluons), we have the additional relation that $\underline{\mathbb{T}}_2 \cdot \underline{\mathbb{T}}_3 = \underline{\mathbb{T}}_4 \cdot \underline{\mathbb{T}}_1$. Similarly, $\mathbb{T}_3 \cdot \mathbb{T}_1 = \underline{\mathbb{T}}_4 \cdot \underline{\mathbb{T}}_2$ and $\mathbb{T}_1 \cdot \mathbb{T}_2 = \underline{\mathbb{T}}_4 \cdot \underline{\mathbb{T}}_3$.

We will need to solve for the 4-gluon evolution of the Hamiltonian (3.8) in perturbation theory in $1/N$ about the $N=\infty$ limit.

### 3.1.4  $N=\infty$ limit

In the $N\to\infty$ limit, (3.10) becomes

$$
\underline{S}_u \to
\begin{pmatrix}
1 & & & & & \\
& \frac{1}{2} & & & & \\
& & \frac{1}{2} & & & \\
& & & 0 & & \\
& & & & 0 & \\
& & & & & 0
\end{pmatrix}
, \qquad
\underline{T}_u \to
\begin{pmatrix}
0 & & & & & \\
& 0 & \frac{1}{4} & & & \\
& \frac{1}{4} & 0 & & & \\
& & & 0 & \frac{1}{2\sqrt{2}} & \frac{1}{2\sqrt{2}} \\
& & & \frac{1}{2\sqrt{2}} & 0 & 0 \\
& & & \frac{1}{2\sqrt{2}} & 0 & 0
\end{pmatrix}
$$

$$
\text{in basis}\quad
\begin{array}{l}
|\mathbf{1}\rangle_u \\
|\mathrm{A_{aa}}\rangle_u \\
|\mathrm{A_{ss}}\rangle_u \\
|\text{``}\mathbf{10+\overline{10}}\text{''}\rangle_u \\
|\text{``}\mathbf{27}\text{''}\rangle_u \\
|\text{``}\mathbf{0}\text{''}\rangle_u\,.
\end{array}
\qquad (3.12)
$$

In the $N = \infty$ limit, the matrices $\underline{S}_u$ and $\underline{T}_u$ commute unlike the finite $N$ case. So, we can find a simultaneous basis for both matrices:

$$|1\rangle \equiv |\mathbf{1}\rangle_u \,,$$

$$|A_+\rangle \equiv \tfrac{1}{\sqrt{2}}|A_{\mathrm{aa}}\rangle_u + \tfrac{1}{\sqrt{2}}|A_{\mathrm{ss}}\rangle_u \,,$$

$$|A_-\rangle \equiv \tfrac{1}{\sqrt{2}}|A_{\mathrm{aa}}\rangle_u - \tfrac{1}{\sqrt{2}}|A_{\mathrm{ss}}\rangle_u \,,$$

$$|A^\times\rangle \equiv \tfrac{1}{\sqrt{2}}|\text{``}\mathbf{27}\text{''}\rangle_u - \tfrac{1}{\sqrt{2}}|\text{``}\mathbf{0}\text{''}\rangle_u \,,$$

$$|1_+^\times\rangle \equiv \tfrac{1}{2}|\text{``}\mathbf{27}\text{''}\rangle_u + \tfrac{1}{2}|\text{``}\mathbf{0}\text{''}\rangle_u + \tfrac{1}{\sqrt{2}}|\text{``}\mathbf{10}{+}\overline{\mathbf{10}}\text{''}\rangle_u \,,$$

$$|1_-^\times\rangle \equiv \tfrac{1}{2}|\text{``}\mathbf{27}\text{''}\rangle_u + \tfrac{1}{2}|\text{``}\mathbf{0}\text{''}\rangle_u - \tfrac{1}{\sqrt{2}}|\text{``}\mathbf{10}{+}\overline{\mathbf{10}}\text{''}\rangle_u \,, \tag{3.13}$$

in terms of which the $N{=}\infty$ limits (3.12) become

$$\underline{S}^{N=\infty} \equiv \begin{pmatrix} 1 & & & & & \\ & \tfrac{1}{2} & & & & \\ & & \tfrac{1}{2} & & & \\ & & & 0 & & \\ & & & & 0 & \\ & & & & & 0 \end{pmatrix}, \qquad \underline{T}^{N=\infty} \equiv \begin{pmatrix} 0 & & & & & \\ & \tfrac{1}{4} & & & & \\ & & -\tfrac{1}{4} & & & \\ & & & 0 & & \\ & & & & \tfrac{1}{2} & \\ & & & & & -\tfrac{1}{2} \end{pmatrix} \quad \text{in basis} \quad \begin{matrix} |1\rangle \\ |A_+\rangle \\ |A_-\rangle \\ |A^\times\rangle \\ |1_+^\times\rangle \\ |1_-^\times\rangle \,. \end{matrix} \tag{3.14}$$

From now on, we will drop the subscript $u$ on $\underline{S}^{N=\infty}$ and $\underline{T}^{N=\infty}$.

Since $\underline{S}^{N=\infty}$ and $\underline{T}^{N=\infty}$ are both diagonal, the potential (3.8b), and so the Hamiltonian, does not mix the states (3.13) for $N=\infty$. Each of these states propagates independently for $N=\infty$ with non-matrix potentials given by using the corresponding eigenvalues from (3.14) instead of the matrices $\underline{S}_u$ and $\underline{T}_u$ in (3.8b). We will find later that we can have transitions between these color singlets when we investigate the $O(1/N)$ perturbations to $\underline{S}^{N=\infty}$ and $\underline{T}^{N=\infty}$.

The motivation for the names $|1\rangle$ and $|A_\pm\rangle$ in (3.13) should be clear enough. We can use the conversion matrices between bases given in appendix B.1.1 to see that the state $|A^\times\rangle$ defined in terms of $u$-channel color singlet states is equivalent in the limit $N \to \infty$, to the combination $\left(|A_{aa}\rangle_s + |A_{ss}\rangle_s\right)/\sqrt{2}$ of $s$-channel basis states. Similarly, the state $|1_-^\times\rangle$ is equivalent to the $s$-channel basis state $|1\rangle_s$, and $|1_+^\times\rangle$ is equivalent to the $t$-channel basis state $|1\rangle_t$. So we mean by the cross "$\times$" in the notation $A^\times$ or $1_\pm^\times$ that, for $N = \infty$, the state involves the representation $R = A$ or $R = 1$ in a cross-channel different from our usual $u$-channel representation.

We will use later the definitions (3.13) of basis states when we analyze large but finite $N$. In this case, the motivation for our notation is not correct. So, for $N < \infty$, one may interpret the cross $\times$ in the colloquial sense of "crossed out": a warning that the motivation for the notation is no longer precise for those states.

### 3.1.5 An aside: Diagrammatic interpretation of basis states for $N = \infty$

We will present here another way to characterize the basis (3.13) for $N = \infty$. This alternative way will shed light on the detailed argument in section 3.3.2, but is not strictly necessary for most of our calculation. The time-ordered diagrams are shown

in refs. [34, 37] such as fig. 3.3 and others on the surface of a cylinder, where time runs along the cylinder. One could state that the large-$N$ requirement that $N=\infty$ diagrams be "planar" [4] is to say that no lines should cross on the surface of the cylinder. For example, fig. 3.3 can be drawn on the cylinder as in fig. 3.5, where we have numbered the lines during the 4-particle part of the evolution according to the convention of ref. [34], which for this diagram corresponds to identifying the longitudinal momentum fractions of the gluons as $(x_1, x_2, x_3, x_4) = (-1, y, 1-x-y, x)$. The medium interactions that give rise to correlations between the high energy particles, such as the black lines drawn in fig. 3.2b (and also higher-point correlations), must also be part of the "planar" diagram and so must lie along the surface of the cylinder without crossing any other lines. So, for $N=\infty$, there can be only correlations between high-energy particles that are neighbors of each other as one goes around the circumference of the cylinder. During the 4-gluon phase of the time evolution in fig. 3.5, the medium interactions of particle 1 can be correlated with those of particles 2 and 4 but not with particle 3. We will refer to this sequence as (1234). Any cyclic permutation, such as (2341), would be an equivalent way to write (1234), and so would the reverse order (4321) or its cyclic permutations. The upshot is that discussing interactions between the particles in large $N$ are determined by which of the four high-energy gluons are neighbors.

The color singlet states (3.13) may be identified as (see appendix B.1.2)

$$|A_+\rangle \to (1324), \qquad |A_-\rangle \to (1234), \qquad |A^\times\rangle \to (1243),$$
$$|1\rangle \to (41)(23), \qquad |1_+^\times\rangle \to (13)(24), \qquad |1_-^\times\rangle \to (12)(34) \qquad (3.15)$$

when $N = \infty$. The notation $(ij)(kl)$ means that particles $i$ and $j$ are contracted into a color singlet and that particles $k$ and $l$ are also contracted into a color singlet.
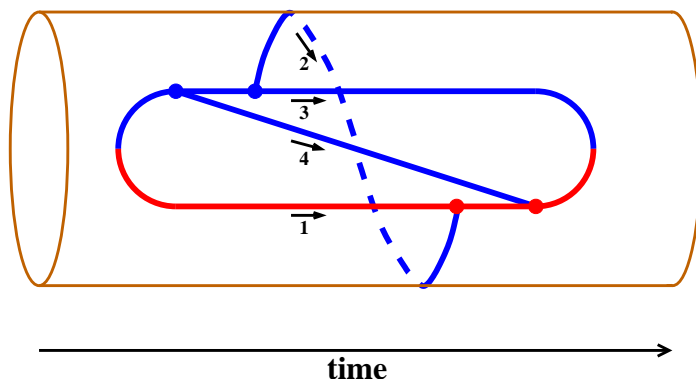
Figure 3.5: Fig. 3.3 drawn on a cylinder. Here, solid lines indicate lines drawn on the front of the cylinder, and dashed lines indicate lines wrapping around the back.

Looking at the cylinder picture of fig. 3.5, we represent states like $(ij)(kl)$ by showing two separate cylinders: one for each single pair. This convenient way corresponds naturally to the large-$N$ topological principle that diagrams requiring handles are suppressed. Specifically, fig. 3.6 shows one type of $1/N^2$ correction to fig. 3.5. As time goes on, during the 4-gluon part of the evolution, there is a $1/N$ suppressed transition from the (1234) color singlet state to the (12)(34) color singlet state, and then later another such transition to the (1243) color singlet state. In terms of our notation (3.13), that's $|A_-\rangle \to |1_-^\times\rangle \to |A^\times\rangle$, where each transition will be due to $1/N$ corrections to the Hamiltonian. Some examples of (2-point[11]) correlations of medium interactions are shown by the black lines. In terms of the large $N$ diagrammatics, the resulting diagram, interpreted here to include the medium correlations shown, cannot be drawn as a planar diagram, which is why it is $1/N^2$ suppressed. In principle, there is a suppression by $1/N^2$ for every handle needed to draw a diagram on a surface without crossing lines [4].[12]

---

[11]There is no reason to only include 2-point correlations here: They are simply easier to draw. All that matters is that no lines cross when the diagram and correlations are drawn on the surface.

[12]See also Coleman's excellent "$1/N$" summer school lecture in ref. [6].
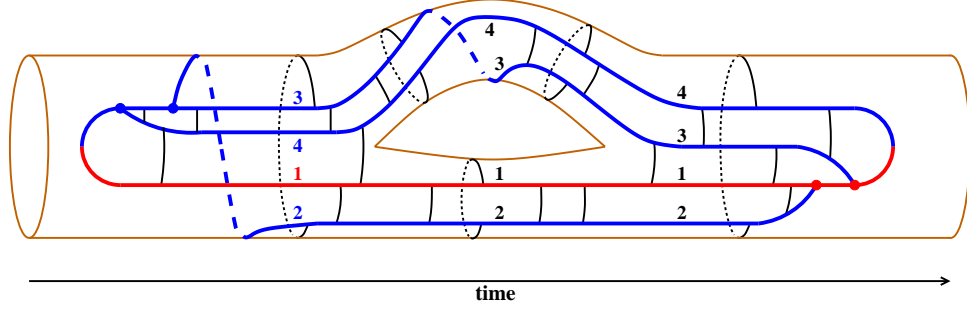
Figure 3.6: A topological depiction of the $O(1/N^2)$ transition $(1234) \rightarrow (12)(34) \rightarrow (1243)$ between $N=\infty$ color singlet states during the 4-gluon phase of evolution of fig. 3.3. The black lines indicate (2-point) examples of correlations of interactions with the medium, which for $N=\infty$ are allowed only between neighbors.

## 3.1.6 $1/N$ and $1/N^2$ corrections to the potential

We will obtain the $1/N$ corrections to the $N=\infty$ limit by expanding the original Hamiltonian (3.8) in powers of $1/N$. The dependence on $N$ appears only in the $\underline{S}_u$ and $\underline{T}_u$ matrices (3.10), which can be expanded in powers of $1/N$. Then, we will want to express the result in the basis (3.13) of states that decouple in the $N=\infty$ limit, not the original basis (3.7) used for presenting $\underline{S}_u$ and $\underline{T}_u$. Doing this change of basis,

$$\underline{S}_u = \underline{S}^{N=\infty} + \delta\underline{S}, \qquad \underline{T}_u = \underline{T}^{N=\infty} + \delta\underline{T} + \delta^2\underline{T} + O(N^{-3}) \qquad (3.16)$$

with $\underline{S}^{N=\infty}$ and $\underline{T}^{N=\infty}$ as in (3.14) and

$$\delta\underline{S} = \frac{1}{\sqrt{2}\,N}\begin{pmatrix} 0 & & & & & \\ & 0 & & & & \\ & & 0 & & & \\ & & & 0 & -1 & -1 \\ & & & -1 & 0 & 0 \\ & & & -1 & 0 & 0 \end{pmatrix}, \qquad \delta\underline{T} = \frac{1}{\sqrt{2}\,N}\begin{pmatrix} 0 & 1 & 1 & 0 & 0 & 0 \\ 1 & 0 & 0 & 0 & 1 & 0 \\ 1 & 0 & 0 & 0 & 0 & 1 \\ 0 & 0 & 0 & 0 & 0 & 0 \\ 0 & 1 & 0 & 0 & 0 & 0 \\ 0 & 0 & 1 & 0 & 0 & 0 \end{pmatrix},$$

$$\text{and} \quad \delta^2\underline{T} = \frac{1}{N^2}\begin{pmatrix} 0 & 0 & 0 & 0 & 0 & 0 \\ 0 & 0 & 0 & \frac{1}{2} & 0 & 0 \\ 0 & 0 & 0 & \frac{1}{2} & 0 & 0 \\ 0 & \frac{1}{2} & \frac{1}{2} & 0 & 0 & 0 \\ 0 & 0 & 0 & 0 & -\frac{5}{4} & 0 \\ 0 & 0 & 0 & 0 & 0 & \frac{5}{4} \end{pmatrix} \quad \text{in basis} \quad \begin{matrix} |1\rangle \\ |A_+\rangle \\ |A_-\rangle \\ |A^\times\rangle \\ |1_+^\times\rangle \\ |1_-^\times\rangle \,. \end{matrix} \qquad (3.17)$$

## 3.2  Sequential diagrams

So far we have only showed one class of diagrams, which we call crossed diagrams [34] because two lines cross when it is drawn as in fig. 3.3 (as opposed to the drawing in fig. 3.5 of the same diagram on the cylinder). It will be easier to start with a different class of diagrams called sequential diagrams [37], shown in fig. 3.7. Since there is no interesting color dynamics for 3-particle evolution as we discussed earlier, this means that there are no finite-$N$ corrections needed for those propagators if one uses the value of $\hat{q}$ appropriate for the desired value of $N$. Only the first diagram $xy\bar{x}\bar{y}$ (and its complex conjugate and permutations) will generate $1/N^2$ corrections. The same is true for the 2-particle propagators. It is only the $xy\bar{x}\bar{y}$ diagram in fig. 3.7 that

$$xy\bar{x}\bar{y} \qquad x\bar{x}y\bar{y} \qquad x\bar{x}\bar{y}y$$

+ conjugates

+ relevant permutations
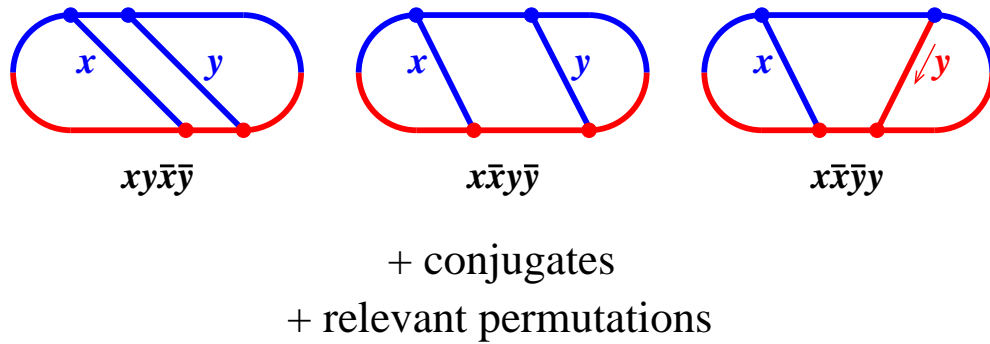
Figure 3.7: The above diagrams contributing to double splitting $g{\to}ggg$ are called the "sequential diagrams" in ref. [37]. As in refs. [34, 37], the diagrams are individually named ($xy\bar{x}\bar{y}$, etc.) by the time order of the vertices. The relevant permutations referenced above are those permutations of the daughters $x$, $y$, and $z \equiv 1{-}x{-}y$ that create distinct diagrams.

has a region of 4-particle evolution and so non-trivial color dynamics, denoted by the shaded region in fig. 3.8.

## 3.2.1  Set-up and allowed color singlet transitions

We will focus now on the $xy\bar{x}\bar{y}$ diagram. Our numbering of particles in the 4-particle evolution in fig. 3.8 follows the same convention as refs. [34, 37]. This diagram contributes to the rate for overlapping double gluon splitting $g{\to}ggg$ an amount

$$xy\bar{x}\bar{y}$$
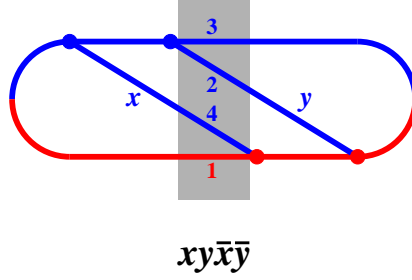
Figure 3.8: The canonical "sequential" diagram for which finite-$N$ corrections must be calculated.

proportional to[13]

$$\int_{t_{\mathrm{x}}<t_{\mathrm{y}}<t_{\bar{\mathrm{x}}}<t_{\bar{\mathrm{y}}}} \int_{\boldsymbol{B}^{\mathrm{y}},\boldsymbol{B}^{\bar{\mathrm{x}}}} \nabla^{\bar{n}}_{\boldsymbol{B}^{\bar{\mathrm{y}}}} \langle \boldsymbol{B}^{\bar{\mathrm{y}}}, t_{\bar{\mathrm{y}}} | \boldsymbol{B}^{\bar{\mathrm{x}}}, t_{\bar{\mathrm{x}}} \rangle \Big|_{\boldsymbol{B}^{\bar{\mathrm{y}}}=0}$$

$$\times \nabla^{\bar{m}}_{\boldsymbol{C}^{\bar{\mathrm{x}}}_{41}} \nabla^{n}_{\boldsymbol{C}^{\mathrm{y}}_{23}} \langle \boldsymbol{C}^{\bar{\mathrm{x}}}_{41}, \boldsymbol{C}^{\bar{\mathrm{x}}}_{23}, t_{\bar{\mathrm{x}}} | \boldsymbol{C}^{\mathrm{y}}_{41}, \boldsymbol{C}^{\mathrm{y}}_{23}, t_{\mathrm{y}} \rangle \Big|_{\boldsymbol{C}^{\bar{\mathrm{x}}}_{41}=0=\boldsymbol{C}^{\mathrm{y}}_{23};\ \boldsymbol{C}^{\bar{\mathrm{x}}}_{23}=\boldsymbol{B}^{\bar{\mathrm{x}}};\ \boldsymbol{C}^{\mathrm{y}}_{41}=\boldsymbol{B}^{\mathrm{y}}}$$

$$\times \nabla^{m}_{\boldsymbol{B}^{\mathrm{x}}} \langle \boldsymbol{B}^{\mathrm{y}}, t_{\mathrm{y}} | \boldsymbol{B}^{\mathrm{x}}, t_{\mathrm{x}} \rangle \Big|_{\boldsymbol{B}^{\mathrm{x}}=0}. \tag{3.18}$$

The times $(t_{\mathrm{x}}, t_{\mathrm{y}}, t_{\bar{\mathrm{x}}}, t_{\bar{\mathrm{y}}})$ are the times of the four vertices in fig. 3.8 from left (earliest) to right (latest). The factors $\langle \boldsymbol{B}^{\mathrm{y}}, t_{\mathrm{y}} | \boldsymbol{B}^{\mathrm{x}}, t_{\mathrm{x}} \rangle$ and $\langle \boldsymbol{B}^{\bar{\mathrm{y}}}, t_{\bar{\mathrm{y}}} | \boldsymbol{B}^{\bar{\mathrm{x}}}, t_{\bar{\mathrm{x}}} \rangle$ represent the propagators for the 3-particle evolution respectively before and after the shaded region of the figure. The factor $\langle \boldsymbol{C}^{\bar{\mathrm{x}}}_{41}, \boldsymbol{C}^{\bar{\mathrm{x}}}_{23}, t_{\bar{\mathrm{x}}} | \boldsymbol{C}^{\mathrm{y}}_{41}, \boldsymbol{C}^{\mathrm{y}}_{23}, t_{\mathrm{y}} \rangle$ represents the propagator for the 4-particle evolution inside the shaded region. The gradient $\nabla$ corresponds to a factor of transverse momentum associated with each splitting vertex. We have not shown the overall factors including how those gradients are contracted together by helicity-dependent DGLAP splitting functions. The non-trivial corrections to the $N=\infty$ result come from the color dynamics of the 4-particle propagator, which we

---

[13]Eq. (3.18) isolates the factors we want to discuss here from the $N=\infty$ expression in eq. (E.1) of ref. [37]. Technically, integrating over *all* of the times $(t_{\mathrm{x}} < t_{\mathrm{y}} < t_{\bar{\mathrm{x}}} < t_{\bar{\mathrm{y}}})$ gives probability, not rate. We should integrate only over time differences, but that detail is unimportant for the present discussion.

now write as

$$G(\boldsymbol{C}_{41}^{\bar{\mathrm{x}}}, \boldsymbol{C}_{23}^{\bar{\mathrm{x}}}, t_{\bar{\mathrm{x}}}; \boldsymbol{C}_{41}^{\mathrm{y}}, \boldsymbol{C}_{23}^{\mathrm{y}}, t_{\mathrm{y}}) \equiv \langle \boldsymbol{C}_{41}^{\bar{\mathrm{x}}}, \boldsymbol{C}_{23}^{\bar{\mathrm{x}}}, t_{\bar{\mathrm{x}}} | \boldsymbol{C}_{41}^{\mathrm{y}}, \boldsymbol{C}_{23}^{\mathrm{y}}, t_{\mathrm{y}} \rangle. \tag{3.19}$$

In writing the initial and final 4-particle states in the propagator, we will need to specify what 4-particle color singlet states we start and end in. We find it convenient to rewrite (3.19) as

$$G(\vec{\boldsymbol{\xi}}^{\bar{\mathrm{x}}}, \Delta t, \lambda^{\bar{\mathrm{x}}}; \vec{\boldsymbol{\xi}}^{\mathrm{y}}, 0, \lambda^{\mathrm{y}}), \tag{3.20}$$

where

$$\vec{\boldsymbol{\xi}} \equiv \begin{pmatrix} \boldsymbol{C}_{41} \\ \boldsymbol{C}_{23} \end{pmatrix} \tag{3.21}$$

is a 2-dimensional vector with entries that are themselves 2-dimensional vectors in the transverse plane. This vector encodes the transverse position state of the system at a given time;

$$\Delta t \equiv t_{\bar{\mathrm{x}}} - t_{\mathrm{y}} \tag{3.22}$$

is the total duration of the 4-particle evolution; and $\lambda^{\mathrm{y}}$ and $\lambda^{\bar{\mathrm{x}}}$ label the initial and final 4-particle color singlet states for that evolution.

Those initial and final singlet states are each $|\mathrm{A_{aa}}\rangle_u$ for the diagram of fig. 3.8 as explained in ref. [42].[14] We can understand this quickly by (i) considering everything to the left of the shaded region of fig. 3.8 which looks like the $u$-channel diagram of fig. 3.4c with a gluon ($R{=}\mathrm{A}$) for the internal line, corresponding to $|\mathrm{A}\rangle_u$; (ii) 3-gluon vertices combine anti-symmetrically via the group structure constants $f^{abc}$, therefore specializing to $|\mathrm{A_{aa}}\rangle_u$; and (iii) there is no color dynamics for 3-particle evolution

---

[14]See section 2.3 of [42]. Because of different labeling of the four particles there (our 1234 here is DBAC in fig. 6 of ref. [42]), what we call $u$-channel here is what is called $s$-channel there.

which means the interactions with the medium in the actual diagram of fig. 3.8 will not affect the correspondence with the color-contraction diagram of fig. 3.4c. The same applies to everything to the right of the shaded region of fig. 3.8.

We can write this in terms of the $N=\infty$ eigenstates (3.13). The initial and final color-singlet states of the 4-particle evolution are then

$$|A_{aa}\rangle_u = \tfrac{1}{\sqrt{2}}|A_+\rangle + \tfrac{1}{\sqrt{2}}|A_-\rangle. \tag{3.23}$$

So, we will be interested in 4-particle evolution Green functions (3.20) where the initial state can be $\lambda^y = A_+$ or $A_-$ and the final state can be $\lambda^{\bar{x}} = A_+$ or $A_-$.

From the structure of the finite-$N$ corrections (3.17) to the $\underline{S}_u$ and $\underline{T}_u$ matrices that appear in the Hamiltonian (3.8), we can now see what 4-particle color-singlet transitions contribute to the $1/N^2$ correction to the $xy\bar{x}\bar{y}$ sequential diagram of fig. 3.8. Note that the transitions must start and end with $A_\pm$. The transition sequences allowed by (3.17) are then

$$|A_-\rangle \xrightarrow{\delta T} |1\rangle \xrightarrow{\delta T} |A_-\rangle, \tag{3.24a}$$

$$|A_-\rangle \xrightarrow{\delta T} |1_-^\times\rangle \xrightarrow{\delta T} |A_-\rangle, \tag{3.24b}$$

$$|A_-\rangle \xrightarrow{\delta T} |1\rangle \xrightarrow{\delta T} |A_+\rangle, \tag{3.24c}$$

$$|A_+\rangle \xrightarrow{\delta T} |1\rangle \xrightarrow{\delta T} |A_+\rangle, \tag{3.24d}$$

$$|A_+\rangle \xrightarrow{\delta T} |1_+^\times\rangle \xrightarrow{\delta T} |A_+\rangle, \tag{3.24e}$$

$$|A_+\rangle \xrightarrow{\delta T} |1\rangle \xrightarrow{\delta T} |A_-\rangle. \tag{3.24f}$$

Note that neither $\delta\underline{S}$ nor $\delta^2\underline{T}$ contribute to any allowed $O(N^{-2})$ corrections for this diagram.

One can see that there are no $O(N^{-1})$ (as opposed to $O(N^{-2})$) corrections to the diagram: neither $\delta\underline{S}$ nor $\delta\underline{T}$ produce a direct $|A_+\rangle \to |A_-\rangle$ or $|A_-\rangle \to |A_+\rangle$ transition. This is consistent with the fact that, for purely gluonic processes, corrections in a large-$N$ analysis should appear in powers of $1/N^2$ [4].

We can write the allowed transitions (3.24) in the alternative language of (3.15) as,

$$(1234) \xrightarrow{\delta T} (41)(23) \xrightarrow{\delta T} (1234), \tag{3.25a}$$

$$(1234) \xrightarrow{\delta T} (12)(34) \xrightarrow{\delta T} (1234), \tag{3.25b}$$

$$(1234) \xrightarrow{\delta T} (41)(23) \xrightarrow{\delta T} (1324), \tag{3.25c}$$

$$(1324) \xrightarrow{\delta T} (41)(23) \xrightarrow{\delta T} (1324), \tag{3.25d}$$

$$(1324) \xrightarrow{\delta T} (13)(24) \xrightarrow{\delta T} (1324), \tag{3.25e}$$

$$(1324) \xrightarrow{\delta T} (41)(23) \xrightarrow{\delta T} (1234). \tag{3.25f}$$

Note that the last three sequences may be obtained from the first three sequences by exchanging $(2\leftrightarrow3)$ particles 2 and 3. The only thing differentiating particles 2 and 3 in the $xy\bar{x}\bar{y}$ diagram of fig. 3.8 is their longitudinal momentum fractions $y$ and $z \equiv 1-x-y$. So one could calculate the first three sequences and then add (i) that result to (ii) the same calculation with the value of $y$ changed to $1-x-y$ to obtain the result for the 6 sequences above.

## 3.2.2  $1/N$ perturbation theory for 4-particle propagator

We will call $G_\lambda^{N=\infty}$ the $N=\infty$ 4-particle propagator for any of the $N=\infty$ color singlet eigenstates of (3.13), indexed by $\lambda$. In perturbation theory in $1/N$, the transitions

$(3.24)$ correspond to $O(N^{-2})$ corrections to the propagator of the form

$$
\begin{aligned}
\delta^2 G_{\lambda_{23} \leftarrow \lambda_{01}}(\vec{\boldsymbol{\xi}}_3, \Delta t; \vec{\boldsymbol{\xi}}_0, 0) & \\
= (-i)^2 \sum_{\lambda_{12}} \int_{0 < t_1 < t_2 < \Delta t} & dt_1 \, dt_2 \int_{\vec{\xi}_1, \vec{\xi}_2} G_{\lambda_{23}}^{N=\infty}(\vec{\boldsymbol{\xi}}_3, \Delta t; \vec{\boldsymbol{\xi}}_2, t_2) \, \delta V_{\lambda_{23} \leftarrow \lambda_{12}}^{(\delta T)}(\vec{\boldsymbol{\xi}}_2) \\
& \times G_{\lambda_{12}}^{N=\infty}(\vec{\boldsymbol{\xi}}_2, t_2; \vec{\boldsymbol{\xi}}_1, t_1) \, \delta V_{\lambda_{12} \leftarrow \lambda_{01}}^{(\delta T)}(\vec{\boldsymbol{\xi}}_1) \, G_{\lambda_{01}}^{N=\infty}(\vec{\boldsymbol{\xi}}_1, t_1; \vec{\boldsymbol{\xi}}_0, t_0).
\end{aligned}
$$

$$(3.26)$$

Here $t_0 = t^{\text{y}}$ and $t_3 = t^{\bar{\text{x}}}$ are the initial and final times of the 4-particle evolution (the shaded region) in fig. 3.8. The two $O(N^{-1})$ perturbations to $N=\infty$ evolution (caused by $\delta \underline{T}$) occur at intermediate times $t_1$ and $t_2$, as seen in fig. 3.9. The $\lambda_{ij}$ represents an $N=\infty$ eigenstate from $(3.13)$. Previously, we discussed that the initial color singlet $\lambda_{01}$ and the final color singlet state $\lambda_{23}$ must be $|A_+\rangle$ or $|A_-\rangle$ as in $(3.23)$ and $(3.24)$. $\delta V_{\lambda \leftarrow \lambda'}^{(\delta T)}$ represents the $(\lambda, \lambda')$ matrix element of the $\delta \underline{T}$ contribution to the potential $(3.8b)$. The non-zero matrix elements are all the same because the non-zero matrix elements of $\delta \underline{T}$ in $(3.17)$ are all the same:

$$
\delta V^{(\delta T)}(\vec{\boldsymbol{\xi}}) = \frac{i \hat{q}_{\text{A}}}{2\sqrt{2} \, N} \, (x_4 + x_1)(x_2 + x_3) \, \boldsymbol{C}_{41} \cdot \boldsymbol{C}_{23} .
$$

$$(3.27)$$

We will find it useful to generalize our notation by introducing some shorthand notation for $(3.27)$ and also by distinguishing the earlier-time and later-time insertions of $\delta V$ in $(3.26)$:

$$
\delta V_{\lambda_{12} \leftarrow \lambda_{01}}^{(\delta T)}(\vec{\boldsymbol{\xi}}_1) = \tfrac{1}{2} \vec{\boldsymbol{\xi}}_1^{\top} R_1 \, \vec{\boldsymbol{\xi}}_1, \qquad \delta V_{\lambda_{23} \leftarrow \lambda_{12}}^{(\delta T)}(\vec{\boldsymbol{\xi}}_2) = \tfrac{1}{2} \vec{\boldsymbol{\xi}}_2^{\top} R_2 \, \vec{\boldsymbol{\xi}}_2 \qquad \text{(for allowed transitions)}
$$

$$(3.28)$$
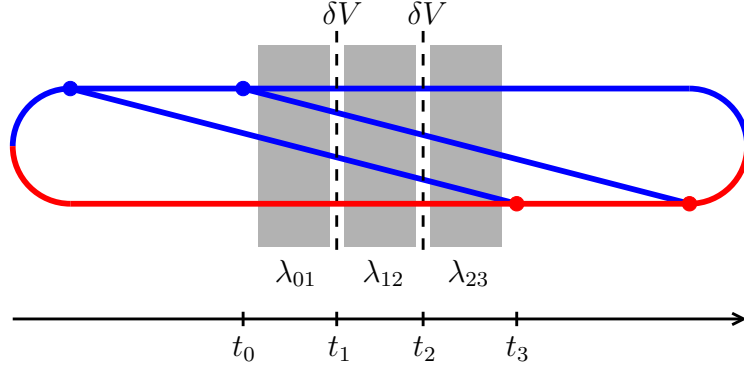
Figure 3.9: A depiction of the 2nd-order perturbative correction (3.26) in $1/N$ to 4-particle evolution. The shading shows regions of 4-particle propagation where $N=\infty$ propagators are used. The dashed lines represent insertions of the $1/N$ correction $\delta V$ to the potential at intermediate times $t_1$ and $t_2$, which are integrated over.

with[15]

$$R_1 = R_2 = R^{(\delta T)} \equiv -\frac{i\hat{q}_A}{2\sqrt{2}\,N}\,(x_1+x_4)^2 \begin{pmatrix} 0 & 1 \\ 1 & 0 \end{pmatrix} \tag{3.29}$$

(where we have used the fact that $x_1+x_2+x_3+x_4 = 0$). $R^{(\delta T)}$ is a 2×2 matrix that mixes the two components $(\boldsymbol{C}_{41}, \boldsymbol{C}_{23})$ of the vector $\vec{\boldsymbol{\xi}}$ defined by (3.21). It does not act on the transverse position space in which each $\boldsymbol{C}$ lives except to contract the transverse indices, as in (3.27). To be explicit, we can think of the matrices $R_i$ shown in (3.28) as really being $R_i \otimes 1$, where the 2×2 identity matrix acts on transverse position space. But we will not speak explicitly about the transverse space. For example, we will refer to $\vec{\boldsymbol{\xi}}$ throughout this calculation as a "2-dimensional" (rather than 4-dimensional) vector, and we will correspondingly refer to the matrices in (3.28) as the 2×2 matrices (3.29).

We will be able to do the integral over the intermediate positions analytically in $\hat{q}$ approximation. This will leave three time integrals ($t_1$, $t_2$, and $\Delta t \equiv t_3 - t_0$) to later

---

[15]We have introduced the name $R$ rather than using the familiar Pauli matrix notation $\sigma_1$ because later in this calculation we will have applications where the corresponding "$R$" is something else.

be done numerically.

Now we will investigate the structure of the $N=\infty$ 4-particle propagators. In the $\hat{q}$ approximation, these are 2-dimensional harmonic oscillator propagators for a coupled set of two oscillators $(C_{41}, C_{23})$. We will refer to the two complex normal-mode frequencies of this system as $\Omega_{\pm}^{(\lambda)}$ and define the 2×2 diagonal matrix

$$\Omega_{(\lambda)} \equiv \begin{pmatrix} \Omega_+^{(\lambda)} & \\ & \Omega_-^{(\lambda)} \end{pmatrix} \tag{3.30}$$

We have introduced the subscript or superscript $\lambda$ to indicate for which color singlet-state (3.13) we are finding the $N=\infty$ propagators. Adapting the notation from refs. [34, 37], we will make a matrix $a$ whose columns are the corresponding normal mode vectors:

$$a_{(\lambda)} = \begin{pmatrix} C_{41}^+ & C_{41}^- \\ C_{23}^+ & C_{23}^- \end{pmatrix}_{(\lambda)} . \tag{3.31}$$

We will leave until later the details of exactly what $\Omega_{\pm}$ and $a$ are for each $N=\infty$ color singlet state $\lambda$. For now, we can write out the structure of the harmonic-oscillator propagator, which is[16]

$$G_\lambda^{N=\infty}(\vec{\xi}, t; \vec{\xi}', 0) = f_\lambda(t) \exp\left[-\tfrac{1}{2}\vec{\xi}^\top A_\lambda(t)\,\vec{\xi} + \vec{\xi}^\top B_\lambda(t)\,\vec{\xi}' - \tfrac{1}{2}\vec{\xi}'^\top A_\lambda(t)\,\vec{\xi}'\right], \quad (3.32)$$

---

[16]It is because we are working in the same basis $(C_{41}, C_{23})$ throughout the 4-particle evolution that the first and last terms in the exponent of (3.32) have the same matrix $A_\lambda$. This is unlike the original $N=\infty$ analysis of diagrams in ref. [34, 37], where it was found more convenient to use a different basis at the two ends of the propagator.

where

$$A_\lambda(t) \equiv -i\big[(a^\top)^{-1}\Omega \cot(\Omega t)\, a^{-1}\big]_{(\lambda)}, \qquad (3.33)$$

$$B_\lambda(t) \equiv -i\big[(a^\top)^{-1}\Omega \csc(\Omega t)\, a^{-1}\big]_{(\lambda)}, \qquad (3.34)$$

and the prefactor[17]

$$f_\lambda(t) \equiv \det\left(\frac{B_\lambda(t)}{2\pi}\right). \qquad (3.35)$$

### 3.2.3   Integrating over $\vec{\xi}_1$ and $\vec{\xi}_2$

We can do the integrals over $\vec{\xi}_1$ and $\vec{\xi}_2$ in the expression (3.26) for $\delta^2 G$ analytically using Gaussian integrals. We will first combine the two integrals into a single integral by defining a 4-dimensional vector

$$\vec{\Xi} \equiv \begin{pmatrix} \vec{\xi}_1 \\ \vec{\xi}_2 \end{pmatrix} \qquad (3.36)$$

from the two intermediate position vectors $\vec{\xi}_1$ and $\vec{\xi}_2$. We can define

$$\vec{z} \equiv \begin{pmatrix} \vec{\xi}_0 \\ \vec{\xi}_3 \end{pmatrix} \qquad (3.37)$$

to be a 4-dimensional vector composed of the initial and final position vectors $\vec{\xi}_0$

---

[17] For $N=\infty$, calculations of individual time-ordered diagrams were ultraviolet (UV) divergent (even for tree-level processes), which was treated with dimensional regularization in ref. [39]. Those divergences, however, were associated with 4-particle evolution times $\Delta t \to 0$ and so with the vacuum limit of the 4-particle propagators $G$. For vacuum evolution, there is no interesting color dynamics, and it is color dynamics that our $1/N$ corrections describe. As a result, there will be no UV divergences in our calculations of corrections in this analysis, which means that we do not need to use dimensional regularization and so may use the 2-transverse dimensional formula (3.35) for $f_\lambda$.

and $\vec{\xi}_3$ for the 4-particle evolution. Then we can write the expression (3.26) for $\delta^2 G$, together with (3.28) for $\delta V$ and (3.32) for $G^{N=\infty}$ as

$$\delta^2 G_{\lambda_{23}\leftarrow\lambda_{01}}(\vec{\xi}_3, \Delta t; \vec{\xi}_0, 0) = (-i)^2 \sum_{\substack{\text{allowed} \\ \lambda_{12}}} f_{(01)}f_{(12)}f_{(23)} \int_{0<t_1<t_2<\Delta t} dt_1\, dt_2\, e^{-\frac{1}{2}\vec{z}^\top \mathcal{A} \vec{z}}$$

$$\times \frac{\partial}{\partial j_1} \frac{\partial}{\partial j_2} \int d^4\Xi\, e^{-\frac{1}{2}\vec{\Xi}^\top \mathcal{U}\vec{\Xi}} e^{\vec{z}^\top \mathcal{B}\vec{\Xi}} \bigg|_{j_1=j_2=0}, \quad (3.38)$$

where we define the 4×4 matrices

$$\mathcal{U} \equiv \begin{pmatrix} A_{(01)} + A_{(12)} - j_1 R_1 & -B_{(12)} \\ -B_{(12)} & A_{(12)} + A_{(23)} - j_2 R_2 \end{pmatrix}, \quad (3.39a)$$

$$\mathcal{A} \equiv \begin{pmatrix} A_{(01)} & \\ & A_{(23)} \end{pmatrix}, \qquad \mathcal{B} \equiv \begin{pmatrix} B_{(01)} & \\ & B_{(23)} \end{pmatrix}. \quad (3.39b)$$

Here we use the shorthand notation

$$A_{(ij)} \equiv A_{\lambda_{ij}}(t_j - t_i), \qquad B_{(ij)} \equiv B_{\lambda_{ij}}(t_j - t_i), \qquad f_{(ij)} \equiv f_{\lambda_{ij}}(t_j - t_i). \quad (3.40)$$

The parameters $j_1$ and $j_2$ are dummy source term coefficients we will use to generate the two factors (3.28) of $\delta V$ in (3.26) from the Gaussian integral appearing in (3.38).

Doing that Gaussian integral gives[18]

$$\delta^2 G_{\lambda_{23}\leftarrow\lambda_{01}}(\vec{\boldsymbol{\xi}}_3, \Delta t; \vec{\boldsymbol{\xi}}_0, 0) = (-i)^2 (2\pi)^4 \sum_{\substack{\text{allowed} \\ \lambda_{12}}} f_{(01)} f_{(12)} f_{(23)} \int_{0<t_1<t_2<\Delta t} dt_1\, dt_2$$

$$\times \frac{\partial}{\partial j_1} \frac{\partial}{\partial j_2} \left[ \det(\mathcal{U}^{-1}) e^{-\frac{1}{2}\vec{z}^\top (\mathcal{A} - \mathcal{B}\mathcal{U}^{-1}\mathcal{B})\vec{z}} \right]_{j_1 = j_2 = 0}. \quad (3.41)$$

### 3.2.4 Evaluating the $xy\bar{x}\bar{y}$ diagram

Instead of repeating the whole calculation of (3.18) for evaluating the $xy\bar{x}\bar{y}$ diagram, involving taking the gradient of the 4-particle propagator, including the initial and final 3-particle propagators, integrating analytically over the the intermediate position $\boldsymbol{B}^{\text{y}}$ and $\boldsymbol{B}^{\bar{\text{x}}}$, integrating analytically over the first and last vertex times $t_{\text{x}}$ and $t_{\bar{\text{y}}}$, and correctly keeping track of all the prefactors not shown explicitly in (3.18), we will use a trick to make our calculation easier by adapting the final result of the same steps that were applied in the original $N=\infty$ calculations of refs. [34, 37]. The trick would be to write the 4-particle propagator (3.41) for our $1/N^2$ correction into the same schematic form as the 4-particle propagator originally used in $N=\infty$ calculations. Let's start with the $N=\infty$ result to introduce the notation $(X, Y, Z)$ that was used in refs. [34, 37, 39].

In ref. [37], there were two color routings to analyze, which in the language of this chapter correspond to taking the full 4-particle propagator $\langle \boldsymbol{C}_{41}^{\bar{\text{x}}}, \boldsymbol{C}_{23}^{\bar{\text{x}}}, t_{\bar{\text{x}}} | \boldsymbol{C}_{41}^{\text{y}}, \boldsymbol{C}_{23}^{\text{y}}, t_{\text{y}} \rangle$ for this diagram in (3.18) to be either $G_{\text{A}_+}^{N=\infty}$ or $G_{\text{A}_-}^{N=\infty}$, corresponding to the two $N=\infty$ eigenstates that appear in (3.23). The calculation done in ref. [37] focused on

---

[18]Even though we have written the Gaussian integral as a 4-dimensional integral $\int d^4 \Xi \cdots$, it is secretly an 8-dimensional integral because each of the four components of $\Xi$ is itself a 2-dimensional position vector $\boldsymbol{C}$ in the transverse plane. For this reason, the Gaussian integral produces an exponential prefactor $\det(2\pi\mathcal{U}^{-1}) = (2\pi)^4 \det(\mathcal{U}^{-1})$ [where det is the 4-dimensional determinant] instead of $\sqrt{\det(2\pi\mathcal{U}^{-1})}$.

the color routing called here $A_- = (1234)$, and the result for the other color routing could be found by swapping the daughters $y$ and $z \equiv 1-x-y$. The calculation of the $A_-$ color routing in ref. [37] was organized such that the exponential piece of the corresponding harmonic oscillator propagator has the form[19]

$$
\langle \boldsymbol{C}_{41}^{\bar{\mathrm{x}}}, \boldsymbol{C}_{23}^{\bar{\mathrm{x}}}, t_{\bar{\mathrm{x}}} | \boldsymbol{C}_{41}^{\mathrm{y}}, \boldsymbol{C}_{23}^{\mathrm{y}}, t_{\mathrm{y}} \rangle =
$$

$$
f \exp\left[ -\frac{1}{2} \begin{pmatrix} \boldsymbol{C}_{41}^{\mathrm{y}} \\ \boldsymbol{C}_{23}^{\mathrm{y}} \end{pmatrix}^{\top} \begin{pmatrix} \mathcal{X}_{\mathrm{y}}^{\mathrm{seq}} & Y_{\mathrm{y}}^{\mathrm{seq}} \\ Y_{\mathrm{y}}^{\mathrm{seq}} & Z_{\mathrm{y}}^{\mathrm{seq}} \end{pmatrix} \begin{pmatrix} \boldsymbol{C}_{41}^{\mathrm{y}} \\ \boldsymbol{C}_{23}^{\mathrm{y}} \end{pmatrix} - \frac{1}{2} \begin{pmatrix} \boldsymbol{C}_{23}^{\bar{\mathrm{x}}} \\ \boldsymbol{C}_{41}^{\bar{\mathrm{x}}} \end{pmatrix}^{\top} \begin{pmatrix} \mathcal{X}_{\bar{\mathrm{x}}}^{\mathrm{seq}} & Y_{\bar{\mathrm{x}}}^{\mathrm{seq}} \\ Y_{\bar{\mathrm{x}}}^{\mathrm{seq}} & Z_{\bar{\mathrm{x}}}^{\mathrm{seq}} \end{pmatrix} \begin{pmatrix} \boldsymbol{C}_{23}^{\bar{\mathrm{x}}} \\ \boldsymbol{C}_{41}^{\bar{\mathrm{x}}} \end{pmatrix} \right.
$$

$$
\left. + \begin{pmatrix} \boldsymbol{C}_{41}^{\mathrm{y}} \\ \boldsymbol{C}_{23}^{\mathrm{y}} \end{pmatrix}^{\top} \begin{pmatrix} X_{\mathrm{y}\bar{\mathrm{x}}}^{\mathrm{seq}} & Y_{\mathrm{y}\bar{\mathrm{x}}}^{\mathrm{seq}} \\ \overline{Y}_{\mathrm{y}\bar{\mathrm{x}}}^{\mathrm{seq}} & Z_{\mathrm{y}\bar{\mathrm{x}}}^{\mathrm{seq}} \end{pmatrix} \begin{pmatrix} \boldsymbol{C}_{23}^{\bar{\mathrm{x}}} \\ \boldsymbol{C}_{41}^{\bar{\mathrm{x}}} \end{pmatrix} \right], \quad (3.42)
$$

where the $\boldsymbol{C}_{ij}$-independent prefactor $f$ is unimportant at the moment. The previous equation gives particular names to the entries of the matrices that in this chapter we would call $A_{A_-}$ and $B_{A_-}$: namely[20]

$$
A_{A_-} = \begin{pmatrix} \mathcal{X}_{\mathrm{y}}^{\mathrm{seq}} & Y_{\mathrm{y}}^{\mathrm{seq}} \\ Y_{\mathrm{y}}^{\mathrm{seq}} & Z_{\mathrm{y}}^{\mathrm{seq}} \end{pmatrix} = \mathcal{S} \begin{pmatrix} \mathcal{X}_{\bar{\mathrm{x}}}^{\mathrm{seq}} & Y_{\bar{\mathrm{x}}}^{\mathrm{seq}} \\ Y_{\bar{\mathrm{x}}}^{\mathrm{seq}} & Z_{\bar{\mathrm{x}}}^{\mathrm{seq}} \end{pmatrix} \mathcal{S}, \qquad B_{A_-} = \begin{pmatrix} X_{\mathrm{y}\bar{\mathrm{x}}}^{\mathrm{seq}} & Y_{\mathrm{y}\bar{\mathrm{x}}}^{\mathrm{seq}} \\ \overline{Y}_{\mathrm{y}\bar{\mathrm{x}}}^{\mathrm{seq}} & Z_{\mathrm{y}\bar{\mathrm{x}}}^{\mathrm{seq}} \end{pmatrix} \mathcal{S}, \quad (3.43)
$$

where

$$
\mathcal{S} \equiv \begin{pmatrix} 0 & 1 \\ 1 & 0 \end{pmatrix} \tag{3.44}
$$

is a matrix that flips the vector $(C_{23}, C_{41})$ appearing in parts of (3.42) to the basis $(C_{41}, C_{23})$ that we have used exclusively in this chapter. The $N=\infty$ formulas for the

---

[19]Our (3.42) is not shown explicitly in ref. [37]. There the argument, in appendix E.2, proceeds by analogy with section 5.3 of ref. [34] and skips over this explicit formula. The analogous formula is eq. (5.41) of ref. [34].

[20]The relationship between $(\mathcal{X}, Y, Z)_{\mathrm{y}}^{\mathrm{seq}}$ and $(\mathcal{X}, Y, Z)_{\bar{\mathrm{x}}}^{\mathrm{seq}}$ follows from eqs. (E.11-12) of ref. [37] and from our (3.50), which shows the relationship between our $\mathcal{X}$ here and the $X$ in ref. [37].

$(X, Y, Z)$'s were given in ref. [37], where the final results for each diagram were given.

Let's now compare the old $N=\infty$ formula to the contribution of a particular color singlet transition sequence $\lambda_{01} \to \lambda_{12} \to \lambda_{23}$ in (3.41) except that we will leave out the operation $\partial_{j_1} \partial_{j_2} [\cdots]_{j_1=j_2=0}$. The dependence on the $\boldsymbol{C}_{ij}$'s is then contained in the 4-vector $\vec{\boldsymbol{z}}$ of (3.37) and so in the exponential factor

$$e^{-\frac{1}{2}\vec{z}^\top (\mathcal{A}-\mathcal{B}\mathcal{U}^{-1}\mathcal{B})\vec{z}} \tag{3.45}$$

of (3.41). Comparing the exponential factor with the one in (3.42), we see that it has the same form, except that it has the $(X, Y, Z)$'s for the $N=\infty$ calculation replaced by $(\tilde{X}, \tilde{Y}, \tilde{Z})$, which is a different version given by

$$\begin{pmatrix} \tilde{\mathcal{X}}_y^{\text{seq}} & \tilde{Y}_y^{\text{seq}} & -\tilde{Y}_{y\bar{x}}^{\text{seq}} & -\tilde{X}_{y\bar{x}}^{\text{seq}} \\ \tilde{Y}_y^{\text{seq}} & \tilde{Z}_y^{\text{seq}} & -\tilde{Z}_{y\bar{x}}^{\text{seq}} & -\tilde{\overline{Y}}_{y\bar{x}}^{\text{seq}} \\ -\tilde{Y}_{y\bar{x}}^{\text{seq}} & -\tilde{Z}_{y\bar{x}}^{\text{seq}} & \tilde{Z}_{\bar{x}}^{\text{seq}} & \tilde{Y}_{\bar{x}}^{\text{seq}} \\ -\tilde{X}_{y\bar{x}}^{\text{seq}} & -\tilde{\overline{Y}}_{y\bar{x}}^{\text{seq}} & \tilde{Y}_{\bar{x}}^{\text{seq}} & \tilde{\mathcal{X}}_{\bar{x}}^{\text{seq}} \end{pmatrix} = \mathcal{A} - \mathcal{B}\mathcal{U}^{-1}\mathcal{B}. \tag{3.46}$$

Calculating $\mathcal{A} - \mathcal{B}\mathcal{U}^{-1}\mathcal{B}$ from the formulas (3.39), we can use (3.46) to read off the corresponding values of the $(\tilde{X}, \tilde{Y}, \tilde{Z})$'s. We can then use those values in place of the $(X, Y, Z)$'s in the final $N=\infty$ result, but we will also need to replace the prefactor $f$ in (3.42) by the prefactors in (3.41), and sum over the allowed color singlet transition sequences. At the end, we will need to act with the $\partial_{j_1} \partial_{j_2} [\cdots]_{j_1=j_2=0}$ that we ignored in order to relate the different calculations.

We will start from the result of ref. [37] for the color routing $A_- = (1234)$, which is[21]

$$\left[\frac{d\Gamma}{dx\,dy}\right]^{N=\infty}_{\substack{xy\bar{x}\bar{y}\\(A_-)}} = -\int_0^\infty d(\Delta t)\,\frac{C_A^2\alpha_s^2 M_i M_f^{\mathrm{seq}}}{8\pi^2(x_1+x_4)^2 E^4}\,f_{A_-}$$

$$\times\left\{(\bar{\beta}Y_y^{\mathrm{seq}}Y_{\bar{x}}^{\mathrm{seq}} + \bar{\alpha}\overline{Y}_{y\bar{x}}^{\mathrm{seq}}Y_{y\bar{x}}^{\mathrm{seq}})I_0^{\mathrm{seq}} + (\bar{\alpha}+\bar{\beta}+2\bar{\gamma})Z_{y\bar{x}}^{\mathrm{seq}}I_1^{\mathrm{seq}}\right.$$

$$+\left[(\bar{\alpha}+\bar{\gamma})Y_y^{\mathrm{seq}}Y_{\bar{x}}^{\mathrm{seq}} + (\bar{\beta}+\bar{\gamma})\overline{Y}_{y\bar{x}}^{\mathrm{seq}}Y_{y\bar{x}}^{\mathrm{seq}}\right]I_2^{\mathrm{seq}}$$

$$\left.- (\bar{\alpha}+\bar{\beta}+\bar{\gamma})(\overline{Y}_{y\bar{x}}^{\mathrm{seq}}Y_{\bar{x}}^{\mathrm{seq}}I_3^{\mathrm{seq}} + Y_y^{\mathrm{seq}}Y_{y\bar{x}}^{\mathrm{seq}}I_4^{\mathrm{seq}})\right\} \qquad (3.47)$$

where

$$I_0^{\mathrm{seq}} = \left[\frac{4\pi^2}{X_y X_{\bar{x}} - X_{y\bar{x}}^2}\right]^{\mathrm{seq}}, \qquad I_1^{\mathrm{seq}} = -\left[\frac{2\pi^2}{X_{y\bar{x}}}\ln\left(\frac{X_y X_{\bar{x}} - X_{y\bar{x}}^2}{X_y X_{\bar{x}}}\right)\right]^{\mathrm{seq}}, \qquad (3.48a)$$

$$I_2^{\mathrm{seq}} = \left[I_0 - \frac{I_1}{X_{y\bar{x}}}\right]^{\mathrm{seq}}, \qquad I_3^{\mathrm{seq}} = \left[\frac{X_{y\bar{x}}I_0}{X_{\bar{x}}}\right]^{\mathrm{seq}}, \qquad I_4^{\mathrm{seq}} = \left[\frac{X_{y\bar{x}}I_0}{X_y}\right]^{\mathrm{seq}} \qquad (3.48b)$$

and[22]

$$f_\lambda = (2\pi i)^{-2}(-x_1 x_2 x_3 x_4)(x_1+x_4)^2 E^2\Omega_+^{(\lambda)}\csc(\Omega_+^{(\lambda)}t)\,\Omega_-^{(\lambda)}\csc(\Omega_-^{(\lambda)}t). \qquad (3.49)$$

The formulas for $(\bar{\alpha},\bar{\beta},\bar{\gamma})$, which represent various combinations of helicity-dependent DGLAP splitting functions, can be found in ref. [37]. The variables $X_y^{\mathrm{seq}}$ and $X_{\bar{x}}^{\mathrm{seq}}$ are related to the variables $\mathcal{X}_y^{\mathrm{seq}}$ and $\mathcal{X}_{\bar{x}}^{\mathrm{seq}}$ we introduced earlier in (3.42) by

$$X_y^{\mathrm{seq}} = |M_i|\Omega_i + \mathcal{X}_y^{\mathrm{seq}}, \qquad (3.50a)$$

$$X_{\bar{x}}^{\mathrm{seq}} = |M_f^{\mathrm{seq}}|\Omega_f^{\mathrm{seq}} + \mathcal{X}_{\bar{x}}^{\mathrm{seq}}, \qquad (3.50b)$$

---

[21]Specifically, see eq. (2.36) of ref. [37], where the $A_-$ color routing of $xy\bar{x}\bar{y}$ is called $xy\bar{x}\bar{y}_2$.

[22]Eq. (3.49) is defined using our conventions in this chapter. To obtain it, start by permuting eqs. (5.35–5.36) of ref. [34] to the basis $(C_{41}, C_{23})$ we use, giving $|\det a_{(\lambda)}|^{-1} = |x_1 x_2 x_3 x_4|^{1/2}|x_1+x_4|E$ in our conventions here. Then our (3.35) and (3.34) give (3.49).

where the additional $|M|\Omega$ terms arise from the integration of the 3-particle propagators, as described in ref. [34]. The formulas for $M_{\mathrm{i}}$, $\Omega_{\mathrm{i}}$, $M_{\mathrm{f}}^{\mathrm{seq}}$, and $\Omega_{\mathrm{f}}^{\mathrm{seq}}$ may be found in ref. [37]. They arise from the 3-particle evolution (which has no interesting color dynamics), and they remain the same in our problem.

To get the desired $1/N^2$ correction to (3.47), we will swap the $(X, Y, Z)$'s to $(\tilde{X}, \tilde{Y}, \tilde{Z})$'s and replace the prefactor $f_{(\mathrm{A}_-)}$ in (3.47) by the analogous non-exponential factors (and operations) in (3.41):

$$
\delta^2 \left[ \frac{d\Gamma}{dx\, dy} \right]_{xy\bar{x}\bar{y}} = \frac{C_{\mathrm{A}}^2 \alpha_{\mathrm{s}}^2 M_{\mathrm{i}} M_{\mathrm{f}}^{\mathrm{seq}}}{8\pi^2 (x_1 + x_4)^2 E^4} \sum_{\substack{\text{allowed} \\ \lambda_{01},\lambda_{12},\lambda_{23}}} \int_{0<t_1<t_2<\Delta t} dt_1\, dt_2\, d(\Delta t)\, (2\pi)^4 f_{(01)} f_{(12)} f_{(23)}
$$

$$
\times \frac{d}{dj_1} \frac{d}{dj_2} \Bigg[ \det(\mathcal{U}^{-1}) \Big\{ (\bar{\beta}\tilde{Y}_{\mathrm{y}}\tilde{Y}_{\bar{\mathrm{x}}} + \bar{\alpha}\tilde{\overline{Y}}_{\mathrm{y}\bar{\mathrm{x}}}\tilde{Y}_{\mathrm{y}\bar{\mathrm{x}}})\tilde{I}_0 + (\bar{\alpha} + \bar{\beta} + 2\bar{\gamma})\tilde{Z}_{\mathrm{y}\bar{\mathrm{x}}}\tilde{I}_1
$$

$$
+ \big[ (\bar{\alpha} + \bar{\gamma})\tilde{Y}_{\mathrm{y}}\tilde{Y}_{\bar{\mathrm{x}}} + (\bar{\beta} + \bar{\gamma})\tilde{\overline{Y}}_{\mathrm{y}\bar{\mathrm{x}}}\tilde{Y}_{\mathrm{y}\bar{\mathrm{x}}} \big] \tilde{I}_2
$$

$$
- (\bar{\alpha} + \bar{\beta} + \bar{\gamma})(\tilde{\overline{Y}}_{\mathrm{y}\bar{\mathrm{x}}}\tilde{Y}_{\bar{\mathrm{x}}}\tilde{I}_3 + \tilde{Y}_{\mathrm{y}}\tilde{Y}_{\mathrm{y}\bar{\mathrm{x}}}\tilde{I}_4) \Big\}^{\mathrm{seq}} \Bigg]_{j_1 = j_2 = 0}. \quad (3.51)
$$

We have summed over all color transition sequences in (3.24).

The result (3.51) includes the product

$$
{}_u\langle \mathrm{A}_{\mathrm{aa}} | \lambda_{23} \rangle \langle \lambda_{01} | \mathrm{A}_{\mathrm{aa}} \rangle_u = \tfrac{1}{2} \quad (3.52)
$$

of overlap factors of the initial and final 4-particle color singlet states (3.23) with $\lambda_{01} = \mathrm{A}_\pm$ and $\lambda_{23} = \mathrm{A}_\pm$ respectively. This is because the same set of factors in the form of

$$
{}_u\langle \mathrm{A}_{\mathrm{aa}} | \mathrm{A}_- \rangle \langle \mathrm{A}_- | \mathrm{A}_{\mathrm{aa}} \rangle_u = \tfrac{1}{2}, \quad (3.53)
$$

were already implicitly included in the $N = \infty$ result (3.47) for the single color routing

$A_-$.[23]

### 3.2.5 Correction to total sequential diagram rate

The $1/N^2$ correction to the total sequential diagram rate can be obtained by (i) taking $2\,\mathrm{Re}[\cdots]$ of (3.51) in order to include the correction to the conjugate diagram $\bar{x}\bar{y}xy$, and (ii) adding all permutations of the three final gluons $(x, y, z)$ which generate distinct diagrams. See fig. 3.10. Correspondingly, the total correction is

$$\delta^2 \left[\Delta \frac{d\Gamma}{dx\,dy}\right]_{\mathrm{seq}} = \delta^2 A_{\mathrm{seq}}(x, y) + \delta^2 A_{\mathrm{seq}}(y, z) + \delta^2 A_{\mathrm{seq}}(z, x) \tag{3.54}$$

with

$$\delta^2 A_{\mathrm{seq}}(x, y) \equiv 2\,\mathrm{Re}\left\{\delta^2 \left[\frac{d\Gamma}{dx\,dy}\right]_{xy\bar{x}\bar{y}}\right\} \tag{3.55}$$

The symbol "$\Delta$" on the left side of (3.54) is not essential to our discussion but is included for the sake of consistency with the $N{=}\infty$ discussion of ref. [37].[24]

One may use the discussion about $y{\leftrightarrow}z$ after (3.25) to write

$$\begin{aligned}
\delta^2 \left[\Delta \frac{d\Gamma}{dx\,dy}\right]_{\mathrm{seq}} = {} & \delta^2 \mathcal{A}_{\mathrm{seq}}(x, y) + \delta^2 \mathcal{A}_{\mathrm{seq}}(y, z) + \delta^2 \mathcal{A}_{\mathrm{seq}}(z, x) \\
& + \delta^2 \mathcal{A}_{\mathrm{seq}}(y, x) + \delta^2 \mathcal{A}_{\mathrm{seq}}(z, y) + \delta^2 \mathcal{A}_{\mathrm{seq}}(x, z)
\end{aligned} \tag{3.56}$$

where $\delta^2 \mathcal{A}_{\mathrm{seq}}(x, y)$ is also defined by (3.55) except that the sum over allowed color

---

[23]The language of color singlet state overlap factors does not appear in the original $N{=}\infty$ calculation of ref. [37]. But (3.53) is equivalent to the $\frac{1}{2}$ in the factor $\frac{1}{2}C_{\mathrm{A}}^2$ discussed immediately after eq. (E.1) of ref. [37].

[24]See, in particular, section 1.1 of ref. [37]. Because the $1/N^2$ corrections to sequential diagrams come *only* from the $xy\bar{x}\bar{y}$ diagram (and its conjugate and permutations), that distinction does not matter here.

Figure 3.10: The sum of diagrams contributing to the total $1/N^2$ correction to the total sequential diagram rate. Note that exchanging the daughters $y \leftrightarrow z$ in the first diagram does not generate an additional diagram if *all* possible color transition possibilities have already been included in the evaluation of each diagram.

sequences $\lambda_{01} \to \lambda_{12} \to \lambda_{23}$ in (3.51) is taken over only the first three sequences of (3.25). The version (3.56) has a similar form to how $N=\infty$ results have been previously presented [37].[25]

## 3.3 Color-representation dependent formulas

The previous formulas are not complete because we need the normal mode frequencies and normal mode vectors for 4-particle evolution, with the vectors written in the $(C_{41}, C_{23})$ basis that we have been using throughout. We need these formulas for each 4-particle color singlet state. So we want the formulas for the $\Omega_{\pm}^{(\lambda)}$ and matrix $a_{(\lambda)}$ of eqs. (3.30) and (3.31). We will give these formulas here in this section for all of our $N=\infty$ eigenstates $(1, A_+, A_-, A^\times, 1_+^\times, 1_-^\times)$, not just the states that appeared in the $xy\bar{x}\bar{y}$ transitions (3.24), because the other states will be useful later in the evaluation of $1/N^2$ contributions to crossed diagrams.

We will use the results for the $|A_+\rangle$ and $|1\rangle$ color singlets. The rest of the formulas can be related to these using permutations symmetries, for which the notation (3.15) for $N=\infty$ color singlet states will be very useful.

---

[25]See eq. (3.1) of ref. [37].

### 3.3.1 Basics

$\underline{|A_-\rangle = (1234)}$

We will call this the canonical color state considered earlier in the $N=\infty$ papers such as [34, 37]. A convenient summary of the relevant formulas for $\Omega_\pm$ and $a$ can be found in eqs. (A.21–22) and (A.27–30) of ref. [47], where our matrix $a$ in the $(C_{41}, C_{23})$ basis used here corresponds to the matrix called $a_y$ there. These formulas depend on the momentum fractions $(x_1, x_2, x_3, x_4) = (-1, y, 1-x-y, x)$ of the four gluons. So

$$\Omega_{(A_-)} = \Omega_{(A_-)}(x_1, x_2, x_3, x_4) \qquad \text{and} \qquad a_{(A_-)} = a_{(A_-)}(x_1, x_2, x_3, x_4), \qquad (3.57)$$

where $\Omega_{(\lambda)}$ is the matrix defined in (3.30).

$\underline{|1\rangle = (41)(23)}$

The $u$-channel color singlet state $|1\rangle$ refers to the case where the particle pairs (41) and (23) are each contracted into a singlet. This gives simple normal modes in the $(C_{41}, C_{23})$ basis. The 4-particle potential (3.8b) for $N=\infty$ acts on the $|1\rangle$ state as

$$\underline{V}(\boldsymbol{C}_{41}, \boldsymbol{C}_{23}) = -\tfrac{i}{4}(x_4 + x_1)^2 \hat{q}_A (C_{41}^2 + C_{23}^2). \qquad (3.58)$$

The normal mode frequencies $\Omega_\pm$ and vectors $(C_{41}, C_{23})^\pm$ are

$$\underline{\Omega}_{(1)} \equiv \begin{pmatrix} \Omega_+^{(1)} & \\ & \Omega_-^{(1)} \end{pmatrix} = \sqrt{-\frac{i\hat{q}_A}{2E} \begin{pmatrix} \frac{1}{x_1} + \frac{1}{x_4} & \\ & \frac{1}{x_2} + \frac{1}{x_3} \end{pmatrix}} \qquad (3.59)$$

and

$$a_{(1)} \equiv \begin{pmatrix} C_{41}^+ & C_{41}^- \\ C_{23}^+ & C_{23}^- \end{pmatrix}_{(1)} = \frac{1}{E^{1/2}} \begin{pmatrix} [x_1 x_4 (x_1 + x_4)]^{-1/2} & \\ & [x_2 x_3 (x_2 + x_3)]^{-1/2} \end{pmatrix}. \tag{3.60}$$

Following refs. [34, 37], the normal modes have been normalized so that

$$\begin{pmatrix} \boldsymbol{C}_{41}^i \\ \boldsymbol{C}_{23}^i \end{pmatrix}^\top \mathfrak{M}' \begin{pmatrix} \boldsymbol{C}_{41}^j \\ \boldsymbol{C}_{23}^j \end{pmatrix} = \delta^{ij}, \tag{3.61}$$

where

$$\mathfrak{M}' = \begin{pmatrix} x_4 x_1 (x_4 + x_1) & \\ & x_2 x_3 (x_2 + x_3) \end{pmatrix} E \tag{3.62}$$

is the mass matrix whose inverse appears in the kinetic term of the Hamiltonian (3.8a)

for the basis $(C_{41}, C_{23})$ that we use here.[26]

## 3.3.2 Permutations

$\underline{|1_-^\times\rangle = (12)(34)}$

Permuting indices $1 \leftrightarrow 3$ in the result (3.59) for the $(41)(23)$ state, we get the eigen frequencies for the $(43)(21) = (12)(34) = |1_-^\times\rangle$ color singlet state:

$$\underline{\Omega}_{(1_-^\times)} = \sqrt{-\frac{i\hat{q}_A}{2E} \begin{pmatrix} \frac{1}{x_3} + \frac{1}{x_4} & \\ & \frac{1}{x_2} + \frac{1}{x_1} \end{pmatrix}}. \tag{3.63}$$

---

[26]See the discussion of eqs. (5.16–18) of ref. [34]. Here we work in the basis $(C_{41}, C_{23})$ instead of $(C_{34}, C_{12})$, and so the indices 1234 there are relabeled 2341 here.

We expressed the modes (3.60) for $(41)(23)$ in the $(C_{41}, C_{23})$ basis. By making the same permutation $1 \leftrightarrow 3$ to (3.60), we obtain normal modes for $|1^\times_-\rangle$ in the $(C_{43}, C_{21})$ basis:

$$\begin{pmatrix} C_{43}^+ & C_{43}^- \\ C_{21}^+ & C_{21}^- \end{pmatrix}_{(|1^\times_-\rangle)} = \frac{1}{E^{1/2}} \begin{pmatrix} [x_4 x_3 (x_4 + x_3)]^{-1/2} & \\ & [x_2 x_1 (x_2 + x_1)]^{-1/2} \end{pmatrix}. \qquad (3.64)$$

Using $C_{ij} = -C_{ji}$, we can convert to the $(C_{34}, C_{12})$ basis by negating (3.64) to get

$$\begin{pmatrix} C_{34}^+ & C_{34}^- \\ C_{12}^+ & C_{12}^- \end{pmatrix}_{(|1^\times_-\rangle)} = -\frac{1}{E^{1/2}} \begin{pmatrix} [x_4 x_3 (x_4 + x_3)]^{-1/2} & \\ & [x_2 x_1 (x_2 + x_1)]^{-1/2} \end{pmatrix}. \qquad (3.65)$$

To convert to the $(C_{41}, C_{23})$ basis used throughout this chapter, now use the relation [34][27]

$$\begin{pmatrix} C_{41} \\ C_{23} \end{pmatrix} = \frac{1}{(x_1 + x_4)} \begin{pmatrix} -x_3 & -x_2 \\ x_4 & x_1 \end{pmatrix} \begin{pmatrix} C_{34} \\ C_{12} \end{pmatrix} \qquad (3.66)$$

to get

$$a_{(1^\times_-)} = -\frac{1}{(x_1 + x_4) E^{1/2}} \begin{pmatrix} -x_3 & -x_2 \\ x_4 & x_1 \end{pmatrix} \begin{pmatrix} [x_3 x_4 (x_3 + x_4)]^{-1/2} & \\ & [x_1 x_2 (x_1 + x_2)]^{-1/2} \end{pmatrix}. \qquad (3.67)$$

---

[27]This relation comes from eq. (5.31) on ref. [34].

$$|1_+^\times\rangle = (13)(24)$$

Permuting indices $3 \leftrightarrow 4$ in (3.59) for the $(41)(23)$ state, we obtain

$$\underline{\Omega}_{(1_+^\times)} = \sqrt{-\frac{i\hat{q}_A}{2E} \begin{pmatrix} \frac{1}{x_1}+\frac{1}{x_3} & \\ & \frac{1}{x_2}+\frac{1}{x_4} \end{pmatrix}} \tag{3.68}$$

and

$$\begin{pmatrix} C_{31}^+ & C_{31}^- \\ C_{24}^+ & C_{24}^- \end{pmatrix}_{(|1_+^\times\rangle)} = \frac{1}{E^{1/2}} \begin{pmatrix} [x_1 x_3(x_1+x_3)]^{-1/2} & \\ & [x_2 x_4(x_2+x_4)]^{-1/2} \end{pmatrix}. \tag{3.69}$$

We also permute the conversion (3.66) by $1 \leftrightarrow 4$ and then use $C_{ij} = -C_{ji}$ to get

$$\begin{pmatrix} \boldsymbol{C}_{41} \\ \boldsymbol{C}_{23} \end{pmatrix} = \frac{1}{(x_1+x_4)} \begin{pmatrix} x_3 & -x_2 \\ x_1 & -x_4 \end{pmatrix} \begin{pmatrix} \boldsymbol{C}_{31} \\ \boldsymbol{C}_{24} \end{pmatrix}. \tag{3.70}$$

We now use this transformation to (3.69) then gives the normal modes in the desired basis:

$$a_{(1_+^\times)} = \frac{1}{(x_1+x_4)E^{1/2}} \begin{pmatrix} x_3 & -x_2 \\ x_1 & -x_4 \end{pmatrix} \begin{pmatrix} [x_1 x_3(x_1+x_3)]^{-1/2} & \\ & [x_2 x_4(x_2+x_4)]^{-1/2} \end{pmatrix}. \tag{3.71}$$

$$\underline{|A_+\rangle = (1324)}$$

We will get these formulas from the formulas for $|A_-\rangle = (1234)$ by similar permutation arguments. Swapping $2 \leftrightarrow 3$,

$$\underline{\Omega}_{(A_+)}(x_1, x_2, x_3, x_4) = \underline{\Omega}_{(A_-)}(x_1, x_3, x_2, x_4) \tag{3.72}$$

and

$$\begin{pmatrix} C_{41}^+ & C_{41}^- \\ C_{32}^+ & C_{32}^- \end{pmatrix}_{(A_+)} = a_{(A_-)}(x_1, x_3, x_2, x_4). \tag{3.73}$$

Since $C_{32} = -C_{23}$, we may rewrite that as

$$a_{(A_+)}(x_1, x_2, x_3, x_4) = \begin{pmatrix} 1 & \\ & -1 \end{pmatrix} a_{(A_-)}(x_1, x_3, x_2, x_4). \tag{3.74}$$

$$\underline{|A^\times\rangle = (1243)}$$

Using the same method, swapping $3 \leftrightarrow 4$ in formulas for $|A_-\rangle = (1234)$ gives

$$\underline{\Omega}_{(A^\times)}(x_1, x_2, x_3, x_4) = \underline{\Omega}_{(A_-)}(x_1, x_2, x_4, x_3) \tag{3.75}$$

and

$$\begin{pmatrix} C_{31}^+ & C_{31}^- \\ C_{24}^+ & C_{24}^- \end{pmatrix}_{(A^\times)} = a_{(A_-)}(x_1, x_2, x_4, x_3). \tag{3.76}$$

$$x y \bar{y} \bar{x}$$
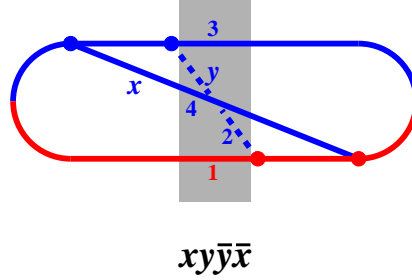
Figure 3.11: The canonical "crossed" diagram. Particles in the (shaded) region of 4-particle evolution are numbered according to the convention of ref. [34].

Then use (3.70) to get

$$a_{(\mathrm{A}^\times)}(x_1, x_2, x_3, x_4) = \frac{1}{(x_1 + x_4)} \begin{pmatrix} x_3 & -x_2 \\ x_1 & -x_4 \end{pmatrix} a_{(\mathrm{A}_-)}(x_1, x_2, x_4, x_3). \tag{3.77}$$

## 3.4 Crossed diagrams

Now we calculate the contribution from what we call the crossed diagrams. We start with the canonical diagram $x y \bar{y} \bar{x}$ diagram shown in fig. 3.11 to which all other diagrams can be related [34].

### 3.4.1 Allowed Color Transitions

The initial color state of the four-particles at the beginning of the shaded region is the same as for the sequential diagram of fig. 3.8, and so the initial 4-particle color singlet state is the same as before:

$$|\mathrm{A}_{\mathrm{aa}}\rangle_u = \tfrac{1}{\sqrt{2}}|\mathrm{A}_+\rangle + \tfrac{1}{\sqrt{2}}|\mathrm{A}_-\rangle \qquad \text{(initial 4-particle state).} \tag{3.78}$$

However, the end of the shaded region is different: It is now gluons 1 and 2 that meet at a vertex. So, the final state is the $s$-channel version $|A_{aa}\rangle_s$ rather than $u$-channel version (3.78). We will stick to the definition (3.13) of our basis states $(1, A_+, A_-, A^\times, 1_+^\times, 1_-^\times)$, which are defined in terms of $u$-channel singlet combinations. So, we will write the final ($s$-channel) color singlet state $|A_{aa}\rangle_s$ in terms of this basis. The matrix that converts (for any $N$) between the $s$-channel and $u$-channel versions of the original basis states (3.7) is given by [42, 19, 36] (see appendix B.1.1)

$$
\begin{pmatrix}
|\mathbf{1}\rangle_s \\
|A_{aa}\rangle_s \\
|A_{ss}\rangle_s \\
|\text{``}\mathbf{10}+\overline{\mathbf{10}}\text{''}\rangle_s \\
|\text{``}\mathbf{27}\text{''}\rangle_s \\
|\text{``}\mathbf{0}\text{''}\rangle_s
\end{pmatrix}
= U
\begin{pmatrix}
|\mathbf{1}\rangle_u \\
|A_{aa}\rangle_u \\
|A_{ss}\rangle_u \\
|\text{``}\mathbf{10}+\overline{\mathbf{10}}\text{''}\rangle_u \\
|\text{``}\mathbf{27}\text{''}\rangle_u \\
|\text{``}\mathbf{0}\text{''}\rangle_u
\end{pmatrix}
\tag{3.79a}
$$

with

$$
U =
\begin{pmatrix}
\frac{1}{N^2-1} & -\sqrt{\frac{1}{N^2-1}} & \sqrt{\frac{1}{N^2-1}} & -\sqrt{\frac{N^2-4}{2(N^2-1)}} & \frac{N}{2(N+1)}\sqrt{\frac{N+3}{N-1}} & \frac{N}{2(N-1)}\sqrt{\frac{N-3}{N+1}} \\
& \frac{1}{2} & -\frac{1}{2} & 0 & \frac{1}{2}\sqrt{\frac{N+3}{N+1}} & -\frac{1}{2}\sqrt{\frac{N-3}{N-1}} \\
& & \frac{N^2-12}{2(N^2-4)} & \sqrt{\frac{2}{N^2-4}} & \frac{N}{2(N+2)}\sqrt{\frac{N+3}{N+1}} & -\frac{N}{2(N-2)}\sqrt{\frac{N-3}{N-1}} \\
& & & \frac{1}{2} & \sqrt{\frac{(N-2)(N+3)}{8(N+1)(N+2)}} & \sqrt{\frac{(N+2)(N-3)}{8(N-1)(N-2)}} \\
& \text{(symmetric)} & & & \frac{N^2+N+2}{4(N+1)(N+2)} & \frac{1}{4}\sqrt{\frac{N^2-9}{N^2-1}} \\
& & & & & \frac{N^2-N+2}{4(N-1)(N-2)}
\end{pmatrix} .
$$

$$\tag{3.79b}$$

In the present calculation, we only care about this piece:

$$|A_{aa}\rangle_s = -\sqrt{\tfrac{1}{N^2-1}}\,|\mathbf{1}\rangle_u + \tfrac{1}{2}\,|A_{aa}\rangle_u - \tfrac{1}{2}\,|A_{ss}\rangle_u + \tfrac{1}{2}\sqrt{\tfrac{N+3}{N+1}}\,|\text{``}\mathbf{27}\text{''}\rangle_u - \tfrac{1}{2}\sqrt{\tfrac{N-3}{N-1}}\,|\text{``}\mathbf{0}\text{''}\rangle_u. \quad (3.80)$$

Then we write this in terms of the basis states $(1, A_+, A_-, A^\times, 1_+^\times, 1_-^\times)$ that we use throughout this calculation, and then expand in $1/N$,

$$|A_{aa}\rangle_s = \frac{|A_-\rangle + |A^\times\rangle}{\sqrt{2}} + \frac{|1_+^\times\rangle + |1_-^\times\rangle - 2|1\rangle}{2N} - \frac{3|A^\times\rangle}{2\sqrt{2}\,N^2} + O(N^{-3})$$

$$\text{(final 4-particle state).} \quad (3.81)$$

Note that the overall sign of $|A_{aa}\rangle_s$ is merely a phase convention choice for that state. Different choices of this sign convention will lead to compensating changes of sign in the rule for the diagrammatic vertex at the end of the 4-particle evolution in fig. 3.11. We will later discuss how to get the overall sign of our answer right without having to drill down into such details.[28]

We can now use the initial and final singlet states (3.78) and (3.81), together with the perturbation matrices $\delta\underline{S}$, $\delta\underline{T}$ and $\delta^2\underline{T}$ of (3.17), to list all possible 4-particle color transition sequences that contribute to $1/N^2$ corrections to the $xy\bar{y}\bar{x}$ diagram of fig. 3.11. They are listed in table 3.1.

### 3.4.2   2nd order in $\delta V$

First, we will discuss the first five lines of table 3.1, which represent the cases that involve two $\delta\underline{V}$ in the 4-particle evolution. In fig. 3.12, we show a schematic picture

---

[28]We did not have to think about the phase convention in our discussion of sequential diagrams because the initial and final color singlet states were both the same: $|A_{aa}\rangle_u$. So changing sign convention $|A_{aa}\rangle_u \to -|A_{aa}\rangle_u$ would have no effect since the sign would appear twice in the calculation of the 4-particle evolution—once at the start and once at the end.

| transition | equivalent | $\delta S,\ \delta T,\ \delta^2 T$ factors | color overlap | $\phi$ |
|---|---|---|---|---|
| $\|A_-\rangle \xrightarrow{\delta T} \|1\rangle \xrightarrow{\delta T} \|A_-\rangle$ | $(1234) \to (41)(23) \to (1234)$ | $\frac{1}{2N^2}$ | $\frac{1}{2}$ | $\frac{1}{2N^2}$ |
| $\|A_-\rangle \xrightarrow{\delta T} \|1_-^\times\rangle \xrightarrow{\delta T} \|A_-\rangle$ | $(1234) \to (12)(34) \to (1234)$ | $\frac{1}{2N^2}$ | $\frac{1}{2}$ | $\frac{1}{2N^2}$ |
| $\|A_+\rangle \xrightarrow{\delta T} \|1\rangle \xrightarrow{\delta T} \|A_-\rangle$ | $(1324) \to (41)(23) \to (1234)$ | $\frac{1}{2N^2}$ | $\frac{1}{2}$ | $\frac{1}{2N^2}$ |
| $\|A_-\rangle \xrightarrow{\delta T} \|1_-^\times\rangle \xrightarrow{\delta S} \|A^\times\rangle$ | $(1234) \to (12)(34) \to (1243)$ | $-\frac{1}{2N^2}$ | $\frac{1}{2}$ | $-\frac{1}{2N^2}$ |
| $\|A_+\rangle \xrightarrow{\delta T} \|1_+^\times\rangle \xrightarrow{\delta S} \|A^\times\rangle$ | $(1324) \to (13)(24) \to (1243)$ | $-\frac{1}{2N^2}$ | $\frac{1}{2}$ | $-\frac{1}{2N^2}$ |
| $\|A_-\rangle \xrightarrow{\delta^2 T} \|A^\times\rangle$ | $(1234) \to (1243)$ | $\frac{1}{2N^2}$ | $\frac{1}{2}$ | $\frac{1}{2N^2}$ |
| $\|A_+\rangle \xrightarrow{\delta^2 T} \|A^\times\rangle$ | $(1324) \to (1243)$ | $\frac{1}{2N^2}$ | $\frac{1}{2}$ | $\frac{1}{2N^2}$ |
| $\|A_-\rangle \xrightarrow{\delta T} \|1\rangle$ | $(1234) \to (41)(23)$ | $\frac{1}{\sqrt{2}\,N}$ | $-\frac{1}{\sqrt{2}\,N}$ | $-\frac{1}{N^2}$ |
| $\|A_-\rangle \xrightarrow{\delta T} \|1_-^\times\rangle$ | $(1234) \to (12)(34)$ | $\frac{1}{\sqrt{2}\,N}$ | $\frac{1}{2\sqrt{2}\,N}$ | $\frac{1}{2N^2}$ |
| $\|A_+\rangle \xrightarrow{\delta T} \|1\rangle$ | $(1324) \to (41)(23)$ | $\frac{1}{\sqrt{2}\,N}$ | $-\frac{1}{\sqrt{2}\,N}$ | $-\frac{1}{N^2}$ |
| $\|A_+\rangle \xrightarrow{\delta T} \|1_+^\times\rangle$ | $(1324) \to (13)(24)$ | $\frac{1}{\sqrt{2}\,N}$ | $\frac{1}{2\sqrt{2}\,N}$ | $\frac{1}{2N^2}$ |

Table 3.1: Allowed 4-particle color transitions at order $1/N^2$ for the $xy\bar{y}\bar{x}$ diagram, along with (i) the associated $\delta T$, $\delta S$ or $\delta^2 T$ factors, and (ii) the product of the initial and final color overlap factors $\langle \lambda_{\mathrm{i}}|A_{\mathrm{aa}}\rangle_u$ and $_s\langle A_{\mathrm{aa}}|\lambda_{\mathrm{f}}\rangle$. Also shown is the product $\phi$ of (i) and (ii) *relative* to what it would be $\left[ _s\langle A_{\mathrm{aa}}|A_-\rangle\langle A_-|A_{\mathrm{aa}}\rangle_u = \frac{1}{2} \right]$ in the $N=\infty$ calculation of the crossed diagram. The horizontal lines separate groups of processes that have to be handled differently: 2nd order in $\delta V$ with two $\delta T$ transitions; 2nd order in $\delta V$ with a $\delta T$ and $\delta S$ transition; 1st order in $\delta V$ with a $T$-based perturbation. There are no non-zero $O(1/N^2)$ contributions at 0th order in $\delta \underline{V}$. [Specifically, the $1/N^2$ term in (3.81) for the final state $|A_{\mathrm{aa}}\rangle_s$ does not directly overlap the initial state $|A_{\mathrm{aa}}\rangle_u$ of (3.23).]
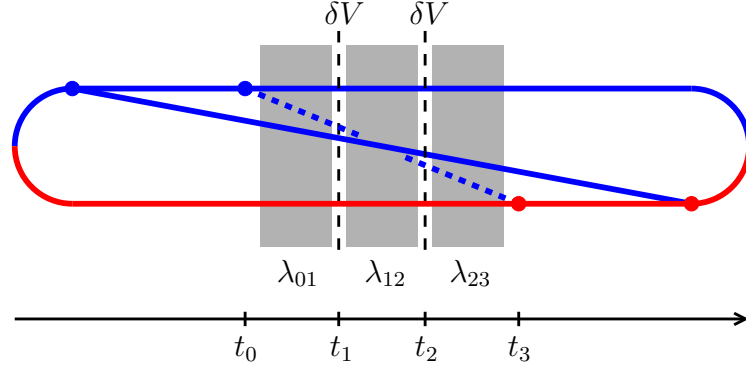
Figure 3.12: The analog of fig. 3.9, now for the $xy\bar{y}\bar{x}$ crossed diagram.

of what these cases represent, similar to fig. 3.9 for the sequential diagram. The formulas for these contributions to the crossed diagram $xy\bar{y}\bar{x}$ are similar to those for the sequential diagram $xy\bar{x}\bar{y}$ found in section 3.2 except for some modifications. We have already talked about one of these modifications, which is using the first five lines of table 3.1. We will discuss now all the other modifications.

**Modification:** $(X, Y, Z)$

We start with the $N=\infty$ rate for the $xy\bar{y}\bar{x}$ diagram, it has a similar form to the $A_-=(1234)$ color routing of the $xy\bar{x}\bar{y}$ diagram in (3.47). The formula for the $xy\bar{y}\bar{x}$ diagram is [34][29]

$$
\left[\frac{d\Gamma}{dx\,dy}\right]_{xy\bar{y}\bar{x}} = -\int_0^\infty d(\Delta t)\,\frac{C_A^2 \alpha_s^2 M_i M_f}{8\pi^2 (x_1+x_4)^2 E^4}\,f_{A_-}
$$
$$
\times \left\{ (\beta Y_y Y_{\bar{y}} + \alpha \overline{Y}_{y\bar{y}} Y_{y\bar{y}}) I_0 + (\alpha + \beta + 2\gamma) Z_{y\bar{y}} I_1 \right.
$$
$$
+ \left[ (\alpha + \gamma) Y_y Y_{\bar{y}} + (\beta + \gamma) \overline{Y}_{y\bar{y}} Y_{y\bar{y}} \right] I_2
$$
$$
\left. - (\alpha + \beta + \gamma)(\overline{Y}_{y\bar{y}} Y_{\bar{y}} I_3 + Y_y Y_{y\bar{y}} I_4) \right\}. \tag{3.82}
$$

---

[29]Unlike $N=\infty$ sequential diagrams, $N=\infty$ crossed diagrams have only a single color routing.

One difference from the sequential case is the $(\alpha, \beta, \gamma)$, which are different combinations of the helicity-dependent DGLAP splitting functions, and their formulas are given in ref. [34]. Another difference is the $I_n$, which has the same form as the $I_n^{\text{seq}}$ of (3.48) except that the superscript "seq" should be removed from everything. This also means that the $(X, Y, Z)$'s are somewhat different from the $(X^{\text{seq}}, Y^{\text{seq}}, Z^{\text{seq}})$'s. These were defined [34] so that the exponential factor in the 4-particle propagator was[30]

$$
\exp\left[-\frac{1}{2}\begin{pmatrix} \boldsymbol{C}_{41}^{\text{y}} \\ \boldsymbol{C}_{23}^{\text{y}} \end{pmatrix}^{\top} \begin{pmatrix} \mathcal{X}_{\text{y}} & Y_{\text{y}} \\ Y_{\text{y}} & Z_{\text{y}} \end{pmatrix} \begin{pmatrix} \boldsymbol{C}_{41}^{\text{y}} \\ \boldsymbol{C}_{23}^{\text{y}} \end{pmatrix} - \frac{1}{2}\begin{pmatrix} \boldsymbol{C}_{34}^{\bar{\text{y}}} \\ \boldsymbol{C}_{12}^{\bar{\text{y}}} \end{pmatrix}^{\top} \begin{pmatrix} \mathcal{X}_{\bar{\text{y}}} & Y_{\bar{\text{y}}} \\ Y_{\bar{\text{y}}} & Z_{\bar{\text{y}}} \end{pmatrix} \begin{pmatrix} \boldsymbol{C}_{34}^{\bar{\text{y}}} \\ \boldsymbol{C}_{12}^{\bar{\text{y}}} \end{pmatrix} \right.
$$
$$
\left. + \begin{pmatrix} \boldsymbol{C}_{41}^{\text{y}} \\ \boldsymbol{C}_{23}^{\text{y}} \end{pmatrix}^{\top} \begin{pmatrix} X_{\text{y}\bar{\text{y}}} & Y_{\text{y}\bar{\text{y}}} \\ \overline{Y}_{\text{y}\bar{\text{y}}} & Z_{\text{y}\bar{\text{y}}} \end{pmatrix} \begin{pmatrix} \boldsymbol{C}_{34}^{\bar{\text{y}}} \\ \boldsymbol{C}_{12}^{\bar{\text{y}}} \end{pmatrix} \right], \quad (3.83)
$$

where

$$
X_{\text{y}} = |M_{\text{i}}|\Omega_{\text{i}} + \mathcal{X}_{\text{y}}, \tag{3.84a}
$$
$$
X_{\bar{\text{y}}} = |M_{\text{f}}|\Omega_{\text{f}} + \mathcal{X}_{\bar{\text{y}}} \tag{3.84b}
$$

similar to (3.50). The formulas for $M_{\text{i}}$, $\Omega_{\text{i}}$, $M_{\text{f}}$, $\Omega_{\text{f}}$ may be found in ref. [34]. The convention in the presentations (3.42) and (3.83) of the sequential and crossed exponentials is that in each vector, the bottom $\boldsymbol{C}_{ij}^{v}$ is the one for which lines $i$ and $j$ come together at the corresponding vertex $v$ of the diagram. The usage of this convention made the $N=\infty$ rate formulas (3.47) and (3.82) for sequential and crossed diagrams have similar structure and made things easier. Equation (3.83) for this crossed dia-

---

[30]See eq. (5.41) of ref. [34], with the caveat that, similar to our previous discussion of the sequential case, our $\mathcal{X}_{\text{y}}$ and $\mathcal{X}_{\bar{\text{y}}}$ here do not contain the effects of the initial and final 3-particle evolution and are related to the $X_{\text{y}}$ and $X_{\bar{\text{y}}}$ of ref. [34] by our eq. (3.84).

gram gives particular names to the entries of the matrices that we call $A_{\mathrm{A}_-}$ and $B_{\mathrm{A}_-}$ similar to the matrices for the sequential diagram (3.43). The relations are

$$A_{\mathrm{A}_-} = \begin{pmatrix} \mathcal{X}_{\mathrm{y}} & Y_{\mathrm{y}} \\ Y_{\mathrm{y}} & Z_{\mathrm{y}} \end{pmatrix} = \mathfrak{S}^{-1\top} \begin{pmatrix} \mathcal{X}_{\bar{\mathrm{y}}} & Y_{\bar{\mathrm{y}}} \\ Y_{\bar{\mathrm{y}}} & Z_{\bar{\mathrm{y}}} \end{pmatrix} \mathfrak{S}^{-1}, \qquad B_{\mathrm{A}_-} = \begin{pmatrix} X_{\mathrm{y}\bar{\mathrm{y}}} & Y_{\mathrm{y}\bar{\mathrm{y}}} \\ \overline{Y}_{\mathrm{y}\bar{\mathrm{y}}} & \tilde{Z}_{\mathrm{y}\bar{\mathrm{y}}} \end{pmatrix} \mathfrak{S}^{-1}, \quad (3.85\mathrm{a})$$

where $\mathfrak{S}$ is the matrix from (3.66) that converts the $(C_{34}, C_{12})$ basis into the $(C_{41}, C_{23})$ basis:

$$\begin{pmatrix} C_{41} \\ C_{23} \end{pmatrix} = \mathfrak{S} \begin{pmatrix} C_{34} \\ C_{12} \end{pmatrix} \tag{3.86a}$$

with

$$\mathfrak{S} \equiv \frac{1}{(x_1 + x_4)} \begin{pmatrix} -x_3 & -x_2 \\ x_4 & x_1 \end{pmatrix}. \tag{3.86b}$$

We want to put the exponential factor

$$e^{-\frac{1}{2}\vec{z}^{\top}(\mathcal{A} - \mathcal{B}\mathcal{U}^{-1}\mathcal{B})\vec{z}} \tag{3.87}$$

for the $1/N^2$ correction into the same form as the exponential factor (3.83) for the known $N = \infty$ result, just like we did for the sequential $xy\bar{x}\bar{y}$ diagram. The only difference is the identification of the $(X, Y, Z)$'s. We can get this by comparing (3.85) with the sequential version (3.43), which helps us to read off the relation of the $(X, Y, Z)$'s of the crossed diagram with the $(X, Y, Z)^{\mathrm{seq}}$ of the sequential diagram:[31]

$$\begin{pmatrix} \tilde{\mathcal{X}}_{\mathrm{y}} & \tilde{Y}_{\mathrm{y}} \\ \tilde{Y}_{\mathrm{y}} & \tilde{Z}_{\mathrm{y}} \end{pmatrix} = \begin{pmatrix} \tilde{\mathcal{X}}_{\mathrm{y}}^{\mathrm{seq}} & \tilde{Y}_{\mathrm{y}}^{\mathrm{seq}} \\ \tilde{Y}_{\mathrm{y}}^{\mathrm{seq}} & \tilde{Z}_{\mathrm{y}}^{\mathrm{seq}} \end{pmatrix}, \qquad \begin{pmatrix} \tilde{\mathcal{X}}_{\bar{\mathrm{y}}} & \tilde{Y}_{\bar{\mathrm{y}}} \\ \tilde{Y}_{\bar{\mathrm{y}}} & \tilde{Z}_{\bar{\mathrm{y}}} \end{pmatrix} = \mathfrak{S}^{\top}\mathcal{S} \begin{pmatrix} \tilde{\mathcal{X}}_{\bar{\mathrm{x}}}^{\mathrm{seq}} & \tilde{Y}_{\bar{\mathrm{x}}}^{\mathrm{seq}} \\ \tilde{Y}_{\bar{\mathrm{x}}}^{\mathrm{seq}} & \tilde{Z}_{\bar{\mathrm{x}}}^{\mathrm{seq}} \end{pmatrix} \mathcal{S}\mathfrak{S}, \quad (3.88\mathrm{a})$$

---

[31] If one removes all of the tildes, then the relations (3.88) *also* relate the $N = \infty$ crossed and sequential formulas for $(X, Y, Z)$, which can be verified from the formulas for $(X, Y, Z)$ in refs. [34, 37], once one uses (3.50) and (3.84) to isolate what we call the $\mathcal{X}$'s from the $X$'s.

$$\begin{pmatrix} \tilde{X}_{y\bar{y}} & \tilde{Y}_{y\bar{y}} \\ \tilde{\bar{Y}}_{y\bar{y}} & \tilde{Z}_{y\bar{y}} \end{pmatrix} = \begin{pmatrix} \tilde{X}_{y\bar{x}}^{\mathrm{seq}} & \tilde{Y}_{y\bar{x}}^{\mathrm{seq}} \\ \tilde{\bar{Y}}_{y\bar{x}}^{\mathrm{seq}} & \tilde{Z}_{y\bar{x}}^{\mathrm{seq}} \end{pmatrix} \mathcal{S}\mathfrak{S}, \qquad (3.88\mathrm{b})$$

where $\mathcal{S}$ is again defined by (3.44). So to get the $(\tilde{X}, \tilde{Y}, \tilde{Z})$'s for the crossed diagrams, one needs to compute the $\mathcal{A} - \mathcal{B}\mathcal{U}^{-1}\mathcal{B}$ as in section 3.2, then read out the $(\tilde{X}, \tilde{Y}, \tilde{Z})^{\mathrm{seq}}$ values using (3.46). Finally, convert those values using (3.88) above.

**Modification: the matrix $R_2$**

Back in (3.29), we have used $R_1 = R_2 = R^{(\delta T)}$ which was based on the fact that only $\delta T$ transitions (3.24) were relevant for the sequential diagram $xy\bar{x}\bar{y}$. This is true for the first three rows of table 3.1, which shows the allowed transition sequences for the crossed diagram $xy\bar{y}\bar{x}$. We will call these the "$\delta T\,\delta T$" transition sequences.

Then, the next two rows of the table have a $\delta S$ transition in the second transition of the sequence. We will call this the "$\delta T\,\delta S$" transition sequences. The $\underline{S}_u$ appears differently in the potential (3.8b) than the $\underline{T}_u$ does. This means that its contribution to $\delta\underline{V}$ matrix elements will be different from those of the $\delta T$ contribution (3.28). The non-zero matrix elements associated with $\delta\underline{S}$ are

$$\delta V^{(\delta S)}(\vec{\xi}) = \frac{i\hat{q}_{\mathrm{A}}}{2\sqrt{2}\,N}\left[x_4 x_1 C_{41}^2 + x_2 x_3 C_{23}^2 + \tfrac{1}{2}(x_4 - x_1)(x_2 - x_3)\boldsymbol{C}_{41}\cdot\boldsymbol{C}_{23}\right], \quad (3.89)$$

which can be written in the form of $\frac{1}{2}\vec{\xi}^{\top} R^{(\delta S)}\vec{\xi}$ with

$$R^{(\delta S)} = +\frac{i\hat{q}_{\mathrm{A}}}{2\sqrt{2}\,N}\begin{pmatrix} 2x_1 x_4 & \tfrac{1}{2}(x_4-x_1)(x_2-x_3) \\ \tfrac{1}{2}(x_4-x_1)(x_2-x_3) & 2x_2 x_3 \end{pmatrix}. \qquad (3.90)$$

So, the final rule is that we need to use

$$(R_1, R_2) = \begin{cases} (R^{(\delta T)}, R^{(\delta T)}) & \text{for } \delta T\, \delta T \text{ transitions;} \\[2ex] (R^{(\delta T)}, R^{(\delta S)}) & \text{for } \delta T\, \delta S \text{ transitions} \end{cases} \tag{3.91}$$

in the construction (3.39a) of the $4{\times}4$ matrix $\mathcal{U}$.

**Final result for 2nd order in $\delta V$**

Using these modifications, the final result for the first five sequences of table 3.1 has the same relation to (3.82) as the sequential result (3.51) did to (3.47):

$$\delta^2 \left[\frac{d\Gamma}{dx\, dy}\right]^{(\delta V)^2}_{xy\bar{y}\bar{x}} = \frac{C_A^2 \alpha_s^2 M_i M_f}{8\pi^2 (x_1 + x_4)^2 E^4} \sum_{\substack{\text{allowed} \\ \lambda_{01}, \lambda_{12}, \lambda_{23}}} \int_{0 < t_1 < t_2 < \Delta t} dt_1\, dt_2\, d(\Delta t)\, (2\pi)^4 f_{(01)} f_{(12)} f_{(23)}$$

$$\times \frac{d}{dj_1} \frac{d}{dj_2} \left[\det(\mathcal{U}^{-1}) \Big\{ (\beta \tilde{Y}_\mathrm{y} \tilde{Y}_{\bar{\mathrm{y}}} + \alpha \tilde{\overline{Y}}_{\mathrm{y}\bar{\mathrm{y}}} \tilde{Y}_{\mathrm{y}\bar{\mathrm{y}}}) \tilde{I}_0 + (\alpha + \beta + 2\gamma) \tilde{Z}_{\mathrm{y}\bar{\mathrm{y}}} \tilde{I}_1 \right.$$

$$+ \big[(\alpha + \gamma) \tilde{Y}_\mathrm{y} \tilde{Y}_{\bar{\mathrm{y}}} + (\beta + \gamma) \tilde{\overline{Y}}_{\mathrm{y}\bar{\mathrm{y}}} \tilde{Y}_{\mathrm{y}\bar{\mathrm{y}}}\big] \tilde{I}_2$$

$$\left. - (\alpha + \beta + \gamma)(\tilde{\overline{Y}}_{\mathrm{y}\bar{\mathrm{y}}} \tilde{Y}_{\bar{\mathrm{y}}} \tilde{I}_3 + \tilde{Y}_\mathrm{y} \tilde{Y}_{\mathrm{y}\bar{\mathrm{y}}} \tilde{I}_4) \Big\} \right]_{j_1 = j_2 = 0}. \tag{3.92}$$

We discussed previously that the initial and final 4-particle color singlet state overlap factors of (i) the calculation of $1/N^2$ corrections in (3.52) and (ii) the $N=\infty$ calculation in (3.53) are the same. The same happens for the first five rows of table 3.1. The calculation of the $1/N^2$ corrections should contain a factor of

$$_s\langle \mathrm{A_{aa}} | \lambda_{23} \rangle \langle \lambda_{01} | \mathrm{A_{aa}} \rangle_u = \tfrac{1}{2}. \tag{3.93}$$

However, we didn't bother to do this because the $N=\infty$ formula (3.82) for the crossed diagram $xy\bar{x}\bar{y}$ already implicitly contained an equal factor of[32]

$$_s\langle \mathrm{A_{aa}}|\mathrm{A_-}\rangle\langle \mathrm{A_-}|\mathrm{A_{aa}}\rangle_u = \tfrac{1}{2}. \tag{3.94}$$

### 3.4.3 A single $\delta T$ or $\delta^2 T$ perturbation

The last group of sequences in table 3.1 is the single $\delta T$ or $\delta^2 T$ perturbation. Fig. 3.13 shows a single $\delta V$ or a $\delta^2 V$. The analog of (3.26) is

$$
\begin{aligned}
\delta G_{\lambda_{12}\leftarrow\lambda_{01}}&(\vec{\boldsymbol{\xi}}_2, \Delta t; \vec{\boldsymbol{\xi}}_0, 0) \\
&= -i\int_{0<t_1<\Delta t} dt_1 \int_{\vec{\boldsymbol{\xi}}_1} G^{N=\infty}_{\lambda_{12}}(\vec{\boldsymbol{\xi}}_2, t_2; \vec{\boldsymbol{\xi}}_1, t_1)\, \delta V^{(\delta^n T)}_{\lambda_{12}\leftarrow\lambda_{01}}(\vec{\boldsymbol{\xi}}_1)\, G^{N=\infty}_{\lambda_{01}}(\vec{\boldsymbol{\xi}}_1, t_1; \vec{\boldsymbol{\xi}}_0, t_0),
\end{aligned}
\tag{3.95}
$$

where $t_0 = t^{\mathrm{y}}$ and $t_2 = t^{\bar{\mathrm{y}}}$ are the initial and final times of the 4-particle evolution. The analog of (3.38) is then

$$
\begin{aligned}
\delta G_{\lambda_{12}\leftarrow\lambda_{01}}(\vec{\boldsymbol{\xi}}_2, \Delta t; \vec{\boldsymbol{\xi}}_0, 0) = -i f_{(01)} f_{(12)} \int_{0<t_1<\Delta t} &dt_1\, e^{-\frac{1}{2}\vec{\boldsymbol{\xi}}_0^\top A_{(01)}\vec{\boldsymbol{\xi}}_0 - \frac{1}{2}\vec{\boldsymbol{\xi}}_2^\top A_{(12)}\vec{\boldsymbol{\xi}}_2} \\
&\times \frac{d}{dj_1} \int d^2\xi_1\, e^{-\frac{1}{2}\vec{\boldsymbol{\xi}}_1^\top U \vec{\boldsymbol{\xi}}_1} e^{\vec{\boldsymbol{\xi}}_1^\top \left(B_{(01)}\vec{\boldsymbol{\xi}}_0 + B_{(12)}\vec{\boldsymbol{\xi}}_2\right)}\bigg|_{j_1=0},
\end{aligned}
\tag{3.96}
$$

where

$$U \equiv A_{(01)} + A_{(12)} - j_1 R_1. \tag{3.97}$$

---

[32]Our (3.94) is equivalent to the $\frac{1}{2}$ in the result $\frac{1}{2}C_{\mathrm{A}}^2$ of eq. (4.17) of ref. [34].
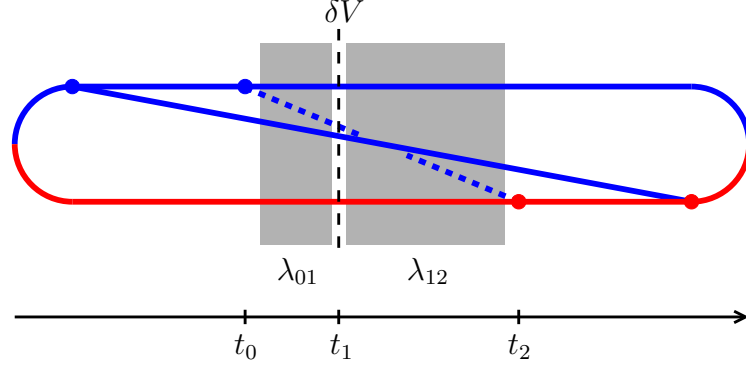
Figure 3.13: Like fig. 3.12 except with only one insertion of $\delta V$ (or $\delta^2 V$) during the 4-particle time evolution.

Doing the Gaussian integral over $\vec{\boldsymbol{\xi}}_1$ yields the analog of (3.41):

$$
\delta G_{\lambda_{12} \leftarrow \lambda_{01}}(\vec{\boldsymbol{\xi}}_2, \Delta t; \vec{\boldsymbol{\xi}}_0, 0) =
$$
$$
- i(2\pi)^2 f_{(01)} f_{(12)} \int_{0<t_1<\Delta t} dt_1 \, \frac{d}{d\tilde{j}_1} \left[ \det(U^{-1}) \, e^{-\frac{1}{2}\vec{\xi}_0^\top A_{(01)} \vec{\xi}_0 - \frac{1}{2}\vec{\xi}_2^\top A_{(12)} \vec{\xi}_2 + \frac{1}{2}\vec{J}^\top U^{-1}\vec{J}} \right]_{j_1=0}
$$

$$(3.98a)$$

with

$$
\vec{J} \equiv B_{(01)}\vec{\boldsymbol{\xi}}_0 + B_{(12)}\vec{\boldsymbol{\xi}}_2 \,.
$$

$$(3.98b)$$

Now we compare the exponential in (3.98) to the $N=\infty$ exponential in (3.83), and taking into account the change of basis (3.86), we get

$$
\begin{pmatrix} \tilde{\mathcal{X}}_{\mathrm{y}} & \tilde{Y}_{\mathrm{y}} \\ \tilde{Y}_{\mathrm{y}} & \tilde{Z}_{\mathrm{y}} \end{pmatrix} = A_{(01)} - B_{(01)}U^{-1}B_{(01)}, \qquad \begin{pmatrix} \tilde{\mathcal{X}}_{\bar{\mathrm{y}}} & \tilde{Y}_{\bar{\mathrm{y}}} \\ \tilde{Y}_{\bar{\mathrm{y}}} & \tilde{Z}_{\bar{\mathrm{y}}} \end{pmatrix} = \mathfrak{S}^\top (A_{(12)} - B_{(12)}U^{-1}B_{(12)})\mathfrak{S},
$$

$$(3.99a)$$

$$
\begin{pmatrix} \tilde{X}_{\mathrm{y}\bar{\mathrm{y}}} & \tilde{Y}_{\mathrm{y}\bar{\mathrm{y}}} \\ \tilde{\bar{Y}}_{\mathrm{y}\bar{\mathrm{y}}} & \tilde{Z}_{\mathrm{y}\bar{\mathrm{y}}} \end{pmatrix} = B_{(01)}U^{-1}B_{(12)}\mathfrak{S}.
$$

$$(3.99b)$$

Also, as before, the $\mathcal{X}$'s are related to the $X$'s by (3.84). The analog of (3.92) is then

$$
\delta^2 \left[ \frac{d\Gamma}{dx\,dy} \right]_{xy\bar{y}\bar{x}}^{\delta T \text{ or } \delta^2 T} = i \frac{C_A^2 \alpha_s^2 M_i M_f}{8\pi^2 (x_1+x_4)^2 E^4} \sum_{\substack{\text{allowed} \\ \lambda_{01}, \lambda_{12}}} \Phi_{\lambda_{01}, \lambda_{12}} \int_{0<t_1<\Delta t} dt_1 \, d(\Delta t) \, (2\pi)^2 f_{(01)} f_{(12)}
$$

$$
\times \frac{d}{dj_1} \Big[ \det(U^{-1}) \Big\{ (\beta \tilde{Y}_y \tilde{Y}_{\bar{y}} + \alpha \tilde{\overline{Y}}_{y\bar{y}} \tilde{Y}_{y\bar{y}}) \tilde{I}_0 + (\alpha + \beta + 2\gamma) \tilde{Z}_{y\bar{y}} \tilde{I}_1
$$

$$
+ \big[ (\alpha + \gamma) \tilde{Y}_y \tilde{Y}_{\bar{y}} + (\beta + \gamma) \tilde{\overline{Y}}_{y\bar{y}} \tilde{Y}_{y\bar{y}} \big] \tilde{I}_2
$$

$$
- (\alpha + \beta + \gamma)(\tilde{\overline{Y}}_{y\bar{y}} \tilde{Y}_{\bar{y}} \tilde{I}_3 + \tilde{Y}_y \tilde{Y}_{y\bar{y}} \tilde{I}_4) \Big\} \Big]_{j_1=0} ,
$$

$$
(3.100)
$$

where the $(\tilde{X}, \tilde{Y}, \tilde{Z})$'s are now those determined by (3.99) and the $\Phi_{\lambda_{01}, \lambda_{12}}$ is a normalization factor we discuss below.

We will take

$$
R_1 = R^{(\delta T)} \tag{3.101}
$$

in the definition (3.97) of $U$ for all the single $\delta V$ processes summarized in table 3.2. Since we are using (3.101) for $\delta^2 T$ as well as $\delta T$ perturbations, this will change the normalization as we will see later.

Acting with $\partial/\partial j_1 [\cdots]_{j_1=0}$ in (3.100) was constructed to introduce one factor of $\frac{1}{2} \vec{\xi}_1^{\top} R_1 \vec{\xi}_1$ (unexponentiated) into the calculation of the overall result. $\delta^2 T$ matrix elements relevant to the transitions in table 3.2 all have value $1/2N^2$ as we see in (3.17). On the other hand, the non-zero matrix elements of $\delta T$ in (3.17) are all $1/\sqrt{2}\,N$. We can correct for this difference by multiplying by the overall factor $\Phi$ in (3.100) which

| transition | equivalent | $\Phi$ |
|---|---|---|
| $\lvert A_-\rangle \xrightarrow{\delta^2 T} \lvert A^\times\rangle$ | $(1234) \to (1243)$ | $\frac{1}{\sqrt{2}\,N}$ |
| $\lvert A_+\rangle \xrightarrow{\delta^2 T} \lvert A^\times\rangle$ | $(1324) \to (1243)$ | $\frac{1}{\sqrt{2}\,N}$ |
| $\lvert A_-\rangle \xrightarrow{\delta T} \lvert 1\rangle$ | $(1234) \to (14)(23)$ | $\frac{-2}{\sqrt{2}\,N}$ |
| $\lvert A_-\rangle \xrightarrow{\delta T} \lvert 1^\times_-\rangle$ | $(1234) \to (12)(34)$ | $\frac{1}{\sqrt{2}\,N}$ |
| $\lvert A_+\rangle \xrightarrow{\delta T} \lvert 1\rangle$ | $(1324) \to (14)(23)$ | $\frac{-2}{\sqrt{2}\,N}$ |
| $\lvert A_+\rangle \xrightarrow{\delta T} \lvert 1^\times_+\rangle$ | $(1324) \to (13)(24)$ | $\frac{1}{\sqrt{2}\,N}$ |

Table 3.2: The last group of transition sequences from table 3.1, along with the corresponding factor $\Phi$ appearing in (3.100).

contain (among other things) a factor of

$$
\begin{cases}
1, & \text{for } \delta T \text{ transition;} \\[2mm]
\frac{1}{\sqrt{2}\,N}, & \text{for } \delta^2 T \text{ transition.}
\end{cases}
\tag{3.102}
$$

Our starting point, the $N{=}\infty$ result, implicitly contains an initial and final color singlet overlap factor (3.94), which equals the similar overlap factors $_s\langle A_{\mathrm{aa}}\lvert\lambda_{23}\rangle\langle\lambda_{01}\lvert A_{\mathrm{aa}}\rangle_u$ needed for both $\delta T\,\delta T$ and $\delta T\,\delta S$ transition sequences. We see in the "color overlap" column of table 3.1 that they are different for some of the other transition sequences. We will need to account for this in the overall normalization in (3.100). Using this together with (3.102), the correct overall normalization factor we need in (3.100) is

$$
\begin{aligned}
\Phi_{\lambda_{01},\lambda_{12}} &\equiv \frac{_s\langle A_{\mathrm{aa}}\lvert\lambda_{12}\rangle\langle\lambda_{01}\lvert A_{\mathrm{aa}}\rangle_u}{_s\langle A_{\mathrm{aa}}\lvert A_-\rangle\langle A_-\lvert A_{\mathrm{aa}}\rangle_u} \times \frac{\delta T \text{ or } \delta^2 T \text{ matrix element}}{\text{non-zero } \delta T \text{ matrix elements}} \\[3mm]
&= 2\,_s\langle A_{\mathrm{aa}}\lvert\lambda_{12}\rangle\langle\lambda_{01}\lvert A_{\mathrm{aa}}\rangle_u \times
\begin{cases}
1, & \text{for } \delta T \text{ transition;} \\[2mm]
\frac{1}{\sqrt{2}\,N}, & \text{for } \delta^2 T \text{ transition.}
\end{cases}
\end{aligned}
\tag{3.103}
$$

The values of $\Phi$ are shown explicitly in Table 3.2. (They are the same as $\sqrt{2}\,N\phi$, where $\phi$ is the last column of table 3.1.)

We note that the $1/N^2$ behavior of (3.100) comes from two places: One factor of $1/N$ comes from the factor $R_1 = R^{(\delta T)}$ (3.29) produced by the operation $\partial/\partial j_1[\cdots]_{j_1=0}$, and the other comes from the values of $\Phi$ in table 3.2.

### 3.4.4 Correction to total crossed diagram rate

Now we collect all the pieces. The $1/N^2$ correction to the $xy\bar{y}\bar{x}$ diagram corresponds to the sum of the results of (3.92) and (3.100), each using the formulas for the $(\tilde{X}, \tilde{Y}, \tilde{Z})$'s appropriate to that particular process $[(3.88)$ or $(3.99)]$ and each summed over the relevant entries of table 3.1. To connect with the $N=\infty$ result, we will call the total $\Delta t$ integrand for the $xy\bar{y}\bar{x}$ diagram $\delta^2 C$:

$$\int_0^\infty d(\Delta t)\,\delta^2 C(x_1, x_2, x_3, x_4, \alpha, \beta, \gamma, \Delta t) \equiv \delta^2 \left[\frac{d\Gamma}{dx\,dy}\right]_{xy\bar{y}\bar{x}}^{(\delta V)^2} + \delta^2 \left[\frac{d\Gamma}{dx\,dy}\right]_{xy\bar{y}\bar{x}}^{\delta T \text{ or } \delta^2 T}.$$
$$(3.104)$$

We will follow the same steps as was shown in the $N=\infty$ calculation in ref. [34]. The total rate was organized by first summing over the diagrams represented by fig. 3.14 to get

$$\delta^2 A(x, y) \equiv \int_0^\infty d(\Delta t)\,2\,\mathrm{Re}\big[\delta^2 B(x, y, \Delta t) + \delta^2 B(y, x, \Delta t)\big] \qquad (3.105)$$

Figure 3.14: The sum of diagrams that define the quantity $A(x, y)$ in ref. [34].

with

$$\delta^2 B(x, y, \Delta t) \equiv \delta^2 C(-1, y, z, x, \alpha, \beta, \gamma, \Delta t) + \delta^2 C\big(-(1-y), -y, 1-x, x, \beta, \alpha, \gamma, \Delta t\big)$$

$$+ \delta^2 C\big(-y, -(1-y), x, 1-x, \gamma, \alpha, \beta, \Delta t\big), \tag{3.106}$$

where we've used the same notation $(A, B, C)$ as ref. [34].[33] At the end, we sum over all permutations of the daughters $(x, y, z)$ that lead to new diagrams. Just as in the $N=\infty$ analysis of ref. [34], this gives[34]

$$\delta^2 \left[ \frac{d\Gamma}{dx\, dy} \right]_{\text{crossed}} = \delta^2 A(x, y) + \delta^2 A(z, y) + \delta^2 A(x, z). \tag{3.107}$$

----

[33]See eqs. (8.1–8.3) of ref. [34]. But, for the $1/N^2$ term corrections being considered here, there are no additional "pole" terms, as previously discussed in footnote 17. For the same reason, it is also unnecessary to make the vacuum subtraction of eq. (8.4) of ref. [34].

[34]See eq. (8.1) of ref. [34].

## 3.5 Numerical results

### 3.5.1 Main results

The $1/N^2$ corrections can be obtained by numerically integrating over $(t_1, t_2, \Delta t)$ or $(t_1, \Delta t)$. In contrast, the $N{=}\infty$ results only require numerical integration over $\Delta t$.[35] Dividing the $1/N^2$ corrections by the corresponding $N{=}\infty$ result gives the relative size of the corrections. In appendix B.2, we discuss our numerical methods.

In figs. 3.15 and 3.16, we show the relative size of $1/N^2$ corrections to crossed and sequential diagrams for overlapping double splitting $g{\to}ggg$ for $N{=}3$ (QCD). In these plots, $y$ represent the energy fraction of the lowest-energy daughter, $x$ represent the next lowest, and then $z = 1{-}x{-}y$ represents the highest-energy daughter. So we restricted the plot to the region $y < x < 1{-}x{-}y$. We see that the $1/N^2$ corrections to sequential diagrams are very small: less than 1%. The corrections to the crossed diagram are relatively larger. The largest relative correction occurs at the apex of the triangular region, $(x, y, z) = (\frac{1}{3}, \frac{1}{3}, \frac{1}{3})$, where the correction is roughly 17%.

We showed the ratio of the crossed and sequential diagram separately because there is a subtlety to discussing relative corrections to the total rate (crossed plus sequential).[36] Fig. 3.17 shows a plot of the ratio

$$\frac{\text{total } 1/N^2 \text{ correction}}{\text{total } N{=}\infty \text{ rate}} \tag{3.108}$$

for $g \to ggg$, but restricted to $y > 0.1$. Similar to fig. 3.15, there is a (local) maximum

---

[35]The $N{=}\infty$ results for crossed and sequential diagrams were derived in refs. [34, 37, 39], but a convenient summary of results may be found in appendix A.2 of ref. [47].

[36]As discussed at the very end of the introduction to chapter 3, our "total" here, defined as the sum of crossed and sequential diagrams, does not quite contain every process that contributes to $g{\to}ggg$.
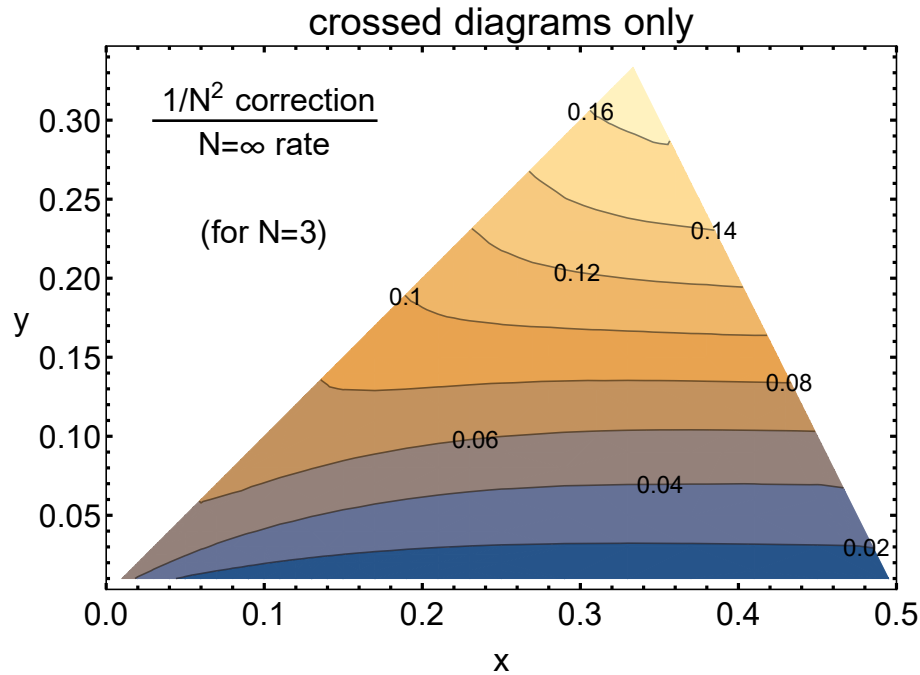
Figure 3.15: The ratio, for *crossed diagrams* only, of (i) the $1/N^2$ correction to (ii) the $N=\infty$ result for the differential rate $d\Gamma/dx\,dy$ for (the crossed diagram contribution to) overlapping double splitting $g \to ggg$. We have used $N=3$ in this plot, but one may multiply the results by $(3/N)^2$ to restore the $N$ dependence of the $1/N^2$ correction. Very tiny wiggles in the contour lines are an artifact of interpolation from a discrete set of numerical data points. We have left out $y < 0.01$ just to simplify the numerical effort that went into making this plot. The ratio goes to zero as $y\to 0$, as one may see from the later discussion of fig. 3.19 for a particular value of $x$.

at the apex of the triangular region, where the $1/N^2$ correction is roughly 17%. Unlike fig. 3.15, however, around $y \sim 0.1$ the rate has started to grow with decreasing $y$. As we will explain, this small-$y$ growth is an artifact of how we have so far chosen to look at the size of $1/N^2$ corrections.

Instead of showing the ratio (3.108), fig. 3.18 shows for a particular value of $x$, the small-$y$ behavior of (i) the $N=\infty$ result for the total rate vs. (ii) the sum of the $N=\infty$ result and the $1/N^2$ correction. We have chosen $x = 0.37$, which corresponds to the
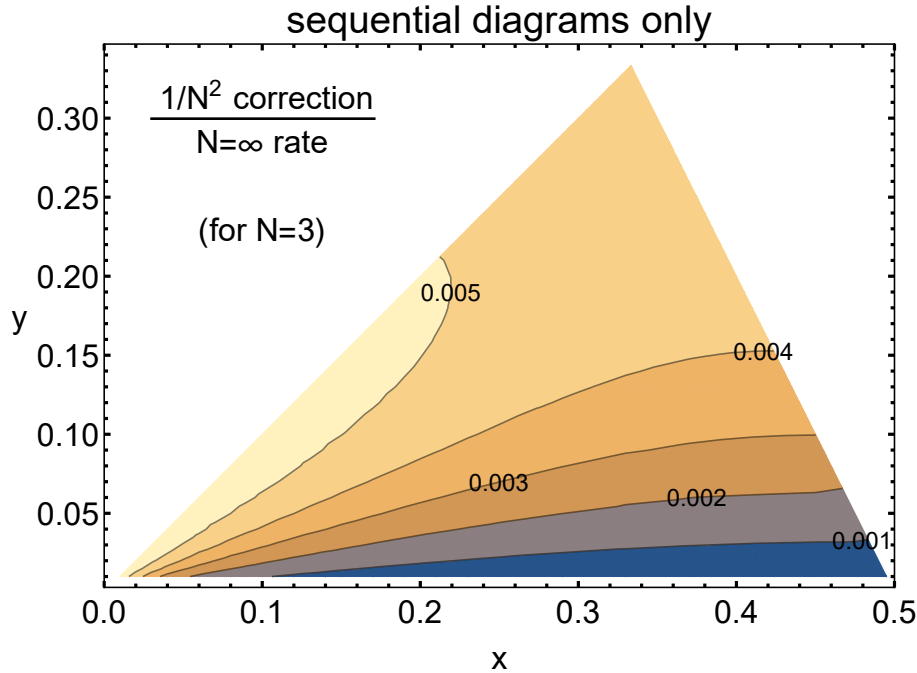
Figure 3.16:   Like fig. 3.15 except now for *sequential diagrams* instead of crossed diagrams.

blue dashed line in fig. 3.17.[37] Since the $N{=}\infty$ results and the total $1/N^2$ correction blow up[38] at small $y$ as $1/y^{3/2}$, we have followed the convention of ref. [37] and instead plotted

$$\pi^2 x y^{3/2} \left[ \Delta \frac{d\Gamma}{dx\,dy} \right]_{\text{total}} \tag{3.109}$$

in fig. 3.18.   The small $y$ values would not be relevant in any real-world physics because, at the very least, one needs $yE \gg T$ for our high-energy approximations.[39] However, it is still instructive to understand the behaviour of our formulas in the small $y$ limit. First, note that the total $N{=}\infty$ result crosses zero at $y \sim 0.01$ (for this value of $x$). This could happen because $\Delta\Gamma/dx\,dy$ does not represent a rate; it represents

---

[37]There is nothing special about the specific choice $x = 0.37$.

[38]For a hand-waving qualitative explanation, see section 1.4 of ref. [37].

[39]There's additionally the issue that, for small enough $y$, one would need to implement resummation of soft radiation.
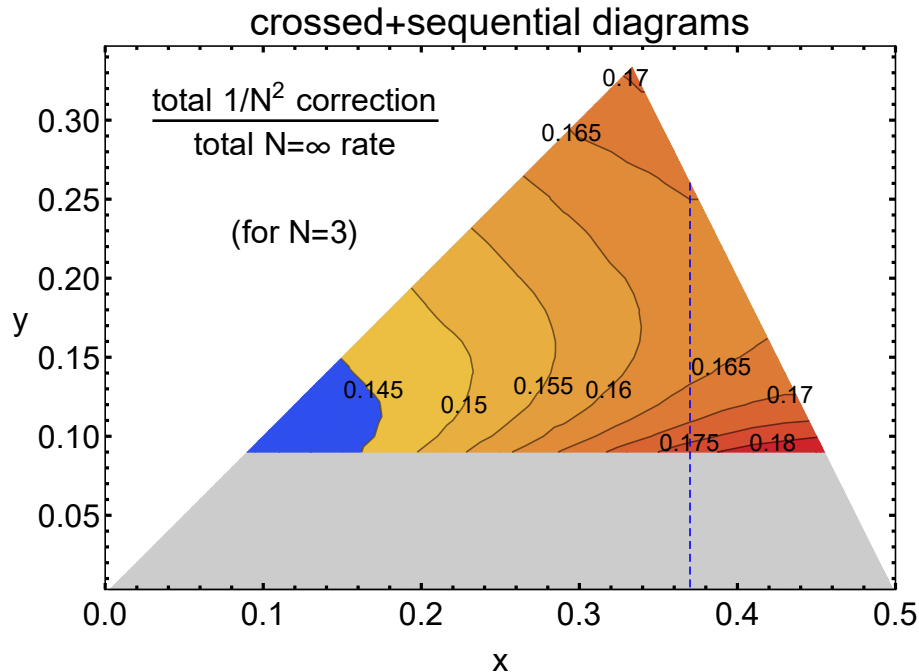
Figure 3.17: Like figs. 3.15 and 3.16 except now for the total $g \to ggg$ rate. The behavior for y<0.1 (the gray shaded region) is discussed in the main text.

the correction to a rate due to overlapping formation times (see section 1.1 of ref. [37] for explanation),[40] and a correction may be positive or negative. So, it makes sense that the relative size (3.108) of the $1/N^2$ correction to that $N=\infty$ result will blow up to infinity when the $N=\infty$ result vanishes. We show in fig. 3.18 that there is little difference between the $N=\infty$ curve and the corrected curve for $y < 0.1$. Also, in applications to energy loss and in-medium shower development, the $1/y^{3/2}$ small-$y$ behavior of overlapping double splitting $g \to ggg$ is canceled [47] by similar behavior of virtual corrections to single splitting $g \to gg$, leaving behind double-log divergences [35, 32, 33] that are *independent* of $N$. So the small-$y$ behavior of fig. 3.18, and in

---

[40]Readers may wonder if one could instead divide the $1/N^2$ corrections by a positive *complete* $g \to ggg$ rate instead of dividing by just the (varying sign) *correction* $\Delta\Gamma/dx\,dy$ from overlap effects. Section 1.1 of ref. [37] explains why it is not meaningful to talk about such a "complete" rate of double splitting in an infinite medium. It has to do with the fact that one way to achieve $g \to ggg$ is via two independent single emissions $g \to gg$ that are arbitrarily far separated in time.

particular the $1/N^2$ corrections to the small-$y$ behavior, are not of much physical interest.[41] Moreover, we only wanted to study the $1/N^2$ corrections to overlapping hard splittings ($y \sim x \sim 1$).

In principle, one should report the relative size of the effect of the $1/N^2$ corrections on an (infrared-safe) characteristic of in-medium shower development, which would require also computing virtual diagrams. Since we do not have the $1/N^2$ corrections for virtual diagrams, we take our results in fig. 3.18 to mean that a reasonable proxy is the largest relative size of the $1/N^2$ corrections to $d\Gamma/dx\,dy$ for $y$ values that are not small, namely the roughly 17% correction at the apex of fig. 3.17.

## 3.5.2   More detail on small-$y$ behavior of crossed vs. sequential

We will discuss now some qualitative features about the small-$y$ behavior of sequential vs. crosses diagrams. In fig. 3.19, we see the different parts that went into the small-$y$ numerics of fig. 3.18.

In ref. [37], it was shown that the $N{=}\infty$ crossed and sequential results individually behave like $\ln(y^{-1})/y^{3/2}$ even though their sum just behaves like $1/y^{3/2}$, and so we

---

[41]The "double log" behavior referred to above arises from $y^{-1}\ln y$ behavior in the combined real and virtual rates, producing a double logarithm when integrated over $y$. This is in contrast to the more divergent $y^{-3/2}$ infrared behavior shown in fig. 3.18 for the real rate by itself. The fact that the soft behavior is $y^{-1}\ln y$ when virtual corrections to single splitting are included has been known since the early work of refs. [35, 32, 33] on energy loss in the soft-$y$ approximation. The lack of $N$ dependence of those double-log results appears in their calculations as a special feature of the dynamics of the soft gluon emission limit. (An explicit calculation showing in detail the cancellation of $y^{-3/2}$ divergences between real and virtual diagrams for the case $N{=}\infty$ may be found in ref. [47], which is focused on generic-$y$ results but also extracts their small-$y$ behavior.)
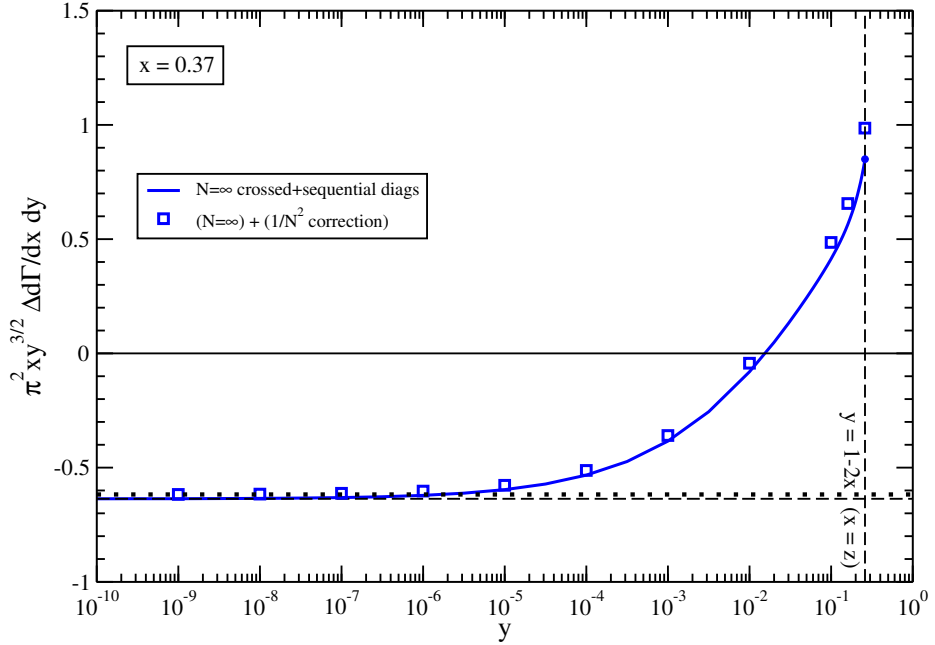
Figure 3.18: A plot for $x = 0.37$ of the $y$ dependence of the total $\Delta\, d\Gamma/dx\, dy$, multiplied by $\pi^2 xy^{3/2}$ [and in units of $N\alpha_s\sqrt{\hat{q}_A/E}$, but remember that $N\alpha_s$ is held fixed as $N{\to}\infty$]. The plot shows (solid curve) the $N{=}\infty$ value and (squares) the $N{=}\infty$ value plus the $1/N^2$ correction. The horizontal dashed line shows the limiting $y{\to}0$ behavior of the $N{=}\infty$ result, and the nearby horizontal dotted line shows the limiting behavior of the corrected result.

chose to plot the contributions to

$$\frac{\pi^2 xy^{3/2}}{\ln(y^{-1})}\left[\Delta\frac{d\Gamma}{dx\,dy}\right] \tag{3.110}$$

here instead of the normalization (3.109) used for fig. 3.18 because the individual contributions have this log dependence.

Note that the absolute size of the $1/N^2$ correction to sequential diagrams (green circles in fig. 3.19) is quite small compared to that for crossed diagrams (blue diamonds). This means that the total $1/N^2$ correction is dominated by crossed diagrams. However, sequential diagrams are still important, as we saw in fig. 3.18, because they
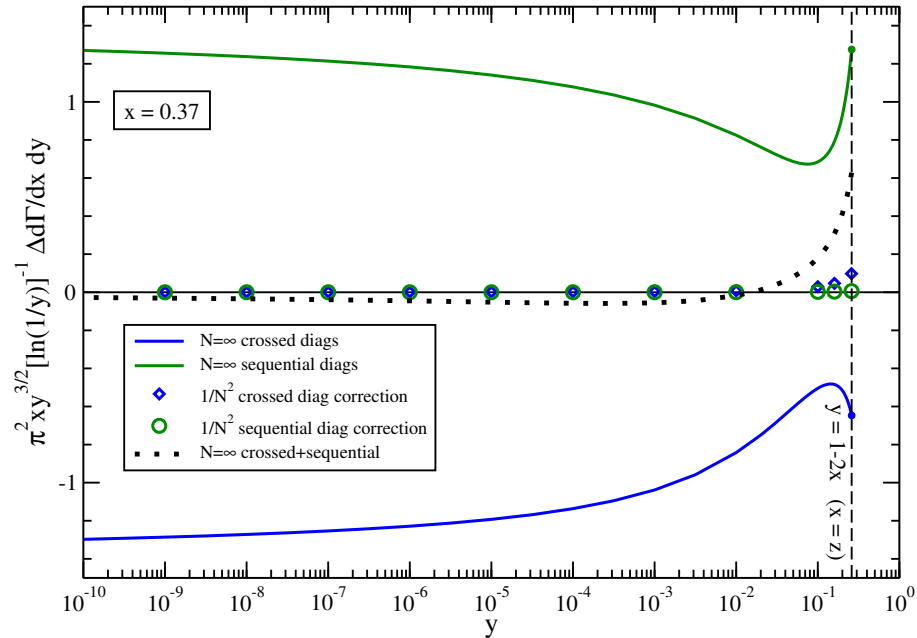
Figure 3.19: A plot for $x = 0.37$ of the $y$ dependence of the different contributions to $\Delta\, d\Gamma/dx\, dy$, multiplied by $\pi^2 xy^{3/2}$ and then divided by $\ln(y^{-1})$. The dotted line shows the total crossed+sequential $N{=}\infty$ result, corresponding to the solid curve in fig. 3.18. Note that the vertical axis is normalized differently here than in fig. 3.18, but still presented in units of $N\alpha_{\mathrm{s}}\sqrt{\hat{q}_{\mathrm{A}}/E}$. [The intended purpose of this plot is qualitative. See fig. 3.20 if interested in the precise values corresponding to the $1/N^2$ data points.]

affect the $N{=}\infty$ denominator of (3.108) even though they do not affect the $1/N^2$ numerator.

Fig. 3.20 shows that the crossed and sequential $1/N^2$ corrections are different in another way as well. We find numerically that the crossed diagram correction behaves like $1/y^{3/2}$ for small $y$, with no $\ln(y^{-1})$ enhancement. So, we see that the corresponding blue diamonds in fig. 3.19 approach zero, because of the additional normalization factor $1/\ln(y^{-1})$ in that plot. On the other hand, the sequential diagram correction has a milder dependence on small $y$, behaving like $1/y^{1/2}$. This means that the $1/N^2$ correction from crossed diagrams will contribute to infrared (IR) divergences (simi-
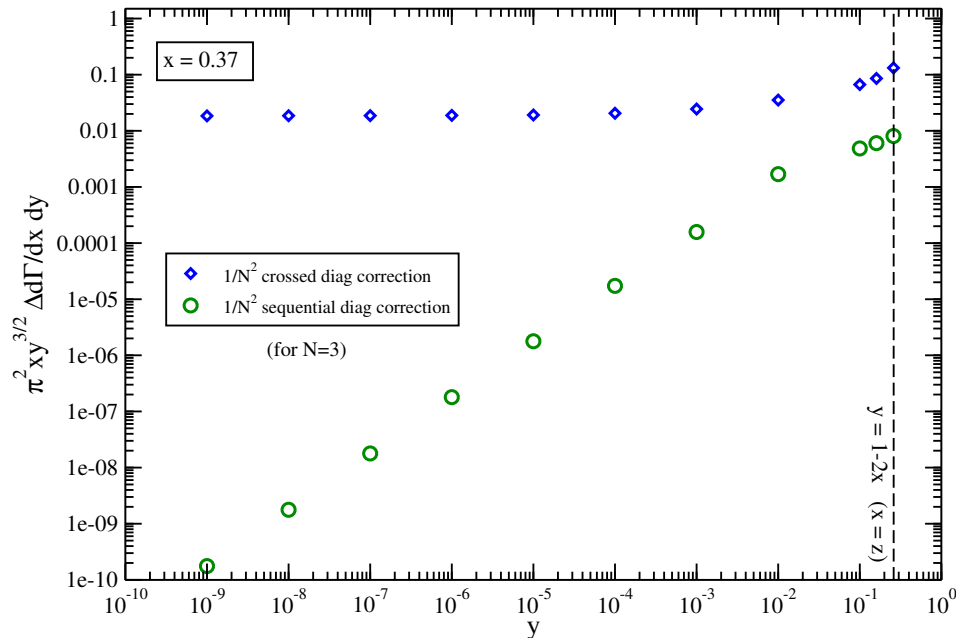
Figure 3.20: A plot for $x = 0.37$ of the $y$ dependence of the different $1/N^2$ contributions to $\Delta\,d\Gamma/dx\,dy$, multiplied by $\pi^2 xy^{3/2}$ as in fig. 3.18. Note that, in contrast to fig. 3.19, we have not divided by $1/\ln(1/y)$.

lar to the IR divergences of the $N=\infty$ results discussed in ref. [47]), but the $1/N^2$ correction from sequential diagrams will be IR finite when we integrate over $y$ in applications.

### 3.5.3 Comparison of size of $1/N^2$ corrections to related work

In our work here, we have only considered the problem of overlapping formation times for the double splitting process $g \to ggg$. We have followed the previous $N=\infty$ work on this problem [34, 37, 47] and only considered rates $\Delta\,d\Gamma/dx\,dy$ that have been integrated over the (small) transverse momenta $\boldsymbol{p}_\perp$ of all three daughters. Studying $\boldsymbol{p}_\perp$-integrated rates allows one to ignore what happens to any daughter after it has

been emitted in both the amplitude and conjugate amplitude.[42] This is why the dynamics of the $y$ gluon is no longer relevant after the first conjugate-amplitude (red) vertex in fig. 3.3 for $xy\bar{y}\bar{x}$ interference diagram. Another type of problem where similar issues of 4-gluon color-singlet dynamics also arise: the *un*-integrated $\boldsymbol{p}_\perp$ distribution $d\Gamma/dx\, d^2p_\perp$ for *single* splitting $g{\to}gg$ in the medium. The difference from fig. 3.1 for the $\boldsymbol{p}_\perp$-integrated $g{\to}gg$ rate is that one must instead follow the color dynamics for a time after the splitting has taken place in both amplitude and conjugate amplitude, corresponding to the shaded region of fig. 3.21. So, one must treat the color dynamics of the four gluons shown in the shaded region.[43] Refs. [19, 45, 46] have studied how to treat this problem beyond the $N{=}\infty$ limit. However, their calculations approximate the trajectories of the high-energy particles as perfectly straight lines, and so they only include color dynamics and not the dynamics of particle trajectories. In this geometry approximation (also known as the "antenna"approximation), they are able to more easily treat finite or expanding media.

What is interesting about ref. [46] is their explicit calculation of the $1/N^2$ correction to the $N{=}\infty$ limit (using a different approach to calculate $1/N^2$ corrections than we have). In their numerics, they study a medium of length $L$ with constant $\hat{q}$, and so their results will depend on $L$. They also study the case where the dimensionless ratio $L\sqrt{\hat{q}/E}$ (which parametrically is the ratio of $L$ to what the formation length $L_\mathrm{f}$ would be in an infinite medium) is $\simeq 0.55$. Given all that, they found that the $1/N^2$ correction to the $N{=}\infty$ distribution for $g{\to}gg$ can be as large as 16%. One should be careful in taking this comparison seriously, however, since (i) the process we study is very different, and (ii) their numerics hold quark $\hat{q}_\mathrm{F}$ fixed as they vary $N$, whereas

---

[42]See, for example, the argument in section 4.1 of ref. [34].

[43]The color dynamics of the two daughters decouple after a time of order the formation time, often referred to in this context as the color decoherence time.
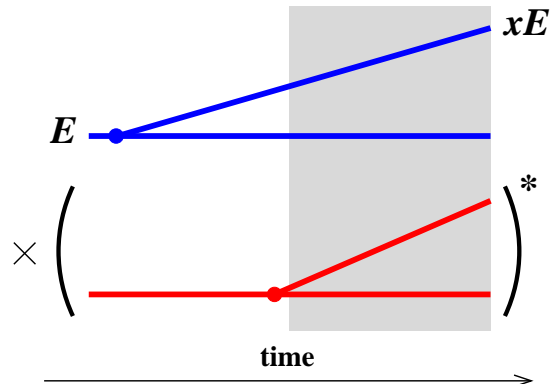
Figure 3.21: Similar to fig. 3.1a for the rate of single splitting $g{\to}gg$, but here including later time-evolution of the daughters (shaded region) that must be included in order to study the $\boldsymbol{p}_\perp$ distribution of the daughters. In the shaded region, the above interference term contains four gluon lines which, in the language we have used in this chapter, requires treating 4-gluon color singlet dynamics in the medium.

we hold gluon $\hat{q}_{\mathrm{A}}$ fixed.

## 3.6   Conclusion

We have found that, with two caveats, $1/N^2$ corrections to $N{=}\infty$ results for overlapping double gluon splitting ($g \to ggg$) can be as large as approximately 17% for $N{=}3$ (QCD). The first caveat is the one explained in section 3.5.1 that measurements of relative corrections become meaningless when the leading ($N{=}\infty$) answer goes through zero at small $y \sim 0.01$, and so we have focused on the size of corrections for not-small $y$. We note also that the small-$y$ emission limit is not a case where large-$N$ techniques were necessary to simplify the problem, because previous work on overlapping formation times with a soft emission [35, 32, 33] (which included the effects of virtual emissions) was done without using the large-$N$ approximation. So we were interested in estimating the reliability of using $N{=}\infty$ results specifically for the case where $y$ is not small.

The second caveat is we have not included other diagrammatic contributions to $g{\to}ggg$ that involve 4-gluon vertices nor, in Light-Cone Perturbation Theory, instantaneous longitudinal gluon exchange. However, our take-away is that the $N{=}\infty$ limit taken in previous analysis is likely a moderately good approximation. Ultimately, a complete analysis of $1/N^2$ effects on energy loss should also include calculation of virtual diagrams for $g \to gg$, as discussed for $N{=}\infty$ in ref. [47].

One may want to calculate the virtual diagrams through order $1/N^2$ for better understanding of soft radiative corrections to hard single splitting $g{\to} gg$. These radiative corrections give rise to IR double logarithms [35, 32, 33] and sub-leading IR single logarithms. The single logarithms have been calculated for $N{=}\infty$ (for infinite medium in the $\hat{q}$ approximation) in refs. [51, 48]. We cannot conclude whether the single logarithms have any non-trivial dependence on $N$.

Finally, we note that our roughly 17% corrections for $N{=}3$ are roughly consistent with (e.g. within a factor of 2 of) the naive guess of $O(1/N^2) \sim 10\%$.

# Appendices

# Appendix A

# Chapter 2 appendices

In appendix A , we show all the relevant appendices to chapter 2.

## A.1 NLO rates in terms of the $\overline{\text{NLO}}$ formulas of ref. [47]

The NLO rates used in subsection 1.3.3 are given in refs. [47, 52] (and in particular appendix A of each). The rate formulas there are called $\overline{\text{NLO}}$ rates, and so we will try to show the difference between the various NLO rates used in chapter 2 and the $\overline{\text{NLO}}$ rate formulas given in refs. [47, 52].

The difference is essentially whether you separate the renormalization scale dependence $\mu$ from the rest of the NLO $g{\to}gg$ rate or not. Writting,

$$\left[\Delta\frac{d\Gamma}{dx}\right]^{\text{NLO}}_{g\to gg} = \left[\Delta\frac{d\Gamma}{dx}\right]^{\overline{\text{NLO}}}_{g\to gg} + \left[\frac{d\Gamma}{dx}\right]_{\text{ren log}} \tag{A.1}$$

with[1]

$$\left[\frac{d\Gamma}{dx}\right]_{\text{ren log}} \equiv -\frac{\beta_0 \alpha_{\text{s}}}{2}\left[\frac{d\Gamma}{dx}\right]^{\text{LO}}\left[\ln\left(\frac{\mu^2}{|\Omega_0|E}\right) + \ln\left(\frac{x(1-x)}{4}\right) + \gamma_{\text{E}} - \frac{\pi}{4}\right] \tag{A.2}$$

and $\beta_0$ given by our (2.25). Here $\Omega_0$ is the complex frequency associated with the leading-order BDMPS-Z $g\to gg$ splitting rate (1.2), given by

$$\Omega_0 = \sqrt{\frac{-i\hat{q}_{\text{A}}}{2E}\left(-1 + \frac{1}{x} + \frac{1}{1-x}\right)} = \sqrt{\frac{-i(1-x+x^2)\hat{q}_{\text{A}}}{2x(1-x)E}}, \tag{A.3}$$

and $\gamma_{\text{E}}$ is the Euler-Mascheroni constant. Note that the $\ln\mu$ dependence in (A.2) is the same as (2.24).

If we use the $\overline{\text{NLO}}$ rates of refs. [47, 52], our eq. (1.4) is then[2]

$$\left[\Delta\frac{d\Gamma}{dx}\right]^{\text{NLO}}_{g\to gg} = \left(\int_0^{1-x} dy \left[\Delta\frac{d\Gamma}{dx\,dy}\right]_{\text{virt I}}\right) + (x\to 1-x)$$
$$+ \int_0^1 dy \left[\Delta\frac{d\Gamma}{dx\,dy}\right]_{\text{virt II}} + \left[\frac{d\Gamma}{dx}\right]_{\text{ren log}}, \tag{A.4}$$

where $[\Delta\,d\Gamma/dx\,dy]_{\text{virt I}}$ and $[\Delta\,d\Gamma/dx\,dy]_{\text{virt II}}$ is the notation in those references for the $\overline{\text{NLO}}$ versions of what we call $[\Delta\,d\Gamma/dx\,dy]^{\text{NLO}}_{\text{class I}}$ and $[\Delta\,d\Gamma/dx\,dy]^{\text{NLO}}_{\text{class II}}$ in chapter 2. Similarly, eqs. (2.9), (2.10), and (2.17) can be written in terms of the rates in refs.

---

[1]Above, eqs. (A.1) and (A.3) corresponds to eqs. (A.49) and (A.4) of ref. [47]. Eq. (A.2) above is a slight rewriting of eq. (A.50) of ref. [47]. For that, we've used eqs. (A.6) and (A.7) of ref. [47], and we've also used the fact that $\Omega_0 = e^{-i\pi/4}|\Omega_0|$ to rewrite $\text{Re}\big(i\Omega_0\ln(1/\Omega_0)\big) = \text{Re}\big(i\Omega_0\big)\big[\ln(1/|\Omega_0|) - \frac{\pi}{4}\big]$.

[2]Eq. (A.4) above is just the combination of eqs. (A.47–49) and (A.52) of ref. [47] for the case of renormalized rates.

[47, 52], as[3]

$$\left[\frac{d\Gamma}{dx}\right]^{\mathrm{NLO}}_{\mathrm{net}} = \left[\frac{d\Gamma}{dx}\right]_{\mathrm{ren\,log}} + \left[\frac{d\Gamma}{dx}\right]^{\overline{\mathrm{NLO}}}_{\mathrm{net}}$$

$$= \left[\frac{d\Gamma}{dx}\right]_{\mathrm{ren\,log}} + \int_0^{1/2} dy \left\{ v(x,y)\,\theta(y < \tfrac{1-x}{2}) + v(1{-}x,y)\,\theta(y < \tfrac{x}{2}) \right.$$

$$\left. + r(x,y)\,\theta(y < \tfrac{1-x}{2}) \right\},$$

$$(A.5)$$

$$v(x,y) \equiv \left( \left[\Delta\frac{d\Gamma}{dx\,dy}\right]_{\mathrm{virt\,I}} + \left[\Delta\frac{d\Gamma}{dx\,dy}\right]_{\mathrm{virt\,II}} \right) + (y \leftrightarrow 1{-}x{-}y), \qquad (A.6a)$$

$$r(x,y) \equiv \left[\Delta\frac{d\Gamma}{dx\,dy}\right]_{g\to ggg}, \qquad (A.6b)$$

and, most importantly,

$$\left[\frac{d\Gamma}{dx}\right]^{\mathrm{NLO,fac}}_{\mathrm{net}} \equiv \left[\frac{d\Gamma}{dx}\right]_{\mathrm{ren\,log}} + \int_0^\infty dy \left\{ v(x,y)\,\theta(y < \tfrac{1-x}{2}) + v(1{-}x,y)\,\theta(y < \tfrac{x}{2}) \right.$$

$$\left. + r(x,y)\,\theta(y < \tfrac{1-x}{2}) + \frac{C_A\alpha_s}{4\pi}\left[\frac{d\Gamma}{dx}\right]^{\mathrm{LO}}\frac{\ln y + \bar{s}(x)}{y}\,\theta(yE < \Lambda_{\mathrm{fac}}) \right\}. \quad (A.7)$$

The last thing to note is that the formulas of $[\Delta\,d\Gamma/dx\,dy]_{g\to ggg}$, $[\Delta\,d\Gamma/dx\,dy]_{\mathrm{virt\,I}}$, and $[\Delta\,d\Gamma/dx\,dy]_{\mathrm{virt\,II}}$ in ref. [47] doesn't include the contributions from F diagrams in ref. [52],[4] and so one needs to add them.

---

[3]The $\overline{\mathrm{NLO}}$ rate in (A.5) above is eq. (1.7) of ref. [47]. $v(x,y)$ and $r(x,y)$ are defined as in eq. (1.8) of ref. [47].

[4]Specifically, see eqs. (A.1), (A.18), and (A.19) of ref. [52].

## A.2   Numerical methods

### A.2.1   Computation of $[d\Gamma/dx]^{\mathrm{NLO,fac}}_{\mathrm{net}}$

After the subtraction of the $y$-integrand in A.7, that removed the $y^{-1}\ln y$ and $y^{-1}$ behavior of the integrand at small $y$ (which integrate to the IR double and single log divergences), one is left with a $y^{-1/2}\ln y$ behaviour for small $y$. It is an integrable divergence, but one still needs to make a change of variable from $y$ to $u = y^{1/2}$. Now the integrand behaves as $\ln u$ as $u \to 0$. Then we use Mathematica [59] for computing the $y$-integrand and the $\Delta t$ integrations in the formulas for $[\Delta\, d\Gamma/dx\, dy]_{\mathrm{virt\,I}}$, $[\Delta\, d\Gamma/dx\, dy]_{\mathrm{virt\,II}}$, and $[\Delta\, d\Gamma/dx\, dy]_{g\to ggg}$ presented in refs. [47, 52]. We tried to use the built-in integration methods in Mathematica to do the $u = y^{1/2}$ integrals, however, we were not successful. Instead, we did the $u$-integration by using a simple mid-point Riemann sum over the integration region $u = 0$ to $u_{\max} = [\max(x/2, (1-x)/2, \Lambda_{\mathrm{fac}}/E)]^{1/2}$ where the integrand is non-zero. The error of our method scales $O((\Delta u)^2)$, where $\Delta u$ is the small step size, for smooth functions. However, there are two things that slows down the convergence of our answer: (i) our integrand has discontinuities at the location of the $\theta$ functions in (A.7), and (ii) diverges as $\ln u$ as $u \to 0$. We corrected for (i) by dividing the integral into three regions where there are no discontinuities and did each region separately using a mid-point Riemann sum.[5] For (ii), we numerically extract the coefficient $c$ of the $c\ln u$ behavior as $u \to 0$, and then we correct

---

[5]Alternatively, one can do a single integral over the total integration region and correct the mid-point rule in the steps where discontinuities occur, given that we know exactly where the points of discontinuity are.

the midpoint Riemann sum approximation to

$$\int_0^{u_{\max}} du \, f(u) = -\frac{\Delta u \, \ln 2}{2} c + \sum_{n=1}^{N} \Delta u \, f\big((n - \tfrac{1}{2})\Delta u\big), \tag{A.8}$$

where $\Delta u = u_{\max}/N$. The factor of $\frac{1}{2}\Delta u \ln 2$ in the correction term comes from the identity

$$\lim_{N \to \infty} \left[ \int_0^{N \Delta u} du \, \ln u - \sum_{n=1}^{N} \Delta u \, \ln\big((n - \tfrac{1}{2})\Delta u\big) \right] = -\tfrac{1}{2} \Delta u \, \ln 2. \tag{A.9}$$

Since our integration method is not adaptive, we need to check its numerical convergence with increasing $N$.

## A.2.2  More details on numerical evaluation of $\hat{\epsilon}(\hat{z})$

In the evaluation of equation (2.101) for $\hat{\epsilon}_{\mathrm{LO}}(\hat{z})$, the integral

$$\int_0^1 dx \, x \left[\frac{d\hat{\Gamma}}{dx}\right]^{\mathrm{LO}} \left\{ x^{-1/2} \, \hat{\epsilon}_{\mathrm{LO}}(x^{-1/2}\hat{z}) - \hat{\epsilon}_{\mathrm{LO}}(\hat{z}) \right\} \tag{A.10}$$

has singularities at the end points. However, these are integrable singularities because the integrand scales as $x^{-1/2}$ as $x \to 0$ and $(1 - x)^{-1/2}$ as $x \to 1$. It is numerically efficient to make a change of variable to reduce the singularity. Changing variables to $u = x^{1/2}$ in (A.10) will help $x \to 0$ but won't do anything for $x \to 1$. We can fix this by splitting the integral as

$$\int_0^1 dx \, \cdots = \int_0^{1/2} dx \, \cdots + \int_{1/2}^1 dx \, \cdots, \tag{A.11}$$

then we change the integration variable $x \to 1-x$ in the last integral. Since $[d\Gamma/dx]^{\text{LO}}$ is symmetric under exchange of its two daughters, (A.10) then becomes

$$\int_0^{1/2} dx \left[\frac{d\hat{\Gamma}}{dx}\right]^{\text{LO}} \left(x\left\{x^{-1/2}\,\hat{\epsilon}_{\text{LO}}(x^{-1/2}\hat{z}) - \hat{\epsilon}_{\text{LO}}(\hat{z})\right\}\right.$$
$$\left. + (1-x)\left\{(1-x)^{-1/2}\,\hat{\epsilon}_{\text{LO}}\big((1-x)^{-1/2}\hat{z}\big) - \hat{\epsilon}_{\text{LO}}(\hat{z})\right\}\right). \quad \text{(A.12)}$$

Now we do the change of variable $u = x^{1/2}$ which will remove now the $1/\sqrt{\phantom{x}}$ divergences. We used Mathematica to interpolate the function and then integrated using that interpolation with the discretized representation of $\hat{\epsilon}(\hat{\zeta})$. We can do the same for (2.104) that determines $\delta\hat{\epsilon}(\hat{z})$ except that one must remember that $[d\Gamma/dx]_{\text{net}}$ is *not* symmetric under $x \to 1-x$. The driving term becomes

$$\int_0^1 dx\, x \left[\frac{d\hat{\Gamma}}{dx}\right]_{\text{net}}^{\text{NLO,fac}} \left\{x^{-1/2}\,\hat{\epsilon}_{\text{LO}}(x^{-1/2}\hat{z}) - \hat{\epsilon}_{\text{LO}}(\hat{z})\right\} \quad \text{(A.13)}$$

for that equation should be replaced by,

$$\int_0^{1/2} dx \left(x\left[\frac{d\hat{\Gamma}}{dx}(x)\right]_{\text{net}}^{\text{NLO,fac}} \left\{x^{-1/2}\,\hat{\epsilon}_{\text{LO}}(x^{-1/2}\hat{z}) - \hat{\epsilon}_{\text{LO}}(\hat{z})\right\}\right.$$
$$\left. + (1-x)\left[\frac{d\hat{\Gamma}}{dx}(1-x)\right]_{\text{net}}^{\text{NLO,fac}} \left\{(1-x)^{-1/2}\,\hat{\epsilon}_{\text{LO}}\big((1-x)^{-1/2}\hat{z}\big) - \hat{\epsilon}_{\text{LO}}(\hat{z})\right\}\right), \quad \text{(A.14)}$$

followed by a change of variables to $u = x^{1/2}$.

Fig. A.1 shows our approach to the $\hat{z}_{\text{max}} \to \infty$ limit for the smallest $\Delta\hat{z}$ value of fig. 2.11. This shows that there is no difference between the results for $\hat{z}_{\text{max}} = 10$ and $\hat{z}_{\text{max}} = 20$, and so the value $\hat{z}_{\text{max}} = 20$ used in fig. 2.11 was large enough.
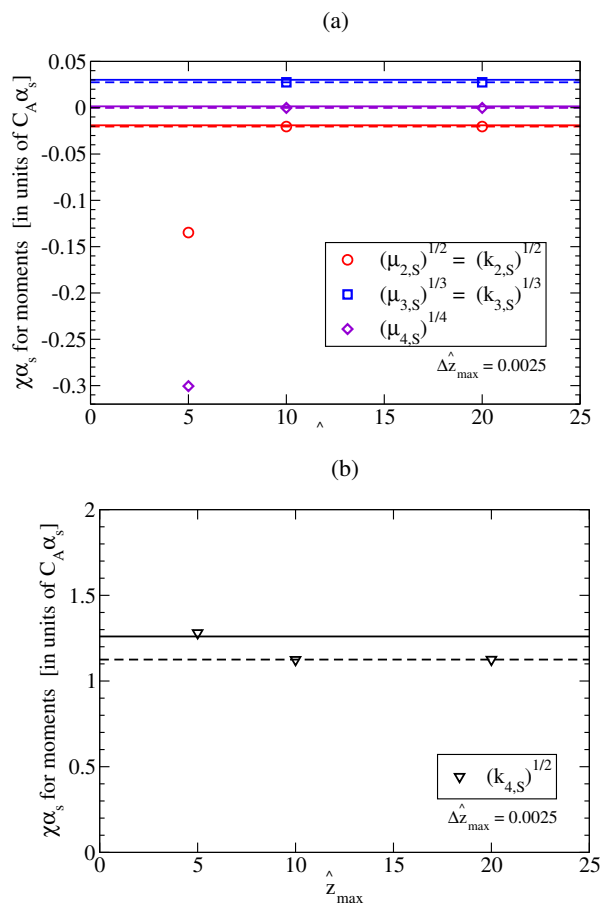
Figure A.1: Like fig. 2.11 but here the data points show the dependence on $\hat{z}_{\max}$ for $\Delta\hat{z} = 0.0025$. The solid horizontal lines again show the results of table 2.3, and their difference with the $(\Delta\hat{z}, \hat{z}_{\max}) = (0.0025, 20)$ data points is the same as that in fig. 2.11, due to the non-zero value of $\Delta\hat{z}$. We've drawn dashed horizontal lines corresponding to the $(\Delta\hat{z}, \hat{z}_{\max}) = (0.0025, 20)$ value to instead emphasize the relevant point for approximating $\hat{z}_{\max} \to \infty$: there is no significant difference between $\hat{z}_{\max} = 10$ and $\hat{z}_{\max} = 20$.

# A.3 More on $\Delta b$ dependence of NLLO resummation

In this appendix, we show that the resummation (2.49) is enough to capture the $\Delta b$ dependence of resummation at next to-leading-log order (NLLO), but is inadequate at the next order (NNLLO). We will ignore the running of $\alpha_s(k_\perp)$, which we argued doesn't affect our conclusions in section 2.2.2.

## A.3.1 Review of LLO resummation

To warm up, we will start by reviewing the leading-log order resummation of LMW [30]. We find it convenient to express the LLO contribution to $\hat{q}_{\text{eff}}$ from $n$-th order in $\alpha_s(\mu)$ as

$$\delta^n \hat{q}(\Delta b) \approx \overline{\alpha}_s^n \hat{q}_{(0)} \tag{A.15}$$

$$\int_{\tau_0}^{\infty} \frac{dt_1}{t_1} \int_{\hat{q}t_1}^{1/(\Delta b)^2} \frac{dk_{\perp 1}^2}{k_{\perp 1}^2} \int_{\tau_0}^{t_1} \frac{dt_2}{t_2} \int_{\hat{q}t_2}^{k_{\perp 1}^2} \frac{dk_{\perp 2}^2}{k_{\perp 2}^2} \cdots \int_{\tau_0}^{t_{n-1}} \frac{dt_n}{t_n} \int_{\hat{q}t_n}^{k_{\perp,n-1}^2} \frac{dk_{\perp n}^2}{k_{\perp n}^2}, \tag{A.16}$$

where in this appendix we use the shorthand notation

$$\overline{\alpha}_s \equiv \frac{C_A \alpha_s}{\pi}. \tag{A.17}$$

In our notation, $(k_{\perp 1}, t_1)$ are the transverse momentum and emission duration[6] of the first soft gluon, $(k_{\perp 2}, t_2)$ are those of an even softer gluon emission, and so forth, with

---

[6]The emission duration $t_1$ is what we called $\Delta t$ in fig. 2.7.

$k_\perp$ ordering

$$\frac{1}{\Delta b} \gg k_{\perp 1} \gg k_{\perp 2} \gg \cdots . \tag{A.18}$$

The first inequality in (A.18) is following the same pattern as the others ($k_{\perp 0} \gg k_{\perp 1}$), because $1/\Delta b$ is the transverse momentum scale ($k_\perp$) associated with the light-like Wilson loop of fig. 2.5 where the first gluon ($k_{\perp 1}$) is emitted. There is also another condition imposed at the leading-log order, softer emissions take place within the duration of harder emissions:

$$t_1 \gg t_2 \gg t_3 \gg \cdots \gg \tau_0. \tag{A.19}$$

The last inequality in (A.19) was implemented in the lower limit of the time integrals and it reflects the breakdown of the $\hat{q}$ approximation when the emission time becomes smaller than the mean free path time $\tau_0$. These constraints were shown in fig. 2.7. For the $k_\perp$ integrals, the lower limit reflects that the transverse momentum kicks accumulated over the duration of an emission will disrupt the vacuum-like logarithms if $\Delta p_\perp$ is as large as the $k_\perp$ of that emission. Note that each double log relies on the nearly-collinear emissions, and so these kicks from the medium disrupts collinearity.

In order to implement the constraints we just discussed, one should understand the $k_\perp$ intergals as setting an upper limit on the corresponding lower limit. For example, the $k_{\perp 1}$ integration sets an upper limit on the $t_1$ integration:

$$t_1 < \frac{1}{\hat{q}(\Delta b)^2}. \tag{A.20}$$

In the LMW paper, the relevant scale for $\Delta b$ was $(\hat{q}L)^{-1/2}$, where $L$ was the length

of the medium traversed:

$$\Delta b \text{ here } \longrightarrow \frac{1}{Q_s} \sim \frac{1}{\sqrt{\hat{q}L}} \text{ in LMW [30].} \tag{A.21}$$

In our application, the scale analogous to $L$ is, parametrically, the formation time for the underlying hard splitting process. For the sake of the argument made in section 2.2, we will keep everything in terms of $\Delta b$.

One can write (A.16) in many different ways, we will provide several for comparison with other papers. In the LMW paper, the authors used the variables[7]

$$\mathfrak{x} \sim \frac{\tau_0}{t} \tag{A.22}$$

in place of our $t$'s. Using this new variable, the formula becomes equivalent to the one presented in the LMW paper:[8]

$$\delta^n \hat{q}(\Delta b) \approx \overline{\alpha}_s^n \hat{q}_{(0)} \int_{\hat{q}\tau_0}^{1/(\Delta b)^2} \frac{dk_{\perp 1}^2}{k_{\perp 1}^2} \int_{\hat{q}\tau_0}^{k_{\perp 1}^2} \frac{dk_{\perp 2}^2}{k_{\perp 2}^2} \cdots \int_{\hat{q}\tau_0}^{k_{\perp,n-1}^2} \frac{dk_{\perp n}^2}{k_{\perp n}^2}$$
$$\times \int_{\hat{q}\tau_0/k_{\perp n}^2}^{1} \frac{d\mathfrak{x}_n}{\mathfrak{x}_n} \cdots \int_{\hat{q}\tau_0/k_{\perp 2}^2}^{\mathfrak{x}_3} \frac{d\mathfrak{x}_2}{\mathfrak{x}_2} \int_{\hat{q}\tau_0/k_{\perp 1}^2}^{\mathfrak{x}_2} \frac{d\mathfrak{x}_1}{\mathfrak{x}_1} . \tag{A.23}$$

In terms of the variables $(t, \omega)$ used in fig. 2.7, use the parametric relation $t \sim \omega/k_\perp^2$

---

[7]LMW represent (A.22) with the symbol $x$. We use $\mathfrak{x}$ here to avoid confusion with our use of $x$ elsewhere in this chapter.

[8]Specifically, see eq. (50) of ref. [30], which only explicitly writes out the example $n{=}2$, and make use of the translation (A.21). Our $\delta^2\hat{q}$ corresponds to their eq. (50) divided by $L$, except that their numbering of the gluons is the reverse of ours, i.e. their $(k_{\perp 1}, \cdots k_{\perp n})$ are our $(k_{\perp n}, \cdots, k_{\perp 1})$ and their $(x_1, \cdots, x_n)$ are our $(\mathfrak{x}_n, \cdots, \mathfrak{x}_1)$. Their $Q_0^2 = \hat{q}\tau_0$.

for the duration of vacuum-like gluon fluctuations,

$$\delta^n \hat{q}(\Delta b) \approx \overline{\alpha}_{\mathrm{s}}^{\,n} \hat{q}_{(0)} \int_{\tau_0}^{\infty} \frac{dt_1}{t_1} \int_{\hat{q}t_1^2}^{t_1/(\Delta b)^2} \frac{d\omega_1}{\omega_1} \int_{\tau_0}^{t_1} \frac{dt_2}{t_2} \int_{\hat{q}t_2^2}^{\omega_1 t_2/t_1} \frac{d\omega_2}{\omega_2}$$
$$\cdots \int_{\tau_0}^{t_{n-1}} \frac{dt_n}{t_n} \int_{\hat{q}t_n^2}^{\omega_{n-1}t_n/t_{n-1}} \frac{d\omega_n}{\omega_n}, \quad \text{(A.24)}$$

where the limits of the $\omega_1$ integration again implicitly set the upper limit (A.20) on $t_1$.

In ref. [31] (which reviews the fixed coupling case as a warm-up), the authors used the variables

$$Y \equiv \ln\left(\frac{t}{\tau_0}\right), \qquad \rho \equiv \ln\left(\frac{k_\perp^2}{\hat{q}\tau_0}\right), \tag{A.25}$$

in terms of which (A.16) can be written

$$\delta^n \hat{q} \approx \overline{\alpha}_{\mathrm{s}}^{\,n} \hat{q}_{(0)} \, f_n\left(\ln\left(\tfrac{1}{\hat{q}\tau_0(\Delta b)^2}\right), \ln\left(\tfrac{1}{\hat{q}\tau_0(\Delta b)^2}\right)\right), \tag{A.26a}$$

where (introducing our own notation "$f_n$")

$$f_n(Y,\rho) \equiv \int_0^Y dY_1 \int_{Y_1}^{\rho} d\rho_1 \int_0^{Y_1} dY_2 \int_{Y_2}^{\rho_1} d\rho_2 \cdots \int_0^{Y_{n-1}} dY_n \int_{Y_n}^{\rho_{n-1}} d\rho_n. \tag{A.26b}$$

We can see from eqs. (A.26) that the LLO result at $n$-th order is just $\overline{\alpha}_{\mathrm{s}}^{\,n} \hat{q}_{(0)}$ times the hyper-volume of the integration region in (A.26). The LMW resummation of all the leading-log $\delta^n \hat{q}$ gives the formula (2.49). Iancu and Triantafyllopoulos [31] give a little more detail, showing that

$$f_n(Y,\rho) = \frac{Y^n \rho^n}{(n!)^2} - \frac{Y^{n+1}\rho^{n-1}}{(n+1)!\,(n-1)!} \qquad (n > 0) \tag{A.27}$$

(which can be proven by induction). If we sum to all orders in $\alpha_s$, we get

$$1 + \sum_{n=1}^{\infty} \overline{\alpha}_s^{\,n} f_n(Y, \rho) = I_0\Big(2\sqrt{\alpha_s Y \rho}\Big) - \frac{Y}{\rho} I_2\Big(2\sqrt{\alpha_s Y \rho}\Big), \qquad (A.28)$$

and setting $Y = \rho = \ln\big(\frac{1}{\hat{q}\tau_0(\Delta b)^2}\big)$ as in (A.26a) then gives (2.49).

## A.3.2  $\Delta b$ dependence of logarithms at $O(\alpha_s)$

We will review some of the qualitative aspects of the double and single logs at $O(\alpha_s)$. The $n = 1$ case of (A.16) gives us the double log approximation:

$$\delta\hat{q}_{\mathrm{eff}}(\Delta b) \approx \overline{\alpha}_s \hat{q}_{(0)} \int_{\tau_0}^{1/\hat{q}(\Delta b)^2} \frac{dt_1}{t_1} \int_{\hat{q}t_1}^{1/(\Delta b)^2} \frac{dk_{\perp 1}^2}{k_{\perp 1}^2}, \qquad (A.29)$$

where we have used (A.20). Fig. A.2a shows the integration region that is equivalent to the one shown before fig. 2.7. The single logarithms were analyzed in the LMW paper. There are some important regions that we will discuss:

(i) Double logarithms are generated by integrating over the interior of the shaded region,

$$\tau_0 \ll t_1 \ll \frac{1}{\hat{q}(\Delta b)^2}, \qquad \hat{q}t_1 \ll k_{\perp 1}^2 \ll \frac{1}{(\Delta b)^2}, \qquad (A.30)$$

such as the point labeled "A" in fig. A.2a. The double log will be proportional to the area of the shaded region in the log-log coordinates of the figure.

(ii) Single logarithms arise from integrating along the edges, e.g. over

$$\tau_0 \ll t_1 \ll \frac{1}{\hat{q}(\Delta b)^2}, \qquad k_{\perp 1}^2 \sim \frac{1}{(\Delta b)^2} \qquad (A.31)$$

for the upper edge in fig. A.2a, which is the edge most sensitive to the value of $\Delta b$. The red line representing the edge $k_{\perp 1}^2 \sim 1/(\Delta b)^2$ should be thought of as having an $O(1)$ thickness in the log-log coordinates used in the figure. The same applies for the other edges and in the limit of the large logarithms, the $O(1)$ thickness of the edges is parametrically small compared to the size of the shaded, double-log region. The point labeled "D" in figure A.3a gives an example of the contribution to the single log.

(iii) No logarithms are generated by the corners, such as

$$\tau_0 \sim \frac{1}{\hat{q}(\Delta b)^2} \, , \qquad k_{\perp 1}^2 \sim \frac{1}{(\Delta b)^2} \, , \tag{A.32}$$

which is labeled "$\gamma$" in the figure.

One can think of the single-log piece as the difference between (a) the full integral over all $(\omega_1, t_1)$ and (b) the double-log approximation (A.29). We will call the integral that gives the difference:

$$\overline{\alpha}_{\mathrm{s}} \hat{q}_{(0)} \int \frac{dt_1}{t_1} \int \frac{dk_{\perp 1}^2}{k_{\perp 1}^2} \, F_{\mathrm{sl}}(t_1, k_{\perp 1}^2), \tag{A.33}$$

where $F_{\mathrm{sl}}$ has support on the edges of the double log region and falls rapidly towards zero as $(Y_1, \rho_1)$ moves away from those edges in fig. A.3a. The subscript "sl" stands for "single log." The important property of $F_{\mathrm{sl}}$ is that it will be uniform along each individual edge, where we mean that the integration of $F_{\mathrm{sl}}$ over the direction perpendicular to an edge gives (to good approximation in the large-log limit) the same result everywhere along that edge. The uniformity of each edge means that the contribution of each edge to (A.33) will be proportional to a single logarithm, with a coefficient depending on the details of how $F_{\mathrm{sl}}$ behaves near that edge.
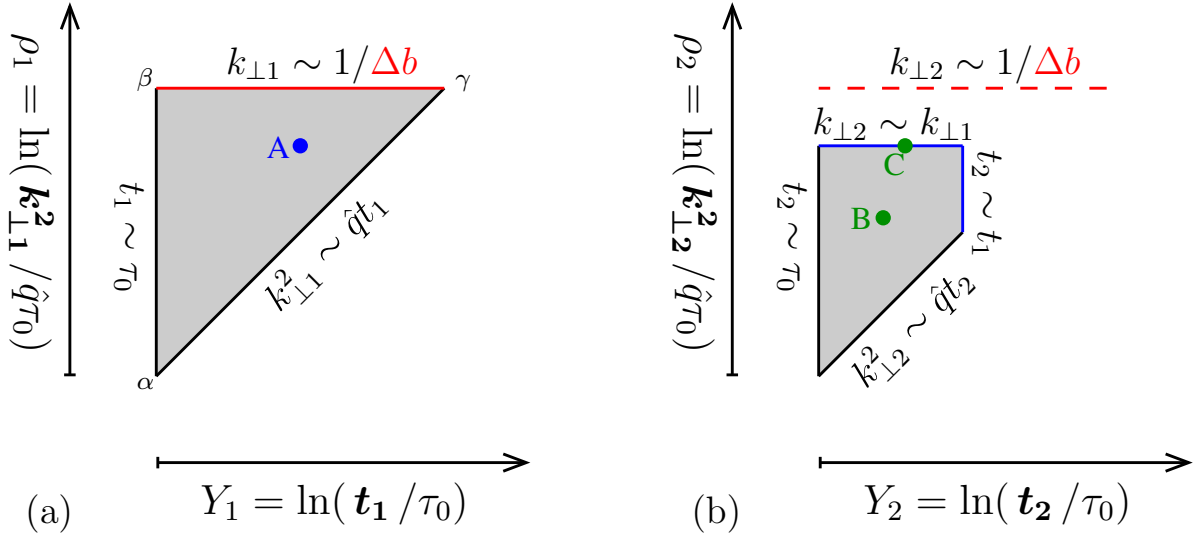
Figure A.2: (a) The double-log region of fig. 2.7 in terms of the variables $(Y, \rho)$ of (A.25). (a+b) A depiction of the leading-log region at order $O(\alpha_s^2)$. In this figure, the extent of the $(Y_2, \rho_2)$ region is drawn for the case where $(Y_1, \rho_1)$ is at point "A."
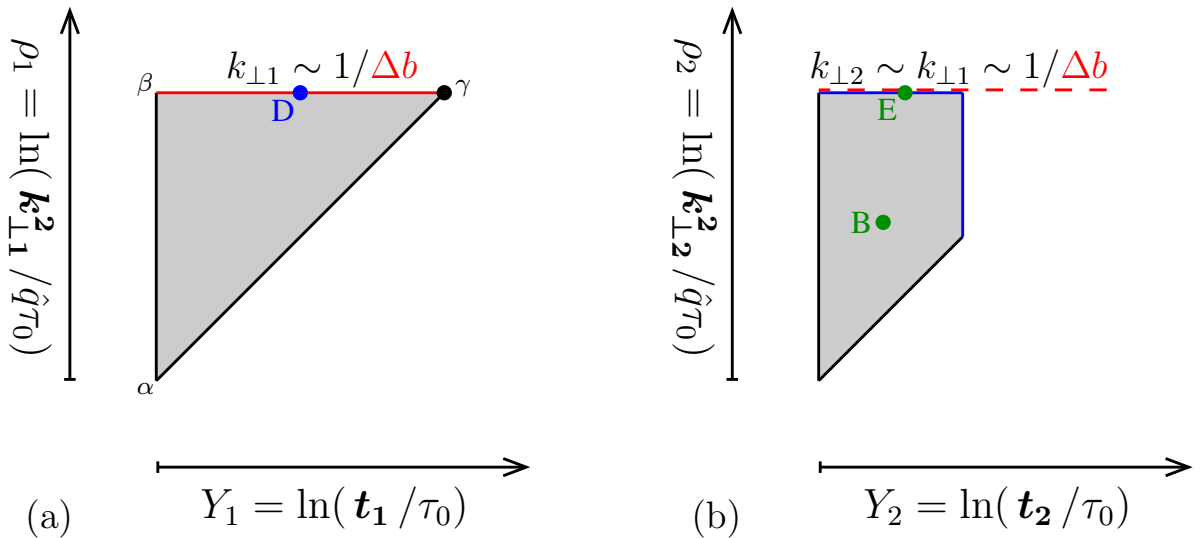


Figure A.3: Like fig. A.2, but here the extent of the $(Y_2, \rho_2)$ region is drawn for the case where $(Y_1, \rho_1)$ is at point "D."

160

Let's give an example. Consider the edge (A.31) that is sensitive to the physics of $k_\perp \sim 1/\Delta b$. The formula for $F_{\rm sl}$ along that edge may be extracted from LMW [30] in terms of the variables $(t_1, \omega_1)$:[9]

$$F_{\rm sl} \simeq F_{\rm sl}^{\rm approx} = \mathrm{Re}\left\{ \frac{1}{3} \left[ \left( 1 + \frac{i\omega_1 (\Delta b)^2}{2t_1} \right) e^{i\omega_1 (\Delta b)^2 / 2t_1} + 2i \frac{(1 - e^{i\omega_1 (\Delta b)^2 / 2t_1})}{\omega_1 (\Delta b)^2 / 2t_1} \right] - \theta\left( \frac{\omega_1 (\Delta b)^2}{2t_1} < 1 \right) \right\}. \quad (A.34)$$

The detailed expression does not matter except to explicitly confirm the important point that this edge's $F_{\rm sl}$ is a function of only $\omega_1 (\Delta b)^2 / 2t_1$. Because $t_1 \approx 2\omega_1 / k_{\perp 1}^2$ in this region of vacuum-like emissions, the $F_{\rm sl}(t_1, k_{\perp 1}^2)$ of (A.33) is now a function only of $k_{\perp 1}^2 (\Delta b)^2$ near the red edge of fig. A.3a, and $k_{\perp 1}^2$ is the variable that parameterizes the direction perpendicular to that edge. This is an example of how $F_{\rm sl}$ is "uniform" along an edge, which means that $F_{\rm sl}^{\rm approx}(t_1, k_{\perp 1}^2) \simeq F_{\rm sl}^{\rm approx}\big((k_{\perp 1} \Delta b)^2\big)$ does not depend on $t_1$.

Because (A.34) is localized near the edge, the limits of $dk_{\perp 1}^2$ integral in (A.33) that is perpendicular to the edge (A.31) can be replaced by 0 to $\infty$ (within the large-log

---

[9]This comes from eq. (32) of ref. [30], where $S$ is $-\frac{1}{4}\hat{q}_{\rm eff} x_\perp^2 L$ and where there is an implicit $\mathrm{Re}\{\cdots\}$ on the right-hand side. Our $\delta\hat{q}_{\rm eff}$ then corresponds to integrating the right-hand side of their (32) with integral

$$-\frac{4}{x_\perp^2 L} \int \frac{d\omega}{\omega}.$$

Comparing to the $(\omega, t)$ version

$$\overline{\alpha}_{\rm s} \hat{q}_{(0)} \int \frac{dt_1}{t_1} \int \frac{d\omega_1}{\omega_1} F_{\rm sl}$$

of our (A.33) then determines $F_{\rm sl}$, except that we must subtract away the double log piece already included in the $n{=}1$ version of (A.24), where the edge we are focused on is the upper limit $t_1/(\Delta b)^2$ of the $\omega_1$ integration there. That subtraction is implemented by the last term in our (A.34). We've written the argument of the $\theta$ function to match the $k_{\perp 1}^2 \leq 1/(\Delta b)^2$ condition in the (A.16) version of the leading-log resummation.

approximation). This leads to

$$\int_0^\infty \frac{dk_{\perp 1}^2}{k_{\perp 1}^2} F_{\rm sl}^{\rm approx}\big((k_{\perp 1}\Delta b)^2\big) = \int_0^\infty \frac{du}{u} F_{\rm sl}^{\rm approx}(u) = \text{an } O(1) \text{ constant independent of } \Delta b \tag{A.35}$$

for that edge. The total result for double and single logs will have the form

$$\hat{q}_{\rm eff}(\Delta b) = \hat{q}_{(0)} + \delta\hat{q}(\Delta b) \simeq \hat{q}_{(0)} \left\{ 1 + \frac{\overline{\alpha}_{\rm s}}{2} \left[ \ln^2\left(\frac{1}{\hat{q}\tau_0(\Delta b)^2}\right) + \kappa \ln\left(\frac{1}{\hat{q}\tau_0(\Delta b)^2}\right) \right] \right\}, \tag{A.36}$$

where the single-log coefficient $\kappa$ is some constant[10] that is independent of $\Delta b$. Eq. (A.36) refines (2.48) to now include the single log term. The large single log does not generate any large $\Delta b$ dependence when included in our earlier discussion of section 2.2.2. This is because we are interested in $\Delta b \sim \mathcal{B}_0$ as in (2.47), and we can write the single log term (A.36) as

$$\kappa \ln\left(\frac{1}{\hat{q}\tau_0(\Delta b)^2}\right) = \kappa \ln\left(\frac{1}{\hat{q}\tau_0\mathcal{B}_0^2}\right) - \kappa \ln\left(\frac{(\Delta b)^2}{\mathcal{B}_0^2}\right). \tag{A.37}$$

the first term on the right hand side is a large logarithm but does not depend on $\Delta b$, but the second term depends on $\Delta b$ but is not a large logarithm and so will not need to be resummed.

---

[10]For details, see eq. (45) of LMW [30], where $\underline{x}$ and $l_0$ are our $\Delta b$ and $\tau_0$. Divide both sides of that equation by $L$ to get $\hat{q}_{\rm eff}$, and use the translation (A.21) to replace the remaining occurrences of $L$ by $1/\hat{q}(\Delta b)^2$. Note that this replaces their $\ln(8ml_0/\underline{x}^2\hat{q}L)$ by a $\Delta b$-independent constant of $O(1)$. The $ml_0$ and the integral in that formula arise from the boundary $t_1 \sim \tau_0$ in our fig. A.2a [what they call "boundary (c)"]. Since this boundary does not generate a logarithm with large dependence on the exact value of $\Delta b \sim \mathcal{B}_0$, we can ignore it in our analysis. We may also ignore the various complications in the analysis of this boundary, recently investigated by Ghiglieri and Weitz [55] for the case of a quark-gluon plasma.

### A.3.3 $\Delta b$ dependence at NLLO and NNLLO

Let's now consider the $n=2$ case of (A.16) which is the next order in $\alpha_{\mathrm{s}}$. This generates an $O(\alpha_{\mathrm{s}}^2 \log^4)$ contribution to $\hat{q}_{\mathrm{eff}}$ which corresponds to the combination of the shaded regions of figs. A.2a and b. For example, the combined pair AB in the interior of the figure produces the leading log. The combined pair AC contributes to NLLO order, which is $O(\alpha_{\mathrm{s}}^2 \log^3)$ for $n = 2$. This corresponds to

$$\frac{1}{\Delta b} \gg k_{\perp 1} \sim k_{\perp 2}. \tag{A.38}$$

If we continue on to yet higher orders in $\alpha_{\mathrm{s}}$, the contributions at NLLO order that involves a pair like AC will have

$$\frac{1}{\Delta b} \gg k_{\perp 1} \sim k_{\perp 2} \gg k_{\perp 3} \gg \cdots. \tag{A.39}$$

None of the points will be sensitive to the exact value of $\Delta b$, and so none of these contributions contribute to what we're interested in, which is the $\Delta b$ dependence of resummed $\hat{q}_{\mathrm{eff}}$.

Now we look at the combination of figs. A.3a and b, with $(t_1, k_{\perp 1}^2)$ along the edge $k_{\perp 1} \sim 1/\Delta b$. Note that if $(t_1, k_{\perp 1}^2)$ were at the vertex $\gamma$, then we would not get any logs from the $(t_1, k_{\perp 1}^2)$ integration, and so this would be a NNLLO contribution instead of an NLLO one. At NLLO, we can replace the upper limit $1/\hat{q}(\Delta b)^2$ of (A.20) on the $t_1$ integration by $1/\hat{q}\mathcal{B}_0^2$ which will only affect NNLLO.

We will focus on combinations like DB, which contributes with

$$\frac{1}{\Delta b} \sim k_{\perp 1} \gg k_{\perp 2} \gg k_{\perp 3} \gg \cdots. \tag{A.40}$$

We cannot have $(t_2, \omega_2)$, $(t_3, \omega_3)$,... on an edge because this will cost us a logarithm other than the one we have already lost by placing $(t_1, \omega_1)$ on an edge (e.g. point D in the figure), and so this would move us to NNLLO instead of NLLO. So we may use the leading-log approximation for all the $(t_i, \omega_i)$ integrals except for $(t_1, \omega_1)$. For the same reason, the $k_{\perp 2}$ integration in (A.16) does not care about the exact value of $k_{\perp 1}$ at this order, only its order of magnitude, and we can replace the upper limit of the $k_{\perp 1}^2$ integration by $1/\mathcal{B}_0$ since $k_{\perp 1} \sim 1/\Delta b \sim 1/\mathcal{B}_0$ in (A.40). Altogether, NLLO contributions of type (A.40) then contribute

$$\overline{\alpha}_{\rm s}^n \hat{q}_{(0)} \int_{\tau_0}^{1/\hat{q}\mathcal{B}_0^2} \frac{dt_1}{t_1} \int_{k_{\perp 1} \sim 1/\Delta b} \frac{dk_{\perp 1}^2}{k_{\perp 1}^2} F_{\rm sl}(t_1, k_{\perp 1}^2) \int_{\tau_0}^{t_1} \frac{dt_2}{t_2} \int_{\hat{q}t_2}^{1/\mathcal{B}_0} \frac{dk_{\perp 2}^2}{k_{\perp 2}^2} \cdots \int_{\tau_0}^{t_{n-1}} \frac{dt_n}{t_n} \int_{\hat{q}t_n}^{k_{\perp,n-1}^2} \frac{dk_{\perp n}^2}{k_{\perp n}^2}$$

$$= \overline{\alpha}_{\rm s}^n \hat{q}_{(0)} \int_{\tau_0}^{1/\hat{q}\mathcal{B}_0^2} \frac{dt_1}{t_1} \int_{k_{\perp 1} \sim 1/\Delta b} \frac{dk_{\perp 1}^2}{k_{\perp 1}^2} F_{\rm sl}(t_1, k_{\perp 1}^2) f_{n-1}\Big(\ln\big(\tfrac{t_1}{\tau_0}\big), \ln\big(\tfrac{1}{\hat{q}\tau_0\mathcal{B}_0^2}\big)\Big) \quad \text{(A.41)}$$

to $\delta^n \hat{q}_{\rm eff}$ at NLLO. $f_n$ is again defined by (A.25) and (A.26b). The $k_{\perp 1}^2$ integral in (A.41) is the one presented in (A.35) and so is independent of $\Delta b$ (at this order in logs). Since there is no other $\Delta b$ in (A.41), we see that NLLO contributions from combinations like DB are independent of $\Delta b$.

For a combination like DE in fig. A.3, E would be sensitive to $\Delta b$ since $1/\Delta b \sim k_{\perp 1} \sim k_{\perp 2}$. But this is an NNLLO contribution, since both points are on edges.

We've now addressed the interesting cases. We conclude that NLLO does not generate any $\Delta b$ dependence not already included in the LLO result (A.16), which sums to the formula (2.49) used in the main text. Our analysis above suggests that additional $\Delta b$ dependence will appear at NNLLO, but that is beyond the scope of what is needed for this paper.

### A.3.4 A loose end: the prefactor of eq. (2.51)

Now we go back to eq. (2.51) where we have ignored a prefactor when discussing the $\Delta b$ dependence of the leading-log resummation. The leading term in the large-argument expansion of $I_1$ in (2.49) actually gives

$$\hat{q}_{\text{eff}}(\Delta b) \approx \hat{q}_{(0)} \left( \frac{1}{\hat{q}\tau_0(\Delta b)^2} \right)^{2\sqrt{\overline{\alpha}_{\text{s}}}} \times \frac{1}{\sqrt{4\pi}} \left[ \sqrt{\overline{\alpha}_{\text{s}}} \ln\left( \frac{1}{\hat{q}\tau_0(\Delta b)^2} \right) \right]^{-3/2} \tag{A.42}$$

instead of (2.51). Including the full prefactor, then changes (2.52) and (2.53) to

$$\hat{q}_{\text{eff}}(\Delta b) \approx \hat{q}_{(0)} \left( \frac{1}{\hat{q}\tau_0 \mathcal{B}_0^2} \right)^{2\sqrt{\overline{\alpha}_{\text{s}}}} \left[ 1 - 2\sqrt{\overline{\alpha}_{\text{s}}} \ln\left( \frac{(\Delta b)^2}{\mathcal{B}_0^2} \right) \right]$$
$$\times \frac{1}{\sqrt{4\pi}} \left[ \sqrt{\overline{\alpha}_{\text{s}}} \ln\left( \frac{1}{\hat{q}\tau_0 \mathcal{B}_0^2} \right) \right]^{-3/2} \left[ 1 - \frac{3\ln\left( (\Delta b)^2/\mathcal{B}_0^2 \right)}{2\ln(1/\hat{q}\tau_0 \mathcal{B}_0^2)} \right] \tag{A.43}$$

and

$$\hat{q}_{\text{eff}}(\Delta b) = \hat{q}_{\text{eff}}(\mathcal{B}_0) \left\{ 1 + O(\sqrt{\overline{\alpha}_{\text{s}}}) + O\left( \frac{1}{\ln(1/\hat{q}\tau_0 \mathcal{B}_0^2)} \right) \right\}. \tag{A.44}$$

When we make the large-argument expansion of $I_1$ in (2.51), we take the large-logarithm limit, where $\alpha_{\text{s}} \ln^2\left( 1/\hat{q}\tau_0(\Delta b)^2 \right) \sim \alpha_{\text{s}} \ln^2(1/\hat{q}\tau_0 \mathcal{B}_0^2)$ is $\gg 1$. So the $O(1/\log)$ term in (A.44) can be ignored compared to the $O(\sqrt{\overline{\alpha}_{\text{s}}})$ term, leaving us with (2.53).

## A.4 Asymptotic behavior of $\hat{\epsilon}_{\text{LO}}(\hat{z})$

We will derive here the asymptotic behavior of the energy deposition distribution $\epsilon_{\text{LO}}(z)$ for large $z$. We follow the same analysis of ref. [44] for the fall-off of the

leading-order charge distribution $\rho_{\mathrm{LO}}(z)$ at large $z$.[11] In that paper, the behavior was

$$\rho_{\mathrm{LO}}(z) \sim e^{-\Gamma_{\mathrm{LO}}(E_0)\,z} \tag{A.45}$$

for large $z$, where $\Gamma_{\mathrm{LO}}$ is the total leading-order rate for the relevant splitting process $e \to e\gamma$. Our case is different because the total rate for $g \to gg$ in $\hat{q}$ approximation is infinite because of the $x^{-3/2}$ [or symmetrically $(1-x)^{-3/2}$] IR divergence of eq. (1.2) for $[d\Gamma/dx]^{\mathrm{LO}}$, and so (A.45) suggests that the fall-off of our $\epsilon_{\mathrm{LO}}(z)$ must be faster than simple exponential decay. We find that our large-$z$ tail is approximately Gaussian.

The starting point will be the leading-order energy deposition equation (2.99):

$$\frac{\partial \hat{\epsilon}_{\mathrm{LO}}(\hat{z})}{\partial \hat{z}} = \int_0^1 dx\, x \left[\frac{d\hat{\Gamma}}{dx}\right]^{\mathrm{LO}} \left\{ x^{-1/2}\,\hat{\epsilon}_{\mathrm{LO}}(x^{-1/2}\hat{z}) - \hat{\epsilon}_{\mathrm{LO}}(\hat{z}) \right\}. \tag{A.46}$$

The $x \to 0$ contribution to the integration converges because (i) $x[d\hat{\Gamma}/dx]^{\mathrm{LO}} \sim x^{-1/2}$ and (ii) $\epsilon_{\mathrm{LO}}(z')$ should fall to zero faster than, for example, $(z')^{-1/2}$ as $z' \to \infty$. The $x \to 1$ contribution to the integration converges because (i) $x[d\hat{\Gamma}/dx]^{\mathrm{LO}} \sim (1-x)^{-3/2}$ and (ii) there is a cancellation between the two terms inside the braces:

$$\left\{ x^{-1/2}\,\hat{\epsilon}_{\mathrm{LO}}(x^{-1/2}\hat{z}) - \hat{\epsilon}_{\mathrm{LO}}(\hat{z}) \right\} \sim 1-x \text{ as } x \to 1. \tag{A.47}$$

We use the WKP-approximation to rewrite $\hat{\epsilon}_{\mathrm{LO}}(\hat{z})$ as

$$\hat{\epsilon}_{\mathrm{LO}}(\hat{z}) \equiv e^{-\mathcal{W}(\hat{z})}, \tag{A.48}$$

where, asymptotically, $\mathcal{W}(\hat{z})$ should be an increasing function of $\hat{z}$ so that $\epsilon_{\mathrm{LO}}(\hat{z}) \to 0$ as $\hat{z} \to \infty$. We plug (A.48) into the leading-order energy deposition equation (A.46)

---

[11]Specifically, see appendix B of ref. [44].

to get

$$\mathcal{W}'(\hat{z}) = \int_0^1 dx\, x \left[\frac{d\hat{\Gamma}}{dx}\right]^{\mathrm{LO}} \left\{1 - x^{-1/2} e^{\mathcal{W}(\hat{z}) - \mathcal{W}(x^{-1/2}\hat{z})}\right\}. \tag{A.49}$$

Let's more carefully examine the cancellation (A.47) as $x \to 1$, now in the language of (A.49). For this limit, we define $\delta \equiv 1 - x \ll 1$, which gives

$$\mathcal{W}(\hat{z}) - \mathcal{W}(x^{-1/2}\hat{z}) \simeq -\tfrac{1}{2}\hat{z}\,\mathcal{W}'(\hat{z})\,\delta \tag{A.50}$$

and so

$$\left\{1 - x^{-1/2} e^{\mathcal{W}(\hat{z}) - \mathcal{W}(x^{-1/2}\hat{z})}\right\} \simeq 1 - (1-\delta)^{-1/2} e^{-\frac{1}{2}\hat{z}\mathcal{W}'(\hat{z})\,\delta}. \tag{A.51}$$

$\hat{z}\mathcal{W}'(\hat{z})$ will be large for large $\hat{z}$. There are two regions of small $\delta$ to consider. For $x$ extremely close to 1, such that

$$\delta \ll \frac{1}{\hat{z}\,\mathcal{W}'(\hat{z})} \ll 1, \tag{A.52}$$

(A.51) gives,

$$\left\{1 - x^{-1/2} e^{\mathcal{W}(\hat{z}) - \mathcal{W}(x^{-1/2}\hat{z})}\right\} \simeq \tfrac{1}{2}\left[\hat{z}\mathcal{W}'(\hat{z}) - 1\right]\delta, \tag{A.53}$$

which vanishes linearly as $\delta \to 0$ and describes the cancellation (A.47). On the other hand, in the other small-$\delta$ region

$$\frac{1}{\hat{z}\,\mathcal{W}'(\hat{z})} \ll \delta \ll 1, \tag{A.54}$$

where $x$ is close but not arbitrarily close to 1, the exponential term in (A.51) will be suppressed, so that

$$\left\{1 - x^{-1/2} e^{\mathcal{W}(\hat{z}) - \mathcal{W}(x^{-1/2}\hat{z})}\right\} \simeq 1. \tag{A.55}$$

This means the $\delta^{-3/2}$ divergence of $x[d\hat{\Gamma}/dx]^{\mathrm{LO}}$ will not be tamed in the integration

region (A.54), and so (when $\hat{z}$ is large) the integral in (A.49) is dominated

$$\delta \sim \frac{1}{\hat{z}\,\mathcal{W}'(\hat{z})} \ll 1, \tag{A.56}$$

which is the transition between the lower end of region (A.54) and region (A.52). We can approximate the full integral (A.49) by approximating $\delta \ll 1$ in the integrand, which corresponds to the approximation (A.51). We can also use the $\delta \ll 1$ approximation to also rewrite,

$$(1 - \delta)^{-1/2} \simeq e^{\delta/2}, \qquad x\left[\frac{d\hat{\Gamma}}{dx}\right]^{\text{LO}} \simeq \frac{1}{\pi\delta^{3/2}}, \tag{A.57}$$

and so (A.49) becomes

$$\mathcal{W}'(\hat{z}) \simeq \int_0^\infty \frac{d\delta}{\pi\delta^{3/2}}\left\{1 - e^{-\frac{1}{2}[\hat{z}\,\mathcal{W}'(\hat{z})-1]\delta}\right\}. \tag{A.58}$$

We also replaced the upper limit of integration by $\infty$. This will introduce a negligible relative error in the large-$\hat{z}$ limit for the same reason that $\delta \ll 1$ dominated over $\delta \sim 1$. The integral gives

$$\mathcal{W}'(\hat{z}) \simeq \sqrt{\tfrac{2}{\pi}\left[\hat{z}\,\mathcal{W}'(\hat{z}) - 1\right]}. \tag{A.59}$$

We can simplify our equation more by remembering that $\hat{z}\,\mathcal{W}'(\hat{z}) \gg 1$ in the large $\hat{z}$ limit, so that (A.59) becomes

$$\mathcal{W}'(\hat{z}) \simeq \sqrt{\tfrac{2}{\pi}\,\hat{z}\,\mathcal{W}'(\hat{z})}. \tag{A.60}$$

Now we solve for $\mathcal{W}$ gives

$$\mathcal{W}(\hat{z}) \simeq \frac{\hat{z}^2}{\pi} \tag{A.61}$$

at large $\hat{z}$, which is equivalent to the asymptotic behavior quoted in (2.100):

$$\hat{\epsilon}_{\mathrm{LO}}(\hat{z}) \sim e^{-\hat{z}^2/\pi}. \tag{A.62}$$

Once we had completed enough of the argument to realize that the calculation of $\mathcal{W}(\hat{z})$ would be dominated by $\delta \ll 1$, we could have replaced $[d\Gamma/dx]^{\mathrm{LO}}$ by the BIM [28] model rate (A.64), which agrees with $[d\Gamma/dx]^{\mathrm{LO}}$ in the limits $x \to 0$ and $x \to 1$. Then, we could have extracted (A.62) from the energy deposition distribution (A.68) of the BIM model.

We could improve our approximation of large-$\hat{z}$ approximation to $\mathcal{W}$ by computing $O(\hat{z})$ corrections to the exponent in (A.62) and even further to find power-law prefactors to the exponential.[12] However, we find that in practice that (A.62) is enough for good numerical convergence of our results in the large-$\hat{z}_{\mathrm{max}}$ limit.

## A.5 $\epsilon_{\mathrm{LO}}(\hat{z})$ in the BIM model

Using the formula $P_{g \to gg}(x) = 2C_{\mathrm{A}}(1 - x + x^2)^2/x(1-x)$ for the DGLAP splitting function, the LO splitting rate (1.2) can be rewritten as

$$\left[\frac{d\Gamma}{dx}\right]^{\mathrm{LO}} = \frac{C_{\mathrm{A}}\alpha_{\mathrm{s}}(1-x+x^2)^{5/2}}{\pi[x(1-x)]^{3/2}}\sqrt{\frac{\hat{q}_{\mathrm{A}}}{E}} . \tag{A.63}$$

Blaizot, Iancu, and Mehtar-Tani (BIM) [28] found that one can replace the leading-

---

[12]We do not expect these corrections to be the same as the BIM model result (A.68).

order splitting rate (A.63) by the simpler function

$$\left[\frac{d\Gamma}{dx}\right]_{\text{BIM}} = \frac{C_{\text{A}}\alpha_{\text{s}}}{\pi[x(1-x)]^{3/2}}\sqrt{\frac{\hat{q}_{\text{A}}}{E}},\tag{A.64}$$

which would make it possible to solve the leading-order shower development analytically. We refer to this as the BIM model of shower development. The BIM rate is equal to the actual LO rate in the limit that one of the two daughters is soft, i.e. $x(1-x) \ll 1$. However, for perfectly democratic splitting $x = 0.5$, the BIM rate overestimates the LO BDMPS-Z rate by a factor of $(4/3)^{5/2} \simeq 2$. Their analytic solution, in our notation, for the time development of the gluon density in $x$ is

$$\hat{n}_{\text{BIM}}(x,\hat{t}) = \frac{\hat{t}\,e^{-\hat{t}^2/\pi(1-x)}}{\pi[x(1-x)]^{3/2}} \quad \text{for } x > 0,\tag{A.65}$$

with $\hat{t} \equiv t/\ell_0$, and $\ell_0$ defined by (2.88).

The energy which is still moving in the medium ($x > 0$) at time $t$ is

$$E_{\text{moving}}(t) = \int_{0^+}^{1} dx\, xE_0\, n(x, E_0, t).\tag{A.66}$$

It decreases with time because the energy is deposited into the medium, and so

$$\epsilon(z) = -\frac{dE_{\text{moving}}}{dt}\bigg|_{t=z} = -\left[\frac{d}{dt}\int_{0^+}^{1} dx\, xE_0\, n(x, E_0, t)\right]_{t=z}.\tag{A.67}$$

After switching to the dimensionless variables (2.97) and plugging in the BIM solution (A.65) yields[13]

$$\hat{\epsilon}(\hat{z}) = -\frac{d}{d\hat{z}}\,e^{-\hat{z}^2/\pi} = \frac{2\hat{z}}{\pi}\,e^{-\hat{z}^2/\pi}.\tag{A.68}$$

---

[13]One way to do the $x$ integral is to switch integration variable to $u \equiv \sqrt{x/(1-x)}$, which leads to a simple Gaussian integral in $u$.

The corresponding stopping distance is

$$\hat{\ell}_{\text{stop}}^{\text{BIM}} = \langle \hat{z} \rangle_{\text{BIM}} = \frac{\pi}{2}, \tag{A.69}$$

and the shape function (2.2) is then

$$S_{\text{BIM}}(Z) = \frac{\pi Z}{2} e^{-\pi Z^2/4}. \tag{A.70}$$

The BIM stopping distance $\langle \hat{z} \rangle_{\text{BIM}} \simeq 1.571$ is shorter than the LO stopping distance $\langle \hat{z} \rangle_{\text{LO}} \simeq 2.1143$ of table 2.2 because the BIM rate (A.64) overestimates the splitting rate for democratic splittings. Other moments of the BIM energy stopping distribution are

$$\langle \hat{z}^n \rangle_{\text{BIM}} = \pi^{n/2} \Gamma\left(1 + \tfrac{n}{2}\right). \tag{A.71}$$

## A.6 Energy conservation for eq. (2.117)

We show here that the evolution equation (2.117) for $D(\zeta, E_0, t)$ conserves energy. First, integrate both sides of the equation over $\zeta$ and then switch the order of the integration on the right-hand side to get

$$\frac{dE_{\text{total}}}{dt} = \int_0^1 dx \int_0^1 d\zeta \left\{ \theta(x > \zeta) \left[ \frac{d\Gamma}{dx}\left(\tfrac{\zeta E_0}{x}, x\right) \right]_{\text{net}} D\left(\tfrac{\zeta}{x}, E_0, t\right) \right.$$
$$\left. - x \left[ \frac{d\Gamma}{dx}(\zeta E_0, x) \right]_{\text{net}} D(\zeta, E_0, t) \right\}. \tag{A.72}$$

The $\zeta$ integral of the first term can be rewritten as

$$\int_0^x d\zeta \left[ \frac{d\Gamma}{dx}\left(\tfrac{\zeta E_0}{x}, x\right) \right]_{\text{net}} D\left(\tfrac{\zeta}{x}, E_0, t\right) = \int_0^1 d\zeta' x \left[ \frac{d\Gamma}{dx}(\zeta' E_0, x) \right]_{\text{net}} D(\zeta', E_0, t), \tag{A.73}$$

where $\zeta' \equiv \zeta/x$. The first term of (A.72) then cancels the second term, giving $dE_{\text{total}}/dt = 0$.

# Appendix B

# Chapter 3 appendices

## B.1 More on $(s, t, u)$ channel color singlet states

### B.1.1 Sign conventions and conversions

We chose the sign conventions for $u$-channel states based on translating the $s$-channel results for the potential $V(\boldsymbol{C}_{12}, \boldsymbol{C}_{34})$ in eqs. (4.3) and (3.12a) of ref. [42] to the $u$-channel version shown here in (3.8). The translation is to relabel the particles $(1, 2, 3, 4)$ there as $(4, 1, 2, 3)$ here, and so we take the basis of our color states (3.7) to be similarly permuted:

$$(1, 2, 3, 4) \longrightarrow (4, 1, 2, 3) \qquad [\text{for } s \to u] \tag{B.1}$$

to go from $s$-channel $|R\rangle_s$ to $u$-channel $|R\rangle_u$. We will write our formulas (3.10) here for the matrices $\underline{S}_u$ and $\underline{T}_u$ just like the corresponding $s$-channel versions in eq. (5.6) of ref. [42], since we have used the same permutations to define our $u$-channel states.

However, (B.1) is not how $u$-channel states were defined in ref. [42]. There, $t$-channel

states were first defined by[1]

$$2 \leftrightarrow 3 \qquad [\text{for } s \to t], \tag{B.2}$$

and then $u$-channel states were defined in terms of $t$-channel states by[2]

$$3 \leftrightarrow 4 \qquad [\text{for } t \to \bar{u}], \tag{B.3}$$

where we will use $\bar{u}$ to denote the $u$-channel conventions of ref. [42]. Performing (B.2) followed by (B.3) gives

$$(1, 2, 3, 4) \longrightarrow (1, 4, 2, 3) \qquad [\text{for } s \to \bar{u}] \tag{B.4}$$

We can see now that the difference between our $u$-channel convention on the right-hand side of (B.1) and the convention on the right-hand side of (B.4) is

$$1 \leftrightarrow 4 \qquad [\text{for } u \to \bar{u}], \tag{B.5}$$

This will negate the states that involve the antisymmetric combinations of particles 1 and 4. From (3.6), these states are $|A_{aa}\rangle_u$ and $|``\mathbf{10} + \overline{\mathbf{10}}"\rangle_u$ as we can see from (3.6).

---

[1]See, for example, eqs. (2.14) vs. (2.15) of ref. [42].
[2]See eq. (2.9) of ref. [42].

174

This can be summarized as

$$
\begin{pmatrix} |\mathbf{1}\rangle_{\bar{u}} \\ |A_{aa}\rangle_{\bar{u}} \\ |A_{ss}\rangle_{\bar{u}} \\ |``\mathbf{10}+\overline{\mathbf{10}}"\rangle_{\bar{u}} \\ |``\mathbf{27}"\rangle_{\bar{u}} \\ |``\mathbf{0}"\rangle_{\bar{u}} \end{pmatrix} = P \begin{pmatrix} |\mathbf{1}\rangle_{u} \\ |A_{aa}\rangle_{u} \\ |A_{ss}\rangle_{u} \\ |``\mathbf{10}+\overline{\mathbf{10}}"\rangle_{u} \\ |``\mathbf{27}"\rangle_{u} \\ |``\mathbf{0}"\rangle_{u} \end{pmatrix} \quad \text{with} \quad P \equiv \begin{pmatrix} +1 & & & & & \\ & -1 & & & & \\ & & +1 & & & \\ & & & -1 & & \\ & & & & +1 & \\ & & & & & +1 \end{pmatrix}.
$$

(B.6)

We can convert (for any $N$) between $s$-channel and $t$-channel versions of the original basis states by refs. [42, 19, 36] as[3]

$$
\begin{pmatrix} |\mathbf{1}\rangle_{s} \\ |A_{aa}\rangle_{s} \\ |A_{ss}\rangle_{s} \\ |``\mathbf{10}+\overline{\mathbf{10}}"\rangle_{s} \\ |``\mathbf{27}"\rangle_{s} \\ |``\mathbf{0}"\rangle_{s} . \end{pmatrix} = V \begin{pmatrix} |\mathbf{1}\rangle_{t} \\ |A_{aa}\rangle_{t} \\ |A_{ss}\rangle_{t} \\ |``\mathbf{10}+\overline{\mathbf{10}}"\rangle_{t} \\ |``\mathbf{27}"\rangle_{t} \\ |``\mathbf{0}"\rangle_{t} . \end{pmatrix}
$$

(B.7)

---

[3]This specific conversion is adapted from table IV of ref. [42], which provides the entries of our (B.8) and whose last column provides the signs $P$ in our (B.9). See footnote 13 of ref. [42] for discussion of how those results are related to refs. [19, 36].

with

$$
V = \begin{pmatrix}
\frac{1}{N^2-1} & \sqrt{\frac{1}{N^2-1}} & \sqrt{\frac{1}{N^2-1}} & \sqrt{\frac{N^2-4}{2(N^2-1)}} & \frac{N}{2(N+1)}\sqrt{\frac{N+3}{N-1}} & \frac{N}{2(N-1)}\sqrt{\frac{N-3}{N+1}} \\[2mm]
& \frac{1}{2} & \frac{1}{2} & 0 & -\frac{1}{2}\sqrt{\frac{N+3}{N+1}} & \frac{1}{2}\sqrt{\frac{N-3}{N-1}} \\[2mm]
& & \frac{N^2-12}{2(N^2-4)} & -\sqrt{\frac{2}{N^2-4}} & \frac{N}{2(N+2)}\sqrt{\frac{N+3}{N+1}} & -\frac{N}{2(N-2)}\sqrt{\frac{N-3}{N-1}} \\[2mm]
& & & \frac{1}{2} & -\sqrt{\frac{(N-2)(N+3)}{8(N+1)(N+2)}} & -\sqrt{\frac{(N+2)(N-3)}{8(N-1)(N-2)}} \\[2mm]
& \text{(symmetric)} & & & \frac{N^2+N+2}{4(N+1)(N+2)} & \frac{1}{4}\sqrt{\frac{N^2-9}{N^2-1}} \\[2mm]
& & & & & \frac{N^2-N+2}{4(N-1)(N-2)}
\end{pmatrix}.
$$

$$\text{(B.8)}$$

Note that $V = V^\top = V^{-1}$. As explained in ref. [42], the conversion between the $s$-channel and the $u$-channel basis of that paper is correspondingly

$$
\begin{pmatrix}
|\mathbf{1}\rangle_s \\
|\mathrm{A_{aa}}\rangle_s \\
|\mathrm{A_{ss}}\rangle_s \\
|\text{``}\mathbf{10+\overline{10}}\text{''}\rangle_s \\
|\text{``}\mathbf{27}\text{''}\rangle_s \\
|\text{``}\mathbf{0}\text{''}\rangle_s .
\end{pmatrix}
= PV
\begin{pmatrix}
|\mathbf{1}\rangle_{\bar{u}} \\
|\mathrm{A_{aa}}\rangle_{\bar{u}} \\
|\mathrm{A_{ss}}\rangle_{\bar{u}} \\
|\text{``}\mathbf{10+\overline{10}}\text{''}\rangle_{\bar{u}} \\
|\text{``}\mathbf{27}\text{''}\rangle_{\bar{u}} \\
|\text{``}\mathbf{0}\text{''}\rangle_{\bar{u}} .
\end{pmatrix}
\qquad \text{(B.9)}
$$

Using (B.6), we convert between the $s$-basis and $u$-basis in our convention here by (3.79a) with $U = PVP$, which equals (3.79b). It is sometimes useful to take the

$N=\infty$ limit of this matrix, which is

$$U^{N=\infty} = \begin{pmatrix} 0 & 0 & 0 & -\frac{1}{\sqrt{2}} & \frac{1}{2} & \frac{1}{2} \\ 0 & \frac{1}{2} & -\frac{1}{2} & 0 & \frac{1}{2} & -\frac{1}{2} \\ 0 & -\frac{1}{2} & \frac{1}{2} & 0 & \frac{1}{2} & -\frac{1}{2} \\ -\frac{1}{\sqrt{2}} & 0 & 0 & \frac{1}{2} & \frac{1}{2\sqrt{2}} & \frac{1}{2\sqrt{2}} \\ \frac{1}{2} & \frac{1}{2} & \frac{1}{2} & \frac{1}{2\sqrt{2}} & \frac{1}{4} & \frac{1}{4} \\ \frac{1}{2} & -\frac{1}{2} & -\frac{1}{2} & \frac{1}{2\sqrt{2}} & \frac{1}{4} & \frac{1}{4} \end{pmatrix}. \tag{B.10}$$

### B.1.2  Alternative descriptions for $N=\infty$

We show here the justification for (3.15). We will start from the potential $V$ is written in directly in terms of the transverse positions $(\boldsymbol{b}_1, \boldsymbol{b}_2, \boldsymbol{b}_3, \boldsymbol{b}_4)$ of the four individual particles instead of in terms of reduced variables such as the $(\boldsymbol{C}_{41}, \boldsymbol{C}_{23})$ of (3.8b). This more direct expression is [42][4]

$$\underline{V}(\boldsymbol{b}_1, \boldsymbol{b}_2, \boldsymbol{b}_3, \boldsymbol{b}_4) = \frac{i\hat{q}_{\mathrm{A}}}{4C_{\mathrm{A}}} \bigg\{ \mathbb{T}_1 \cdot \mathbb{T}_2 \big[ (\boldsymbol{b}_1 - \boldsymbol{b}_2)^2 + (\boldsymbol{b}_3 - \boldsymbol{b}_4)^2 \big]$$
$$+ \mathbb{T}_1 \cdot \mathbb{T}_3 \big[ (\boldsymbol{b}_1 - \boldsymbol{b}_3)^2 + (\boldsymbol{b}_2 - \boldsymbol{b}_4)^2 \big]$$
$$+ \mathbb{T}_1 \cdot \mathbb{T}_4 \big[ (\boldsymbol{b}_1 - \boldsymbol{b}_4)^2 + (\boldsymbol{b}_2 - \boldsymbol{b}_3)^2 \big] \bigg\}. \tag{B.11}$$

This expression only assumes the $\hat{q}$ approximation and not that the medium is itself weakly coupled. Now we will use the expressions (3.9)[5] for the $\mathbb{T}_i \cdot \mathbb{T}_j$ in terms of $\underline{S}_u$ and $\underline{T}_u$. Remember that for $N=\infty$ our basis states $(1, \mathrm{A}_+, \mathrm{A}_-, \mathrm{A}^\times, 1_+^\times, 1_-^\times)$ are

---

[4]Specifically, see eq. (3.10) of ref. [42].
[5]See also footnote 10.

simultaneous eigenstates of $\underline{S}_u$ and $\underline{T}_u$ with eigenvalues given by the corresponding diagonal entries of (3.14). Putting all of this together, we can write the explicit 4-particle potential for each of our basis states.

For example, for $|A_-\rangle$, we get from eq. (3.14) that $(S_u, T_u) = (\frac{1}{2}, -\frac{1}{4})$ for $N=\infty$. Now we use (3.9) to get that the potential (B.11) is then

$$V_{(A_-)}^{N=\infty}(\boldsymbol{b}_1, \boldsymbol{b}_2, \boldsymbol{b}_3, \boldsymbol{b}_4) = -\frac{i\hat{q}_A}{8}\Big[(\boldsymbol{b}_1-\boldsymbol{b}_2)^2 + (\boldsymbol{b}_2-\boldsymbol{b}_3)^2 + (\boldsymbol{b}_3-\boldsymbol{b}_4)^2 + (\boldsymbol{b}_4-\boldsymbol{b}_1)^2\Big]. \quad (B.12)$$

This is the large-$N$ behavior that we called "(1234)," where each particle can interact only with its neighbors going around the cylinder.

Doing the same for $|A^\times\rangle$, which has $(S_u, T_u) = (0,0)$ for $N=\infty$, gives,

$$V_{(A^\times)}^{N=\infty}(\boldsymbol{b}_1, \boldsymbol{b}_2, \boldsymbol{b}_3, \boldsymbol{b}_4) = -\frac{i\hat{q}_A}{8}\Big[(\boldsymbol{b}_1-\boldsymbol{b}_2)^2 + (\boldsymbol{b}_2-\boldsymbol{b}_4)^2 + (\boldsymbol{b}_4-\boldsymbol{b}_3)^2 + (\boldsymbol{b}_3-\boldsymbol{b}_1)^2\Big], \quad (B.13)$$

which corresponds to what we called (1243).

For $|1_-^\times\rangle$, which has $(S_u, T_u) = (0, -\frac{1}{2})$ for $N=\infty$, we get

$$V_{(1_-^\times)}^{N=\infty}(\boldsymbol{b}_1, \boldsymbol{b}_2, \boldsymbol{b}_3, \boldsymbol{b}_4) = -\frac{i\hat{q}_A}{4}\Big[(\boldsymbol{b}_1-\boldsymbol{b}_2)^2 + (\boldsymbol{b}_3-\boldsymbol{b}_4)^2\Big], \quad (B.14)$$

where particles 1 and 2 interact only with each other, and similarly particles 3 and 4 interact only with each other. This is what we called (12)(34). Note that the same applies for the rest of (3.15).

## B.2   Numerical method

Here we will discuss more the numerical methods we used. We didn't figure out the most efficient way but have used a brute-force approach implemented in Mathematica [59]. However, there are some issues we need to discuss.

First, we did the intermediate calculations with much more than machine precision in order to succeed in a brute force approach, because of round-off errors caused by subtractive cancellations. So all of the calculations are done using higher precision arithmetic in Mathematica.

Some formulas, like (3.51), involve derivatives such as $\partial_{j_1}\partial_{j_2}[\cdots]\Big|_{j_1=j_2=0}$ which are implemented numerically as

$$\partial_{j_1}\partial_{j_2}f(j_1,j_2)\Big|_{j_1=j_2=0} \simeq \frac{f(+\epsilon,+\epsilon)-f(+\epsilon,-\epsilon)-f(-\epsilon,+\epsilon)+f(-\epsilon,-\epsilon)}{(2\epsilon)^2} \qquad (\epsilon \text{ small})$$

$$(B.15)$$

rather than doing them analytically (or using a more sophisticated numerical estimate of the derivative).[6]

The numerical evaluation of matrix inverses and determinants is done by Mathematica. We found that doing the integral using Mathematica's adaptive integration routines took too much CPU time and caused a lot of problems. We tried to fix these

---

[6]If one wished to take the derivatives analytically, one could make use of small-$j$ expansions such as

$$\mathcal{U}^{-1} = \mathcal{U}_0^{-1} + \mathcal{U}_0^{-1}(j_1\mathcal{R}_1+j_2\mathcal{R}_2)\mathcal{U}_0^{-1} + j_1j_2\mathcal{U}_0^{-1}(\mathcal{R}_1\mathcal{U}_0^{-1}\mathcal{R}_2+\mathcal{R}_2\mathcal{U}_0^{-1}\mathcal{R}_1)\mathcal{U}_0^{-1} + O(j_1^2) + O(j_2^2)$$

and

$$\det(\mathcal{U}^{-1}) = \det(\mathcal{U}_0^{-1})\Big\{\big[1+j_1\,\mathrm{tr}(\mathcal{U}_0^{-1}\mathcal{R}_1)\big]\big[1+j_2\,\mathrm{tr}(\mathcal{U}_0^{-1}\mathcal{R}_2)\big]+j_1j_2\,\mathrm{tr}(\mathcal{U}_0^{-1}\mathcal{R}_1\mathcal{U}_0^{-1}\mathcal{R}_2)\Big\}+O(j_1^2)+O(j_2^2),$$

where we have promoted the 2×2 matrices $R_1$ and $R_2$ to 4×4 block-diagonal matrices by defining $\mathcal{R}_1 \equiv \left(\begin{smallmatrix} R_1 & \\ & 0 \end{smallmatrix}\right)$ and $\mathcal{R}_2 \equiv \left(\begin{smallmatrix} 0 & \\ & R_2 \end{smallmatrix}\right)$. However, this leads to more complicated formulas, which take extra CPU time to evaluate.

problems, but we gave up at the end and used midpoint Riemann sums. For the $\Delta t$ integral (as opposed to $t_1$ and $t_2$ integrals), we found it convenient to change variables as $\int_0^\infty d(\Delta t)\, f(\Delta t) = \int_{-\infty}^\infty dz\, e^z f(e^z)$. We also found that replacing the infinite $z$ integration region $(-\infty, +\infty)$ by a finite region $(z_{\min}, z_{\max})$ is adequate to cover everywhere the integrand is non-negligible [a choice which must be adjusted to study small values of $y$].

Our brute-force method, because it is not adaptive, will cost us an annoying number of numerical approximations one must check to be sure that the results are accurate, e.g. the size of the $\epsilon$ in the numerical derivatives, the number of Riemann intervals for the $(t_1, t_2, z)$ integrals, and the cut-offs $(z_{\min}, z_{\max})$.

Finally, we would like to mention the various checks we used to avoid human error in our analytical and numerical calculation. The result (3.41) for the $1/N^2$ correction $\delta^2 G$ to the 4-particle propagator was initially derived independently, and implemented numerically, by each of us in very different ways. One way was the method presented in the text, the other method did not use the compact way of writing the transverse-position integrations into higher-dimensional vectors and matrices like eqs. (3.21), (3.36) and (3.39) but instead did the Gaussian integrals separately and explicitly, resulting in very long mathematical expressions for $\delta^2 G$. Once the two methods agreed numerically, we then both switched to the method and code that most quickly produced results for $\delta^2 G$, which was the method based on (3.41). Now, using the same code for $\delta^2 G$, we each independently calculated the various results presented. Of course, we consulted each other on various methods and techniques [e.g. equations like (3.46)], and helped each other to spot sources of numerical discrepancy, our work was not completely independent, but the most error-prone aspects of our numerical work were done independently.

# Bibliography

[1]   L. D. Landau and I. Pomeranchuk. "Electron cascade process at very high-energies". In: *Dokl. Akad. Nauk Ser. Fiz.* 92 (1953), pp. 735–738.

[2]   L. D. Landau and I. Pomeranchuk. "Limits of applicability of the theory of bremsstrahlung electrons and pair production at high-energies". In: *Dokl. Akad. Nauk Ser. Fiz.* 92 (1953), pp. 535–536.

[3]   A. B. Migdal. "Bremsstrahlung and pair production in condensed media at high-energies". In: *Phys. Rev.* 103 (1956), pp. 1811–1820. DOI: 10.1103/PhysRev.103.1811.

[4]   G.'t Hooft. "A planar diagram theory for strong interactions". In: *Nuclear Physics B* 72.3 (1974), pp. 461–473. ISSN: 0550-3213. DOI: https://doi.org/10.1016/0550-3213(74)90154-0. URL: https://www.sciencedirect.com/science/article/pii/0550321374901540.

[5]   R P Bickerstaff et al. "3jm and 6j tables for some bases of SU6 and SU3". In: *Journal of Physics A: Mathematical and General* 15.4 (Apr. 1982), p. 1087. DOI: 10.1088/0305-4470/15/4/014. URL: https://dx.doi.org/10.1088/0305-4470/15/4/014.

[6]   Sidney Coleman. *Aspects of Symmetry: Selected Erice Lectures.* Cambridge University Press, 1985. DOI: 10.1017/CBO9780511565045.

[7]   R. Baier et al. "The Landau-Pomeranchuk-Migdal effect in QED". In: *Nucl. Phys. B* 478 (1996), pp. 577–597. DOI: 10.1016/0550-3213(96)00426-9. arXiv: hep-ph/9604327.

[8] B. G. Zakharov. "Fully quantum treatment of the Landau-Pomeranchuk-Migdal effect in QED and QCD". In: *JETP Lett.* 63 (1996), pp. 952–957. DOI: 10.1134/1.567126. arXiv: hep-ph/9607440.

[9] R. Baier et al. "Radiative energy loss of high-energy quarks and gluons in a finite volume quark - gluon plasma". In: *Nucl. Phys. B* 483 (1997), pp. 291–320. DOI: 10.1016/S0550-3213(96)00553-6. arXiv: hep-ph/9607355.

[10] R. Baier et al. "Medium induced radiative energy loss: Equivalence between the BDMPS and Zakharov formalisms". In: *Nucl. Phys. B* 531 (1998), pp. 403–425. DOI: 10.1016/S0550-3213(98)00546-X. arXiv: hep-ph/9804212.

[11] B. G. Zakharov. "Light cone path integral approach to the Landau-Pomeranchuk-Migdal effect". In: *Phys. Atom. Nucl.* 61 (1998), pp. 838–854. arXiv: hep-ph/9807540.

[12] K. Adcox et al. "Suppression of Hadrons with Large Transverse Momentum in Central $Au + Au$ Collisions at $\sqrt{s_{\mathrm{NN}}} = 130$GeV". In: *Phys. Rev. Lett.* 88 (2 Dec. 2001), p. 022301. DOI: 10.1103/PhysRevLett.88.022301. URL: https://link.aps.org/doi/10.1103/PhysRevLett.88.022301.

[13] C. Adler et al. "Centrality Dependence of High-$p_T$ Hadron Suppression in Au + Au Collisions at $\sqrt{s_{NN}} = 130$ GeV". In: *Phys. Rev. Lett.* 89 (20 Oct. 2002), p. 202301. DOI: 10.1103/PhysRevLett.89.202301. URL: https://link.aps.org/doi/10.1103/PhysRevLett.89.202301.

[14] J. Adams et al. "Evidence from $d + $Au Measurements for Final-State Suppression of High-$p_T$ Hadrons in Au + Au Collisions at RHIC". In: *Phys. Rev. Lett.* 91 (7 Aug. 2003), p. 072304. DOI: 10.1103/PhysRevLett.91.072304. URL: https://link.aps.org/doi/10.1103/PhysRevLett.91.072304.

182

[15]  S. S. Adler et al. "Absence of Suppression in Particle Production at Large Transverse Momentum in $\sqrt{s_{NN}} = 200$ GeV $d + $Au Collisions". In: *Phys. Rev. Lett.* 91 (7 Aug. 2003), p. 072303. DOI: 10.1103/PhysRevLett.91.072303. URL: https://link.aps.org/doi/10.1103/PhysRevLett.91.072303.

[16]  I. Arsene et al. "Transverse momentum spectra in Au+Au and d+Au collisions at s**(1/2) = 200-GeV and the pseudorapidity dependence of high p(T) suppression". In: *Phys. Rev. Lett.* 91 (2003), p. 072305. DOI: 10.1103/PhysRevLett.91.072305. arXiv: nucl-ex/0307003.

[17]  Henriette Elvang, Predrag Cvitanovic, and Anthony D. Kennedy. "Diagrammatic young projection operators for U(n)". In: (July 2003). arXiv: hep-th/0307186.

[18]  L. M. Kaplan and M. Resnikoff. "Matrix Products and the Explicit 3, 6, 9, and 12-j Coefficients of the Regular Representation of SU(n)". In: *Journal of Mathematical Physics* 8.11 (Dec. 2004), pp. 2194–2205. ISSN: 0022-2488. DOI: 10.1063/1.1705141. eprint: https://pubs.aip.org/aip/jmp/article-pdf/8/11/2194/11225135/2194\_1\_online.pdf. URL: https://doi.org/10.1063/1.1705141.

[19]  N. N. Nikolaev, W. Schafer, and B. G. Zakharov. "Nonlinear k(perpendicular)-factorization for gluon-gluon dijets produced off nuclear targets". In: *Phys. Rev. D* 72 (2005), p. 114018. DOI: 10.1103/PhysRevD.72.114018. arXiv: hep-ph/0508310.

[20]  Predrag Cvitanovic. *Group theory: Birdtracks, Lie's and exceptional groups.* 2008.

[21]    Peter Brockway Arnold. "Simple Formula for High-Energy Gluon Bremsstrahlung in a Finite, Expanding Medium". In: *Phys. Rev. D* 79 (2009), p. 065025. DOI: 10.1103/PhysRevD.79.065025. arXiv: 0808.2767 [hep-ph].

[22]    Peter Brockway Arnold, Sean Cantrell, and Wei Xiao. "Stopping distance for high energy jets in weakly-coupled quark-gluon plasmas". In: *Phys. Rev. D* 81 (2010), p. 045017. DOI: 10.1103/PhysRevD.81.045017. arXiv: 0912.3862 [hep-ph].

[23]    Collaboration CMS. "CMS collision events: from lead ion collisions". CMS Collection. 2010. URL: https://cds.cern.ch/record/1309898.

[24]    S. Chatrchyan et al. "Observation and studies of jet quenching in PbPb collisions at $\sqrt{s_{NN}} = 2.76$ TeV". In: *Phys. Rev. C* 84 (2 Aug. 2011), p. 024906. DOI: 10.1103/PhysRevC.84.024906. URL: https://link.aps.org/doi/10.1103/PhysRevC.84.024906.

[25]    Georges Aad et al. "Measurement of the jet radius and transverse momentum dependence of inclusive jet suppression in lead-lead collisions at $\sqrt{s_{NN}} = 2.76$ TeV with the ATLAS detector". In: *Phys. Lett. B* 719 (2013), pp. 220–241. DOI: 10.1016/j.physletb.2013.01.024. arXiv: 1208.1967 [hep-ex].

[26]    Georges Aad et al. "Observation of Associated Near-Side and Away-Side Long-Range Correlations in $\sqrt{s_{NN}} = 5.02$ TeV Proton-Lead Collisions with the ATLAS Detector". In: *Phys. Rev. Lett.* 110.18 (2013), p. 182302. DOI: 10.1103/PhysRevLett.110.182302. arXiv: 1212.5198 [hep-ex].

[27]    Betty Abelev et al. "Long-range angular correlations on the near and away side in $p$-Pb collisions at $\sqrt{s_{NN}} = 5.02$ TeV". In: *Phys. Lett. B* 719 (2013), pp. 29–41. DOI: 10.1016/j.physletb.2013.01.012. arXiv: 1212.2001 [nucl-ex].

184

[28]   Jean-Paul Blaizot, Edmond Iancu, and Yacine Mehtar-Tani. "Medium-induced QCD cascade: democratic branching and wave turbulence". In: *Phys. Rev. Lett.* 111 (2013), p. 052001. DOI: 10.1103/PhysRevLett.111.052001. arXiv: 1301.6102 [hep-ph].

[29]   Serguei Chatrchyan et al. "Observation of Long-Range Near-Side Angular Correlations in Proton-Lead Collisions at the LHC". In: *Phys. Lett. B* 718 (2013), pp. 795–814. DOI: 10.1016/j.physletb.2012.11.025. arXiv: 1210.5482 [nucl-ex].

[30]   Tseh Liou, A. H. Mueller, and Bin Wu. "Radiative $p_\perp$-broadening of high-energy quarks and gluons in QCD matter". In: *Nucl. Phys. A* 916 (2013), pp. 102–125. DOI: 10.1016/j.nuclphysa.2013.08.005. arXiv: 1304.7677 [hep-ph].

[31]   E. Iancu and D. N. Triantafyllopoulos. "Running coupling effects in the evolution of jet quenching". In: *Phys. Rev. D* 90.7 (2014), p. 074002. DOI: 10.1103/PhysRevD.90.074002. arXiv: 1405.3525 [hep-ph].

[32]   Edmond Iancu. "The non-linear evolution of jet quenching". In: *JHEP* 10 (2014), p. 095. DOI: 10.1007/JHEP10(2014)095. arXiv: 1403.1996 [hep-ph].

[33]   Bin Wu. "Radiative energy loss and radiative $p_\perp$-broadening of high-energy partons in QCD matter". In: *JHEP* 12 (2014), p. 081. DOI: 10.1007/JHEP12(2014)081. arXiv: 1408.5459 [hep-ph].

[34]   Peter Arnold and Shahin Iqbal. "The LPM effect in sequential bremsstrahlung". In: *JHEP* 04 (2015). [Erratum: JHEP 09, 072 (2016)], p. 070. DOI: 10.1007/JHEP09(2016)072. arXiv: 1501.04964 [hep-ph].

[35] Yacine Mehtar-Tani. "Renormalization of the jet-quenching parameter". In: *J. Phys. Conf. Ser.* 612 (2015), p. 012003. DOI: 10.1088/1742-6596/612/1/012003.

[36] Malin Sjodahl and Johan Thorén. "Decomposing color structure into multiplet bases". In: *JHEP* 09 (2015), p. 055. DOI: 10.1007/JHEP09(2015)055. arXiv: 1507.03814 [hep-ph].

[37] Peter Arnold, Han-Chih Chang, and Shahin Iqbal. "The LPM effect in sequential bremsstrahlung 2: factorization". In: *JHEP* 09 (2016), p. 078. DOI: 10.1007/JHEP09(2016)078. arXiv: 1605.07624 [hep-ph].

[38] Peter Arnold, Han-Chih Chang, and Shahin Iqbal. "The LPM effect in sequential bremsstrahlung: 4-gluon vertices". In: *JHEP* 10 (2016), p. 124. DOI: 10.1007/JHEP10(2016)124. arXiv: 1608.05718 [hep-ph].

[39] Peter Arnold, Han-Chih Chang, and Shahin Iqbal. "The LPM effect in sequential bremsstrahlung: dimensional regularization". In: *JHEP* 10 (2016), p. 100. DOI: 10.1007/JHEP10(2016)100. arXiv: 1606.08853 [hep-ph].

[40] Jean-Paul Blaizot and Yacine Mehtar-Tani. "Energy flow along the medium-induced parton cascade". In: *Annals Phys.* 368 (2016), pp. 148–176. DOI: 10.1016/j.aop.2016.01.002. arXiv: 1501.03443 [hep-ph].

[41] Peter Arnold and Shahin Iqbal. "In-medium loop corrections and longitudinally polarized gauge bosons in high-energy showers". In: *JHEP* 12 (2018), p. 120. DOI: 10.1007/JHEP12(2018)120. arXiv: 1806.08796 [hep-ph].

[42] Peter Arnold. "Landau-Pomeranchuk-Migdal effect in sequential bremsstrahlung: From large-$N$ QCD to $N$=3 via the SU($N$) analog of Wigner 6-$j$ symbols". In:

186

*Phys. Rev. D* 100.3 (2019), p. 034030. DOI: 10.1103/PhysRevD.100.034030. arXiv: 1904.04264 [hep-ph].

[43]  Peter Arnold. "Multi-particle potentials from light-like Wilson lines in quark-gluon plasmas: a generalized relation of in-medium splitting rates to jet-quenching parameters $\hat{q}$". In: *Phys. Rev. D* 99.5 (2019), p. 054017. DOI: 10.1103/PhysRevD.99.054017. arXiv: 1901.05475 [hep-ph].

[44]  Peter Arnold, Shahin Iqbal, and Tanner Rase. "Strong- vs. weak-coupling pictures of jet quenching: a dry run using QED". In: *JHEP* 05 (2019), p. 004. DOI: 10.1007/JHEP05(2019)004. arXiv: 1810.06578 [hep-ph].

[45]  B. G. Zakharov. "Color randomization of fast gluon-gluon pairs in the quark-gluon plasma". In: *J. Exp. Theor. Phys.* 128.2 (2019), pp. 243–258. DOI: 10.1134/S1063776119020146. arXiv: 1806.04723 [hep-ph].

[46]  Johannes Hamre Isaksen and Konrad Tywoniuk. "Wilson line correlators beyond the large-$N_c$". In: *JHEP* 21 (2020), p. 125. DOI: 10.1007/JHEP11(2021)125. arXiv: 2107.02542 [hep-ph].

[47]  Peter Arnold, Tyler Gorda, and Shahin Iqbal. "The problem of overlapping formation times: A (nearly) complete result for QCD". In: *PoS* HardProbes2020 (2021), p. 181. DOI: 10.22323/1.387.0181.

[48]  Peter Arnold. "Universality (beyond leading log) of soft radiative corrections to $\hat{q}$ in p broadening and energy loss". In: *JHEP* 03 (2022), p. 134. DOI: 10.1007/JHEP03(2022)134. arXiv: 2111.05348 [hep-ph].

[49]  Peter Arnold and Omar Elgedawy. "The LPM effect in sequential bremsstrahlung: $1/N_c^2$ corrections". In: *JHEP* 08 (2022), p. 194. DOI: 10.1007/JHEP08(2022)194. arXiv: 2202.04662 [hep-ph].

[50] Peter Arnold, Omar Elgedawy, and Shahin Iqbal. "Are gluon showers inside a quark-gluon plasma strongly coupled? a theorist's test". In: (Dec. 2022). arXiv: 2212.08086 [hep-ph].

[51] Peter Arnold, Tyler Gorda, and Shahin Iqbal. "The LPM effect in sequential bremsstrahlung: analytic results for sub-leading (single) logarithms". In: *JHEP* 04 (2022), p. 085. DOI: 10.1007/JHEP04(2022)085. arXiv: 2112.05161 [hep-ph].

[52] Peter Arnold, Tyler Gorda, and Shahin Iqbal. "The LPM effect in sequential bremsstrahlung: incorporation of "instantaneous" interactions for QCD". In: *JHEP* 11 (2022), p. 130. DOI: 10.1007/JHEP11(2022)130. arXiv: 2209.03971 [hep-ph].

[53] Paul Caucal and Yacine Mehtar-Tani. "Anomalous diffusion in QCD matter". In: *Phys. Rev. D* 106.5 (2022), p. L051501. DOI: 10.1103/PhysRevD.106.L051501. arXiv: 2109.12041 [hep-ph].

[54] Paul Caucal and Yacine Mehtar-Tani. "Universality aspects of quantum corrections to transverse momentum broadening in QCD media". In: *JHEP* 09 (2022), p. 023. DOI: 10.1007/JHEP09(2022)023. arXiv: 2203.09407 [hep-ph].

[55] Jacopo Ghiglieri and Eamonn Weitz. "Classical vs quantum corrections to jet broadening in a weakly-coupled Quark-Gluon Plasma". In: *JHEP* 11 (2022), p. 068. DOI: 10.1007/JHEP11(2022)068. arXiv: 2207.08842 [hep-ph].

[56] Peter Arnold, Omar Elgedawy, and Shahin Iqbal. "The LPM effect in sequential bremsstrahlung: gluon shower development". In: (Feb. 2023). arXiv: 2302.10215 [hep-ph].

[57]   M. Arslandok et al. "Hot QCD White Paper". In: (Mar. 2023). arXiv: 2303.17254 [nucl-ex].

[58]   Imanol Corredoira. "Measurements of collectivity in the forward region at LHCb". In: *EPJ Web Conf.* 276 (2023), p. 01022. DOI: 10.1051/epjconf/202327601022.

[59]   Wolfram Research Inc. *Mathematica, Version 13.2*. Champaign, IL, 2022. URL: https://www.wolfram.com/mathematica.